

論文 / 著書情報  
Article / Book Information

題目(和文)	LHC-ATLAS実験の重心系8TeV陽子陽子衝突における3つのレプトンと消失エネルギーを最終状態に含むチャージノー・ニュートラリーノ直接生成事象の探索
Title(English)	Search for direct production of charginos and neutralinos in final states with three leptons and missing transverse momentum in proton-proton collisions at $\sqrt{s} = 8$ TeV with the ATLAS detector
著者(和文)	永井遼
Author(English)	Ryo Nagai
出典(和文)	学位:博士(理学), 学位授与機関:東京工業大学, 報告番号:甲第9950号, 授与年月日:2015年9月25日, 学位の種別:課程博士, 審査員:陣内 修,久世 正弘,柴田 利明,河合 誠之,伊藤 克司
Citation(English)	Degree:., Conferring organization: Tokyo Institute of Technology, Report number:甲第9950号, Conferred date:2015/9/25, Degree Type:Course doctor, Examiner:,,,,,
学位種別(和文)	博士論文
Type(English)	Doctoral Thesis

Ph.D Thesis

Search for direct production of charginos and neutralinos  
in final states with three leptons and missing transverse momentum  
in proton-proton collisions at  $\sqrt{s} = 8 \text{ TeV}$  with the ATLAS detector

Ryo Nagai

*Department of Physics, Tokyo Institute of Technology*

August, 2015



# ABSTRACT

Search for direct production of charginos and neutralinos decaying via  $W$ ,  $Z$  or Higgs bosons is presented. The analysis is based on  $20.3 \text{ fb}^{-1}$  of proton-proton collision data with the centre-of-mass energy of  $\sqrt{s} = 8 \text{ TeV}$  delivered by the Large Hadron Collider and recorded with the ATLAS detector in 2012. This thesis discusses the search in the channels with three leptons ( $\ell = e, \mu, \tau$ ) and missing transverse momentum in final states, in particular the detail of the setting of the optimal selections and a method of estimating fake lepton contributions in order to achieve the best sensitivity with the acquired data.

The validation of the estimates of the Standard Model background works satisfactorily within the uncertainties. No significant deviation from the Standard Model expectation is observed. Exclusion limits for masses of the charginos and the neutralinos are set at 95% confidence level at simplified models for  $WZ$  and  $Wh$  decay channels, as

$$m_{\tilde{\chi}_1^\pm, \tilde{\chi}_2^0} > 360 \text{ GeV}, \text{ if } m_{\tilde{\chi}_1^0} = 0 \text{ GeV (} WZ \text{ channel),}$$

$$m_{\tilde{\chi}_1^\pm, \tilde{\chi}_2^0} > 150 \text{ GeV}, \text{ if } m_{\tilde{\chi}_1^0} = 0 \text{ GeV (} Wh \text{ channel).}$$

The exclusion limits for the  $Wh$  channel has been set for the first time.

The specific analysis for the scenario with the mass difference between the second lightest neutralino and the lightest neutralino of less than  $50 \text{ GeV}$  is also carried out. The region has leptons with low transverse momenta, hence it is difficult to suppress the fake contribution. In this thesis, the control method of the fakes are investigated and applied to the signal regions. The exclusion limit is set to the compressed mass scenario, as

$$m_{\tilde{\chi}_1^\pm, \tilde{\chi}_2^0} > 110 \text{ GeV}, \text{ if } \Delta m_{\tilde{\chi}_2^0, \tilde{\chi}_1^0} = 25 \text{ GeV (} WZ \text{ channel).}$$

These results are consistent with the CMS results. The interpretation for the scenario with the sleptons and the pMSSM are discussed. Discussions in terms of the dark matter limits and the deviation of the muon anomalous magnetic moment are given in this thesis.

The prospects for the improvement of this analysis for next LHC Run-2 are also discussed. The suppressing and estimating precisely for fakes are important for upcoming experiments.



# Contents

<b>1</b>	<b>Introduction</b>	<b>1</b>
1.1	The Standard Model . . . . .	2
1.1.1	Electroweak interaction . . . . .	3
1.1.2	Spontaneous Symmetry Breaking . . . . .	4
1.1.3	Higgs boson . . . . .	6
1.2	Remaining Problems in the Standard Model . . . . .	6
1.2.1	Hierarchy problem in the gauge theory . . . . .	7
1.2.2	Dark matter . . . . .	8
1.2.3	Muon Anomalous Magnetic Moment . . . . .	9
1.3	Supersymmetry . . . . .	9
1.3.1	Supersymmetry breaking . . . . .	12
1.3.2	SUSY models . . . . .	14
1.4	Electroweak gauginos . . . . .	15
1.4.1	Mass spectra . . . . .	15
1.4.2	Production modes . . . . .	16
1.4.3	Decay modes . . . . .	18
1.5	SUSY searches . . . . .	20
1.5.1	LEP Experiments . . . . .	20
1.5.2	Tevatron Experiments . . . . .	22
1.5.3	LHC Experiments . . . . .	23
1.5.4	Summary of the SUSY searches . . . . .	26
<b>2</b>	<b>LHC-ATLAS Experiment</b>	<b>27</b>
2.1	Overview of the LHC accelerator . . . . .	27
2.2	Overview of the ATLAS Detector System . . . . .	30
2.2.1	Variables used to specify the location in the detector . . . . .	30
2.2.2	Inner Detector . . . . .	31
2.2.3	Calorimeter . . . . .	34
2.2.4	Muon Spectrometer . . . . .	37
2.2.5	Magnets . . . . .	39
2.2.6	Forward Detector . . . . .	40
2.3	Triggering System . . . . .	41

2.3.1	Electron Triggers . . . . .	42
2.3.2	Muon Triggers . . . . .	43
<b>3</b>	<b>Particle Reconstruction</b>	<b>45</b>
3.1	Overview of the particle identification . . . . .	45
3.2	Tracking . . . . .	46
3.3	Vertex Reconstruction . . . . .	48
3.4	Electrons . . . . .	50
3.4.1	Cluster reconstruction . . . . .	50
3.4.2	Track matching . . . . .	51
3.4.3	Energy calibration . . . . .	51
3.4.4	Electron Identification . . . . .	52
3.4.5	Baseline Electron Definition . . . . .	52
3.4.6	Signal Electron Definition . . . . .	53
3.5	Muons . . . . .	54
3.5.1	Baseline Muon Definition . . . . .	54
3.5.2	Signal Muon Definition . . . . .	54
3.6	Jets . . . . .	55
3.6.1	Topological Clustering . . . . .	55
3.6.2	Anti- $k_r$ Algorithm . . . . .	55
3.6.3	Jet Calibration . . . . .	56
3.6.4	Jet Identification . . . . .	56
3.6.5	Tagging Heavy Flavour Jets . . . . .	57
3.6.6	Baseline Jet Definition . . . . .	58
3.6.7	Signal Jet Definition . . . . .	59
3.7	Taus . . . . .	59
3.7.1	Reconstruction . . . . .	59
3.7.2	Tau Identification . . . . .	59
3.7.3	Baseline Tau Definition . . . . .	60
3.7.4	Signal Tau Definition . . . . .	60
3.8	Overlap removal . . . . .	60
3.9	Missing transverse momentum . . . . .	61
<b>4</b>	<b>Data and Simulation Samples</b>	<b>63</b>
4.1	Monte Carlo Simulated samples . . . . .	63
4.1.1	The Standard Model MC samples . . . . .	63
4.1.2	New Physics MC samples . . . . .	65
4.2	Data taken in 2012 . . . . .	65
<b>5</b>	<b>Signal Region Optimisation</b>	<b>67</b>
5.1	Event pre-selection . . . . .	68
5.1.1	Trigger Selection . . . . .	68

5.1.2	Event Quality Cuts . . . . .	68
5.2	Statistical method . . . . .	69
5.3	Signal Regions for Category-A . . . . .	69
5.3.1	Decay via $WZ$ scenario . . . . .	71
5.3.2	Decay via $Wh$ scenario . . . . .	72
5.3.3	Sensitivity for the target scenarios . . . . .	83
5.4	Signal Regions for Category-B . . . . .	83
5.4.1	Signal Regions with three low $p_T$ leptons . . . . .	84
5.4.2	Signal Regions with three low $p_T$ leptons and ISR jets . . . . .	85
5.4.3	Sensitivity for the target scenarios . . . . .	88
<b>6</b>	<b>Background Estimation</b>	<b>91</b>
6.1	Monte Carlo simulation, for well-known background . . . . .	91
6.2	Estimation for reducible background . . . . .	92
6.2.1	Principle of the matrix method . . . . .	92
6.2.2	Matrix Method Procedure . . . . .	96
6.2.3	Fake Rates . . . . .	97
6.2.4	Scale Factor Measurement in Control Regions . . . . .	98
<b>7</b>	<b>Uncertainties</b>	<b>109</b>
7.1	Uncertainties on the irreducible backgrounds . . . . .	109
7.2	Uncertainties on the reducible backgrounds . . . . .	112
7.2.1	Uncertainties on the reducible background for signal regions . . . . .	114
7.3	Summary of Total Uncertainties for Signal Regions . . . . .	115
<b>8</b>	<b>Validation of the Background Modelling</b>	<b>117</b>
8.1	Validation with the MC closure test . . . . .	117
8.2	Validation Regions . . . . .	119
8.3	Validation with Data . . . . .	121
<b>9</b>	<b>Results and Interpretation</b>	<b>135</b>
9.1	Observed data . . . . .	135
9.2	Statistical Interpretation of Results . . . . .	140
9.2.1	Model-independent limits . . . . .	141
9.2.2	Model-dependent limits . . . . .	144
9.3	Discussion . . . . .	147
9.3.1	Comparison to the CMS analyses . . . . .	147
9.3.2	Improvement of the analyses . . . . .	148
9.3.3	Interpretation for “via sleptons” scenario and a pMSSM model . . . . .	149
9.3.4	Excesses in $SR0\tau_a$ . . . . .	151
9.3.5	Dark matter limits . . . . .	152
9.3.6	Muon $g - 2$ interpretation . . . . .	153



9.3.7	Signal acceptances in the $WZ$ compressed region . . . . .	155
9.3.8	Fake suppression in the optimisation stage . . . . .	157
<b>10</b>	<b>Conclusion</b>	<b>159</b>
<b>A</b>	<b>Monte Carlo Samples</b>	<b>179</b>
A.1	The Standard Model MC samples . . . . .	179
A.2	New Physics MC samples . . . . .	183

# Chapter 1

## Introduction

Seeking for the ultimate elements that compose our universe is an everlasting odyssey of humankind. The modern particle physics has had huge developments in the last decades to answer this fundamental question.

The established theory of the particle physics is composed of the description of the elementary particles that form the materials and their interactions. This theory has been successful, and is known as the Standard Model. It was verified by numerous experiments with high precision, and has a strong predictive power to almost all the phenomena in the particle physics processes. Furthermore, the last missing piece in the list of the Standard Model particles, which is called Higgs boson, has been finally discovered in 2012.

However, there are various intrinsic problems in the Standard Model. One is the internal contradiction in the theoretical framework, the other is the experimental observations that cannot be explained by the Standard Model. Therefore it is natural to look for the new theories or frameworks beyond the Standard Model. Although a great deal of new frameworks have been proposed hitherto, there were no clear hints ever for the new physics in the experimental data.

This thesis reports the results of a search for new particles with the data taken in 2012 at ATLAS experiment. First, in this chapter, the overview of the Standard Model for the particle physics and the problems of the theory will be discussed in Sec. 1.1 and Sec. 1.2, respectively. In Sec. 1.3, a possible candidate beyond the Standard Model, the Supersymmetry, is introduced, and the phenomena for the new physics are provided in order to be clear why it is important to study the theme of the thesis. Detail of the target scenario is shown in Sec. 1.4. The section describes the production and the decay modes of charginos and neutralinos. In Sec. 1.5, the results of the Supersymmetry searches from experiments operated until now will be presented. This section also summarises the importance of the search taken up in the thesis, based on the discussion up to there.

An explanation of a series of the experimental equipment used in the study is described in Chap. 2, the manner of the particle reconstruction in Chap. 3, the data and simulation samples in Chap. 4, and a detail discussion about a method of the event selection in Chap. 5. The important thing is the background estimation methods, which will be shown in Chap. 6. Uncertainties, validations of the background modelling and the final results will be shown in Chap. 7, Chap. 8 and Chap. 9, respectively. The interpretation for the models and the prospect for the upcoming experiments are also discussed in Chap. 9. Finally Chap. 10 summarises the study.

Table 1.1: Set of the Standard Model particles except the Higgs boson.

(a) The particles which compose materials (fermions).

	spin	charge	1st gen.	2nd gen.	3rd gen.
Quarks	1/2	+2/3	$u$ (up)	$c$ (charm)	$t$ (top)
	1/2	-1/3	$d$ (down)	$s$ (strange)	$b$ (bottom)
Leptons	1/2	0	$\nu_e$	$\nu_\mu$	$\nu_\tau$
	1/2	-1	$e$	$\mu$	$\tau$

(b) The Interactions and the corresponding bosons.

	strength	distance [cm]	potential	particle	spin	theory
Strong	$\sim 0.1$	$10^{-13}^*$	$k_1 \frac{1}{r} + k_2 r$	$g$	1	QCD <sup>†</sup>
Electromagnetic	1/137	$\infty$	$1/r$	$\gamma$	1	GWS <sup>‡</sup>
Weak	$10^{-5}$	$10^{-16}$	$\exp(-m_W r)/r$	$W^\pm, Z$	1	

\* Nuclear force.

† Quantum Chromodynamics

‡ Glashow-Weinberg-Salam theory

## 1.1 The Standard Model

The Standard Model (SM) of particle physics is the most comprehensive framework describing nature supported by numerous experimental validations. The SM claims that there are twelve fermion fields, four gauge fields and a Higgs field. There are corresponding elementary particles. The set of the SM particles except the Higgs boson is shown in Tab. 1.1. The SM fermions compose the matters. They can be divided into three generations, however, the particles of the first generation, which includes the up quark, the down quark, the electron and the electron neutrino, usually exist in nature. Since the neutrinos can interact only with the weak interaction, neutrinos are rarely observed. The gauge bosons are in charge of three kinds of interactions: strong, weak and electromagnetic interactions. Gluon  $g$ , which is the particle that mediates the strong interaction, makes a force among quarks. Weak bosons  $W^\pm, Z^0$  make a force with the weak interaction, which affects all of the SM fermions. Photon  $\gamma$  is the particle which mediates the electromagnetic interaction.

The interactions follow the gauge field theory of the Standard Model,  $SU(3)_C \times SU(2)_L \times U(1)_Y$ . The  $SU(3)_C$  component is the Quantum Chromodynamics (QCD), which is in charge of the strong interactions of coloured particles [1]. The colour is a quantum number of the strong interaction, which is introduced to solve the Fermi-Dirac statistics of quarks in hadrons [2]. The  $SU(2)_L \times U(1)_Y$  describes the electroweak interaction, which is composed of gauge fields  $W$  and  $B$  for the  $SU(2)_L$  and the  $U(1)_Y$ , respectively. This is based on the Glashow-Weinberg-Salam (GWS) theory [3–5], which integrates the electromagnetic and the weak interactions.

### 1.1.1 Electroweak interaction

The electromagnetic interaction is described by the Quantum Electrodynamics (QED). The QED introduces the electromagnetic gauge field  $A_\mu$ , which is required to satisfy the local gauge invariance:

$$A_\mu(x) \rightarrow A'_\mu(x) = A_\mu(x) + \partial_\mu \chi(x) \quad \text{in case} \quad \psi(x) \rightarrow \psi'(x) = e^{-iq\chi(x)} \psi(x), \quad (1.1)$$

where the  $\chi(x)$  expresses the local transformation factor which depends on the time and the space  $x$ . This phase transformation is categorised as the 1-dimensional unitary matrices  $U(1)_{\text{QED}}$ . In this case, there are no mass term in the QED Lagrangian, as

$$\mathcal{L}_{\text{QED}} = \bar{\psi} (i \not{D} - m) \psi - \frac{1}{4} F^{\mu\nu} F_{\mu\nu}, \quad (1.2)$$

$$\not{D} = \gamma^\mu (\partial_\mu + iqA_\mu), \quad (1.3)$$

$$F_{\mu\nu} = \partial_\mu A_\nu - A_\nu \partial_\mu, \quad (1.4)$$

where  $\gamma^\mu$  and  $F_{\mu\nu}$  are Dirac gamma matrices and the electromagnetic field tensor, respectively. The first term shows the covariant derivative and the second term shows the electromagnetic field interaction. The electromagnetic interaction has zero-mass gauge field, which is known as photon.

It is possible to discuss the weak interaction in similar manner to the QED. The fermion field doublet should be considered for the weak interaction:

$$\psi = \begin{pmatrix} \nu_e \\ e \end{pmatrix}, \begin{pmatrix} \nu_\mu \\ \mu \end{pmatrix}, \begin{pmatrix} \nu_\tau \\ \tau \end{pmatrix}. \quad (1.5)$$

In this case, this follows the special unitary group in 2 dimensions  $SU(2)$ , which was investigated as Yang-Mills theory [6]. In the same manner as the QED, the weak Lagrangian can be written as follows:

$$\mathcal{L}_{\text{weak}} = \bar{\psi} (i \not{D} - m) \psi - \frac{1}{4} \mathbf{W}^{\mu\nu} \cdot \mathbf{W}_{\mu\nu}, \quad (1.6)$$

$$\not{D} = \gamma^\mu \left( \partial_\mu + i \frac{g}{2} \mathbf{W}_\mu \cdot \boldsymbol{\sigma} \right), \quad (1.7)$$

where  $\boldsymbol{\sigma} = (\sigma^1, \sigma^2, \sigma^3)$  is Pauli matrix and  $g$  is a coupling constant.  $\mathbf{W}_\mu$  also has three fields,  $\mathbf{W}_\mu = (W^1, W^2, W^3)$ . Although Eq. (1.6) claims that the weak Lagrangian has no mass term, the observed weak bosons have masses. Even though we can put a mass term by hand, it induces the intrinsic breaks of the local gauge invariance of the Lagrangian  $\mathcal{L}_{\text{weak}}$ . Moreover, the observed phenomena suggest that the weak current is only left-handed, though the Lagrangian Eq. (1.6) does not explain why the parity is broken.

In order to solve these problems, the unification theory for the electromagnetic and the weak interactions is considered. This is called Glashow-Weinberg-Salam theory [3–5]. The unified gauge group  $SU(2)_L \times U(1)_Y$  is considered. The left-handed fermion fields transform as  $SU(2)_L$  doublet, and the right-handed fields do as singlet:

$$\psi_L = \begin{pmatrix} \nu_L \\ \ell_L \end{pmatrix} = \begin{pmatrix} \frac{1}{2}(1 - \gamma_5) \psi_\nu \\ \frac{1}{2}(1 - \gamma_5) \psi_\ell \end{pmatrix} \quad (1.8)$$

$$\psi_R = \frac{1}{2}(1 + \gamma_5) \psi_\ell, \quad (1.9)$$

where  $\gamma^5$  is the ‘‘fifth’’ gamma matrix  $\gamma^5 = i\gamma^0\gamma^1\gamma^2\gamma^3$ . At this time, the weak hypercharge  $Y$  is introduced as satisfying the following equation:

$$Q = T^3 + \frac{Y}{2}, \quad (1.10)$$

where  $Q$  is the electromagnetic charge and  $T^3$  is the third component of the weak isospin. Eq. (1.10) has the same structure known as Gell-Mann-Nishijima formula [7, 8]. Using the weak hypercharge and the weak isospin, the unified electroweak Lagrangian can be written with a similar expression as Eqs. (1.2) and (1.6), respectively. The covariant derivative terms are obtained from replacement of  $\partial_\mu$  as

$$\text{For } SU(2) : \partial_\mu \longrightarrow D_\mu = \partial_\mu + i\frac{g'}{2}B_\mu Y + i\frac{g}{2}\mathbf{W}_\mu \cdot \boldsymbol{\sigma} \quad (1.11)$$

$$\text{For } U(1) : \partial_\mu \longrightarrow D_\mu = \partial_\mu + i\frac{g'}{2}B_\mu Y. \quad (1.12)$$

The gauge interaction term is expressed as

$$\mathcal{L}_{\text{int}} = -\frac{1}{4}B_{\mu\nu}B^{\mu\nu} - \frac{1}{4}\mathbf{W}_{\mu\nu}\mathbf{W}^{\mu\nu}, \quad (1.13)$$

$$B_{\mu\nu} = \partial_\mu B_\nu - \partial_\nu B_\mu, \quad (1.14)$$

$$W_{\mu\nu}^i = \partial_\mu W_\nu^i - \partial_\nu W_\mu^i - \sum_{jk} \varepsilon_{ijk} W_\mu^j W_\nu^k. \quad (1.15)$$

As a result, there are four fields:  $B_\mu$  and  $W_\mu^i$  ( $i = 1, 2, 3$ ). They corresponds the electroweak gauge bosons  $\gamma$ ,  $W^\pm$  and  $Z$ . The neutral elements are mixed and form the neutral electroweak bosons  $\gamma$  and  $Z$ , which is expressed as

$$\begin{pmatrix} A_\mu \\ Z_\mu \end{pmatrix} = \begin{pmatrix} \cos \theta_W & \sin \theta_W \\ -\sin \theta_W & \cos \theta_W \end{pmatrix} \begin{pmatrix} B_\mu \\ W_\mu^3 \end{pmatrix}, \quad (1.16)$$

where  $A_\mu$  and  $Z_\mu$  are neutral electromagnetic and weak fields, respectively, and the Weinberg angle  $\theta_W$  is defined as

$$\tan \theta_W = \frac{g'}{g}. \quad (1.17)$$

There are still no mass terms in the simple  $SU(2)_L \times U(1)_Y$  model. In order to provide masses to bosons and fermions, a mechanism is essential.

### 1.1.2 Spontaneous Symmetry Breaking

It is contradictory that there are no mass terms for fermions and bosons in the Lagrangian, whilst the large masses are observed in the experiment. They cannot be explained by the perturbative argument. In order to solve the problem, the Brout-Englert-Higgs mechanism [9, 10] is introduced to the  $SU(2)_L \times U(1)_Y$ . A complex scalar Higgs doublet,

$$\phi = \begin{pmatrix} \phi^+ \\ \phi^0 \end{pmatrix} = \frac{1}{\sqrt{2}} \begin{pmatrix} \phi_1 + i\phi_2 \\ \phi_3 + i\phi_4 \end{pmatrix}, \quad (1.18)$$

is added with the potential given by,

$$V(\phi) = \mu^2 \phi^\dagger \phi + \lambda (\phi^\dagger \phi)^2, \quad (1.19)$$

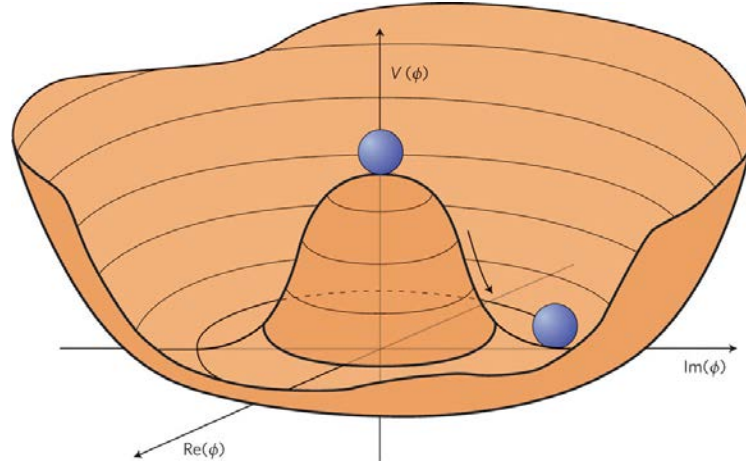


Figure 1.1: Illustration of the Higgs potential [11].  $\text{Re}(\phi)$  and  $\text{Im}(\phi)$  represent  $\phi_3$  and  $\phi_4$  in Eq. (1.18).

where  $\mu$  and  $\lambda$  are a mass and an interaction parameters, respectively. Since the potential needs to have minimal points, the  $\lambda$  should be positive. If  $\mu^2 > 0$ , while this is the normal situation that the minimal point is  $\phi = 0$ , the masses of weak bosons are also zero. On the other hand, if  $\mu^2 < 0$ , the shape of the potential  $V$  is the *Mexican-hat* or *champagne-bottle profile*, as shown in Fig. 1.1. In this case, the potential is minimum if the  $\phi$  is non-zero value:

$$\phi = \pm \sqrt{\frac{-\mu^2}{2\lambda}} \equiv \pm \frac{v}{\sqrt{2}}, \quad (1.20)$$

where  $v$  is called the vacuum expectation value (VEV). The vacuum state is chosen as  $\phi_1 = \phi_2 = \phi_4 = 0$  and  $\phi_3 = v$ , then the scalar field is written as

$$\phi = \frac{1}{\sqrt{2}} \begin{pmatrix} 0 \\ v+h \end{pmatrix}, \quad (1.21)$$

where  $h$  is a neutral Higgs field. The assumption with only one Higgs field is adequate to give masses to the weak bosons. The non-zero VEV implies the breaking of rotational symmetry among the  $\phi_1, \phi_2, \phi_3$  and  $\phi_4$ . This is called the spontaneous symmetry breaking [12]. Then the Higgs potential can be written as

$$V = \frac{1}{2}\mu^2(v+h)^2 + \frac{1}{4}\lambda(v+h)^4, \quad (1.22)$$

and the mass of Higgs boson is determined from the coefficient of the  $h^2$  term,

$$m_h = \sqrt{-2\mu^2}. \quad (1.23)$$

The masses of  $W$  and  $Z$  bosons appear in the covariant derivative terms of the Higgs Lagrangian

$$\mathcal{L}_{\text{Higgs}} = (D^\mu \phi)^\dagger (D_\mu \phi) - V(\phi), \quad (1.24)$$

which is added to the electroweak interaction Lagrangian, Eq. (1.13). Taking into account only the weak

bosons term, the weak bosons obtain the mass terms as

$$\frac{1}{2}m_W^2 (W^{+\mu}W_\mu^- + W^{-\mu}W_\mu^+), \text{ and } \frac{1}{2}m_Z^2 Z^\mu Z_\mu, \quad (1.25)$$

$$\text{where } W_\mu^\pm = \frac{1}{\sqrt{2}} (W_\mu^1 \mp iW_\mu^2), \quad Z_\mu = \frac{gW_\mu^3 - g'B_\mu}{\sqrt{g^2 + g'^2}} \quad (1.26)$$

$$m_W = \frac{gv}{2}, \quad m_Z = \frac{\sqrt{g^2 + g'^2}v}{2}. \quad (1.27)$$

Since we already know  $W$  and  $Z$  boson masses, 80 GeV and 91 GeV, respectively, the VEV can be calculated as  $v \sim 246$  GeV.

### 1.1.3 Higgs boson

The Higgs boson is introduced to describe the spontaneous symmetry breaking in the electroweak theory. As expected, it was discovered with the mass of 125 GeV at ATLAS [13] and CMS [14] in 2012. It should interact not only with gauge bosons but also with fermions in order to obtain the mass of the fermions. Starting from Eq. (1.8) and Eq. (1.9), the Lagrangian of the interaction between leptons and Higgs boson (Yukawa interaction) are written as

$$\mathcal{L}_{\text{mass}} = -\lambda_\ell \left( \psi_L^\dagger \phi \psi_R + \psi_R^\dagger \phi^\dagger \psi_L \right). \quad (1.28)$$

Taking into account the expression of the vacuum state Eq. (1.21), the Lagrangian is calculated to

$$\mathcal{L}_{\text{mass}} = -\frac{\lambda_\ell v}{\sqrt{2}} \bar{\ell} \ell - \frac{\lambda_\ell}{\sqrt{2}} h \bar{\ell} \ell, \quad (1.29)$$

where  $\bar{\ell} \ell = \bar{\ell}_L \ell_R + \bar{\ell}_R \ell_L$ . The first term is the mass term of the lepton, the mass is expressed as

$$m_\ell = \frac{\lambda_\ell v}{\sqrt{2}}. \quad (1.30)$$

The second term is the Yukawa interaction term. The  $\lambda_\ell$  is called Yukawa coupling constant, which is not predicted by the GWS theory. While this is the example of the lepton case, the quark mass can be introduced using the same manner using the  $SU(3)$  theory.

According to Eq. (1.30), the Yukawa coupling constant is in proportion to the mass of the particle. This is an important characteristic of the SM. After the discovery of the Higgs boson with the mass of 125 GeV in 2012, the Yukawa coupling constant is measured by the ATLAS and the CMS experiments. These results show the proportion between the mass and its Yukawa coupling constant, as shown in Fig. 1.2. The largest Yukawa coupling constant is for the top quark in the SM because the top quark is the heaviest particle in the SM particles.

## 1.2 Remaining Problems in the Standard Model

As introduced in the previous section, the SM is very successful to explain the framework of the particle physics. However, the SM has several theoretical discontents, for example, the SM does not include the gravitational interaction. The gravitational interaction has been understood as an interaction following the

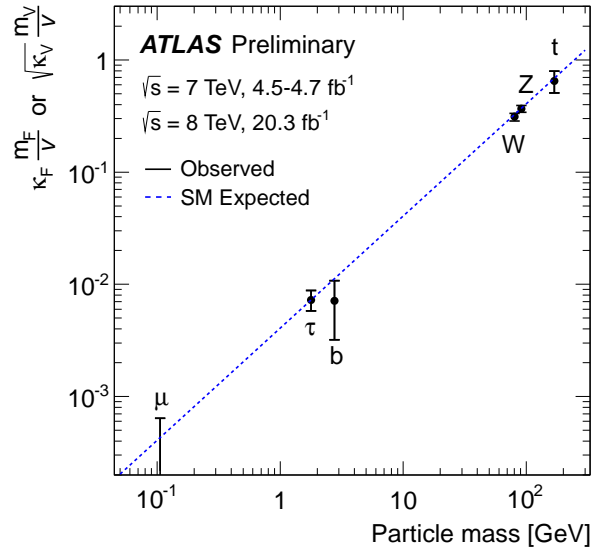


Figure 1.2: Result of the measurement of the Yukawa coupling constant from the ATLAS experiment [15]. The blue dashed line shows the fitting results.

General Relativity. The General Relativity is expressed within the framework of the classical physics, and so it is not successfully described using the framework of the quantum field theory at the moment. In this thesis, the following three problems, the gauge hierarchy problem, the dark matter, and the muon anomalous magnetic moment are focused. Their detailed descriptions are given in following subsections.

### 1.2.1 Hierarchy problem in the gauge theory

One of the problems is known as the hierarchy problem in the gauge theory, which is the difference between electroweak scale  $M_{EW} \sim 10^2 \text{ GeV}$  and the Planck scale  $M_{Pl} \sim 10^{19} \text{ GeV}$ .

The difference affects the Higgs mass calculation. A particle mass is calculated with not only the leading order but several contributions from higher order interactions. The fermions and the gauge bosons have the mechanisms of the symmetries, such as chiral or gauge symmetries, then the quadratic terms of energy scales for the radiation effect are automatically cancelled. In the case of Higgs boson, there is no symmetry to suppress the effect of the quadratic terms. Thus the Higgs mass should be calculated applying simply the higher order calculation. Actually, the observable Higgs mass  $m_h$  is calculated as

$$m_h^2 = m_{h_0}^2 + \delta m_h^2, \quad (1.31)$$

where  $m_{h_0}$  and  $\delta m_h^2$  are the Higgs bare mass and the quantum corrections, which include the quantum loops from every particles that interact with Higgs. The magnitude of the interaction with Higgs depends on the mass of the particle, thus the effect of the top quark is the largest in the SM, as described in Sec. 1.1.3. The quantum correction from the top quark is expressed as follows:

$$\delta m_h^2 = -\frac{|\lambda_f|^2}{8\pi^2} \Lambda^2 + (\text{higher order}), \quad (1.32)$$

where  $\lambda_f$  and  $\Lambda$  are the Yukawa coupling constant for the fermion such as the top quark and the cut-off scale parameter. The first correction term implies that the correction depends on the new physics scale. If



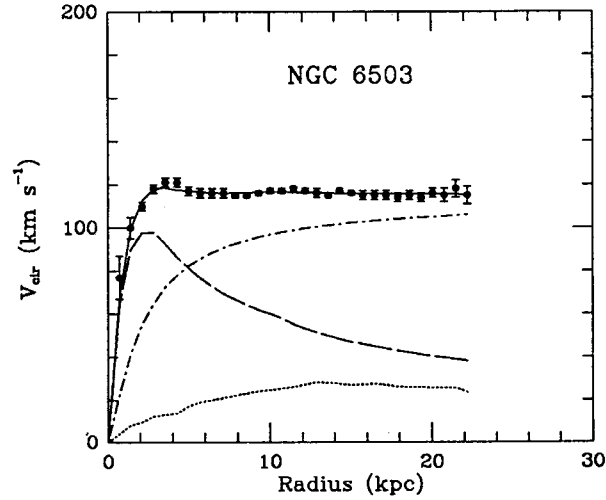


Figure 1.3: The rotation velocity of the matters around the NGC6503 galaxy [16]. The data are fitted with the three parameters: the visible components like stars (dashed curve), the gas (interstellar medium; dotted curve), and the dark matter (dash-dot curve). The contribution of the dark matter is approximately seven times larger than the contribution of the stars at the 20 kpc distance.

there are no other new physics, in other words the Standard Model is the ultimate theory of the particle physics, the cut-off parameter should be the Planck Scale  $\sim 10^{19}$  GeV. Therefore the Higgs mass is tuned by the order of  $10^{17}$  in order to make the mass of 125 GeV. This should be considered to be unnatural, thus the new symmetrical mechanism in addition to the SM is desired.

## 1.2.2 Dark matter

The second problem is the dark matter. According to the astrophysics results [16], the unknown particles and energies should exist in order to describe the orbital rotation velocity of galaxies. The velocity  $v$  of the stars or the interstellar medium in the galaxy should be a function of the radius  $r$  from the centre of the galaxy as

$$v(r) = \sqrt{\frac{GM(r)}{r}}, \quad (1.33)$$

where  $G$  and  $M(r)$  are the gravitational constant and the mass inside the orbit. If the mass of the galaxy is mainly from the stars in the galaxy, the velocity should be in inverse proportion to a square root of radius,  $v(r) \propto 1/\sqrt{r}$ . However, the measurement results do not agree with this hypothesis. The velocity is almost constant even though the stars or the interstellar medium are far from the centre of the galaxy, as shown in Fig. 1.3. Therefore, the invisible matter called “dark matter” is necessary to describe the behaviour. In addition, the results from the Type Ia supernovae [17, 18] and the cosmic microwave background studies [19, 20] claim that there would be unknown energy capable of expanding the universe with acceleration, which is called “dark energy.” Dark energy is investigated in terms of the cosmological constant.

According to the latest results from *Planck* [21], which is the satellite of the European Space Agency for the space experiment in the field of cosmic microwave background [22], the expected existence ratios are 4.9% (baryons), 26.4% (dark matter), and 68.5% (dark energy). Dark matter is expected to interact with the others weakly and is difficult to detect. Many candidates for the dark matter have been considered

in the framework of the SM, such as neutrinos. However, the neutrino hypothesis is almost excluded by the measurements of the cosmic microwave background [23].

### 1.2.3 Muon Anomalous Magnetic Moment

The third problem is the discrepancy of the anomalous magnetic moment of muons [24]. A magnetic moment of the lepton can be noted

$$\mu = -g \frac{e}{2m} S \quad (1.34)$$

where  $S$  is its spin then  $S = \frac{1}{2} \sigma$  and  $g$  is the g-factor for the spin. Calculating only with the leading order, the g-factor should be  $g = 2$  by the standard calculation of Dirac Equation. Actual physics phenomena are based on the calculation with higher order terms. Deviation of the g-factor from 2 is called the anomalous magnetic moment. The anomalous magnetic moment of muons (muon  $g - 2$ ;  $a_\mu$ ) is defined as

$$a_\mu \equiv \frac{g - 2}{2}. \quad (1.35)$$

The  $a_\mu$  has been measured at the E821 experiment at Brookhaven National Laboratory, the average of the anomalous magnetic moment was obtained as [25]

$$a_\mu^{\text{exp}} = 116\,592\,091(54)(33) \times 10^{-11}. \quad (1.36)$$

The SM prediction has also been calculated [26, 27]. It is divided into three contributions as

$$a_\mu^{\text{SM}} = a_\mu^{\text{QED}} + a_\mu^{\text{EW}} + a_\mu^{\text{had}}. \quad (1.37)$$

The largest contribution is from  $a_\mu^{\text{QED}}$ , which includes the photonic and the leptonic loops. It is precisely calculated with the tenth-order QED terms of the muon [27]. The electroweak term  $a_\mu^{\text{EW}}$  has been calculated up to two-loop order [28–31]. The hadronic term  $a_\mu^{\text{had}}$  has the largest uncertainty of the three parts. It cannot be calculated using perturbative QCD because the contribution of the virtual photons with low momentum are dominant. It is then calculated with the latest experimental results, such as KLOE [32, 33] and BaBar [34], of the hadron interactions [26]. As a result, the theoretical contribution is calculated as [27]

$$a_\mu^{\text{SM}} = 116\,591\,840(59) \times 10^{-11}. \quad (1.38)$$

The discrepancy between the experimental result and the theoretical prediction has been approximately three sigmas. Moreover, the difference has the same order of the electroweak contribution,  $a_\mu^{\text{EW}} = 154(2) \times 10^{-11}$  [28–31]. Therefore if the discrepancy is occurred by new physics, the scale of the new physics would be similar to the electroweak interaction.

## 1.3 Supersymmetry

Supersymmetry (SUSY) [35–43] is the most hopeful candidate for the theory of beyond the Standard Model. The theory claims that all the SM particles have corresponding super-partners which differ in the spin by a half from them. In other words, SUSY introduces the new symmetry between bosons and fermions. The SUSY particle set is shown in Tab. 1.2. If we write the states of bosons and fermions as  $|B\rangle$

Table 1.2: The SM particles and corresponding SUSY particles.

spin	SM particles	spin	SUSY particles
1/2	Neutrinos ( $\nu_e, \nu_\mu, \nu_\tau$ )	0	Sneutrinos ( $\tilde{\nu}_e, \tilde{\nu}_\mu, \tilde{\nu}_\tau$ )
	Charged leptons ( $e, \mu, \tau$ )		Charged sleptons ( $\tilde{e}, \tilde{\mu}, \tilde{\tau}$ )
	Quarks ( $u, d, c, s, t, b$ )		Squarks ( $\tilde{u}, \tilde{d}, \tilde{c}, \tilde{s}, \tilde{t}, \tilde{b}$ )
1	Gluon ( $g$ )	1/2	Gluino ( $\tilde{g}$ )
	Weak bosons ( $W, Z$ )		Wino, Zino ( $\tilde{W}, \tilde{Z}$ )
	Photon ( $\gamma$ )		Photino ( $\tilde{\gamma}$ )
0	Higgs ( $H$ )	1/2	Higgsino ( $\tilde{H}$ )

and  $|F\rangle$ , respectively, the theory makes it possible to transform them with the operator  $Q$  as

$$Q|B\rangle = |F\rangle, \quad Q|F\rangle = |B\rangle. \quad (1.39)$$

The  $Q$  is the operator of a spinor. Thus the operator  $Q$  should satisfy an algebra of anticommutation and commutation relations (called ‘‘pseudo Lie algebra’’ [44]),

$$\{Q_\alpha, Q_\beta^\dagger\} = c \sigma_{\alpha\beta}^\mu P_\mu, \quad (1.40)$$

$$[Q_\alpha, P^\mu] = 0, \quad (1.41)$$

$$\{Q_\alpha, Q_\beta\} = \{Q_\alpha^\dagger, Q_\beta^\dagger\} = 0, \quad (1.42)$$

where  $c$  is a normalisation factor, and  $P^\mu$  is the four-momentum generator of spacetime translations. According to the relations  $P_\mu P^\mu = m^2$  and Eqs. (1.40)–(1.42), the operator  $Q$  cannot change the mass of the particle.

The particle and its super-partner pairs are formed as supermultiplets, which follow the SUSY algebra. The super-partner has same quantum number in terms of  $SU(3)_C \times SU(2)_L \times U(1)_Y$ .

In the SM, there assumed one Higgs doublet to adequately give mass terms to the SM particles. However, in the SUSY assumption, at least two types of Higgs doublets are needed. If the minimal supersymmetric standard model (MSSM) is assumed, there are two types of Higgs doublets defined as

$$H_u = \begin{pmatrix} H_u^+ \\ H_u^0 \end{pmatrix}, \quad H_d = \begin{pmatrix} H_d^0 \\ H_d^- \end{pmatrix}. \quad (1.43)$$

They are the  $SU(2)$ -doublet complex scalar fields with  $Y = 1/2$  and  $Y = -1/2$ , respectively. The  $Y = 1/2$  doublet  $H_u$  can interact only to charge  $+2/3$  up-type quarks (up, charm, top) and the  $Y = -1/2$  doublet  $H_d$  can interact only to charge  $-1/3$  down-type quarks (down, strange, bottom) and to the charged leptons ( $e, \mu, \tau$ ). Their VEVs are defined as

$$\langle H_u \rangle = v_u, \quad \langle H_d \rangle = v_d. \quad (1.44)$$

The ratio of the VEV is written as

$$\tan \beta \equiv \frac{v_u}{v_d}, \quad (1.45)$$

which is usually used as a basic parameter of the SUSY models. According to the  $CP$  conservation, five types of Higgs bosons exist: CP-even  $h^0$  and  $H^0$ , CP-odd  $A^0$ , and charged  $H^\pm$ . By definition, the mass of

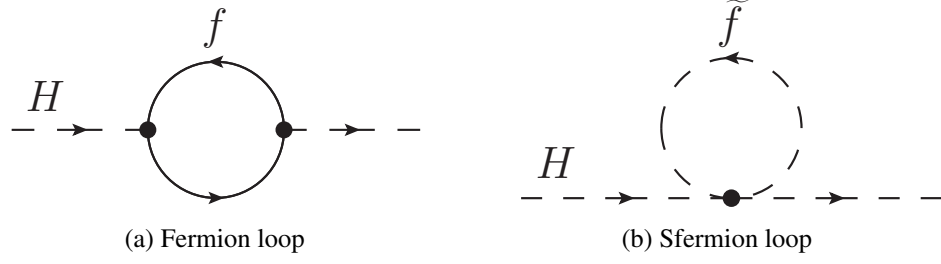


Figure 1.4: Examples of the diagram of the one-loop quantum corrections for a fermion (a) and for a sfermion (b).

$h^0$  is smaller than  $H^0$ . The lightest CP-even Higgs boson  $h^0$  is usually assumed to be the SM-like Higgs boson. These Higgs bosons should have corresponding super-partners (Higgsinos):  $\tilde{h}^0, \tilde{H}^0, \tilde{A}^0, \tilde{H}^\pm$ . The Higgsinos mix with the super-partners of the electroweak bosons, electroweak gauginos ( $\tilde{W}$  and  $\tilde{B}$ ). They are formed as mass eigenstates charginos  $\tilde{\chi}_i^\pm$  ( $i = 1, 2$ ) and neutralinos  $\tilde{\chi}_j^0$  ( $j = 1, 2, 3, 4$ ). The detail of the electroweak gauginos and Higgsinos will be described in Sec. 1.4.

The squarks  $\tilde{q}_L, \tilde{q}_R$  and the sleptons  $\tilde{\ell}_L, \tilde{\ell}_R$  are the super-partners of the corresponding quarks and leptons, respectively. Quarks and leptons have left-handed and right-handed particles. In the SUSY theory, the super-partners of the left-handed and the right-handed particles are distinguished. Gluino  $\tilde{g}$  is the super-partner of a gluon, and is the strong gaugino. It interacts via the strong forces, thus it cannot mix the other gauginos and Higgsinos.

The theory has some powerful characteristics to solve the remaining problems in the SM, as described below.

**Hierarchy problem in the gauge theory** Figures 1.4 shows the examples of Higgs one loop quantum corrections for fermions and sfermions. As described in Sec. 1.2.1, the Higgs quantum correction from the top quark contribution expressed as Eq. (1.32) is dominant. With respect to the scalar fermion in particular *stop*, shown in Fig. 1.4b, the contribution is calculated as

$$\delta m_h^2 = \frac{\lambda_s}{16\pi^2} \left[ \Lambda^2 - 2m_s^2 \ln \left( \frac{\Lambda}{m_s} \right) + (\text{higher order}) \right], \quad (1.46)$$

where the  $\lambda_s$  and the  $m_s$  are the Yukawa coupling constant and the mass for the scalar particle, such as *stop*. There are two complex scalars with  $\lambda_s = |\lambda_f|^2$  corresponding left-handed and right-handed, then the quadratic term is cancelled.

**Dark matter** If the superpotential is written based on the simplest SUSY model of minimal SUSY  $SU(5)$ , there are terms which lead to violate the baryon number ( $B$ ) and the lepton number ( $L$ ) as

$$W_{\Delta L=1} = \frac{1}{2} \lambda^{ijk} L_i L_j \bar{e}_k + \lambda'^{ijk} L_i Q_j \bar{d}_k + \mu^i L_i H_u \quad (1.47)$$

$$W_{\Delta B=1} = \frac{1}{2} \lambda''^{ijk} \bar{u}_i \bar{d}_j \bar{d}_k, \quad (1.48)$$

where  $H_u, H_d, Q, L, \bar{u}, \bar{d}, \bar{e}$  are superfields corresponding to the supermultiplets: up-type Higgs, down-type Higgs, left-handed quarks, left-handed leptons, right-handed up-type quarks, right-handed down-type

quarks and right-handed charged leptons, respectively. These terms lead to make the lifetime of protons short. The expectation of the lifetime of protons is calculated with minimal SUSY  $SU(5)$  as [45]

$$\tau_{\text{SUSY } SU(5)}(p \rightarrow K^+ \bar{\nu}) \leq 2.9 \times 10^{30} \text{ yrs}, \quad (1.49)$$

whilst the experimental result from Super-Kamiokande [46] was evaluated the lifetime as

$$\tau_{\text{exp}}(p \rightarrow K^+ \bar{\nu}) > 5.9 \times 10^{33} \text{ yrs (90\% CL)}. \quad (1.50)$$

Thus the minimal SUSY  $SU(5)$  model was already excluded with greater than 90% confidence level. The fact indicates the minimal SUSY  $SU(5)$  needs to add some mechanisms to suppress the phenomena to violate the baryon and the lepton numbers. One of the simple solution is the assumption of  $R$ -parity conservation.  $R$ -parity is defined with the amount of spin  $s$  by the following equation:

$$R = (-1)^{3(B-L)+2s}, \quad (1.51)$$

where the  $R$ -parity is  $+1$  for the SM or  $-1$  for the SUSY. In the case of  $R$ -parity conservation, the interaction terms shown in Eqs. (1.47) and (1.48) are strictly prohibited.

For the lightest SUSY particle (LSP), there is no way to decay into the other particles because of  $R$ -parity conservation. Therefore the LSP would be a good candidate for the dark matter. When the SUSY is introduced in the SM, usually “ $R$ -parity” is defined and assumed to be conserved.

**Muon  $g - 2$  deviation** Assuming that SUSY makes additional quantum loops in muons, the contribution for muon  $g - 2$  is favoured with the electroweak interacting SUSY masses of  $\mathcal{O}(100)$  GeV and  $\tan\beta$  of  $\mathcal{O}(10)$  [47, 48]. As a result, SUSY particles which interact with the electroweak interaction are expected to be light.

### 1.3.1 Supersymmetry breaking

As SUSY particles have not been observed with the same mass as corresponding SM particles hitherto, the SUSY has to be broken. However, the breaking mechanism is not arbitrary and simply spontaneous SUSY breaking is unsuitable in terms of solving the hierarchy problem in the gauge theory. The “soft” breaking term is then introduced by hand to break the symmetry spontaneously [49, 50]:

$$\mathcal{L}_{\text{MSSM}} = \mathcal{L}_{\text{SUSY}} + \mathcal{L}_{\text{soft}}. \quad (1.52)$$

The  $\mathcal{L}_{\text{MSSM}}$  is the effective Lagrangian of the MSSM. The  $\mathcal{L}_{\text{SUSY}}$  contains gauge and Yukawa interaction terms and preserves SUSY invariance. The quantum correction terms are kept symmetric in the scalar corrections. The  $\mathcal{L}_{\text{soft}}$  is a term to violate SUSY, which is added by hand. This term gives the additional mass contribution for the SUSY particles, as following [51]:

- Soft trilinear scalar interactions:  $\frac{1}{3!} A_{ijk} \phi_i \phi_j \phi_k$
- Soft bilinear scalar interactions:  $\frac{1}{2} b_{ij} \phi_i \phi_j$
- Soft scalar mass-squares:  $m_i^2 \phi_i^\dagger \phi_i$
- Soft gaugino masses:  $\frac{1}{2} M_a \lambda^a \lambda^a$ ,

where the  $A$ ,  $b$ ,  $m^2$  and  $M$  are the parameters of corresponding interactions, and  $\phi$  and  $\lambda$  are the fields of scalar particles and gauginos. In the soft breaking, the spontaneous symmetry breaking is occurred in the “hidden sector,” where the SUSY particles interact with a “messenger.” The SUSY breaking models are categorised according to their fields of messenger interaction. Three candidates are proposed: gravity-mediation, anomaly-mediation and gauge-mediation scenarios, as described below.

**Gravity-mediation** Supergravity (SUGRA) [52] is the most popular mechanism of the SUSY breaking models, in which the supersymmetry breaking is mediated by gravitational interaction. This scenario introduces the gravity supermultiplet  $(G, \tilde{G})$ , where  $G$  is a spin 2 graviton and  $\tilde{G}$  is a spin 3/2 gravitino. The hidden sector communicates with visible sector only via the gravitational interaction. The soft breaking terms  $A$ ,  $b$ ,  $m^2$  and  $M$  are proportional to the gravitino mass  $m_{3/2}$ . The gravitino mass term  $m_{3/2}$  is related to the SUSY breaking scale of  $M_S = \sqrt{F} \sim 10^{11-13}$  GeV [51],

$$m_{3/2} \sim \frac{M_S^2}{M_{\text{Pl}}} = \frac{F}{M_{\text{Pl}}}, \quad (1.53)$$

the gravitino mass is thus  $\mathcal{O}(\text{TeV})$ . The couplings of the gravitino are gravitational strength, this is thus extremely weakly interacting to the other fields.

The LSP is usually assumed to be the lightest neutralino, which is a good candidate for the dark matter. Whereas the gravitino would be a candidate as the LSP, the relic density of the dark matter restricts the gravitino LSP scenario with the gravitino mass less than a few keV or heavier than  $\sim 10^{11}$  GeV [53, 54].

The minimal model of the Supergravity, minimal Supergravity (mSUGRA), has been used as a benchmark model to reduce the free parameters. The parameters of mSUGRA are listed as following [51]:

- $m_{1/2}$ : a common gaugino mass,
- $m_0$ : a common soft scalar mass,
- $A_0$ : a common soft trilinear parameter,
- $b_0$ : a bilinear term,
- the sign of  $\mu$  term.

In this scenario, the LSP is usually the bino-like neutralino. The simplified models which are used in this analysis are based on the mass spectra of the standard SUGRA case.

**Anomaly-mediation** Anomaly-mediated SUSY breaking (AMSB) [55, 56] is a particular case of the SUGRA. Whereas SUGRA has an advantage to extend the theory to the string theory, it has a disadvantage that at present it has not been successful to explain the degeneracy of squark masses to avoid large flavour-changing neutral current effects [55]. In order to solve it, the contribution of the conformal anomaly for the gauginos is introduced as an origin of the gaugino masses. Thus the gaugino masses are determined by the following equation:

$$M_a = \frac{\beta(g^2)}{2g^2} m_{3/2} \quad (1.54)$$

where  $\beta(g^2)$  is the gauge beta function. The breaking mass terms are related to the gravitino mass  $m_{3/2} \sim \mathcal{O}(100\text{TeV})$ . The gaugino mass ratio is obtained as

$$M_1 : M_2 : M_3 = 2.8 : 1 : 7.1, \quad (1.55)$$

thus the LSP is the neutral wino [51]. The next to the lightest SUSY particle (NLSP) is the charged wino with the mass difference of a few hundred MeV. The charged wino would be long-lived particle, which is a very interesting phenomenon of the AMSB scenario. Searches for the long-lived charged wino are performed using the *disappearing track*, which is the track disappeared in the middle of the detector [57].

**Gauge-mediation** If the messenger interaction is a gauge interaction, the model is called as the Gauge-mediated SUSY breaking (GMSB) [58–62]. A messenger field  $S_i$  is introduced in order to couple to the goldstino field of the hidden sector, the MSSM gauge bosons and gauginos. The gaugino masses are obtained by

$$M_a \sim \frac{g_a^2}{(4\pi)^2} \frac{F_S}{M_S}, \quad (1.56)$$

where  $F_S$  and  $M_S$  are the auxiliary field VEV and the SUSY breaking mass scale. If the breaking mass parameter  $M_S \sim 10^5$  GeV, the auxiliary field VEV is  $F_S \sim M_S^2$ . For larger value of  $F_S \sim 10^{14}$  GeV<sup>2</sup>,  $M_S \sim 10^9$  GeV. In general, the  $M_S$  in the GMSB is much smaller than that in SUGRA. The gravitino mass is written as

$$m_{3/2} \sim \frac{M_S^2}{M_{\text{Pl}}}, \quad (1.57)$$

thus the gravitino has very low mass of the order of a few keV, which satisfies the observed relic density of the gravitino LSP [63]. Searches for the GMSB signals are performed based on detecting the SM particles emitted from the NLSP decays, for example, photons from the bino-like neutralino decays  $\tilde{\chi}_1^0 \rightarrow \gamma + \tilde{G}$ , and Higgs or  $Z$  boson from the Higgsino-like neutralino decays  $\tilde{\chi}_1^0 \rightarrow h/Z + \tilde{G}$  [64].

### 1.3.2 SUSY models

The SUSY models are needed because the MSSM has many parameters which cannot be determined in the theory. Many models are proposed to simplify the SUSY parameter space. Two specific models, the simplified model and the phenomenological MSSM are described in this thesis below.

**Simplified models** To reduce the parameter of the MSSM, the simplest spectra compatible with SUSY structure are defined. They are called the simplified models [65]. They contain a few parameters. In this thesis, only two free parameters are employed, the masses of the lightest chargino  $\tilde{\chi}_1^\pm$  and the lightest neutralino  $\tilde{\chi}_1^0$ . The other parameters are assumed not to affect the phenomenologies of the SUSY signals. Not only the SUSY production, but also the decay modes are simplified. As described below, the decay modes via  $WZ$  and  $Wh$  are considered with 100% branching ratios.

**pMSSM** The phenomenological MSSM (pMSSM) [66, 67] is formed from MSSM with several basic assumptions. Actually, there are more than 100 parameters in the  $R$ -parity conserving MSSM in addition to the SM, mainly soft-breaking terms. Then, three assumption are added to the MSSM: no new source of CP-violation, no flavour changing neutral currents, and first and second generation universality. This leads to reduce parameters to 19.

In this search, the masses of the coloured sparticles, of the CP-odd Higgs boson, and of the sleptons are fixed at high values. Then the dominant process would be direct chargino and neutralino production decaying via  $W$ ,  $Z$  or Higgs bosons.

## 1.4 Electroweak gauginos

The main target of the analysis is search for supersymmetric particles produced by electroweak process and decaying via bosons. In this section, the phenomena of the electroweak SUSY particles, in particular with respect to the charginos and the neutralinos are shown. There have been no evidence for squarks and gluinos in the results of ATLAS and CMS experiments at present [68, 69]. Thus they are assumed to be heavy in the order of  $\mathcal{O}(10)$  TeV in this thesis.

### 1.4.1 Mass spectra

In the MSSM, there should be at least two Higgs doublets. Accordingly four super-partners of the Higgs bosons exist, called Higgsinos,  $\tilde{H}_u^+$ ,  $\tilde{H}_u^0$ ,  $\tilde{H}_d^-$  and  $\tilde{H}_d^0$  (gauge eigenstates), as described in Sec. 1.3. These Higgsinos and electroweak gauginos ( $\tilde{W}$  and  $\tilde{B}$ ) are mixed and form the mass eigenstates with unitary matrices for neutralinos  $N(\tilde{\chi}^0)$  and for charginos  $N(\tilde{\chi}^\pm)$  as

$$\begin{pmatrix} \tilde{\chi}_1^0 \\ \tilde{\chi}_2^0 \\ \tilde{\chi}_3^0 \\ \tilde{\chi}_4^0 \end{pmatrix} = N(\tilde{\chi}^0) \begin{pmatrix} \tilde{B} \\ \tilde{W}^0 \\ \tilde{H}_d^0 \\ \tilde{H}_u^0 \end{pmatrix}, \quad (1.58)$$

$$\begin{pmatrix} \tilde{\chi}_1^\pm \\ \tilde{\chi}_2^\pm \end{pmatrix} = N(\tilde{\chi}^\pm) \begin{pmatrix} \tilde{W}^\pm \\ \tilde{H}^\pm \end{pmatrix}, \quad (1.59)$$

where  $\tilde{H}^\pm$  represents  $\tilde{H}_u^+$  or  $\tilde{H}_d^-$ . The mixing matrices  $N(\tilde{\chi}^0)$  and  $N(\tilde{\chi}^\pm)$  are unitary matrices satisfying

$$N^\dagger M N^{-1} = N_D, \quad (1.60)$$

where  $N_D$  represents a diagonal mass matrix for neutralinos or charginos, and  $M$  is the mass matrix of neutralinos or charginos. The mass matrices of neutralinos and charginos can be noted as following equation [50]:

$$M(\tilde{\chi}^0) = \begin{pmatrix} M_1 & 0 & -c_\beta s_W m_Z & s_\beta s_W m_Z \\ 0 & M_2 & c_\beta c_W m_Z & -s_\beta c_W m_Z \\ -c_\beta s_W m_Z & c_\beta c_W m_Z & 0 & -\mu \\ s_\beta s_W m_Z & -s_\beta c_W m_Z & -\mu & 0 \end{pmatrix} \quad (1.61)$$

$$M(\tilde{\chi}^\pm) = \begin{pmatrix} M_2 & \sqrt{2} s_\beta m_W \\ \sqrt{2} c_\beta m_W & \mu \end{pmatrix}, \quad (1.62)$$

where  $M_1$ ,  $M_2$ ,  $\mu$ ,  $c_\beta$ ,  $s_\beta$ ,  $c_W$  and  $s_W$  stand for the bino mass term, the wino mass term, the Higgsino mass term,  $\cos \beta$ ,  $\sin \beta$ ,  $\cos \theta_W$  and  $\sin \theta_W$ , respectively. With these notations, the masses of neutralinos and



charginos can be written as following equations:

$$m_{\tilde{\chi}_1^0} = M_1 - \frac{m_Z^2 s_W^2 (M_1 + \mu \sin 2\beta)}{\mu^2 - M_1^2} + \dots \quad (1.63)$$

$$m_{\tilde{\chi}_2^0} = M_2 - \frac{m_W^2 (M_2 + \mu \sin 2\beta)}{\mu^2 - M_2^2} + \dots \quad (1.64)$$

$$m_{\tilde{\chi}_3^0, \tilde{\chi}_4^0} = |\mu| + \frac{m_Z^2 (I - \sin 2\beta) (\mu + M_1 c_W^2 + M_2 s_W^2)}{2(\mu + M_1)(\mu + M_2)} + \dots, \quad (1.65)$$

$$|\mu| + \frac{m_Z^2 (I + \sin 2\beta) (\mu - M_1 c_W^2 - M_2 s_W^2)}{2(\mu - M_1)(\mu - M_2)} + \dots \quad (1.66)$$

$$m_{\tilde{\chi}_1^\pm} = M_2 - \frac{m_W^2 (M_2 + \mu \sin 2\beta)}{\mu^2 - M_2^2} + \dots \quad (1.67)$$

$$m_{\tilde{\chi}_2^\pm} = |\mu| + \frac{m_W^2 I (\mu + M_2 \sin 2\beta)}{\mu^2 - M_2^2} + \dots, \quad (1.68)$$

where  $I$  is a sign then  $I = \pm 1$ . If the Higgsino mass term  $|\mu|$  is assumed to be much larger than the other variables ( $|\mu| \gg M_1, M_2$ ), the masses of charginos and neutralinos are as follows:

$$m_{\tilde{\chi}_1^0} \sim M_1 \text{ (bino-like)}, \quad (1.69)$$

$$m_{\tilde{\chi}_2^0} \sim m_{\tilde{\chi}_1^\pm} \sim M_2 \text{ (wino-like)}, \quad (1.70)$$

$$m_{\tilde{\chi}_3^0} \sim m_{\tilde{\chi}_4^0} \sim m_{\tilde{\chi}_2^\pm} \sim |\mu| \text{ (Higgsino-like)}. \quad (1.71)$$

Thus the masses of the lightest charged wino and neutral wino can be assumed to be degenerate  $m_{\tilde{\chi}_1^\pm} = m_{\tilde{\chi}_2^0}$ . In this thesis, this simple model is adopted as a target scenario.

## 1.4.2 Production modes

The cross sections of the chargino-neutralino pair production depends on the mass of the  $\tilde{\chi}_1^\pm$  or  $\tilde{\chi}_2^0$ . For the scenarios the squarks are all heavy in the order of  $\mathcal{O}(10)$  TeV comparing to the weak boson  $\mathcal{O}(100)$  GeV. Thus only the  $s$ -channel would be dominant and the  $t$  and  $u$ -channels are strongly suppressed since the cross-section of  $t$  and  $u$ -channels are in proportion to  $1/(p - m_q)^2$ , where  $p$  is a momentum for the virtual squark. The Feynman diagrams for the  $\tilde{\chi}_1^\pm \tilde{\chi}_2^0$  production are shown in Fig. 1.5. The production cross section of  $\tilde{\chi}_1^\pm \tilde{\chi}_2^0$  is shown in Fig. 1.6. If the lightest chargino  $\tilde{\chi}_1^\pm$  and the second lightest neutralino  $\tilde{\chi}_2^0$  are not electroweak gaugino-like, their cross sections are significantly smaller than that for the electroweak gaugino production.

This thesis focuses on the search for direct  $\tilde{\chi}_1^\pm \tilde{\chi}_2^0$  production. The other modes, such as searches for  $\tilde{\chi}_1^0 \tilde{\chi}_1^0$ ,  $\tilde{\chi}_1^\pm \tilde{\chi}_1^0$ ,  $\tilde{\chi}_i^0 \tilde{\chi}_j^0$  and  $\tilde{\chi}_1^+ \tilde{\chi}_1^-$ , are not considered in this thesis. The  $\tilde{\chi}_1^0 \tilde{\chi}_1^0$  production is difficult to be detected due to the assumption where the  $\tilde{\chi}_1^0$  is the LSP. For  $\tilde{\chi}_1^\pm \tilde{\chi}_1^0$ , if  $\tilde{\chi}_1^\pm$  is wino-like and  $\tilde{\chi}_1^0$  is bino-like, the production rate is very small because the direct coupling between wino and bino is prohibited. The  $\tilde{\chi}_i^0 \tilde{\chi}_j^0$  production, in particular the case where  $i = 2$  and  $j = 2, 3$ , is also a promising candidate. However, the neutral production cross section is smaller than the charged production in the  $pp$  collision. For the same reason, the cross section of the  $\tilde{\chi}_1^+ \tilde{\chi}_1^-$  production is also smaller than that of the  $\tilde{\chi}_1^\pm \tilde{\chi}_2^0$  production. Therefore, the direct production of  $\tilde{\chi}_1^\pm \tilde{\chi}_2^0$  is the most sensitive search for the gauginos. In this case, the final states would have three leptons. Thus this thesis focuses on this channel.

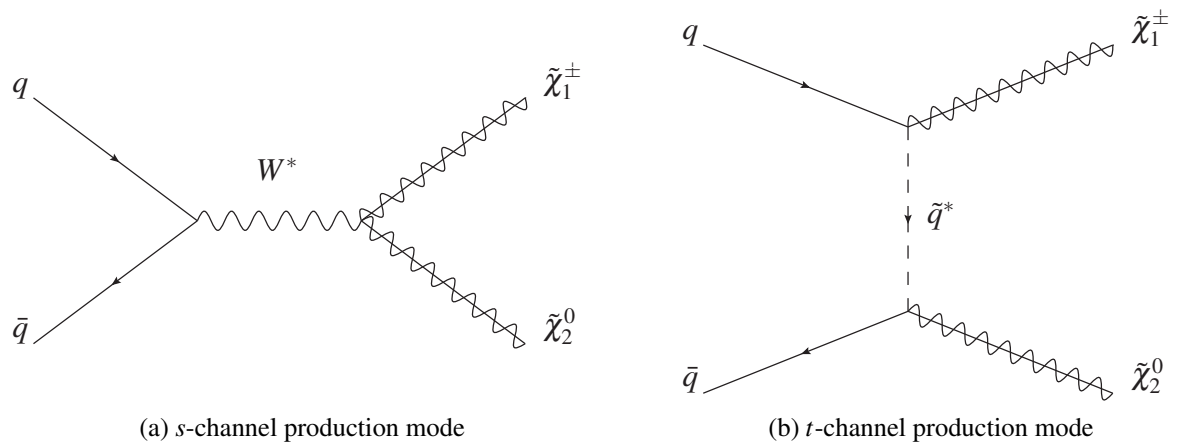


Figure 1.5: Feynman diagrams for the  $\tilde{\chi}_1^\pm \tilde{\chi}_2^0$  production via  $s$ -channel (a) and via  $t$ -channel (b). In figures,  $W^*$  and  $\tilde{q}^*$  represent the off-shell  $W$  boson and the off-shell squark, respectively. If the squarks have heavy mass spectra, the  $s$ -channel production mode (a) is dominant and the  $t$ -channel production mode (b) is strongly suppressed because of the heavy squark mass.

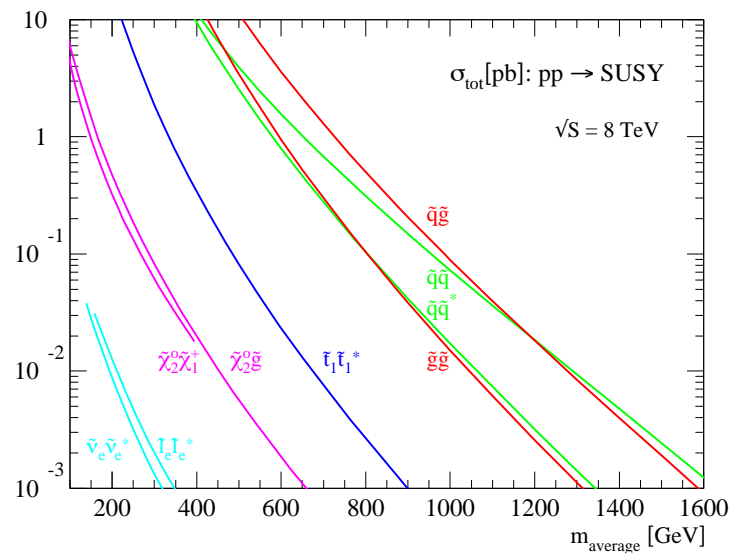


Figure 1.6: Cross sections for pair production of SUSY particles as a function of their mass at the LHC for a centre-of-mass energy of 8 TeV [24, 70–74]. The cross section of the direct production of charginos and neutralinos is several orders of magnitude smaller than the production of coloured SUSY particles.

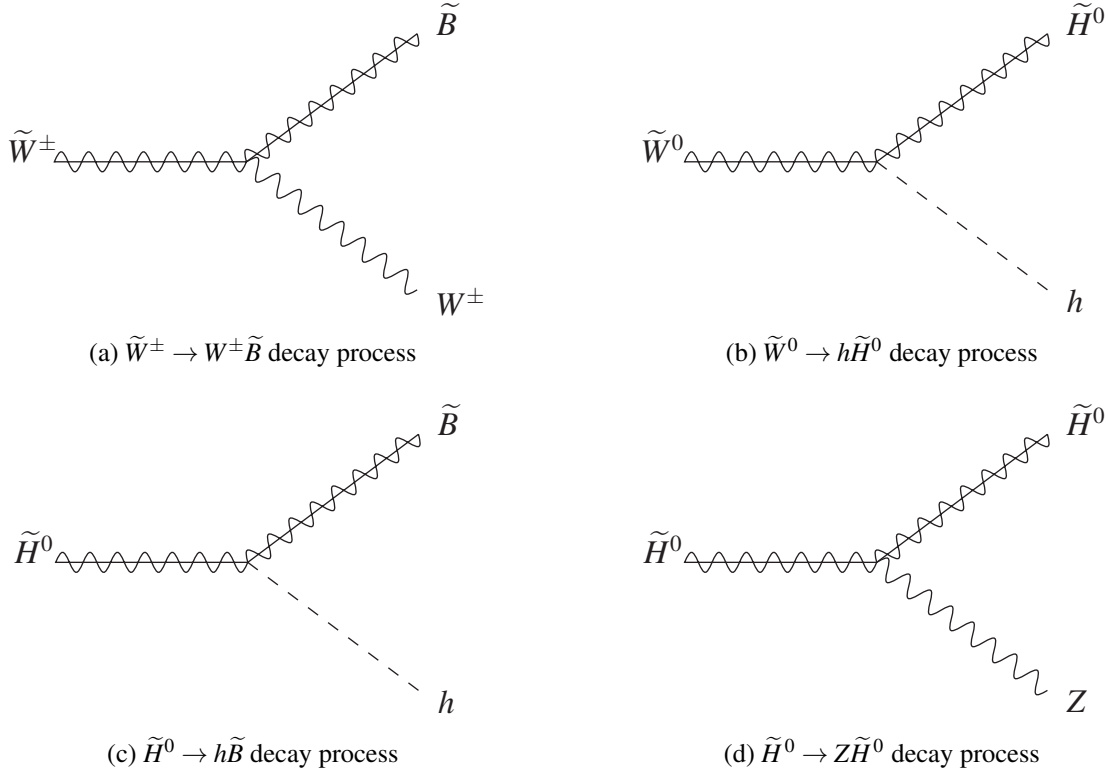


Figure 1.7: Decay process for  $\tilde{\chi}_1^\pm$  and  $\tilde{\chi}_2^0$  via SM bosons. There are four possible decay modes: (a)  $\tilde{W}^\pm \rightarrow W^\pm + \tilde{B}$ , (b)  $\tilde{W}^0 \rightarrow h + \tilde{H}^0$ , (c)  $\tilde{H}^0 \rightarrow h + \tilde{B}$ , and (d)  $\tilde{H}^0 \rightarrow Z + \tilde{H}^0$ . In the case where all squarks, gluinos and sleptons are much heavier than the SM bosons, charginos and neutralinos decays via the SM bosons are dominant processes.  $\tilde{H}$  represents one of the Higgs super-partner expressed in gauge eigenstates ( $\tilde{H}_d^-, \tilde{H}_u^+, \tilde{H}_d^0, \tilde{H}_u^0$ ).

### 1.4.3 Decay modes

In this thesis, the NLSPs are assumed to be  $\tilde{\chi}_1^\pm$  and  $\tilde{\chi}_2^0$  as wino-like gauginos, and the LSP is assumed to be  $\tilde{\chi}_1^0$  as a bino-like gaugino. Both wino and bino interact with the electroweak field because they are super-partners of weak bosons and photon. Decay modes for charginos and neutralinos related this analysis are shown in Fig. 1.7. The interaction among the super-partners of  $Z$  and  $\gamma$  is prohibited as well as the interactions among the neutral SM electroweak gauge bosons such as  $Z \rightarrow ZZ$  or  $\gamma \rightarrow ZZ$  are prohibited. The other decay modes to be considered would be decay scenarios via slepton-mediation. Since the sleptons with the mass smaller than 300 GeV are excluded [75], the parameter spaces of the slepton-mediated scenarios has been limited.

In order to decay from wino-like  $\tilde{\chi}_2^0$  to bino-like  $\tilde{\chi}_1^0$ , Higgsino contribution is essential because wino-like  $\tilde{\chi}_2^0$  and bino-like  $\tilde{\chi}_1^0$  cannot interact directly. Figures 1.8 show the decay chain for the wino-like  $\tilde{\chi}_2^0$ . Since couplings of  $Z$ -wino and  $Z$ -bino are prohibited, the mixing of neutral gauginos and Higgsinos is necessary twice to decay via  $Z$ . Thus, it is expected that the Higgs decay mode is dominant if the difference of the mass between winos and binos is larger than the Higgs mass ( $\sim 125$  GeV) [76]. Figure 1.9 shows the branching ratio for  $\tilde{W} \rightarrow h \tilde{B}$  decay mode, where  $M_1 = 0$  and  $M_2 = 175$  GeV. In this case, high  $\tan\beta$  suppresses the Higgs branch, whereas there is high branching ratio of the decays to Higgs (greater than 90%). The branching ratio should be taken into account since the sensitivity of the  $WZ$  decay scenario should be weakened in the region with the large mass difference between NLSP and LSP.

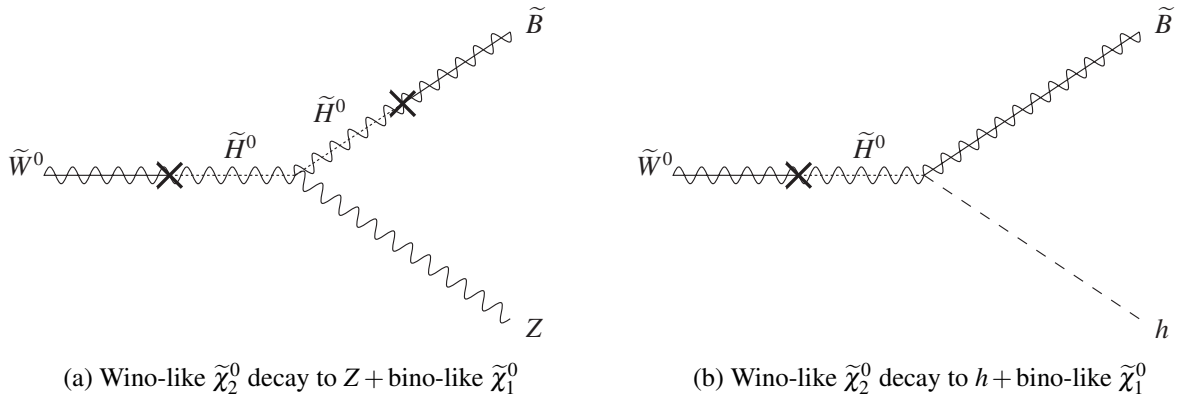


Figure 1.8: Wino-like  $\tilde{\chi}_2^0$  decay via SM boson mediated scenario. The black point shows the mixing. Since mixing of neutral gauginos and Higgsinos is needed twice to decay via  $Z$  shown in (a), the process can be suppressed if the mass difference is greater than Higgs mass because only one mixing is needed to decay via Higgs shown in (b).

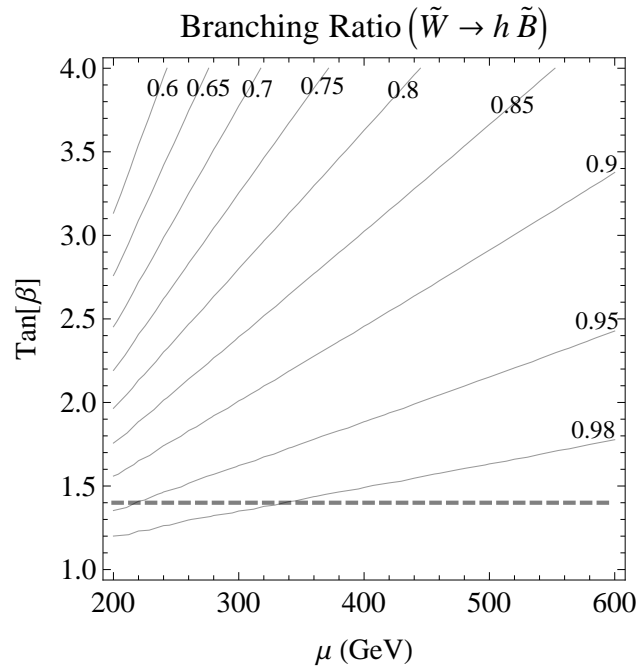


Figure 1.9: Branching ratio of a neutral wino NLSP to a Higgs and a bino LSP as a function of  $\mu$  and  $\tan\beta$ , for the wino mass term  $M_2$  of 175 GeV and the Higgs mass of 125 GeV. The branching ratio is computed using tree-level neutralino masses and mixing, with the input  $M_1 = 0$  [76].

## 1.5 SUSY searches

Searches for SUSY have been presented hitherto in several experiments with the high centre-of-mass energy colliders such as the LEP, the Tevatron and the LHC. The LEP was a synchrotron electrons-positron collider with the centre-of-mass energy of up to 209 GeV, and operated at CERN from 1989 to 2000. The Tevatron was a synchrotron proton-antiproton collider with the centre-of-mass energy of 1.8 TeV, and operated at Fermilab from 1987 to 2011. The LHC is a synchrotron proton-proton collider with the centre-of-mass energy of 7 TeV in 2010 and 2011 and 8 TeV in 2012, as described in Chap. 2.

### 1.5.1 LEP Experiments

The Large Electron-Positron Collider (LEP) was a circular collider located on CERN at Genève, Switzerland. The LEP was operated with the centre-of-mass energy of  $\sqrt{s} = 183\text{--}209\text{ GeV}$  and provided total luminosity of  $\sim 2.6\text{ fb}^{-1}$  from 1997 to 2000 (LEP2). There are four complementary experiments: ALEPH [77, 78], DELPHI [79, 80], OPAL [81] and L3 [82]. These detectors are designed as multi-purpose detectors to detect signals from electron-positron collision at the centre of the detectors. The results of four collaboration during the LEP2 were analysed separately and were combined statistically [83–93].

At the LEP experiments, the SUSY would be produced with electroweak interaction because of the collision of leptons. The following production scenarios have been taken into account:

- $e^+e^- \rightarrow \tilde{q}\tilde{q}$  (squark production),
- $e^+e^- \rightarrow \tilde{\ell}\tilde{\ell}$  (slepton production),
- $e^+e^- \rightarrow \tilde{\chi}^\pm\tilde{\chi}^\mp$  or  $\tilde{\chi}^0\tilde{\chi}^0$  (chargino and neutralino production).

Since the beam energy is up to 209 GeV, the SUSY mass of up to  $\sim 100\text{ GeV}$  can be produced in the collision of the LEP. Following paragraphs show the final results of LEP searches.

**Squark search** Squarks could be pair produced via the  $s$ -channel production:  $e^+e^- \rightarrow Z/\gamma^* \rightarrow \tilde{q}_L\tilde{q}_L$  or  $\tilde{q}_R\tilde{q}_R$ , where  $\tilde{q}_L$  and  $\tilde{q}_R$  represent the super-partners of left-handed and right-handed quarks. Stops and sbottoms are expected to be lighter than the squarks of the first two families. Thus the searches for stops and sbottoms are concentrated as searches for squarks.

The expected signals from stops and sbottoms are based on the signals from their decays:

$$\tilde{t} \rightarrow c + \tilde{\chi}_1^0, \quad (1.72)$$

$$\tilde{t} \rightarrow b + \ell + \tilde{\nu} (\rightarrow \nu + \tilde{\chi}_1^0), \quad (1.73)$$

$$\tilde{b} \rightarrow b + \tilde{\chi}_1^0. \quad (1.74)$$

Each decay process is assumed to have a 100% branching ratio (simplified model).

The exclusion limits for these channels at LEP are shown in Fig. 1.10 with CDF and  $D\emptyset$  results [84]. Searches at LEP have an advantage to cover the region with small  $\Delta m_{\tilde{q}, \tilde{\chi}_1^0}$  because of the lepton collider. The statistics are enough to exclude the squark mass of 100 GeV. In Fig. 1.10, the angle  $\theta$  represents the mixing angle between  $\tilde{q}_L$  and  $\tilde{q}_R$ ,  $\tilde{q}_1 = \tilde{q}_L \cos \theta + \tilde{q}_R \sin \theta$ , where  $\tilde{q}_1$  is the lowest mass eigenstate, and  $\theta = 0$  corresponds to the pure left-handed squark case.

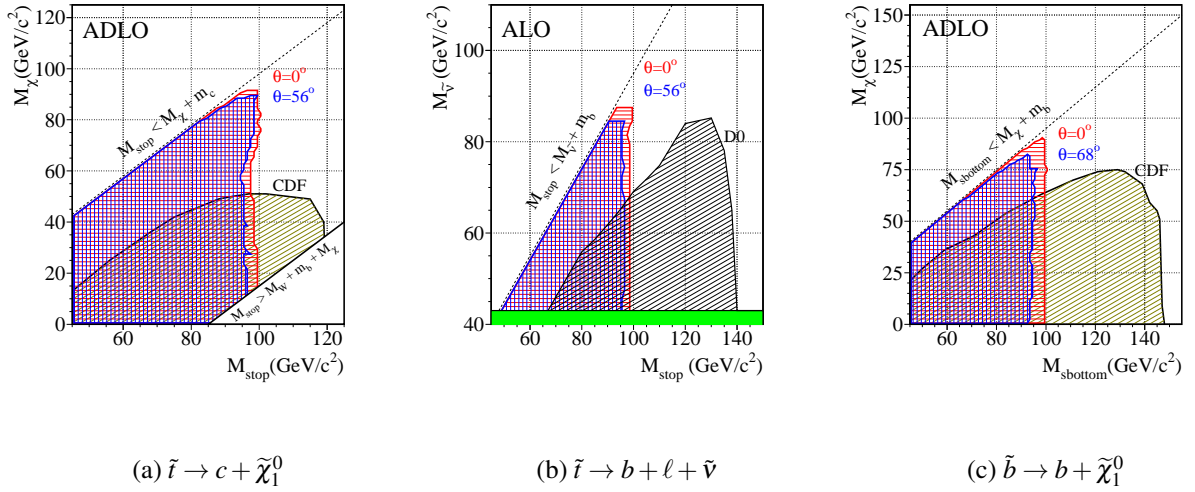


Figure 1.10: Results of searches for stops and sbottoms at LEP (ALEPH, DELPHI, L3 and OPAL) [84]. The figures are also shown the first results of searches in Tevatron (CDF and DØ) [94, 95]. The  $\theta$  represents the mixing angle between left-handed and right-handed squarks,  $\tilde{q}_1 = \tilde{q}_L \cos \theta + \tilde{q}_R \sin \theta$ . The blue region is an exclusion limit with  $\theta = 56^\circ$  and the red region is an exclusion limit with  $\theta = 0^\circ$  (left-handed like squark).

**Slepton search** Sleptons could be pair produced via the  $s$ -channel and  $t/u$ -channel production. For the  $s$ -channel, the production process is  $e^+e^- \rightarrow Z/\gamma^* \rightarrow \tilde{\ell}_L\tilde{\ell}_L$  or  $\tilde{\ell}_R\tilde{\ell}_R$ , where  $\tilde{\ell}_L$  and  $\tilde{\ell}_R$  represent the superpartners of left-handed and right-handed leptons. For the  $t$ -channel production, the sleptons are produced with an exchange of a neutralino. The production process is  $e^+e^- \rightarrow \tilde{\ell}_L\tilde{\ell}_R$ . Slepton searches at LEP [83] are based on detecting two leptons from the slepton decays:

$$\tilde{\ell}^\pm \rightarrow \ell^\pm + \tilde{\chi}_1^0, \quad (1.75)$$

where  $\tilde{\chi}_1^0$  is assumed to be the LSP. The bino mass term  $M_1$  is assumed to satisfy the relation

$$M_1 = \frac{5}{3} \tan^2 \theta_W M_2, \quad (1.76)$$

which is based on the framework of the MSSM. The relation is necessary to calculate the cross section for sleptons via  $t$ -channel production.

The final results of searches for selectrons, smuons and staus are shown separately in Fig. 1.11. The exclusion limits are set with the assumption that the contribution of the SUSY is only from right-handed sleptons. The assumption is conservative because the cross section for the right-handed sleptons is smaller than that for left-handed sleptons in general. Finally, almost all of sleptons are excluded with the mass of up to 100 GeV with any mass of the LSP.

**Chargino and Neutralino search** Charginos searches with the relation  $|\mu| \ll M_2$  and  $|\mu| \gg M_2$  are performed. The direct production processes are considered as follows:

$$e^+e^- \rightarrow \tilde{\chi}_1^\pm \tilde{\chi}_1^\mp, \quad (1.77)$$

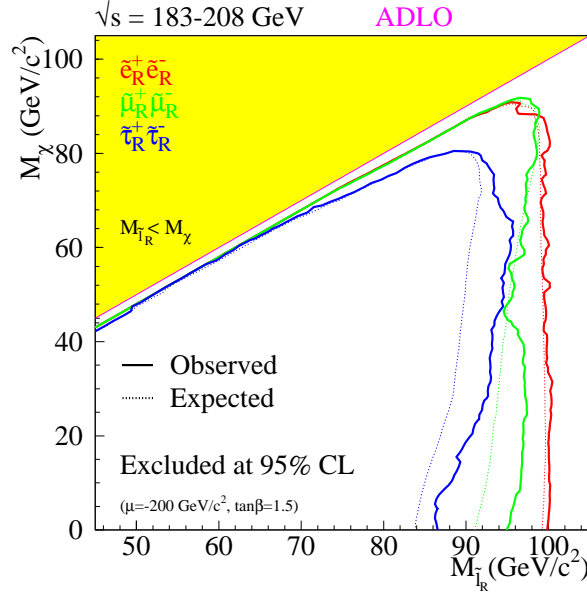


Figure 1.11: Exclusion limits at LEP for the right-handed selectrons (red), smuons (green) and staus (blue). The exclusion limits are calculated at 95% confidence level [83]. The  $\mu$  and  $\tan\beta$  parameters are assumed to be 200 GeV and 1.5, respectively.

where  $s$ -channel and  $t/u$ -channels are taken into account. Searches are based on detecting signals from the charginos decays:

$$\tilde{\chi}_1^\pm \rightarrow \tilde{\chi}_1^0 + \ell^\pm \nu / q\bar{q}', \quad (1.78)$$

where the chargino decays via  $W^*$ , slepton or squark. The exclusion limits for the case with  $|\mu| = 200$  GeV and  $\tan\beta = 2$  are set as  $m_{\tilde{\chi}_1^\pm} < 103.5$  GeV (gaugino case) [85].

The degenerate mass region ( $\Delta m_{\tilde{\chi}_1^\pm, \tilde{\chi}_1^0} \sim O(100)$  GeV) has been investigated with the assumptions  $|\mu| \ll M_2$  (Higgsino-like) or  $|\mu| \gg M_2$  (gaugino-like). The results of the exclusion limits are obtained as  $m_{\tilde{\chi}_1^\pm} > 92.4$  GeV (Higgsino-like) and  $m_{\tilde{\chi}_1^\pm} > 91.9$  GeV (gaugino-like).

Neutralino searches are based on the scenario of the SUSY breaking framework of GMSB or no-scale supergravity [96]. In these cases, the LSP would be the gravitino and the lightest neutralino decays into a gravitino and a photon as

$$\tilde{\chi}_1^0 \rightarrow \tilde{G} + \gamma, \quad (1.79)$$

where the mass of the gravitino is assumed to be negligible ( $< 1$  GeV). The neutralino is produced with the gravitino ( $ee \rightarrow \tilde{G}\tilde{\chi}_1^0$ ) or one more neutralino ( $ee \rightarrow \tilde{\chi}_1^0\tilde{\chi}_1^0$ ). Thus the signal should have one or two photons in final states. The exclusion limit for these channels is shown in Fig. 1.12. The parameter space with the gravitino mass less than  $\sim 2 \times 10^{-5}$  GeV and neutralino mass less than  $\sim 200$  GeV with the framework of no-scale supergravity is excluded with 95% confidence level.

## 1.5.2 Tevatron Experiments

The Tevatron was the largest hadron collider in America, which is located at the Fermilab, Chicago, the United States. The Tevatron collider has provided 0.9 TeV proton and antiproton beams from 1987 to

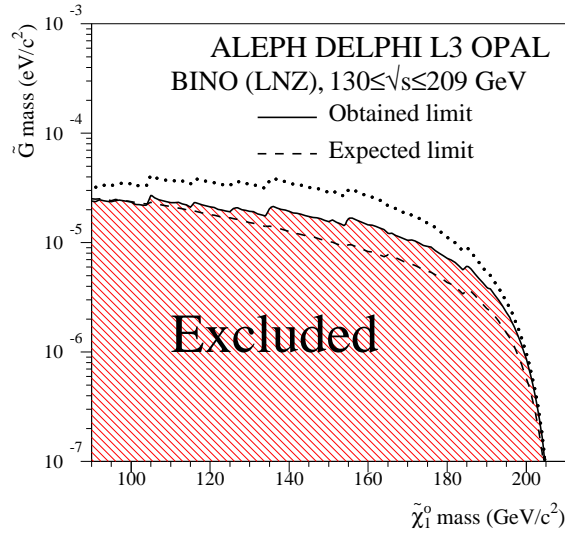


Figure 1.12: Exclusion limits at LEP for no-scale supergravity model (shown as “LNZ”) as a plane of gravitino and neutralino (bino-like) masses [91].

2011. During the Run-1 of the Tevatron, 1992–1996, the top quark has been discovered at the experiments using the Tevatron [97,98]. There are two experiments, CDF [99] and DØ [100], which have multi-purpose detectors.

The SUSY particles are produced mainly from  $q\bar{q}$  collisions. The production of  $\tilde{q}\tilde{q}$ ,  $\tilde{q}\tilde{g}$ ,  $\tilde{g}\tilde{g}$  and  $\tilde{\chi}_1^+\tilde{\chi}_2^0$  were taken into account. The searches for squarks are based on the assumption where the super-partner of the third generation is lighter than the others. Thus only stop and sbottom searches are performed at Tevatron, as well as searches at LEP. The decay modes are assumed to be the same processes as that assumed in the LEP searches. Stop mass less than 240 GeV was excluded with 95% confidence level at CDF and DØ, as shown in Fig. 1.13.

Direct charginos and neutralinos production was searched in Tevatron experiments. There are two scenarios taken into account separately. One is mSUGRA scenario, where the masses of the lightest chargino and the second lightest neutralino are degenerate  $m_{\tilde{\chi}_1^\pm} = m_{\tilde{\chi}_2^0}$  and the LSP is the lightest neutralino. This mode emits three leptons and missing transverse energy, thus the final states suppresses the SM background processes. The chargino mass limit has been set as shown in Fig. 1.14a.

The other is GMSB scenario. In this case, as the LSP is the gravitino, the lightest neutralino decays into a gravitino and a photon. Thus the final states include the two photons and the missing transverse energy. The combined exclusion limits from the results of CDF and DØ are shown in Fig. 1.14b. The observed exclusion limit was set with the mass of chargino below 210 GeV.

### 1.5.3 LHC Experiments

The LHC [105] is a hadron collider operated from 2009, which have two complementary experiments: the ATLAS [106] and the CMS [107]. The descriptions for the LHC and the ATLAS will be found in Chap. 2.

Since the beams from the LHC is the highly accelerated protons, the gluon-gluon scattering is the dom-



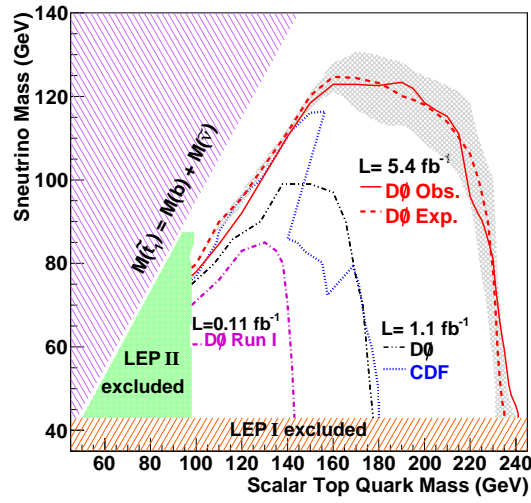
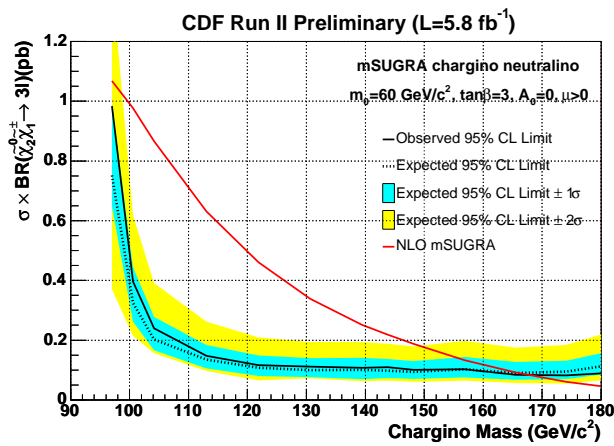
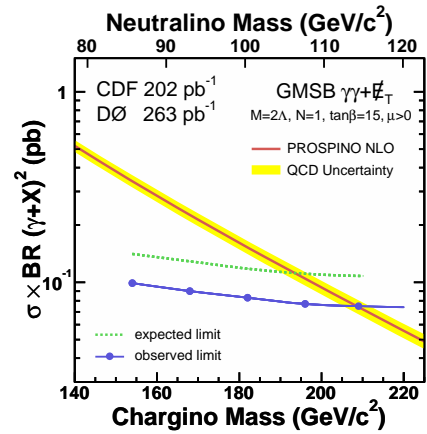


Figure 1.13: Observed and expected exclusion limits in the sneutrino and stop masses plot at DØ (red lines) [101]. The previous results from LEP2 (green region), DØ (purple and black lines) and CDF (blue line) are also shown.



(a) Chargino for mSUGRA [102]



(b) Chargino for GMSB [103]

Figure 1.14: Chargino exclusion limits at CDF for mSUGRA (a) and GMSB (b) scenarios. The red lines show the theoretical prediction using PROSPINO [104].

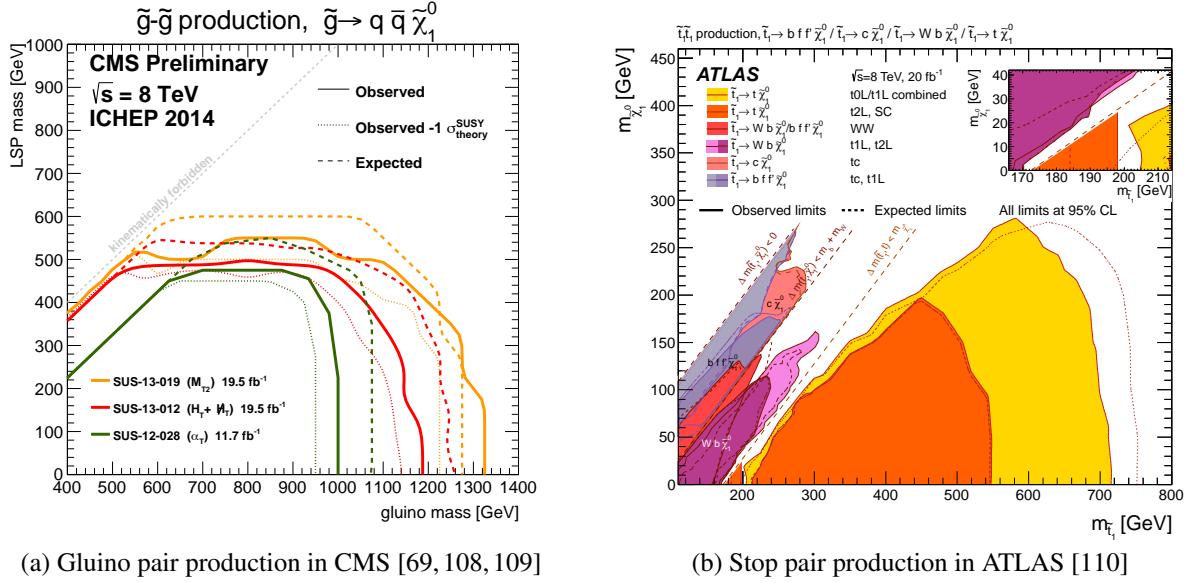


Figure 1.15: Exclusion limits for the gluino pair production at CMS (a) and the stop pair production at ATLAS (b).

inant process in contrast to the Tevatron processes (quark-antiquark scattering). Thus the SUSY production modes with  $s$ -channel exchange of gluons or  $t$ -channel exchange of gluino/squark are much larger than the electroweak processes, as the cross section plots can be found in Fig. 1.6. In the LHC experiment, squarks and gluinos searches have been carried out with great effort because of the high cross sections. These searches are based on detecting the final states with multi-jets and zero or a few leptons. A variety of decay processes of the squarks can be considered. In order to be simply, squark decays into quark and the LSP:  $\tilde{q} \rightarrow q + \tilde{\chi}_1^0$ . Thus squark pair production includes at least two jets and the missing transverse momentum in the final states. The gluinos are pair produced and decay as basically  $\tilde{g} \rightarrow q\bar{q} + \tilde{\chi}_1^0$ . In this simple case, the final states should include at least four jets.

The search results for gluinos in CMS [69, 108, 109] and for stops in ATLAS [110] are shown in Fig. 1.15. Three colours in Fig. 1.15a represent the analyses with different criteria and five colours in Fig. 1.15b represent the results for different decay processes shown in the legend. The gluino with its mass below 1.3 TeV with zero mass LSP has been excluded with 95% confidence level in CMS. ATLAS also has excluded 1.3 TeV mass of gluinos [111]. The inclusive squark pair productions with the mass below 850 GeV and 920 GeV are excluded in ATLAS and CMS, respectively. Especially for the stops, as shown in Fig. 1.15b, the mass below  $\sim 700 \text{ GeV}$  has been excluded in ATLAS and CMS.

For the electroweak SUSY searches, the searches for direct production of sleptons are shown. As the LHC provides the high energy proton beam, sleptons can be produced  $q\bar{q}$  scattering via  $s$ -channel exchange of a weak boson or  $t$ -channel scattering exchange of a squark. Since squarks should have mass greater than 700 GeV according to the squark searches, only  $s$ -channel production mode has been taken into account. The slepton decays into the corresponding lepton and the LSP:  $\tilde{\ell} \rightarrow \ell + \tilde{\chi}_1^0$ , as explained in Sec.1.5.1. Results are shown in Fig. 1.16 for the left-handed (Fig. 1.16a) and right-handed (Fig. 1.16b) sleptons in ATLAS [112]. They also show the exclusion limits in the LEP combined results. Whereas the exclusion limits have been extended to 250 GeV and 300 GeV for both left-handed and right-handed sleptons, respectively, the regions with the difference of the masses between sleptons and the LSP  $m_{\tilde{\ell}, \tilde{\chi}_1^0} < \sim$

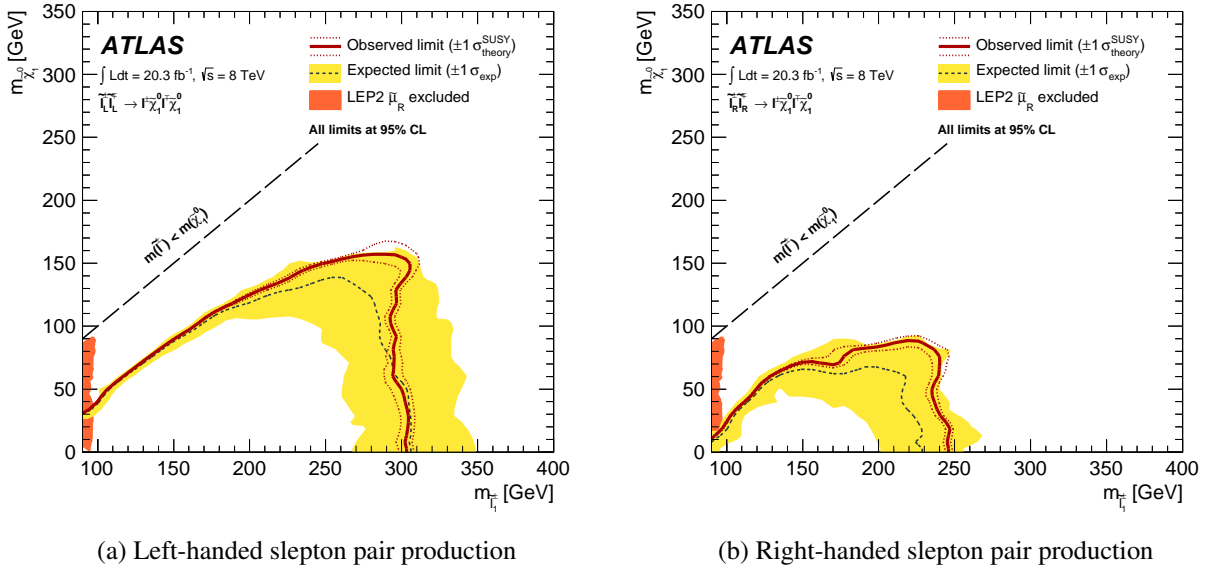


Figure 1.16: Exclusion limits for directly pair produced left-handed (a) and right-handed (b) sleptons in ATLAS [112].

70 GeV and the slepton mass greater than 100 GeV have not excluded. This is because the emitted leptons from slepton decays have low momenta. In contrast to the LEP searches, the collision of the proton beams have a large amount of hadronic background. Since leptons with low momenta tend to be misidentified, the analyses are difficult in these region.

All other results in ATLAS [111] and CMS [113] can be found in the corresponding references.

#### 1.5.4 Summary of the SUSY searches

Searches for the SUSY has been reviewed up to the previous sections. According to the current results, there have been no evidence of the SUSY particles and the exclusion limits have been extended with the masses as follows:

- squarks:  $m_{\tilde{q}} \sim 1 \text{ TeV}$ ,
- gluinos:  $m_{\tilde{g}} \sim 1.4 \text{ TeV}$ ,
- stops:  $m_{\tilde{t}} \sim 700 \text{ GeV}$ ,
- sleptons:  $m_{\tilde{\ell}} \sim 300 \text{ GeV}$ ,
- gauginos (except the LSP):  $m_{\tilde{\chi}} \sim 160 \text{ GeV}$  (LEP and Tevatron searches taken into account).

Therefore, if the SUSY particles with the light masses exist, the possible candidates are light charginos and neutralinos. As described in Sec. 1.2, the light electroweak SUSY particles are favoured to solve the muon  $g - 2$  problem. Thus it is important to improve the searches for charginos and neutralinos.

## Chapter 2

# LHC-ATLAS Experiment

Experimental equipments used in this analysis will be described in this chapter. A Toroidal LHC Apparatus (ATLAS) detector [106] is a detector to capture and record the signals of proton-proton collisions in the Large Hadron Collider (LHC). The detector is located at the LHC Point1 of the European Organization for Nuclear Research (CERN) and the LHC is located at a suburb of Genève in Switzerland, as shown in Fig. 2.1. Overview of the LHC and the ATLAS detector in Sec. 2.1 and Sec. 2.2, respectively.

### 2.1 Overview of the LHC accelerator

The LHC [105] is the highest energy proton collider in the world at present. It is designed to collide two counter rotating proton (or lead) beams, which are accelerated to 4 TeV in 2012 (LHC Run-1), whereas designed energy is 7 TeV. The beam pipes and magnets are installed in the 26.7 km long tunnel that was constructed for the LEP. This tunnel lies between 45 m and 170 m below the surface with 1.4% inclination towards the Léman lake, stretched for two countries, France and Switzerland, as shown in Fig. 2.1.

The LHC can be divided to eight arcs and straight parts. The half of the straight parts have beam crossing points. The other four parts contain RF systems, collimation systems or a dump. In arc parts, superconducting dipole and quadrupole magnets are located. They are designed to provide above 8 T magnetic fields.

Figure 2.2 shows the sequence of the beam injection [115]. The accelerated protons are injected into the accelerators in following order, Linear Accelerator 2 (LINAC2), Proton Synchrotron Booster (PSB), Proton Synchrotron (PS), and Super Proton Synchrotron (SPS). The LINAC2 is the primary source of protons for CERN accelerators. The protons from LINAC2 form into 180 mA current beam with 50 MeV, injected into the PSB. In the PSB, the beam is accelerated to 1.4 GeV. The bunch spacing (50 ns for Run-1) is implemented at the PS, where the beam energy rises to 25 GeV. The LHC injection energy is 450 GeV from SPS acceleration. At the LHC, the 4 TeV beams including  $10^{11}$  protons are formed and used in the collision.

The observed number of events per second from the LHC collisions is given by following relation:

$$N_{\text{event}} = \mathcal{L} \sigma_{\text{event}}, \quad (2.1)$$

where the  $\sigma_{\text{event}}$  is the cross section for the event under study and  $\mathcal{L}$  is the instantaneous luminosity. The instantaneous luminosity in the LHC is not constant value but decreases during each fill. This is because

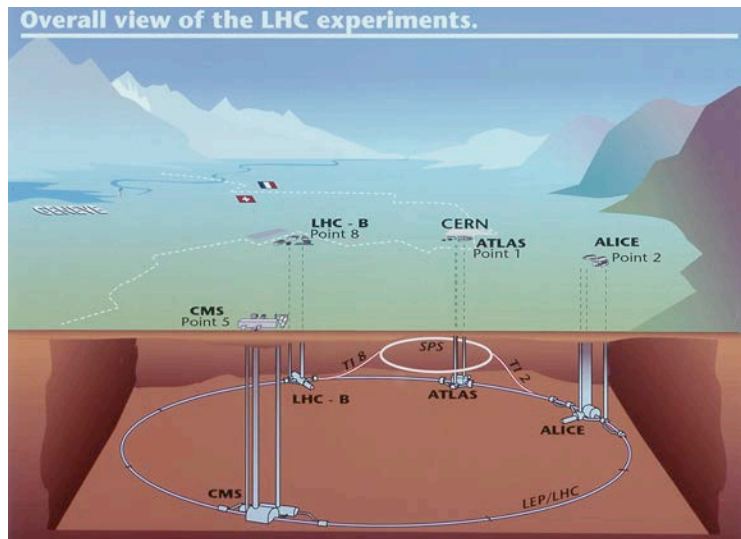


Figure 2.1: Location of the LHC and the ATLAS detector. The ATLAS is located in CERN Meyrin site, Genève, Switzerland [114].

### CERN's Accelerator Complex

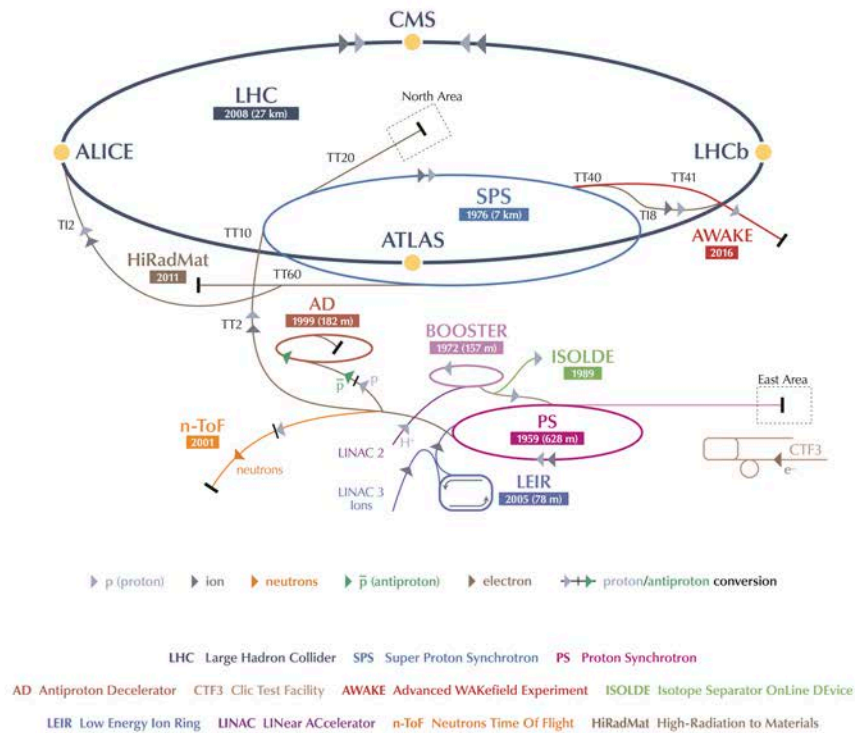


Figure 2.2: LHC injection complex, drawn by Julie Haffner [116]

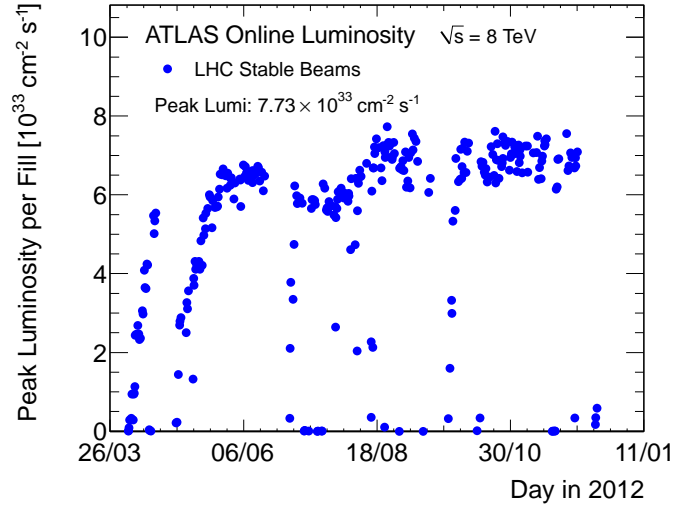


Figure 2.3: Peak luminosity per day in 2012 [117].

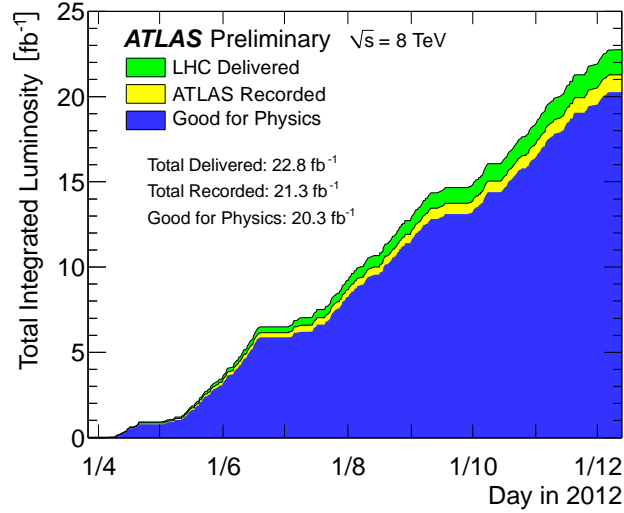


Figure 2.4: Total Integrated Luminosity and Data Quality in 2012 [117].

the particles in bunches will be lost due to the collision and the beam loss during the circulation. The peak instantaneous luminosity has been observed  $7.7 \times 10^{33} \text{ cm}^{-2} \text{ s}^{-1}$  in Run-1, whereas the designed value is  $1 \times 10^{34} \text{ cm}^{-2} \text{ s}^{-1}$ . The online monitoring result of the LHC peak luminosity in 2012 is shown in Fig. 2.3. The integration of the instantaneous luminosity called the integrated luminosity is utilised as an indicator of the total amount of observed data. Using this notation, the total observed number of events under study is written as

$$N_{\text{event}} = \sigma_{\text{event}} \times \int \mathcal{L} dt. \quad (2.2)$$

The development of the total integrated luminosity in 2012 is shown in Fig. 2.4. The total integrated luminosity delivered from the LHC has been  $22.8 \text{ fb}^{-1}$ , while recorded integrated luminosity and analysed integrated luminosity have been  $21.3 \text{ fb}^{-1}$  and  $20.3 \text{ fb}^{-1}$ . The inefficiency of the recorded and analysed integrated luminosity were caused by the DAQ performance and the detector qualities, as discussed in

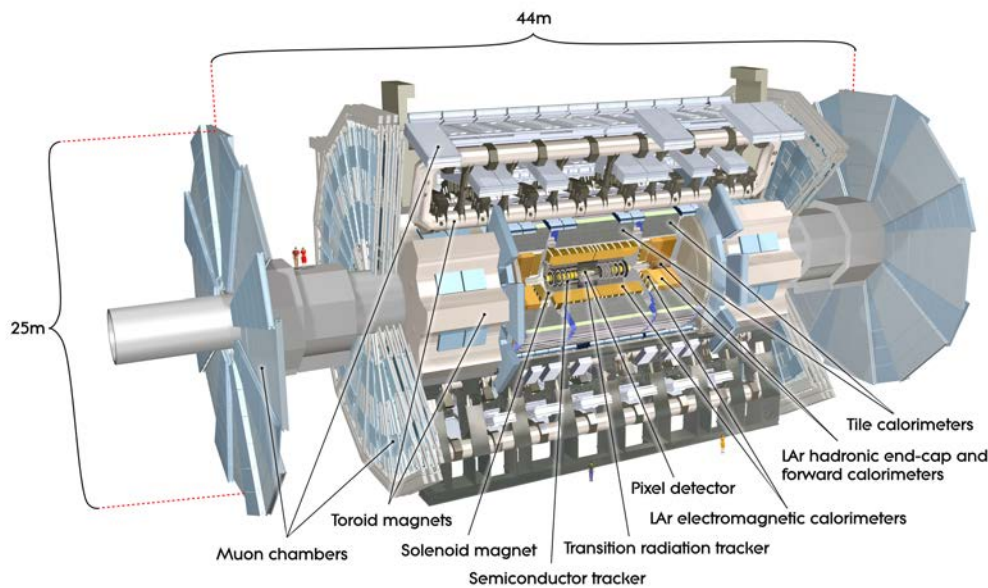


Figure 2.5: The image of the whole ATLAS detector [106].

Sec. 4.2.

## 2.2 Overview of the ATLAS Detector System

The ATLAS Detector is the multi-purpose detector for the experiment of the particle physics. Figure 2.5 shows a whole view of the ATLAS detector. It consists mainly of five parts: the Inner Detector, the Calorimeter, the Muon Spectrometer, the Forward Detector, and the Magnet System.

The parts of the ATLAS detector can be classified by the role in detecting particles, which are the tracking, the energy measurement and the triggering. The tracking part is composed of the Inner Detector and the components of the Muon Spectrometer. These detect electric signals made by interaction between the detector materials and charged particles. The tracks of charged particles are reconstructed using these. The Calorimeter is employed to measure the energy of the passed particles. Combining the information of the tracking and the energy measurement give us to the four-momentum of the passed particle. The trigger is composed of the components of the Calorimeter and the Muon Spectrometer. These detects the several patterns and determines whether the data should be recorded or not. Detail would be found in the following sections.

### 2.2.1 Variables used to specify the location in the detector

The ATLAS detector surrounds the solid angle of approximately  $4\pi$  from the interaction point in order to have a good resolution of the missing transverse momentum. There are some important variables to understand the geometry of the ATLAS detector.

The origin of the ATLAS detector is the nominal interaction point. The beam direction defines the  $z$  axis, the positive direction of which is defined as anticlockwise, and its transverse plane defines  $x$ - $y$  plane,

where the  $x$  axis points to the centre of LHC ring and the  $y$  axis points upwards. The azimuthal angle  $\phi$  is defined as the angle around the  $z$  axis in the  $x$ - $y$  plane, and the polar angle  $\theta$  is defined as the angle from the  $z$  axis in the  $r$ - $z$  plane, where the radius  $r = \sqrt{x^2 + y^2}$ . The pseudo-rapidity  $\eta$  is defined with the polar angle as following equation:

$$\eta = -\ln \left[ \tan \left( \frac{\theta}{2} \right) \right]. \quad (2.3)$$

Usually the position of the detector is explained with the radius  $r$ , the azimuthal angle  $\phi$  and the pseudo-rapidity  $\eta$ .

The distance  $\Delta R$  in the pseudo-rapidity-azimuthal angle space is defined as

$$\Delta R = \sqrt{\Delta \eta^2 + \Delta \phi^2}. \quad (2.4)$$

The transverse momentum  $p_T$  is defined as the momentum vector in the  $x$ - $y$  plane as

$$\mathbf{p}_T = \begin{pmatrix} p_x \\ p_y \end{pmatrix}, \quad (2.5)$$

$$p_T = \sqrt{p_x^2 + p_y^2}. \quad (2.6)$$

The transverse energy  $E_T$  is defined by the  $p_T$  as

$$E_T \equiv \sqrt{m^2 + p_T^2} \sim |\mathbf{p}_T|. \quad (2.7)$$

The approximation in Eq. (2.7) is permitted if the particle mass  $m$  can be negligible. The particles which are selected in this analysis have at least a few GeV, so that the mass of the light particles such as electrons are usually negligible.

### 2.2.2 Inner Detector

The Inner Detector (ID) consists of detectors for vertexing and tracking particles. The components of the ID System are the Pixel, the Semiconductor Tracker (SCT) and the Transition Radiation Tracker (TRT). Figure 2.6 illustrates the overview of the ID. Each detector component of ID can be divided two parts, the barrel and the end-cap parts. A barrel part is set up in parallel to the beam axis and located around the interaction point as the origin. The modules of a barrel part is also laid in parallel with the beam axis. An end-cap part, on the other hand, is located outside of the barrel part on a vertical plane with respect to the  $z$  axis. The ID covers the pseudo-rapidity of  $|\eta| < 2.5$ .

The Pixel and the SCT sensors are always kept within the temperature of approximately  $-10^\circ\text{C}$  in order to maintain the good performance for sensor noise, in particular after the radiation damage. In contrast, the TRT is not necessary to be kept in the low temperature. Thus it operates at the room temperature.

**Pixel** The innermost part of ID is the Pixel Detector [118]. This part surrounds the interaction point with three barrel layers and three end-cap disks. It consists of 112 barrel staves and 48 end-cap sectors, which composes totally 1741 pixel modules.

A module has a silicon sensor tile and 16 readout chips, which are connected with bump-bonding technique. A rough sketch of a barrel module is shown in Fig. 2.7. The total number of channel is 47232



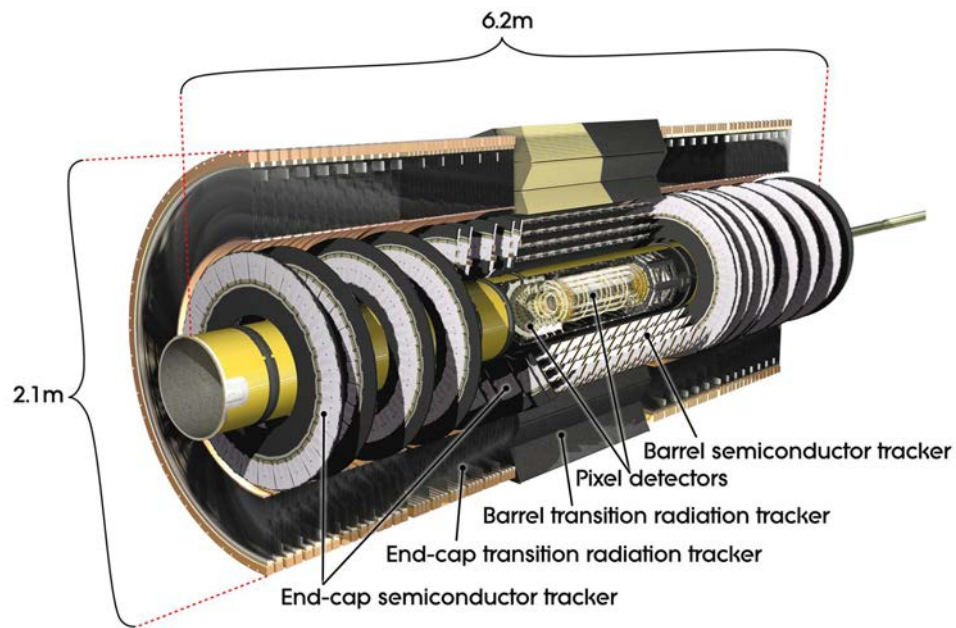


Figure 2.6: Overview of the Inner Detector [106].

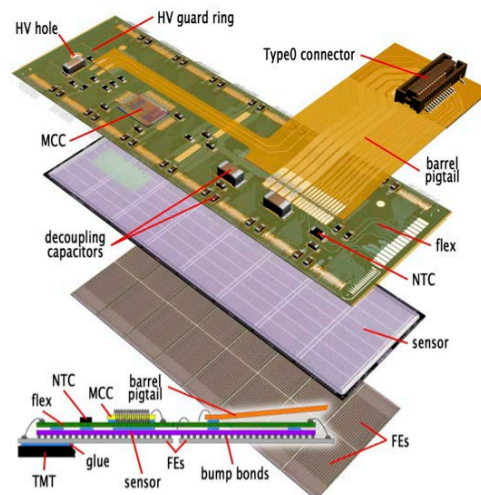


Figure 2.7: A pixel module located on barrel part [106].

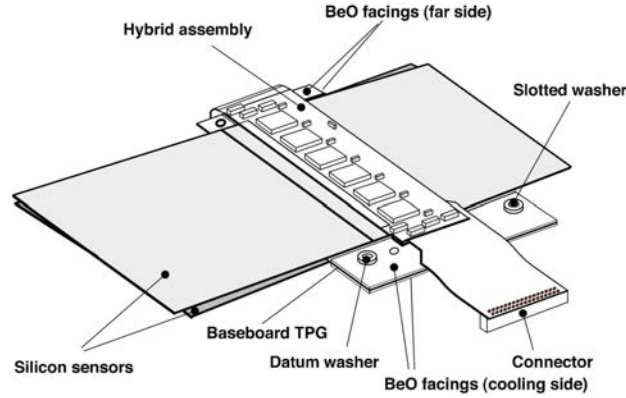


Figure 2.8: A SCT module located in the barrel part [106].

arranged in 144 columns and 328 rows. The size of a pixel is  $r\text{-}\phi \times z$  of  $50 \times 400 \mu\text{m}^2$  for approximately 90% pixels and  $50 \times 600 \mu\text{m}^2$  for the others. The latter long pixels for the  $z$  direction are located on the boundary of the readout chips. This is because the readout chips cannot be completely linked to the next readout chips in the order of  $\sim \mathcal{O}(1) \mu\text{m}$ . Furthermore, since the readout chips stand in two lines along the short side of the pixel, the interval of the two lines also has a larger gap than the gap at the long pixels. The signals of the pixels located on the gaps is read out together with the neighboring pixels, which are called *ganged* pixels. The design of the ganged pixels makes it possible to distinguish which pixel is fired. The performance in the boundary between the readout chips has been kept by the positioning.

The Pixel is set from the  $\sim 5 \text{ cm}$  radius of the interaction point. The intrinsic accuracy on the detection of the Pixel is  $10 \mu\text{m}$  in  $r\text{-}\phi$  and  $115 \mu\text{m}$  along  $z(r)$  in the barrel layers (end-cap disks).

**Semiconductor Tracker (SCT)** The SCT is the second innermost part and located to cover Pixel. This part is 4 barrel layers and 9 end-cap disks in each side. The barrel layers have 2112 modules and forward and backward end-caps have 988 modules. Thus there are totally 4088 modules in the SCT part. A SCT module has two silicon microstrip sensor bulks and 12 readout chips with 768 channels. The strip pitch is approximately  $80 \mu\text{m}$ . A SCT barrel module is illustrated in Fig. 2.8. The two sensor bulks are set with the stereo angle of  $40 \text{ mrad}$  in order to reconstruct a point for a hit in each module from the 1-dimensional information. The point is called the space-point, which represents the 3-dimensional hit point. All the barrel modules have same structures, whilst the end-cap modules have different structures since the end-cap sensors has a sector shape.

The intrinsic accuracy of the SCT detection is  $17 \mu\text{m}$  in  $r\text{-}\phi$  and  $580 \mu\text{m}$  along  $z(r)$  in the barrel layers (end-cap disks).

**Transition Radiation Tracker (TRT)** The TRT [119, 120] surrounds the SCT and covers  $|\eta| < 2.0$ . This is the detector employing the transition radiation, which is emitted when a particle is passing through the boundary between the materials with the different dielectric constant. This is useful to distinguish electrons and pions. The energy of the transition radiation is in proportion to the Lorentz factor  $\gamma = E/m$  of the passing particle. For example, the energy of the transition radiation for the  $\gamma \sim 10^3$  is in the range 2 to 40 keV [24]. Since the masses between electrons and pions are very different, thus the  $\gamma$  factors cover

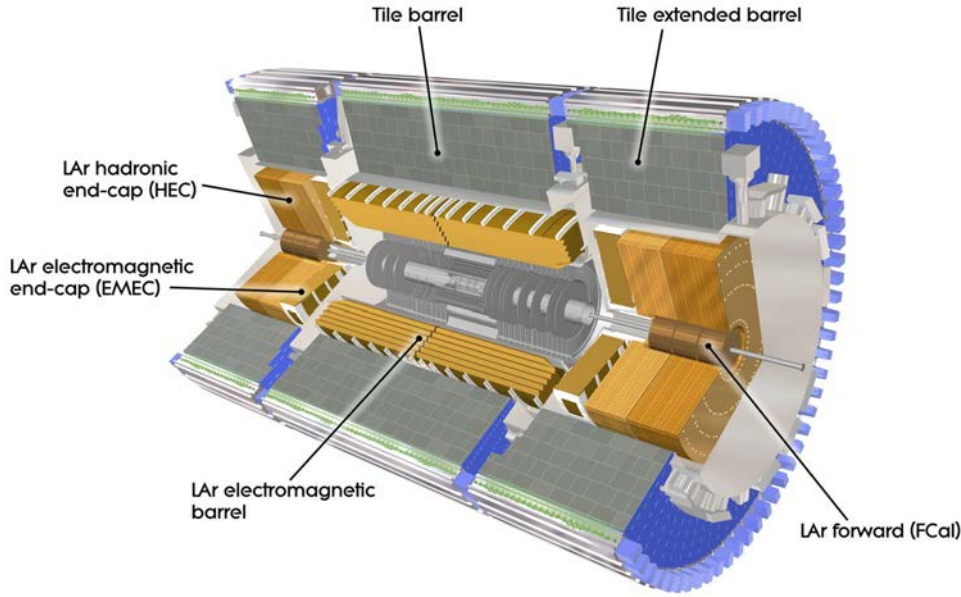


Figure 2.9: Whole view of the Calorimeter [106]

the different range. Then the high threshold of  $\sim 6$  keV for the transition radiation photons is optimised to take advantage of the relation, as well as the low threshold of 300 eV is prepared for the tracking.

The TRT consists of many proportional drift tubes called straw tubes. In the barrel part, 52544 straw tubes with 4 mm diameter and 144 cm long lie parallel to the beam axis. The end-cap parts have the 122880 tubes with 4 mm diameter and 37 cm long, pointing outwards in the radial direction. The gas mixture of 70% Xe, 27% CO<sub>2</sub> and 3% O<sub>2</sub> with 5–10 mbar over-pressure is used. Using Xe has an advantage to getting high efficiency to absorb the transition radiation photons with the energy of 6–15 keV.

Each track is expected to have an average of 34 hits in the TRT barrel region and 25 hits in the region between barrel and end-caps and at  $|\eta| > 1.7$ . The intrinsic accuracy of the measurement is  $130 \mu\text{m}$  along  $r$ - $\phi$ .

### 2.2.3 Calorimeter

The Calorimeter is a device for energy measurement for the particles passing through its volume. The ATLAS Calorimeter has two main parts the electromagnetic (EM) calorimeter and the hadronic calorimeter. Whole image of the calorimeter part is illustrated in Fig. 2.9. The Calorimeter adopts the sampling detectors covering full  $\phi$  direction and  $|\eta| < 4.9$ .

**Electromagnetic Calorimeter** The EM calorimeter [121] is made of the liquid argon (LAr) detectors with lead absorber plates. This part covers  $|\eta| < 1.475$  for the barrel part and  $1.375 < |\eta| < 3.2$  for the two end-cap parts. The barrel calorimeter has two identical half-barrels, separated by a small gap of 4 mm at  $z = 0$ .

The EM calorimeter is for the energy measurement for the electromagnetic interacting particles, mainly electrons and photons. Figure 2.10 shows a picture of an EM calorimeter module. A module has *Accordion*

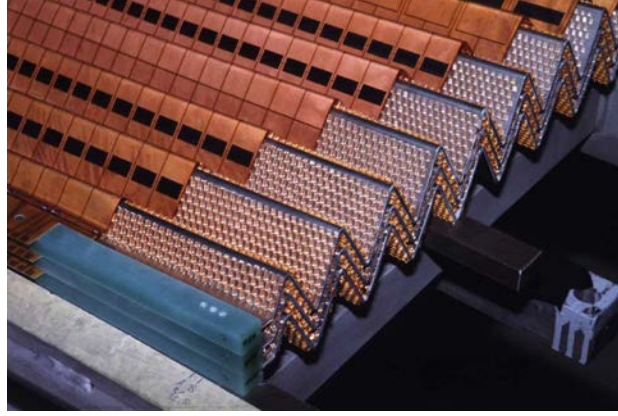


Figure 2.10: A photo of the accordion structure of the EM calorimeter [106]

structure of the copper electrode layers and the lead absorber. The accordion waves are axial direction and run in the azimuthal angle  $\phi$  in the barrel, and are parallel to the radial direction and run axially in the end caps.

A module has three layers, shown in Fig. 2.11. The inner layer is a strip detector, which is finely segmented by the  $\eta$  direction with  $\Delta\eta = 0.0031$ . The other two layers, called “middle” and “back” from inner side, is finely segmented by both  $\phi$  and  $\eta$ . The  $\phi$  direction length of the inner layer is four times longer than those of the middle and the back layers. The depth is varied by the detector  $|\eta|$  to optimise its resolution, increasing from  $22X_0$  to  $30X_0$  between  $|\eta| = 0$  and  $|\eta| = 0.8$  and from  $24X_0$  to  $33X_0$  between  $|\eta| = 0.8$  and  $|\eta| = 1.3$ , where the  $X_0$  represents the radiation length. The number of readout cells is totally 3424 per module, including the presampler cells. The presampler detects shower sampling in front of the active EM calorimeter and inside the barrel cryostat. Its modules are made of interleaved cathode and anode electrodes glued between glass-fibre composite plates. The segment values for each barrel and end-cap module of the EM calorimeter are shown in Tab. 2.1. The energy resolution is designed as  $\sigma_E/E = 10\%/\sqrt{E [\text{GeV}]} \oplus 0.7\%$ , where the first term is related to the sampling and second is a constant. The first term depends on the  $|\eta|$ , and is expected to be worse at larger  $|\eta|$  because of the increase of the materials.

**Hadronic Calorimeter** The hadronic calorimeter is located out side of the EM calorimeter, and it consists of three components. One is the tile calorimeters, which are located on the outside of the EM calorimeter barrel ( $|\eta| < 1.7$ ) and uses scintillating tiles and iron absorber. The others use LAr calorimeter, which are located on the outer side of the end-cap EM calorimeter and forward region.

**Tile Calorimeter** The tile calorimeter covers the pseudo-rapidity range of  $|\eta| < 1.7$ , where it can be divided into the barrel region ( $|\eta| < 1.0$ ) and two extended barrels ( $0.8 < |\eta| < 1.7$ ). The shape of a module is a wedge of size  $\Delta\phi \sim 0.1$ . The 64 modules cover the full  $\phi$ . The scintillators in the module are connected to the readout photomultiplier tubes shown in the top of Fig. 2.12. The size of the scintillator of 3 mm thickness are varied with the radial lengths ranging from 97 mm to 187 mm and azimuthal lengths ranging from 200 mm to 400 mm.

By grouping the fibre, the three radial sampling layers are defined, approximately 1.5, 4.1 and 1.8

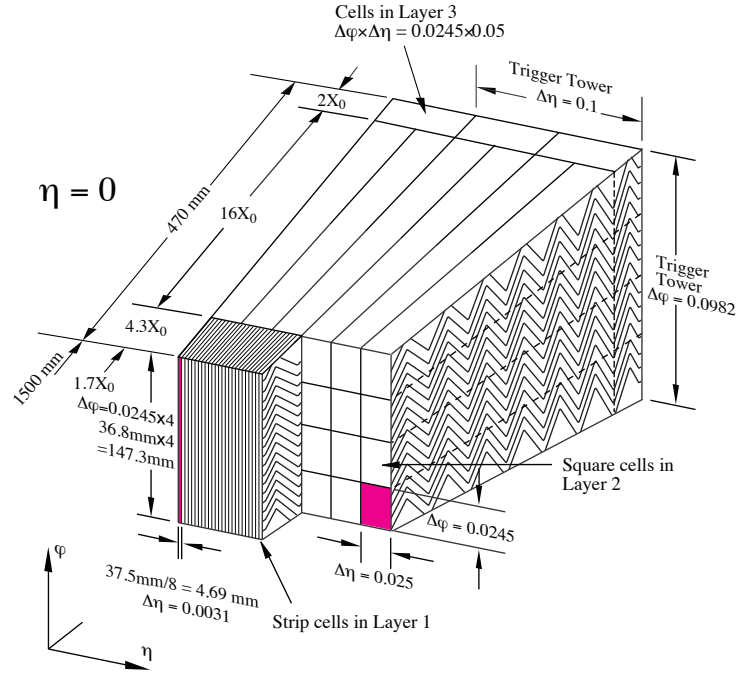
Figure 2.11: A module of EM calorimeter, located on near  $\eta = 0$  [106].

Table 2.1: Segment sizes per module of the EM calorimeter.

	Layer	Segment size ( $\Delta\eta \times \Delta\phi$ )	$ \eta $ region
Barrel	Presampler	$0.025 \times 0.1$	$ \eta  < 1.52$
	Strip	$0.025/8 \times 0.1$	$ \eta  < 1.40$
		$0.025 \times 0.025$	$1.40 <  \eta  < 1.475$
	Middle	$0.025 \times 0.025$	$ \eta  < 1.40$
		$0.075 \times 0.025$	$1.40 <  \eta  < 1.475$
	Back	$0.050 \times 0.025$	$ \eta  < 1.35$
End-cap	Presampler	$0.025 \times 0.1$	$1.5 <  \eta  < 1.8$
		$0.050 \times 0.1$	$1.375 <  \eta  < 1.425$
		$0.025 \times 0.1$	$1.425 <  \eta  < 1.5$
	Strip	$0.025/8 \times 0.1$	$1.5 <  \eta  < 1.8$
		$0.025/6 \times 0.1$	$1.8 <  \eta  < 2.0$
		$0.025/4 \times 0.1$	$2.0 <  \eta  < 2.4$
		$0.025 \times 0.1$	$2.4 <  \eta  < 2.5$
	Middle	$0.1 \times 0.1$	$2.5 <  \eta  < 3.2$
		$0.050 \times 0.025$	$1.375 <  \eta  < 1.425$
		$0.025 \times 0.025$	$1.425 <  \eta  < 2.5$
Back	$0.075 \times 0.025$	$2.5 <  \eta  < 3.2$	
	$0.050 \times 0.025$	$1.5 <  \eta  < 2.5$	

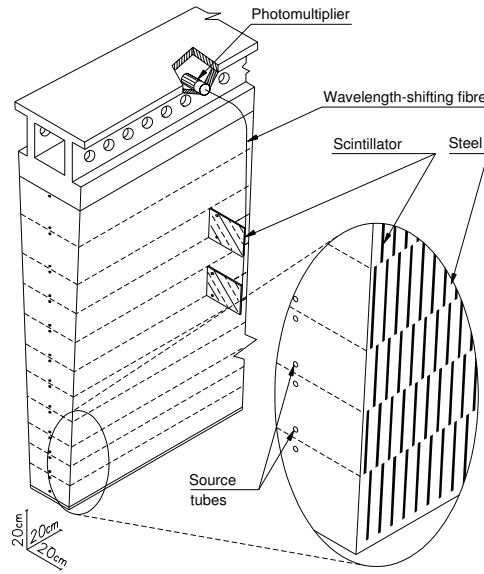


Figure 2.12: A module of the tile calorimeter [106].

interaction lengths thickness for the barrel and 1.5, 2.6 and 3.3 interaction length thickness for the extended barrel. The  $|\eta|$  direction segments of the tile calorimeter are optimised for the particles from the interaction point.

The resolution of the barrel and end-cap hadronic calorimeters is designed as  $\sigma_E/E = 50\%/\sqrt{E [\text{GeV}]} \oplus 3\%$ .

**LAr end-cap calorimeter** The LAr end-cap calorimeter (HEC) is a copper/liquid-argon sampling calorimeter with a flat-plane design. This part covers  $1.5 < |\eta| < 3.2$ , and located directly behind the end-cap EM calorimeter. The HEC shares the end-cap cryostats with the end-cap EM calorimeter and also forward calorimeters. It consists of two wheels per side, which are cylindrical with an outer radius of 2030mm. Each wheel has 32 identical wedge-shaped modules. The size of the readout cells is segmented by  $\Delta\eta \times \Delta\phi = 0.1 \times 0.1$  in the region  $|\eta| < 2.5$  and  $0.2 \times 0.2$  for larger  $\eta$ .

**Forward calorimeter** The forward calorimeters (FCal) are located on the outside of HEC and in the same cryostats as the HEC. The FCal covers  $3.1 < |\eta| < 4.9$ , which is the highest eta region in the ATLAS detector. The FCal consists of three 45 cm deep modules, corresponding approximately 10 interaction lengths deep. The inner one is the electromagnetic module (FCal1) and the others are hadronic modules (FCal2 and FCal3). The absorber media are different between FCal1 and the others: FCal1 uses the copper, whilst FCal2 and FCal3 use the tungsten, to suppress the wide hadronic showers. The FCal resolution is required to be  $\sigma_E/E = 100\%/\sqrt{E [\text{GeV}]} \oplus 10\%$ .

### 2.2.4 Muon Spectrometer

Muons can pass the EM and the hadronic calorimeters and can be detected in the Muon Spectrometer (MS). The MS is placed on the most outer layer of the ATLAS detector, as shown in Fig. 2.13. It is for tracking and triggering muons in the pseudo-rapidity range of  $|\eta| < 2.7$  and  $|\eta| < 2.4$ , respectively. The

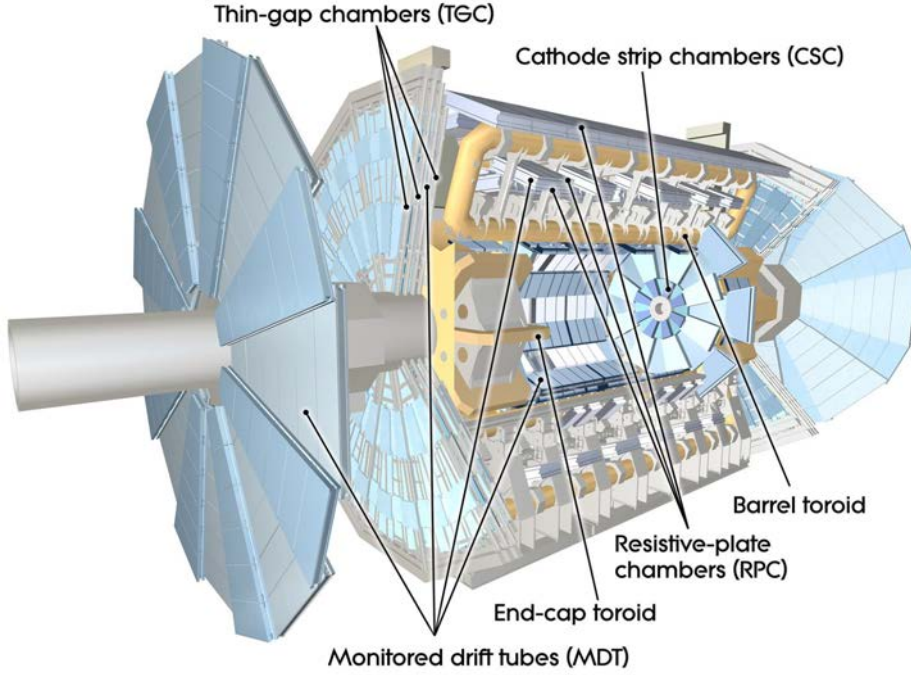


Figure 2.13: Whole view of the Muon Detector [106].

Table 2.2: Main parameters for the components of the muon spectrometer.

	MDT	CSC	RPC	TGC
Coverage	$ \eta  < 2.7$	$2.0 <  \eta  < 2.7$	$ \eta  < 1.05$	$1.05 <  \eta  < 2.7$
Num. of chambers	1150	32	606	3588
Num. of channels	354,000	31,000	373,000	318,000
Function	Precision tracking		Triggering, second coordinate	

MS consists of alternate eight large and eight small parts. The MS has four components listed in Tab. 2.2: the Monitored Drift Tubes (MDT) and the Cathode Strip Chambers (CSC) are used for precision tracking for muons, and the Resistive Plate Chambers (RPC) and the Thin Gap Chambers (TGC) are used for mainly triggering.

The toroidal magnetic fields are generated for the MS by the magnet system (see Sec. 2.2.5).

**Tracking part** The tracking detectors are located between the coils of the barrel toroid magnet for the barrel and in front and behind the end-cap toroid magnets for the end-cap. The MDT are composed of pressurised drift tubes with diameters of 29.970 mm with mixture of gases at 3 bar, where the ratio of the gas is 93% Ar and 7% CO<sub>2</sub>. There is a tungsten-rhenium wire with a diameter of 50  $\mu\text{m}$  at the centre of the tube, with the high voltage of 3080 V. It is held at the tube ends to keep an accuracy of less than 10  $\mu\text{m}$ . If a muon comes across the tube, the gas inside the tube is ionised and then the ionised particles are collected in the wire. The MDT is located in both barrel part and end-cap part, with  $|\eta| < 1.0$  and  $1.0 < |\eta| < 2.7$ , respectively. A chamber is composed of two multi-layers, which are the groups of three or four drift tube layers. The two multi-layers are separated by a spacer. The barrel chambers are rectangular where the

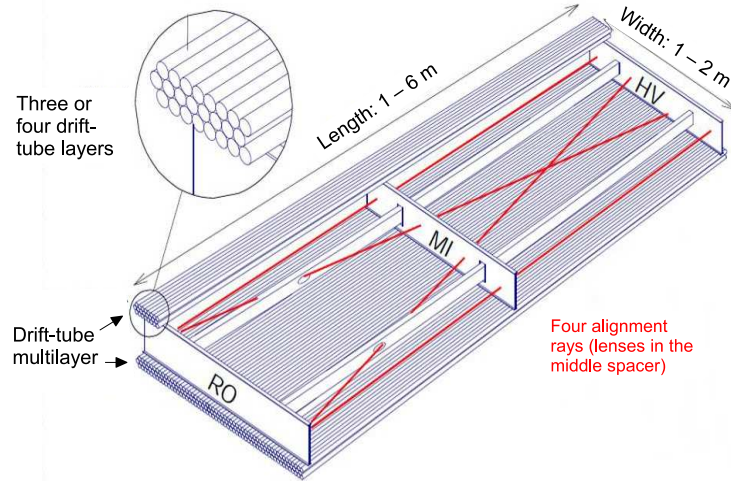


Figure 2.14: Sketch of the MDT chamber. Three spacer bars separate between two drift tube multi-layers [106].

tube layers lie in parallel with the beam axis. The end-cap chambers are trapezium where the tube layers are set vertically. Figure 2.14 represents the MDT chamber. The MDT modules are distributed in three MDT layers in the barrel and the end-caps. The momentum resolution for the track with three MDT hits is expected  $\delta p/p = 45 \mu\text{m} \times p/500 \mu\text{m}$ , where  $p$  is given in units of TeV.

In the  $|\eta|$  region of  $2 < |\eta| < 2.7$ , the first layer MDT chambers are replaced by the CSC due to the high counting rate. The chamber has high spatial, time and track resolution with high counting rate capability and low neutron sensitivity. The CSC is designed to operate with the counting rates of about  $1000 \text{ Hz/cm}^2$ , whereas the operation of the MDT is limited at counting rates of about  $150 \text{ Hz/cm}^2$ . The CSCs are multi-wire proportional chambers setting parallel to the central wire.

**Triggering part** The RPC and the TGC are for triggering, in the barrel and the end-caps, respectively. The parts cover the range  $|\eta| \leq 2.4$  and over the full  $\phi$ -range.

The RPC cover the pseudo-rapidity range of  $|\eta| < 1.0$  and are arranged in three layers, which is set close to the MDT. The RPC consists of gaseous parallel electrode-plate detector, which has no wire in the centre. The gas is a mixture of approximately 95%  $\text{C}_2\text{H}_2\text{F}_4$  and 5% Iso- $\text{C}_4\text{H}_{10}$ . It provides a space-time resolution of  $1 \text{ cm} \times 1 \text{ ns}$  and a rate capability of about  $1 \text{ kHz/cm}^2$ .

The TGC is a multi-wire proportional chamber with a 1.4 mm distance between wire and Graphite layer, and with a 1.8 mm distance between wires. The mixture gas of 55%  $\text{CO}_2$  and 45% n- $\text{C}_5\text{H}_{12}$  are filled in the chamber. It covers the  $\eta$  range of  $1.0 < |\eta| < 2.4$ , corresponding the end-cap part.

### 2.2.5 Magnets

The magnet systems are essential, as they provide the magnetic fields for the momentum measurement of charged particles to the ID and MS. Figure 2.15 illustrates the whole view of the ATLAS magnet system [106, 122]. The ATLAS magnet system, which is 22 m in diameter and 26 m in length, consists of one solenoid and two toroid superconducting magnets.

A solenoid is aligned to the beam axis and provides a 2 T axial magnetic field for the ID. The material



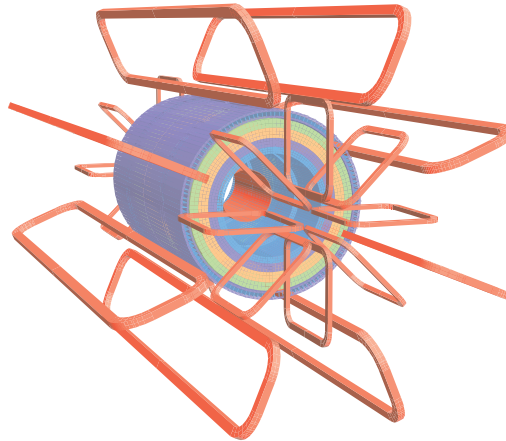


Figure 2.15: Illustration of the ATLAS magnet system [106]. The orange parts are magnets, and the other colour parts are tile calorimeter steel. The eight barrel toroid coils are most outer parts of the magnet system, surrounding the tile calorimeter barrel. The endcap toroid coils are located the forward and the backward directions of the tile calorimeters. A solenoid is located inside the calorimeter, surrounding the ID.

thickness of the solenoid is carefully considered to achieve the desired calorimeter performance, hence, the solenoid assembly contributes a total of approximately 0.66 radiation length [123] at normal incidence.

A barrel toroid surrounds the calorimeters and both endcap toroids, which is located forward and backward the calorimeters. The toroids produce a toroidal magnetic field of approximately 0.5 T and 1 T for the MS in the central barrel and endcap regions respectively.

### 2.2.6 Forward Detector

The forward detector [106, 124] is the outside part of the main ATLAS detector system. This is for measurement of elastic scattering and the luminosity. This consists of three smaller sets of detectors which are built to provide good coverage in the very forward region.

The closest detector is the Cerenkov detector called LUCID (LUminosity measurement using Cerenkov Integrating Detector), which is located at  $\pm 17$  m from the interaction point. The LUCID is the only detector which is primarily dedicated to online luminosity monitoring. This detects inelastic  $pp$  scattering in the forward direction in order to measure the integrated luminosity and to online monitor the instantaneous luminosity and beam conditions. It consists 16 aluminum tubes filled with  $C_4F_{10}$  gas surrounded the beam pipe. The tubes are 1.5 m and have a 15 mm diameter with a 1 mm wall thickness [125].

The second detector is Zero-Degree Calorimeter (ZDC), which is located at  $\pm 140$  m. This detector is used to detect forward neutrons with  $|\eta| > 8.3$  in heavy-ion collisions. Thus it is not used in this analysis.

The furthest detector is ALFA (Absolute Luminosity For ATLAS), which is located at  $\pm 240$  m. This detector is also used to measure the luminosity, however, it performs the measurements with elastic scattering. The main component of the detector is a scintillating fibre tracker.

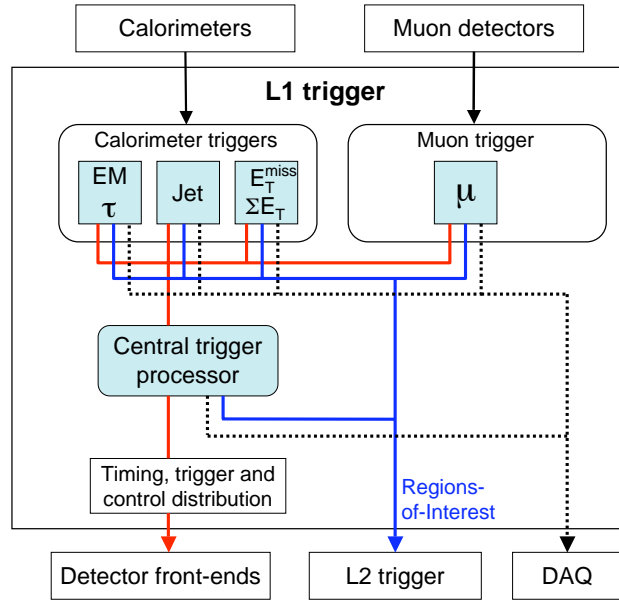


Figure 2.16: Trigger Flow of the L1 trigger [106]. EM shows the electron/photon trigger menus.

## 2.3 Triggering System

The ATLAS trigger system [106, 126, 127] is based on three levels of event selection designed to capture the physics of interest with high efficiency. The three trigger levels are Level 1 (L1), the Level 2 (L2) and Event Filter (EF). The L1 trigger is the hardware based trigger which uses ASICs and FPGAs. The L2 and EF trigger levels (High-Level Trigger; HLT) are based on software algorithms analysing the data on large computing farms. In this analysis, only lepton ( $e$  or  $\mu$ ) triggers are used, whilst the ATLAS standard trigger menu has additionally jets,  $\tau$  and  $E_T^{\text{miss}}$  triggers. Thus only lepton triggers will be described below.

The flow of the L1 trigger is shown in Fig. 2.16. The L1 trigger searches for signatures from high  $p_T$  muons with the information from RPC and TGC, and from high  $E_T$  electrons, photons, jets and the missing transverse momentum with the information from all the calorimeter sub-layers. It reduces the triggered event rate including not only hard interaction but also the effect of multiple proton-proton collisions from the same or nearby beam bunch crossings (called pile-up) contribution from the order of 1 GHz to 70 kHz. The calorimeter based L1 trigger system is called as the L1Calo [128], which aims to identify high- $E_T$  objects, such as electrons/photons, jets and  $E_T^{\text{miss}}$ . The L1 muon trigger is based on signals in the muon trigger chambers, RPC in the barrel and TGC in the endcaps. The trigger is performed by the pattern recognition for the high- $p_T$  muons originating from the interaction region. The overall L1 trigger is determined by the Central Trigger Processor, which combines the information from the trigger objects. The decision is sent to the detector front-end and readout systems, with the approximately 40 MHz clock and other signals.

The HLT is performed in the Regions-of-Interest (ROI). This is the region including the objects from the L1 output. The size of the ROI depends on the type of trigger objects. For example, the size for electrons is smaller than that for jets since the electron trigger requires the isolated electron. From the L2 trigger, information from the several detector parts are used, such as a track from the ID and the clusters from calorimeter. The track information is formed using a fast pattern recognition algorithm from space

Table 2.3: Electron trigger definition used in this analysis.

Elec trig.	$p_T$ threshold	EF requirement
e7T_medium1	7 GeV	One or more <i>medium</i> electron with $p_T > 7$ GeV, L1 uses higher threshold.
e12Tvh_loose	12 GeV	One or more <i>loose</i> electron with $p_T > 12$ GeV, L1 uses higher threshold, $\eta$ -dependent threshold and hadronic core veto.
e18vh_medium1	18 GeV	One or more <i>medium</i> electron with $p_T > 18$ GeV, L1 uses $\eta$ -dependent threshold and hadronic core veto.
e24vhi_medium1	24 GeV	One or more <i>medium</i> electron with $p_T > 24$ GeV and $\sum_{\Delta R < 0.2} p_T^{\text{rk}} / p_T < 0.1$ , L1 uses $\eta$ -dependent threshold and hadronic veto.

points of the ID. At the EF, more time is available. The EF track reconstruction is performed with the same offline reconstruction software in ROI.

### 2.3.1 Electron Triggers

Electron triggers are performed using the EM calorimeter segments. The size of segments for the L1 triggers is defined  $\Delta\eta \times \Delta\phi \approx 0.1 \times 0.1$  (trigger towers) from the calorimeters to identify the positions of ROIs and compute the transverse energy  $E_T$  of EM clusters with a precision of 1 GeV [129]. At L2, the ROIs are defined as the segment with  $\Delta\eta \times \Delta\phi = 0.4 \times 0.4$  identified by the L1. Cluster seeds from clusters of towers in the EM calorimeter with a window size of  $N_\eta \times N_\phi = 3 \times 7$  are formed. If a seed matches an ID track with  $p_T > 5$  GeV, an electron candidate is formed.

In the offline reconstruction, the standard identification criteria are used for the electrons candidates, *loose*, *medium*, and *tight*, which will be described in Sec. 3.4. The trigger menu which is used in the analysis is shown in Tab. 2.3. Since keeping the trigger rate below 60 kHz, some of the electron trigger introduces the  $\eta$ -dependence of the  $p_T$  threshold in L1. The trigger applied the  $\eta$ -binned threshold is expressed as “v” in the trigger name shown in Tab. 2.3. The hadronic leakage requirement is also considered, which consists of a veto on hadronic energy of more than or equal to 1 GeV deposited in the hadronic layers of the calorimeter, within a region of  $\eta \times \phi = 0.2 \times 0.2$  behind the EM cluster. The trigger using the hadronic vetoing is expressed as “h” in the name of the triggers. If the trigger requires the isolated electron, the trigger have the character “i” in the name.

Trigger efficiencies are validated by the comparison between data and MC samples using a tag-and-probe method with  $Z$  boson decays. The correction factor  $sf_{\text{trig}}$  is calculated as

$$sf_{\text{trig}} = \frac{\epsilon_{\text{trig}}^{\text{data}}}{\epsilon_{\text{trig}}^{\text{MC}}}, \quad (2.8)$$

where the  $\epsilon_{\text{trig}}$  is a trigger efficiency calculated as

$$\epsilon_{\text{trig}} = \frac{N_{\text{trig}}^{\text{pass}}}{N_{\text{trig}}^{\text{pass}} + N_{\text{trig}}^{\text{fail}}}. \quad (2.9)$$

The  $N_{\text{trig}}^{\text{pass}}$  and  $N_{\text{trig}}^{\text{fail}}$  are the numbers of events with the probe lepton passing and failing triggers, respectively.

Table 2.4: Correction factors of the electron trigger efficiencies.

Trigger	$sf_{\text{trig}}(p_T)$	$sf_{\text{trig}}( \eta )$	$sf_{\text{trig}}(N_{\text{vtx}})$
e24vhi_medium1	0.9898	0.9923	0.9896
e12Tvh_loose1	0.9987	0.9947	0.9980
e7T_medium1	0.9942	0.9921	0.9939

Table 2.5: Muon trigger definition used in this analysis [130].

Muon trig.	$p_T$ threshold	EF requirement
mu4_EFFS	4 GeV	One or more muon with $p_T > 4$ GeV with full scan algorithm at EF only.
mu6	6 GeV	One or more muon with $p_T > 6$ GeV.
mu8_EFFS	8 GeV	One or more muon with $p_T > 18$ GeV with full scan algorithm at EF only.
mu13	13 GeV	One or more muon with $p_T > 13$ GeV.
mu18_tight	18 GeV	One or more <i>tight</i> muon with $p_T > 18$ GeV.
mu24i	24 GeV	One or more muon with $p_T > 24$ GeV and $\sum_{\Delta R < 0.2} p_T^{\text{trk}} / p_T < 0.12$ .

The correction factor for the corresponding triggers are shown in Tab. 2.4. The correction factor is fitting a constant function on the distribution of  $p_T$ ,  $|\eta|$  and the number of vertices  $N_{\text{vtx}}$ . These results show the consistencies to 1.0 within a few %.

### 2.3.2 Muon Triggers

The muon triggers [130] are generated by RPC and TGC hits. The L1 triggers based on the RPC require a coincidence of hits in the three layers for the highest three  $p_T$  thresholds and a coincidence of hits in two of the three layers for the rest of thresholds. The L1 triggers based on the TGC require a coincidence of hits in the three layers, except for limited areas in the lowest threshold. The size of the formed ROI is typically  $\Delta\eta \times \Delta\phi = 0.1 \times 0.1$  and  $0.03 \times 0.03$  in the RPCs and TGCs, respectively. At L2, MDT tracks are reconstructed and associated to the ID tracks with the ATLAS standard combining criteria, which will be described in Sec. 3.5.

The full-scan procedure is used in the EF to find additional muons that are not found by the ROI based method. In this procedure, the muon candidates are searched in the whole of MS, without the ROIs.

Table 2.5 shows the muon trigger list which is used in this analysis. The ‘‘EFFS’’ label represents the method with the full-scan procedure in the EF.

The correction factor for the muon trigger efficiency is also performed with the same manner as the electrons’. The results are shown in Tab. 2.6, which show the consistencies to 1.0 within 1%.

Table 2.6: Correction factors of the muon trigger efficiencies.

Trigger	$sf_{\text{trig}}(p_T)$	$sf_{\text{trig}}( \eta )$	$sf_{\text{trig}}(N_{\text{vtx}})$
mu24i_tight	0.9925	0.9971	0.9917
mu18_tight	0.9926	0.9974	0.9917
mu13	1.001	1.002	1.000
mu8_EFFS	1.002	1.006	1.002
mu6	1.002	1.003	1.002
mu4T_EFFS	1.007	1.006	1.003

## Chapter 3

# Particle Reconstruction

In this analysis, the lepton information is mainly used. Thus precise identification of particles is essential. The several algorithms, such as the tracking, the calorimeter clustering and the jet reconstruction, are used in order to perform the identification. Tracking is implemented in the ID and the MS to identify charged particles. The latter two methods are implemented in the electromagnetic and hadronic calorimeters.

In this chapter, the overview of the particle identification will be provided in Sec. 3.1. The basic methods used in the analyses will be described individually. Tracking method is shown in Sec. 3.2. Then other methods and the particle identification criteria are shown.

### 3.1 Overview of the particle identification

This analysis requires three leptons (electrons, muons and taus) and the missing transverse momentum. Thus the identification for these are important.

As described in Chap. 2, the ATLAS detector has three detector parts: the Inner Detector, the Calorimeter and the Muon Spectrometer. The calorimeter includes the electromagnetic (EM) and the hadronic calorimeters. Figure 3.1 shows the wedge-shaped illustration of the ATLAS detector with the interaction of particles. All particles in an event which are necessary for this analysis are from the interaction point, which are reconstructed as *primary vertex*. Electrons, muons and the other charged particles leave signals in the ID from the primary vertices as *tracks*. After passing the ID, the EM and the hadronic calorimeters absorb the energy of passing particles. Electrons and photons would produce the electromagnetic showers in the EM calorimeter and stop there. Hadrons would hadronically interact with materials and produce hadronic showers mostly inside the hadronic calorimeter. The shower shapes are reconstructed as structures called ‘jets.’ Jets are reconstructed with the specific algorithms. Since muons have approximately 200 times heavier mass of  $m_\mu \sim 105 \text{ MeV}$  than the electron mass, the bremsstrahlung is strongly suppressed. Muons do not make electromagnetic showers in the calorimeters, while they make a track in the ID and the MS. Taus immediately decay into hadrons with the fraction of approximately 60% or into the other leptons with the fraction of approximately 30% due to their short lifetime of  $\tau_\tau \sim 290 \times 10^{-15} \text{ s}$ . The leptonic decaying taus are reconstructed as electrons or muons because the leptonic taus and the light leptons cannot be distinguished by their characteristics. On the other hand, the hadronically decaying taus can be

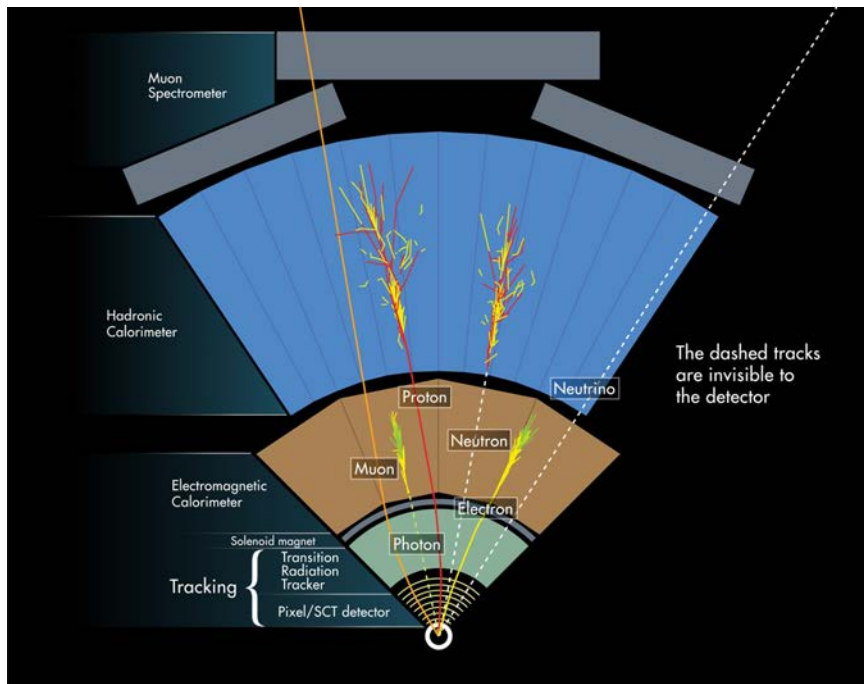


Figure 3.1: Wedge-shaped illustration of the ATLAS detector with the particle passing [114].

identified as jets.

Generally, the momentum conservation should be satisfied within the transverse direction to the beam axis. Thus the vector sum of the transverse momenta of the produced particles should be zero if all of the produced particles can be detected at the ATLAS detector. However, there are undetectable particles at the ATLAS detector, such as neutrinos. The undetectable particles lead the non-zero vector sum of the transverse momenta of the detected particles. This momentum vector is called the missing transverse momentum  $E_T^{\text{miss}}$ . The  $E_T^{\text{miss}}$  is evaluated by calculating a vector sum of the transverse momenta of all the detected particles;

$$E_T^{\text{miss}} = - \sum_{\text{"detected"}} p_T. \quad (3.1)$$

The detail will be described in the last part of the chapter.

## 3.2 Tracking

As described in the previous chapter, the ID and the MS detect the signals from the passing charged particles. Tracking is the work which connects the recorded space-points and makes a curved line which is the candidate for a *track* of the charged particle. The space-points are made in the ID and the MS, therefore the tracking is performed in the ID and the MS. The tracking algorithm used in ATLAS is called the ATLAS New Tracking (NEWT) [131].

There are three strategies of the tracking based on NEWT. Usually used *inside-out* track reconstruction and a consecutive *outside-in* tracking. Both track reconstruction algorithms are performed mainly in the ID, whilst the MS should be considered for the muons.

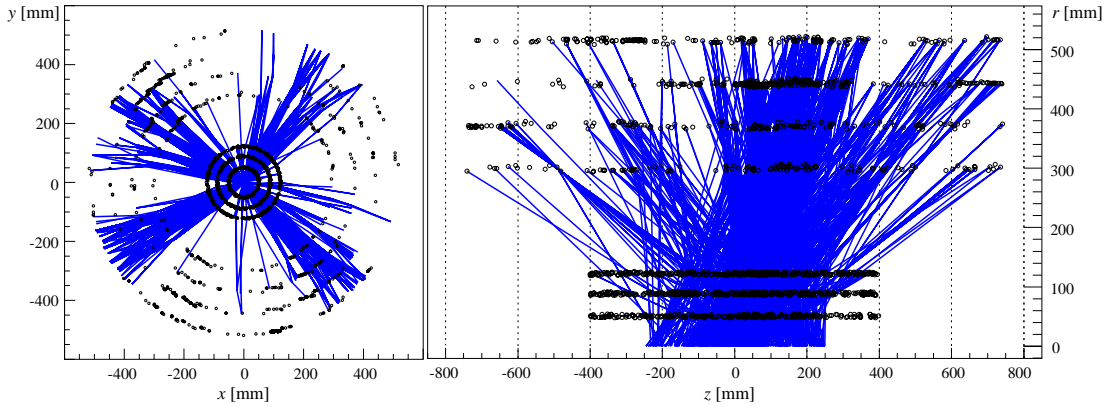


Figure 3.2: Space-points distribution and track candidates [131]. This is an example of  $t\bar{t}$  event display with the cross section of the ATLAS ID (Pixel and SCT) barrel part.

**Inside-out track reconstruction** The inside-out track reconstruction is the primary algorithm for the primary charged particles, which are defined as particles with mean lifetimes of greater than  $3 \times 10^{-11}$  s directly produced in a  $pp$  interaction or from the subsequent decays or interactions of particles with lifetimes shorter than  $3 \times 10^{-11}$  s. The inside-out algorithm targets the particles with the transverse momenta  $p_T$  greater than 400 MeV.

The first step of the inside-out track reconstruction is finding space-points in the silicon detectors, the Pixel and the SCT. A space-point is defined as a three-dimensional information with the radius  $r$ , the azimuthal angle  $\phi$  and the pseudo-rapidity  $\eta$ , which indicates a hit point of the particle. For the Pixel Detector, which has two-dimensional hit points, it is easy to compose the space-points with considering the Pixel layers. The SCT, on the other hand, is the set of the silicon strip sensors, which have only one-dimensional information. As described in the Detector section, Sec. 2.2.2, each module of the SCT has two silicon sensor planes with 40 mrad stereo angle. Combining the two information from the sensor planes makes it possible to get two-dimensional information.

After finding the space-points in all of Pixel and SCT, finding the track seeds is implemented at the Pixel. The track seeds are defined as having at least three space-points. The rough vertex is also built in the process of track candidate creation. Figure 3.2 shows the seed and track distribution. As a result, huge amount of track candidates are composed and many hits are shared by the track seeds. These shared hits should be resolved with the likelihood in order to reduce the amount of tracks before the extension to the TRT. The TRT track extension uses the remaining track candidates.

**Outside-in track reconstruction** The outside-in track reconstruction, on the other hand, is performed in the TRT firstly. This is useful to reconstruct tracks which are not seeded in silicon detectors, for example the  $K_s$  decays or the photon conversions.

This sequence starts with a segment finding in the TRT. The hit information from the TRT drift tubes cannot have any space-points, thus the adequate projection planes are used, which is  $r$ - $\phi$  plane for the TRT barrel part and  $r$ - $z$  plane for the TRT end-cap plane. If segments in the TRT are found, these are extended to the silicon detector hits.



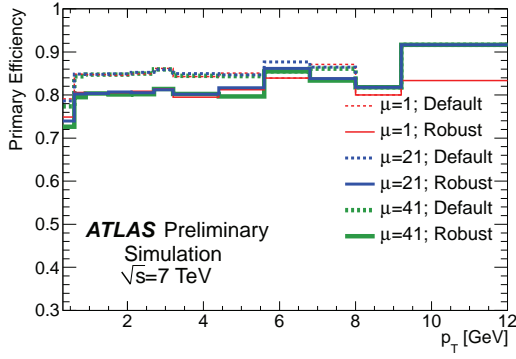
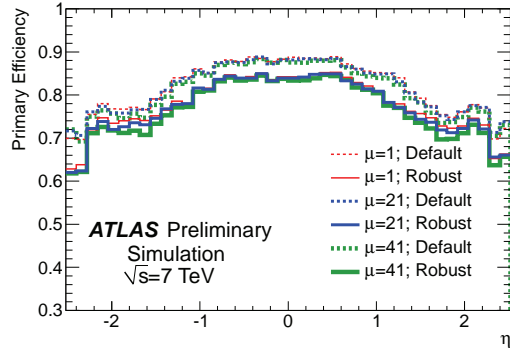
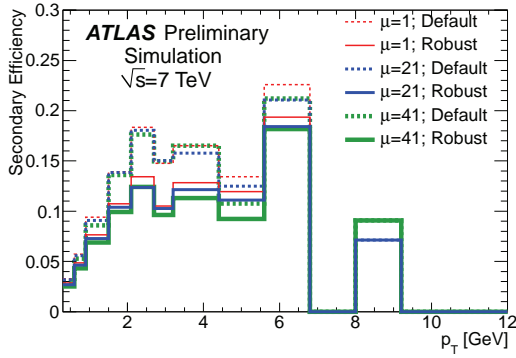
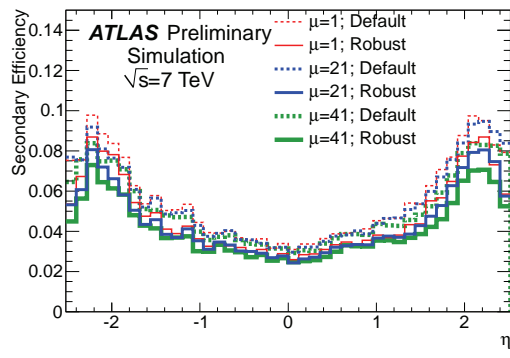
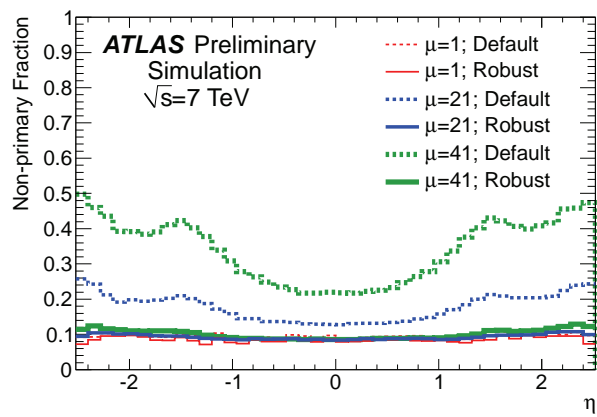
(a) Primary track reconstruction efficiency vs  $p_T$ (b) Primary track reconstruction efficiency vs  $\eta$ (c) Secondary efficiency vs  $p_T$ (d) Secondary efficiency vs  $\eta$ 

Figure 3.3: The primary and secondary track reconstruction efficiency in minimum bias Monte Carlo samples [132].

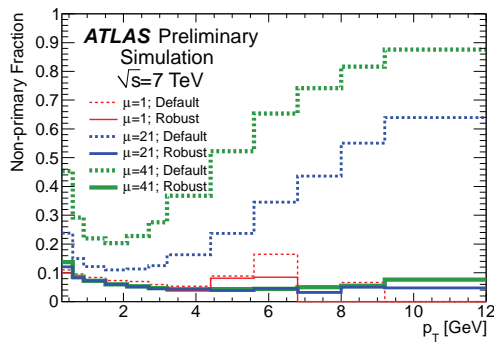
In the high luminosity environment, the occupancies in the ID get significantly high due to the pile-up events. Then the tracking reconstruction will be difficult. Thus the tracks are required to satisfy the following conditions (which is called *Robust*): at least nine hits in the silicon detectors (Pixel + SCT) and exactly zero holes in the Pixel. A hole represents a space-point where there is no hit on the track. The track reconstruction efficiency is used to evaluate if the reconstruction process is performed well. It is defined as the fraction of primary particles with  $p_T > 400\text{MeV}$  and  $|\eta| < 2.5$  matched to a reconstructed track. Figures 3.3 and 3.4 shows the comparison of the efficiency and non-primary fraction as a function of  $p_T$  and  $\eta$  with no pile-up ( $\mu = 1$ ) and corresponding pile-up contribution, respectively, between the *Robust* and *Default* condition, which is defined as at least seven hits in the silicon detectors and at most two holes in the Pixel [132]. These figure claim that the *Robust* condition is not affected by the number of pile-up, whilst the average efficiency of the *Robust* is 5% less than that of the *Default*. Since the average  $\mu$  value is  $\sim 20$  in the Run-1, the *Robust* condition has been adopted.

### 3.3 Vertex Reconstruction

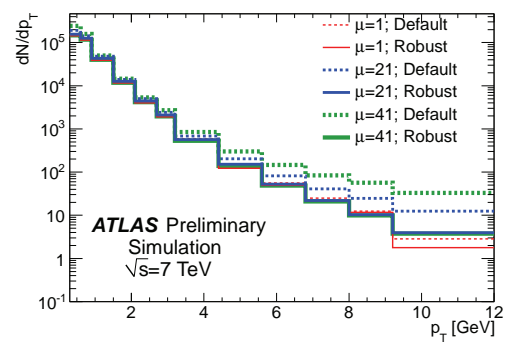
The primary vertices represent the interaction points with the highest energies in each event. The knowledge of the information of the vertices is important for the hadron collider analyses. The primary vertices reconstruction [133] is implemented with two steps: vertex finding and vertex fitting. In the process



(a) Non-primary fraction vs  $\eta$



(b) Non-primary fraction vs  $p_T$



(c) Track  $p_T$  Distribution

Figure 3.4: Non-primary fraction in minimum bias Monte Carlo simulation results [132].

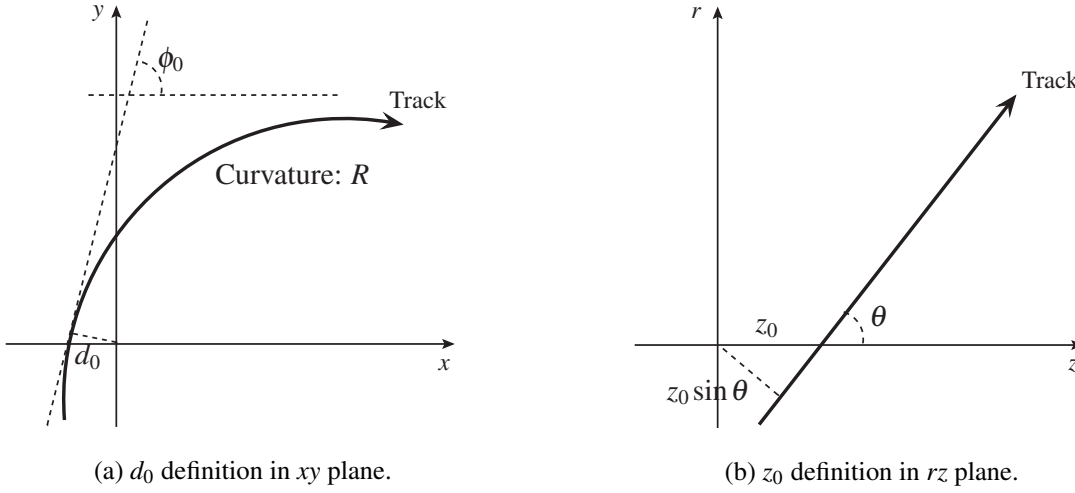


Figure 3.5: Impact Parameters definition in  $xy$  plane (a) and  $rz$  plane (b).

of those, the tracks satisfied following requirement are employed:

- $p_T > 150 \text{ MeV}$ ,
- $|d_0| < 4 \text{ mm}$ ,
- $\sigma(d_0) < 5 \text{ mm}$ ,
- $\sigma(z_0) < 10 \text{ mm}$ ,
- at least 4 hits in the SCT,
- at least 6 hits in the Pixel and SCT.

In the list,  $d_0$  and  $z_0$  signify the transverse and longitudinal impact parameters of tracks, as shown in Fig. 3.5. These are perigee parameters with respect to the centre of the beams in ATLAS. They are measured in an unbiased way, where the track under consideration is not used in determination of the origin vertex for these parameters [134]. The parameters  $\sigma(d_0)$  and  $\sigma(z_0)$  are the corresponding resolutions in the track fit.

## 3.4 Electrons

Electrons are reconstructed with the ATLAS standard identification criteria [135] based on the information about the shower shape in the EM calorimeter with the sliding window clustering algorithm [136], energy leakage into the hadronic calorimeters and the property of the track and the track-cluster matching. Photons are reconstructed using same criteria as electrons, without matching tracks.

### 3.4.1 Cluster reconstruction

The sliding window clustering algorithm uses calorimeter cells within a fixed-size rectangular window. The first step of the sliding-window clustering is to define a tower as a unit of the process. A tower is defined as a  $\eta \times \phi$  rectangle. Whole calorimeter can be considered to covered by  $N_\eta \times N_\phi = 200 \times 256$  of the towers, corresponding the tower segment of  $\Delta\eta \times \Delta\phi = 0.025 \times 0.025$ . The unit size is same as the size of the segment of middle layer of the EM calorimeter.

A movable window is defined using the tower unit. The window can move across each element of the tower grid in step of  $\Delta\eta$  and  $\Delta\phi$ . The window size is defined as  $N_{\eta}^{\text{window}} \times N_{\phi}^{\text{window}} = 5 \times 5$ . If the sum of the energy within the window is a local maximum and is above a threshold of 2.5 GeV, this is defined as a “seed.” The seed position is computed as the energy-weighted  $\eta$  and  $\phi$  barycentre of all cells in the region including a fixed-size window next to the sliding window, the size of which is  $N_{\eta}^{\text{pos}} \times N_{\phi}^{\text{pos}} = 3 \times 3$ . Due to the small window, the position is less sensitive to noise. If two cluster seeds exist with the distance in  $\Delta\eta_{\text{dupl}} \times \Delta\phi_{\text{dupl}} = 2 \times 2$ , the cluster seeds are removed except the seed with the largest transverse energy.

After the seed finding, clusters are reformed using the information of the seed position. The construction of the clusters are performed with the order by layers: middle, strips, presampler, and back. The size of clusters are different by the location of the detector. In the barrel, the cluster size is  $3 \times 7$ , and in the end-caps  $5 \times 5$ . A region-of-interest is defined as the region with the cone-size of  $\Delta R = 0.3$  around the barycentre of the seed cluster which satisfies the following requirement: the ratio of the energy in  $3 \times 7$  cells over the energy  $7 \times 7$  cells centred at the electron cluster position,  $R_{\eta}$ , should be larger than 0.3, and the ratio of  $E_{\text{T}}$  in the hadronic calorimeter to  $E_{\text{T}}$  in the EM cluster,  $R_{\text{had}}$  should be smaller than 0.1.

### 3.4.2 Track matching

The electron-seeds from calorimeter clustering will be associated to reconstructed tracks of charged particles in the ID. The tracking algorithm is already described in Sec. 3.2. The *loosely* matched tracks are considered if they pass either of two requirements. One is the standard criterion that the track extrapolated to the middle layer of the EM calorimeter have to satisfy  $|\Delta\phi| < 0.2$  when the track is bending towards of the EM cluster or  $|\Delta\phi| < 0.05$  when the track is bending on the opposite side. The other requirement is, to recover tracks of typically low momentum that potentially suffered significant energy loss before reaching the calorimeter, that the extrapolated track after rescaling its momentum is either  $|\Delta\phi| < 0.1$  (towards) or  $|\Delta\phi| < 0.05$  (opposite). Both requirements have  $\eta$  requirement of  $|\Delta\eta| < 0.05$  of the EM cluster for the tracks with at least four silicon hits. These loosely matched track parameters of all electron-track candidates with at least four silicon hits are precisely re-estimated using an optimised electron track fitter, which is a non-linear generalisation of the Kalman filter [137]. Then the refitted tracks–cluster matching proceeds with two requirements, which are tighter than those which described above. For the standard criterion, the  $\Delta\phi$  requirement is tightened to  $|\Delta\phi| < 0.1$ . Additionally, the tracks with less than four silicon hits need to satisfy  $|\Delta\eta| < 0.35(0.2)$  in the TRT barrel (endcap) and  $|\Delta\eta| < 0.03(0.02)$  on the towards (opposite) side. If a cluster has multiple matched tracks, the primary track is chosen in the matched tracks with at least one hit in the Pixel.

Electron candidate should have at matched track, whilst the photon candidate does not. The electron candidate with a matched track which is consistent with originating from a photon conversion and has a conversion vertex, is categorised as a converted photon.

### 3.4.3 Energy calibration

The cluster energy calibration [121] has been performed with the multivariate techniques [138] with the Monte Carlo (MC) samples. The correction factors, such as the electron energy scale and the electron energy resolution, are determined in the functions of its  $\eta$  and  $p_{\text{T}}$ . In order to precise MC-based calibration,

Table 3.1: Selection efficiency and background rejection for the electron transverse energy region  $20 < E_T < 50 \text{ GeV}$ , for *loose*, *medium* and *tight* cut [135]. The *tight* cuts are useful to reject hadron contribution.

Selection	Data eff. $Z \rightarrow ee$ signal	MC eff. for Background	BG composition [%]			MC eff. [%] for Background		
			non-iso $e$	bkg $e$	hadron	non-iso $e$	bkg $e$	hadron
Track Quality	100.0	100.00	1.1	16.1	82.8	100.0	100.00	100.000
<i>loose</i> cuts	$95.7 \pm 0.2$	$4.76 \pm 0.04$	7.8	48.4	44.2	$32.5 \pm 0.8$	$14.3 \pm 0.2$	$2.54 \pm 0.03$
<i>medium</i> cuts	$88.1 \pm 0.2$	$1.11 \pm 0.02$	25.8	50.5	23.7	$26.5 \pm 0.8$	$3.46 \pm 0.08$	$0.32 \pm 0.01$
<i>tight</i> cuts	$77.5 \pm 0.2$	$0.46 \pm 0.01$	54.5	29.9	15.6	$23.0 \pm 0.7$	$0.85 \pm 0.04$	$0.086 \pm 0.006$

it is necessary to measure the detector geometry and the interaction of particles with matter. The material distribution is measured in data using the ratio of the first layer energy to the second in the longitudinally segmented EM calorimeter. Then the response calibration is applied to the cluster energies measured from collision data and MC samples. For the calorimeter absolute energy scale measurement, the electrons from  $Z$  boson decays are used. In this condition, the calibration achieved with less than 1% for overall bins.

### 3.4.4 Electron Identification

Though the electron candidates are reconstructed by the manner described above, they include not only the signal electrons, but also background objects from Dalitz decays and semi-leptonic heavy flavour hadron decays. In order to reject these background objects while keeping the efficiency for signal electrons, the selection with some discrimination variables are used. In the ATLAS standard criteria, there are three selection levels: *loose*, *medium* and *tight*. They are optimised in two dimensional bins, 10 bins for the  $|\eta|$  direction and 11 bins for the  $E_T$  range. This binning allows to take into account the characteristics of the electrons, such as a dependence of the shower shapes on the amount of passive material traversed before entering the EM calorimeter. These three selections are in the inclusion relation, the *tight* is a subset of *medium*, which is a subset of *loose*. The selections uses some variables which are related to the energy fraction in the calorimeter and the tracking parameters. In this analysis, the *tight* and the *medium* are used. The *medium* selection uses the hadronic leakage energy fractions, the energy fractions between layers in the EM calorimeter, the numbers of hits in the silicon detectors, and the number of hits in the TRT. The *tight* selection uses the variables used in *medium* selection and the additional track-cluster matching parameters:  $\Delta\phi$  between the cluster position and the tracks. The *tight* selection also vetoes the electron candidates which matches to the reconstructed photon conversions. These selection efficiencies are shown in Tab. 3.1.

### 3.4.5 Baseline Electron Definition

The baseline electrons are defined for the analysis. The *medium* cuts and additional selection cuts are applied for constructing the *pre*-electrons for this analysis, as shown in Tab. 3.2. One is the standard selection which is used in the Category-A analysis, described in Chap. 5. The other is to select low  $p_T$  electrons to keep acceptance for signals. The *pre*-electrons are sorted to the order of  $p_T$ . Then the overlap removal criteria, which is described in Sec. 3.8, are applied to the *pre*-electrons. The passed electrons are

Table 3.2: Pre-electron identification criteria

	Standard selection	low $p_T$ selection
ATLAS identification criteria	medium	
$E_T$ threshold	10 GeV	7 GeV
Cluster pseudorapidity	$ \eta^{\text{cl}}  < 2.47$	
Track passed dead modules in Calo.	discarded	

Table 3.3: Signal selection for electrons

	Standard isolation	Tight isolation
$d_0$ significance	$< 5$	
$ z_0 \sin \theta $	$< 0.4 \text{ mm}$	
ATLAS standard selection	<i>tight</i>	
$p_{T\text{cone}30}/E_T$	$< 0.16$	$< 0.07$
$E_{T\text{cone}30}^{\text{corrected}}/E_T$	$< 0.18$	$< 0.13$

formed as baseline electrons. The baseline electrons are needed for the data-driven background estimation method described in Sec. 6.2.

### 3.4.6 Signal Electron Definition

The signal electrons are chosen in the baseline electrons by requiring a signal selection listed in Tab. 3.3. There are two signal selection strategies used in this analysis. One is the standard signal selection. It is based on the ATLAS standard tight identification criteria described in Sec. 3.4.4 with several impact parameter cuts and the isolation criteria. For the impact parameter cuts,  $d_0$  significance and unbiased  $|z_0 \sin \theta|$  are used. In order to further rejection for the hadronic jets which are mis-identified as electrons, the isolation cut in addition to the identification cuts are required to the baseline leptons.

The isolation criteria contain two variables based on the tracking and the calorimeter output. The track based isolation is applied as the ratio of the track isolation variable  $p_{T\text{cone}30}$  and its transverse energy  $E_T$ . The track isolation variable  $p_{T\text{cone}30}$  is the sum of the transverse momenta of all tracks  $p_T > 1 \text{ GeV}$  within a cone of  $\Delta R \leq 0.3$  around the electron track, excluding the track of the electron itself. The calorimeter based isolation is applied as the ratio of the track isolation variable  $E_{T\text{cone}30}$  and its transverse energy  $E_T$ . The energy-density corrected isolation variable  $E_{T\text{cone}30}^{\text{corrected}}$  is defined as the sum of the transverse energy deposited in the calorimeter cells in a cone of  $\Delta R \leq 0.3$  around the electron cluster, excluding the contribution within  $\Delta \eta \times \Delta \phi = 0.125 \times 0.175$  around the electron cluster barycentre. It is corrected for energy leakage from the electron to the cone and for the effect of pile-up as

$$E_{T\text{cone}30}^{\text{corrected}} = E_{T\text{cone}30} - A \times N_{\text{vtx}} \quad (3.2)$$

where the  $A$  is a correction factor defined as  $A = 20.15 \text{ MeV}$  for the data and  $A = 17.94 \text{ MeV}$  for the MC simulation. The  $N_{\text{vtx}}$  is the number of vertices with at least five tracks. Their selections are shown in Tab. 3.3. The tight isolation contributes to reduce mis-identification of the low  $p_T$  electrons.

Table 3.4: Muons baseline selection criteria. In this table, the variable  $n$  is defined as  $n \equiv N_{\text{TRT}}^{\text{hits}} + N_{\text{TRT}}^{\text{outliers}}$ .

	Standard selection	Low $p_{\text{T}}$ selection
ATLAS identification criteria	STACO	
$p_{\text{T}}$ threshold	10 GeV	5 GeV
Pseudorapidity	$ \eta  < 2.5$	
Pixel b-layer hit	at least one hit	
# of hits in the ID	$> 1$ pixel hit and $\leq 6$ SCT hits	
# of holes in the ID	less than 3 holes in the pixel and SCT	
TRT requirement	$0.1 <  \eta  < 1.9$	$n > 5$ and $N_{\text{TRT}}^{\text{outliers}} < 0.9 \times n$
	$ \eta  < 0.1$ or $ \eta  > 1.9$	If $n > 5$ , then $N_{\text{TRT}}^{\text{outliers}} < 0.9 \times n$

## 3.5 Muons

Muons are reconstructed with the information from the ID and the MS, using the STACO algorithm, which provides the statistical combination of independent measurements in the ID and in the MS by means of their covariance matrices [126].

The track reconstruction in the ID is already described in Sec. 3.2. For the track reconstruction in the MS, it is difficult to assume simple trajectories because of the inhomogeneous magnetic field from the toroidal magnet system. Furthermore, the large size of the MS induce the significant extrapolation uncertainties and large background. From these reasons, the pattern recognition need to be multilayer and/or chamber levels.

The first step of the pattern recognition is that the segmented region of MS, region of activity, is defined as the segment to comprise several chambers in the  $(\eta, \phi)$  space. The size is roughly  $\Delta\eta \times \Delta\phi = 0.4 \times 0.4$  in the trigger chambers. Then the straight track segments are formed from the MDT hits in each muon station belonging to a region of activity. After that, the segments in different stations are combined and fitted. For this operation, the toroidal magnetic field is taken into account. By iterated momentum scan, the magnet field is measured precisely. Then the fitted MS tracks are combined with the ID tracks with the STACO algorithm, taking into account the energy loss passing through the calorimeter region.

### 3.5.1 Baseline Muon Definition

In this analysis, in order to obtain high purity for real muon and the rejection of the background, the additional cuts are applied, which is shown in Tab. 3.4. The  $p_{\text{T}}$  threshold is defined as  $p_{\text{T}} > 10 \text{ GeV}$  for the standard selection and  $p_{\text{T}} > 5 \text{ GeV}$  for the low  $p_{\text{T}}$  selection. Additionally, several tracking conditions are required. The hit requirement for the TRT is different by the barrel or the end-cap, an object with the number of TRT hits less than five is discarded. The overlap removal among the objects are applied, then the remained muons are formed as baseline muons.

### 3.5.2 Signal Muon Definition

The signal muons are chosen in the baseline muons satisfying the signal selection listed in Tab. 3.5. There are two signal muon criteria as well as the signal electron criteria.

Table 3.5: Signal Muons selection criteria.

	Standard isolation	Tighter isolation
$d_0$ significance	$< 3$	
$ z_0 \sin \theta $	$< 1$ mm	
$p_{\text{Tcone30}}^{\text{corrected}}/p_{\text{T}}$	$< 0.12$	$< 0.06$
$E_{\text{Tcone30}}^{\text{corrected}}/E_{\text{T}}$	–	$< 0.14$

The tracking based variable  $p_{\text{Tcone30}}$  is corrected with the data and the MC as

$$p_{\text{Tcone30}}^{\text{corrected}} = p_{\text{Tcone30}} - A \times N_{\text{vtx}}, \quad (3.3)$$

where the constant  $A = 10.98 \text{ MeV} (6.27 \text{ MeV})$  in data (MC simulation). For same reason, calorimeter based variable  $E_{\text{Tcone30}}^{\text{corrected}}$  is defined as

$$E_{\text{Tcone30}}^{\text{corrected}} = E_{\text{Tcone30}} - a \times N_{\text{vtx}} - b \times N_{\text{vtx}}^2 \quad (3.4)$$

where the terms  $a = 0.0648 (0.0692)$  and  $b = 0.00098 (0.00076)$  in data (MC).

## 3.6 Jets

Jets are the objects from QCD hadronisation processes. They are reconstructed from topological clusters [136] via the anti- $k_t$  jet algorithm [139] with a distance parameter  $R = 0.4$ . MC simulation is used to optimise the corrections applied to the topological clusters. The final jet energy calibration includes the jet energy scale (JES) which corrects the calorimeter response to the true jet energy.

### 3.6.1 Topological Clustering

Jet clustering is performed with topological clustering algorithm with the calibration using the local cluster weighting calibration (LCW) [140]. The basic idea of the LCW is to prepare the different types of energy depositions, i.e. whether it arises from EM showers or the hadronic showers.

The basic idea of the topological clustering algorithm is that the clusters are formed with the cells which have significant energies over the expected noise. This is performed in the hadron calorimeter. First, finding seeds are simply performed by the way that cells are chosen which have a signal to noise ratio above the threshold  $t_{\text{seed}} = 4$ . All of these seed candidates are listed as *proto-clusters* in the seed list. The cells neighbouring proto-cluster seeds are added to the proto-clusters if their signal to noise ratio are above the threshold  $t_{\text{neighbour}} = 2$ . If such a neighbour cell is adjacent to multiple proto-clusters, the proto-clusters are merged. If the neighbour cell has not larger signal to noise ratio than the  $t_{\text{neighbour}}$ , the cell is included only in the first adjacent proto-cluster.

### 3.6.2 Anti- $k_t$ Algorithm

Jets are formed from the topological clusters with the anti- $k_t$  algorithm.



The inclusive  $k_t$  algorithm is expressed as the following equation:

$$d_{ij} = \min \left( k_{ti}^{2p}, k_{tj}^{2p} \right) \frac{\Delta_{ij}^2}{R^2}, \quad (3.5)$$

$$d_{iB} = k_{ti}^{2p}, \quad (3.6)$$

where  $\Delta_{ij}^2 = (y_i - y_j)^2 + (\phi_i - \phi_j)^2$ , and  $k_{ti}$ ,  $y_i$  and  $\phi_i$  are respectively the transverse momentum, rapidity and azimuthal angle of the cluster  $i$ . The parameter  $p$  is the relative power of the energy versus geometrical ( $\Delta_{ij}$ ) scales. For the anti- $k_t$  algorithm, the  $p$  is set to  $-1$ . The anti- $k_t$  algorithm is performed as that the  $d_{ij}$  and  $d_{iB}$  are calculated with  $i, j$  clusters, and are compared each other. If  $d_{ij}$  is larger than the  $d_{iB}$ , the new cluster combined clusters  $i$  and  $j$  is reconstructed. The process is iterated until the case that  $d_{iB}$  is larger than  $d_{ij}$ .

It is possible to consider that there are a few well-separated hard clusters with transverse momenta  $k_{t1}, k_{t2}, \dots$  and many soft clusters in an event. If the hard cluster 1 is focused, the soft clusters within the circle with the radius  $R$  tend to cluster with hard one.

An example of the comparison among jet reconstruction algorithms including the anti- $k_t$  algorithm is illustrated in Fig. 3.6, where  $k_t$  algorithm [141] and Cambridge/Aachen algorithm [142, 143] are using the variable  $p = 1$  and  $p = 0$ , respectively, and SIScone (Seedless Infrared Safe Cone) algorithm [144] is using a stable cone with split-merge algorithm. The anti- $k_t$  algorithm is stable against the soft cluster effects comparing to the other three algorithms.

### 3.6.3 Jet Calibration

The jets reconstructed from the topological clusters are calibrated using a transverse momentum  $p_T$  and  $\eta$  dependent MC based calibration scheme independent of quark flavour, with in situ corrections based on data [146]. The jet energy scale (JES) [147] is a part of the correction of the energy and momentum of the jets detected in the calorimeters. The baseline energy scale in the calorimeters is measured using test-beam measurements for electrons and muons, called the electromagnetic scale. However, the electromagnetic scale is not always correct for the jet energy, while it is correct for the energy of photons and electrons. The JES corrects the difference from the calibration of the electrons. The jet energy is calibrated using the MC simulated samples. The JES is measured as a function of  $p_T$  of the electromagnetic scale and the pseudo-rapidity  $\eta$ . The jet energy resolution (JER) [148] is measured with the JES calibrated jets. In addition, the data-driven calibration method is useful to correct mis-modelling in the simulation [149].

### 3.6.4 Jet Identification

The reconstructed jets should be affected by the pile-up interaction overlap. To subtract the pile-up effect, the jet vertex fraction (JVF) is employed [150, 151]. The variable is defined as the scalar transverse momentum  $p_T$  sum of the tracks associated with the jet and originate from the hard-scatter vertex divided by the scalar  $p_T$  sum of all associated tracks, as

$$\text{JVF} = \frac{\sum_k p_T^{\text{trk}_k}(\text{PV}_0)}{\sum_n \sum_l p_T^{\text{trk}_l}(\text{PV}_n)}, \quad (3.7)$$

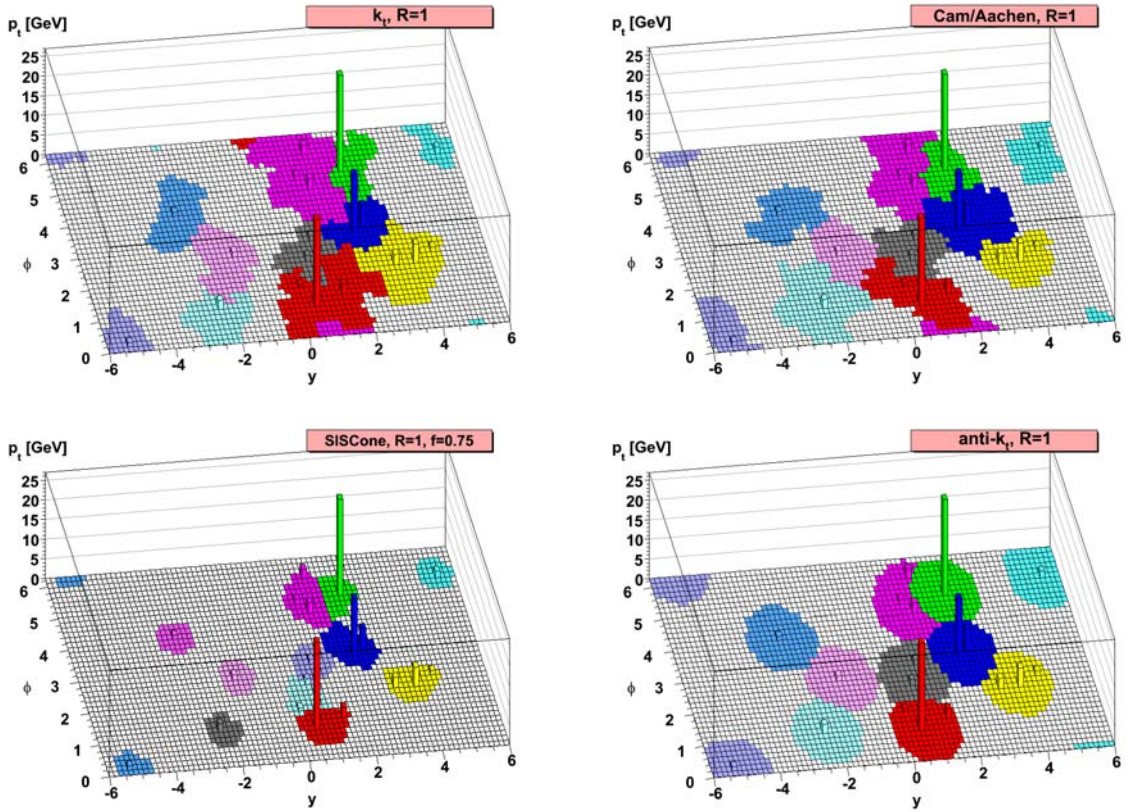


Figure 3.6: Comparison results among the  $k_t$  (left-top), Cambridge/Aachen (right-top), SISCone (left-bottom) and Anti- $k_t$  (right-bottom) algorithms with a sample parton-level event generated with HERWIG [145], together with  $\sim 10^4$  random soft clusters [139]. The anti- $k_t$  algorithm is stable behaviour against the many soft cluster effects.

where  $PV_j$  is the primary vertices,  $j = 0$  corresponds to the hard-scatter vertex and the others correspond to vertices of pile-up interaction in the same bunch crossing. The hard-scatter vertex is selected as the primary vertex with the highest  $\sum_{\text{tracks}}(p_T^2)$ . The JVF value is usually between 0 and 1, whilst a value of  $-1$  is assigned to jets with no associated tracks. The difference of the JVF value between pile-up jets and hard-scatter jets are shown in Fig. 3.7. In general, the pile-up events has many low  $p_T$  vertices, thus the JVF values of the pile-up events tend to distribute near zero. The JVF cut is applied in the signal jet selection.

### 3.6.5 Tagging Heavy Flavour Jets

In the ATLAS, the jets from  $b$  or  $c$  quarks (heavy flavour quarks) are identified separately from the jets from  $u$ ,  $d$ ,  $s$  quarks or gluons  $g$ . For the  $b$ -tagging performance relies on the accuracy of the charged particle reconstruction in the inner detector. Especially the Pixel innermost layer, which is called B-layer, is important to measure the locations of tracks and displaced vertices. Several algorithms for identification of heavy flavour jets have been developed, based on following two algorithms [152, 153].

**Impact parameter-based algorithm** Tracks are associated to the jets with a matching in the distance parameter  $\Delta R_{j,\text{track}} = \sqrt{\Delta \eta_{j,\text{track}}^2 + \Delta \phi_{j,\text{track}}^2}$ . Then the impact parameters for the associated track is calculated. The impact parameters for  $b$ -jets tend to large comparing to the light flavour jets.

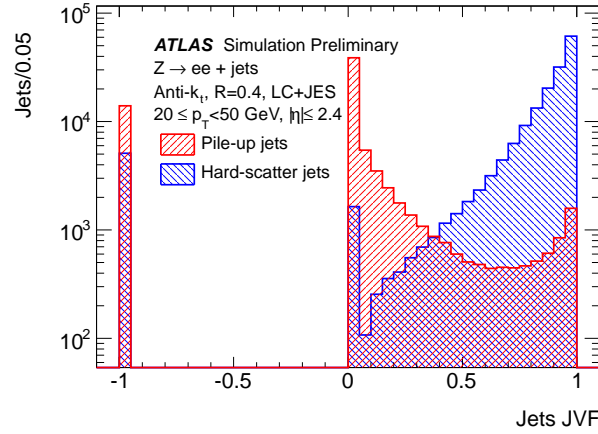


Figure 3.7: JVF value distribution for hard-scatter jets and pile-up jets with  $20\text{ GeV} < p_T < 50\text{ GeV}$  and  $|\eta| < 2.4$  in  $Z+\text{jets}$  simulated samples [151].

This is because the  $b$ -hadron runs long and makes secondary vertex since the life time for the  $b$ -hadrons are slightly long ( $c\tau \sim 500\ \mu\text{m}$ ). The impact parameter-based  $b$ -tagging algorithm (IP3D) uses a likelihood ratio technique in which input variables are compared to pre-defined smoothed and normalised distributions for both the  $b$ - and light flavour jet hypotheses, obtained from Monte Carlo simulation. The distributions are two-dimensional histograms for the transverse impact parameter significance  $d_0/\sigma(d_0)$  and longitudinal impact parameter significance  $z_0/\sigma(z_0)$ .

**Secondary vertex-based algorithm** The secondary vertex-based algorithm (SV1) uses a looser track selection, at least one hit in the Pixel, no more than one hit on the track being shared with another track,  $p_T > 400\text{ MeV}$ ,  $|d_0| < 3.5\text{ mm}$  and no cut on  $z_0$ . The decay length  $L_{3D}$  is measured in three-dimension. Its significance  $L_{3D}/\sigma(L_{3D})$  can discriminate between  $b$ -jets and light flavour jets. Moreover, the invariant mass of all tracks associated to the vertex, the ratio of the sum of the energies of the tracks in the vertex to the sum of the energies of all tracks in the jets, and the number of two-track vertices are used. These variables are combined with a likelihood ratio technique.

The MV1 algorithm [154] is used in this analysis, which employs an artificial neural network based on the simple algorithms based on IP3D and SV1. It is trained with  $b$ -jets as signal and light flavour jets as background. Then it computes a tag weight for each jet, which is corresponding to a probability that the jet is from  $b$ .

The performance of the MV1 algorithm has been calibrated at working points corresponding to the efficiencies of 60%, 70%, and 80% to the  $b$ -jets. For the 70% efficiency benchmark, the scale factor of the  $b$ -tagging efficiency is measured and is consistent with uncertainties. It depends on the jet  $p_T$ , from 8% to 15% [154].

### 3.6.6 Baseline Jet Definition

Baseline jets are defined as the objects satisfied the selection shown in Tab. 3.6. The baseline jets are used to overlap removal criteria for other objects. After passing these selections, the jets are subject to an overlap removal scheme explained in Sec. 3.8.

Table 3.6: Jet baseline selection criterion.

	Standard selection
Jet reconstruction algorithm	Anti- $k_t$ with $R = 0.4$
$p_T$ threshold	20 GeV
Pseudo-rapidity	$ \eta  < 4.5$

### 3.6.7 Signal Jet Definition

The signal jets are requested to satisfy  $p_T > 20 \text{ GeV}$  and  $|\eta| < 2.5$ . Signal jets with  $p_T < 50 \text{ GeV}$  and  $|\eta| < 2.4$  must also satisfy  $JVF > 0.5$ .

Signal jets are classified as  $b$ -jet candidates by the MV1 algorithm if the jet has  $|\eta| < 2.5$  and BDT output value corresponding  $b$ -tagging efficiency of 80%.

## 3.7 Taus

Tau leptons decay leptonically ( $\tau \rightarrow \ell \nu_\ell \nu_\tau$ ,  $\ell = e, \mu$ ) or hadronically ( $\tau \rightarrow \text{hadrons} + \nu_\tau$ , denoted  $\tau_h$ ) with their mean lifetime of  $2.9 \times 10^{-13} \text{ s}$ , typically before reaching active region of the ATLAS detector. Leptonic decaying taus can not be identified as taus anymore since they can not be distinguished from the leptons ( $e, \mu$ ). Thus only hadronic decaying taus are considered. The tau decays hadronically with 65% of all possible decay modes. In these, the hadronic decay produces one or three charged pions in 72% and 22% of all modes, respectively, and the rest are producing mainly charged kaons. A neutral pion would be produced associated with the hadronic decays. All of the neutral and charged hadrons from the tau decay are formed as the visible decay products of the tau lepton,  $\tau_h$ .

### 3.7.1 Reconstruction

Hadronic taus are reconstructed with jets with  $p_T > 10 \text{ GeV}$  and  $|\eta| < 2.5$ , formed using the anti- $k_t$  algorithm with a distance parameter  $R = 0.4$  with topological clusters calibrated using LCW [155]. The four-momentum of the tau candidate is formed from the topological clusters, assuming zero mass for each of the constituents [156]. Tracks within  $\Delta R < 0.2$  around the barycentre of the tau candidate are associated to each tau candidate if tracks have  $p_T > 1 \text{ GeV}$ , at least two associated hits in the pixel layers of the inner detector, at least seven hits in total in the silicon detectors,  $|d_0| < 1.0 \text{ mm}$ , and  $|z_0 \sin \theta| < 1.5 \text{ mm}$ . The tracks within the isolation region  $0.2 < \Delta R < 0.4$  are also used for the calculation of identification variables.

### 3.7.2 Tau Identification

Discriminating track and cluster variables are used within a boosted decision tree algorithm (BDT) to optimise hadronic tau identification. For the jet rejection, BDT is trained separately on 1-prong (associated one charged jet) and 3-prong (associated three charged jets) candidates. Three selections, loose, medium and tight, on the jet BDT score are defined, corresponding the tau signal efficiency of 60%, 45% and 30%, respectively. The input parameters are the track radius, leading track momentum fraction against the

Table 3.7: Tau baseline selection criterion

	Standard selection
$p_T$ threshold	20 GeV
Pseudorapidity	$ \eta  < 2.5$
# of tracks associated to the tau	1 or 3 (1-prong, 3-prong)
Charge	$\pm 1$

transverse momentum of the tau candidate, the fraction of transverse energy within  $\Delta R < 0.1$  of the tau candidate, the number of tracks in the isolation region, the shower information in the EM and hadronic calorimeters, the cluster and the track masses, the significance of the decay length and the impact parameters, and the cluster energy fraction against the total energy of all clusters.

Electrons mis-identified as taus are vetoed using transition radiation and calorimeter information. The signature of the 1-prong taus can be similar to the electrons. Several properties can be used to distinguish between them, for example, the emission of transition radiation of the electron track and the fact that the shower produced by a tau in the calorimeter tends to be longer and wider than the shower from electron. In a same manner for the jet rejection, BDT can perform to the electron discrimination. The electron discrimination has three working points: loose, medium and tight, corresponding the signal efficiency of 95%, 85% and 75%, respectively.

### 3.7.3 Baseline Tau Definition

The baseline tau is defined as the selection shown in Tab. 3.7.

### 3.7.4 Signal Tau Definition

Signal taus are baseline taus satisfying the medium tau selection, which is defined as requiring the loose electron discrimination BDT value and the medium jet rejection BDT value.

## 3.8 Overlap removal

The final step of the composition of baseline objects are the overlap removal among several particle candidates. Sometimes the identified objects are overlapped among the kind of objects. The overlapping is removed with discarding one of the overlapped objects using the cone “distance”  $\Delta R$ . The cone distance  $\Delta R$  is defined as:

$$\Delta R = \sqrt{(\Delta\eta)^2 + (\Delta\phi)^2} \quad (3.8)$$

The thing which overlapped object should be removed should be taken into account. In our analysis, it is important to keep leptons comparing to the jets. Thus roughly the jets are discard if leptons and jets are overlapped.

This overlap removal processes are sequentially applied as shown in Tab. 3.8. For the low  $p_T$  selection, the SFOS mass requirement is reformed to the condition  $m_{\text{SFOS}} < 2\text{ GeV}$  in order to cover the low mass differences.

Table 3.8: Overlap removal sequence.

Step	Comparing		keep	discard	Reason
1	$e_1, e_2$	$\Delta R < 0.05$	highest $E_T$	lowest $E_T$	Duplicated with different clusters and sharing tracks
2	$e, \text{jet}$	$\Delta R < 0.2$	$e$	jet	Remove duplication of objects across both containers
3	$\tau, e$	$\Delta R < 0.2$	$e$	$\tau$	Remove electrons duplicated in tau container
4	$\tau, \mu$	$\Delta R < 0.2$	$\mu$	$\tau$	Remove muons duplicated in tau container
5	$e, \text{jet}$	$\Delta R < 0.4$	jet	$e$	Remove electrons within jets
6	$\mu, \text{jet}$	$\Delta R < 0.4$	jet	$\mu$	Remove muons within jets
7	$e, \mu$	$\Delta R < 0.01$	neither	$e, \mu$	Muons undergoing bremsstrahlung
8	$\mu_1, \mu_2$	$\Delta R < 0.05$	neither	Both	Muons share tracks
9	SFOS pair	$m_{\text{SFOS}} < 12 \text{ GeV}$	neither	both	Suppress low mass pairs
10	signal $\tau, \text{jet}$	$\Delta R < 0.2$	signal $\tau$	jet	Remove signal taus duplicated among jets

### 3.9 Missing transverse momentum

The missing transverse momentum  $E_T^{\text{miss}}$  is calculated from reconstructed objects. In this analysis, the definition of the missing transverse momentum vector follows the standard definition of the ATLAS analysis group, which is defined as:

$$\begin{cases} E_x^{\text{miss}} = -E_x^e - E_x^\gamma - E_x^\mu - E_x^{\text{jets}} - E_x^{\text{cl}} \\ E_y^{\text{miss}} = -E_y^e - E_y^\gamma - E_y^\mu - E_y^{\text{jets}} - E_y^{\text{cl}}. \end{cases} \quad (3.9)$$

where the  $E_{x,y}^e$ ,  $E_{x,y}^\gamma$ ,  $E_{x,y}^\mu$ ,  $E_{x,y}^{\text{jets}}$  and  $E_{x,y}^{\text{cl}}$  are the transverse energy of the calibrated electrons, photons, muons, jets and the topological clusters falling outside of these objects, respectively. The electron term  $E_{x,y}^e$  is calculated with electrons passing the medium electron selection and with  $E_T > 10 \text{ GeV}$ . The photon term  $E_{x,y}^\gamma$  is calculated with photons passing the tight electron selection and with  $E_T > 10 \text{ GeV}$ . The jet term  $E_{x,y}^{\text{jets}}$  is calculated with jets applied with the local calibration criteria [157], and with  $p_T > 20 \text{ GeV}$ . The tau contribution is included in the jet contribution. Thus the tau contribution itself is not calculated.

Topological clusters which are not associated with electrons, photons or jets with  $p_T > 20 \text{ GeV}$  are used to calculate the soft jet term with local calibration. These are combined with remaining low energy calorimeter deposits to form the corrected cell out term, which is expressed as  $E_{x,y}^{\text{cl}}$ . The muon term  $E_{x,y}^\mu$  is calculated with all STACO muons passing the baseline selection. Under the low  $p_T$  selection criteria, the thresholds for the lepton terms are slightly lower in order to be same as the lepton object setting;  $E_T > 7 \text{ GeV}$  for the electron and photon terms and  $E_T > 6 \text{ GeV}$  for the muon term.

The total amount of the missing transverse momentum is calculated by

$$E_T^{\text{miss}} = \sqrt{E_x^{\text{miss}2} + E_y^{\text{miss}2}}. \quad (3.10)$$



## Chapter 4

# Data and Simulation Samples

### 4.1 Monte Carlo Simulated samples

Estimation for the SM background contribution is performed with the MC simulated samples. The proton-proton collision makes complex states from quarks and gluons (partons) in protons. A lot of MC samples generated separately by processes have been utilised to reproduce the final states.

There are several algorithms of the generator employed in the analysis. The algorithm called PYTHIA [158] is a multi-purpose event generator. It is employed to construct the shower for the MADGRAPH [159], POWHEG [160] and some of ALPGEN [161] samples. The HERWIG [145] is also a multi-purpose event generator. It is used to calculate fragmentation and the hadronisation for MC@NLO [162] and some of ALPGEN samples.

Two Parton Density Function (PDF) sets are employed to duplicate the phenomena from the high density  $pp$  collision: CTEQ6L1 [163] and CT10 [164].

The MC samples used for the analysis are produced with the ATLAS detector simulation based on the GEANT4 [165, 166] and the pile-up contribution based on “tunes.” The “tunes” are included to improve the performance of the MC simulation with the results of the previous experiments. The “tunes” employed in the analysis are ATLAS Underlying Event Tune 2B (AUET2B) [167], AU2 [168] and PERUGIA2011C [169].

The SM background samples used in the analysis are listed in Tab. 4.1. More detail will be found in following subsections.

#### 4.1.1 The Standard Model MC samples

The Standard Model processes as the background of the target signals should be considered which can be much contribution in final states.

**Diboson** The diboson productions can be considered with  $WZ/\gamma^*$ ,  $ZZ/\gamma^*$  and  $WW$ , which are generated with the NLO generator POWHEG.

Since  $WZ^{(*)}$  and  $ZZ^{(*)}$  processes can have at least three real leptons in final state if all bosons decay leptonically, they cannot be distinguished from the target signals by the selection of the number of leptons. Thus these two processes can be candidates of the main background. It is important to keep their statistics



Table 4.1: List of the MC simulated samples used in the analysis.

Process	Generator	Cross-section	Tune	PDF set
Diboson ( $VV$ )	POWHEG	NLO QCD	AU2	CT10
Triboson	MADGRAPH	NLO	AUET2B	CTEQ6L1
$V + \gamma$	SHERPA	NLO	–	CT10
$t\bar{t} + V$	ALPGEN	NLO	AUET2B	CTEQ6L1
$t + Z$	MADGRAPH	NLO	AUET2B	CTEQ6L1
$t\bar{t}$	POWHEG	NNLO+NNLL	PERUGIA2011C	CT10
$t$ -channel $t$	ACERMC	NNLO+NNLL	AUET2B	CTEQ6L1
$s$ -channel $t$	aMC@NLO	NNLO+NNLL	AUET2B	CT10
$V$ +jets	ALPGEN	DYNNLO	PERUGIA2011C	CTEQ6L1
SM higgs (ggF/VBF)	POWHEG	NNLL QCD, NLO EW	AU2	CT10
SM higgs ( $VH$ )	PYTHIA	NNLO QCD, NLO EW	AU2	CT10
SM higgs ( $t\bar{t}H$ )	PYTHIA	NNLO QCD	AU2	CT10
SUSY Signals	HERWIG++	PROSPINO2	–	CT10

due to estimate them precisely. The  $WZ$  and  $ZZ$  samples are produced with the integrated luminosity of 200–4000 and 7000–15000  $\text{fb}^{-1}$ , whilst the integrated luminosity of the data is 20.3  $\text{fb}^{-1}$ . Some samples have been applied lepton filters due to keeping the statistics. These filters select events with a generator level mass of the off-shell  $Z$  larger than 0–4 GeV and two leptons with their transverse momenta  $p_T(e, \mu) > 5 \text{ GeV}$  or  $p_T(\tau_h) > 15 \text{ GeV}$ .

The  $WW^{(*)}$  process, on the other hand, has two real leptons even if both  $W$  bosons decay leptonically. Although these processes should not be observed since we require three leptons in final states if we think about the phenomena in principle, the process can be observed due to the detector effects in practice.

The  $W + \gamma$  and  $Z + \gamma$  samples are generated with the Sherpa generator.

**Triboson** The triboson processes include  $WWW$ ,  $ZWW$  and  $ZZZ$  production modes. They can have three leptons if bosons in the processes decay leptonically. Whilst the cross sections for these processes are quite small of approximately  $O(1) \text{ fb}$ , these cannot be reduced only by the requirement for the kind of the lepton selection. The processes are generated with the generator MADGRAPH with the total amount of events of approximately 6.5–100  $\text{fb}^{-1}$ .

**$t\bar{t}$ +bosons** Although the cross sections of the  $t\bar{t}$ +bosons processes are very small approximately 0.0001–0.1 pb, there exist final states with three leptons if top quarks and bosons decay leptonically. In addition, this process should be suppressed by the  $b$ -jets veto due to the fact included top quarks, which decay bottom quarks and  $W$  bosons. These are not so important background processes for the analysis, while it should be included the estimation sequence. They are generated with ALPGEN and MADGRAPH generators with the total integrate luminosity of 100–10000  $\text{fb}^{-1}$ .

**Top** The top quark production except  $t\bar{t}$ +bosons can be much contribution in the three lepton analyses, whilst this process has no longer events with three leptons. If a top quark decays a  $b$ -quark and a  $W$  boson which decays leptonically, this process can have at most two leptons in final states. Moreover, an

appearance of the final states can have three leptons if at least one lepton is misidentified from a jet. The  $t\bar{t}$  production with at least one lepton has a high cross-section of approximately 250 pb. This is the reason why this process contaminates the signal events.

On the other hand, the single top production processes have a few contribution. Their cross-sections are approximately 0.5–20 pb.

The  $t\bar{t}$  process and the other top contribution are generated with POWHEG, aMC@NLO and ACERMC.

**Boson+jets** Boson+jets processes are considered of  $W$ +jets and  $Z$ +jets. Whilst they have quite large cross-sections of 12000 and 5000 pb, respectively, they should have small missing transverse momentum  $E_T^{\text{miss}}$  in final states. Almost all events are abandoned due to three leptons and  $E_T^{\text{miss}}$  requirements.

The MC production is performed by the generator ALPGEN with the total integrated luminosity of 10–100  $\text{fb}^{-1}$ . Although the amounts of the samples are not so enough as the amount of taken data 20.3  $\text{fb}^{-1}$ , it is not critical issue because they are used only for region definition. For the precise estimation for the background including the Boson+jets processes, the data-driven method described in Chap. 6 is performed.

**Standard Model Higgs** The Standard Model Higgs production processes are important because the final states of those are similar to the signal processes. They can be considered two categories. One is that the Higgs boson decays into  $VV$ . This is similar to the diboson production processes described above. The other is the  $VH$  production. For example, the Standard Model  $WH$  production has same final states as the signal SUSY  $Wh$  scenario.

The Standard Model Higgs production processes are generated with the generator POWHEG and the standard PYTHIA.

#### 4.1.2 New Physics MC samples

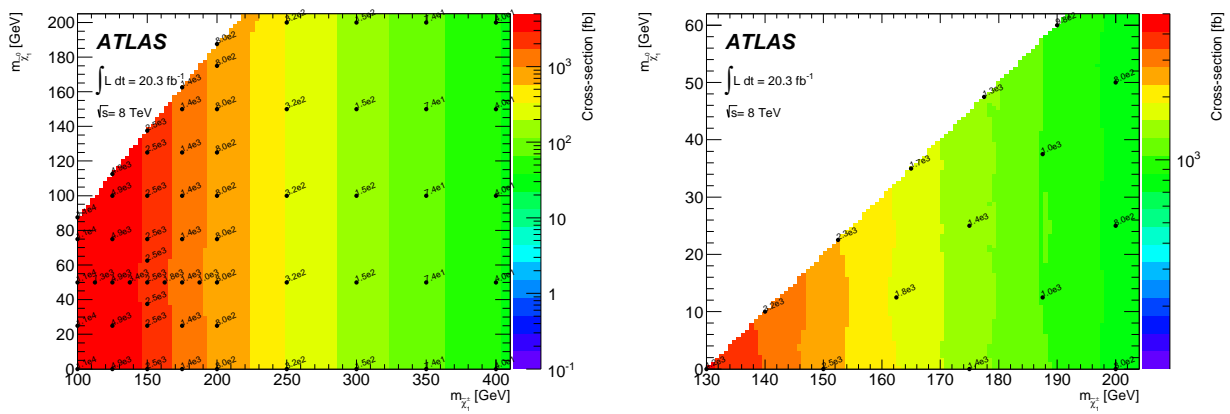
The SUSY signal samples are generated using HERWIG++ [170], which is rewritten in C++, while the standard HERWIG is written in Fortran, with the PDF set of CTEQ6L1. The target scenarios are simplified to the branching ratio of 100% (simplified model [65]).

Figures 4.1 show the production cross-sections for  $WZ/h$ -mediated scenarios. The produced  $\tilde{\chi}_1^\pm/\tilde{\chi}_2^0$  and  $\tilde{\chi}_1^0$  are assumed to be pure winos and bino, respectively. Thus the cross-section depends only on the mass of  $\tilde{\chi}_1^\pm/\tilde{\chi}_2^0$ .

## 4.2 Data taken in 2012

The data used in this analysis is full data taken in 2012 at ATLAS detector. The data is stored with complex sequence of the ATLAS data acquisition (DAQ) systems [106]. In the DAQ process, the data have been selected to reject the data with bad quality, for example, there are hits in the noisy modules in the subsystems.

The qualities of the data are monitored during data taking. They are defined as whether the event is taken in the period that the LHC was stable, the ATLAS detector was properly operating, and the magnet system was stable. The total amount of data which can be used in the physics analysis is 20.3  $\text{fb}^{-1}$ , as shown in Fig. 2.4.

(a)  $WZ$ -mediated scenario(b)  $Wh$ -mediated scenarioFigure 4.1: Signal grids and their cross-sections for  $WZ/h$ -mediated scenarios.

## Chapter 5

# Signal Region Optimisation

In order to detect the SUSY signal processes, the sensitivity of the signal should be maximised as much as possible. The selection criteria can be determined from the kinematic differences between the background and the signal processes. This selection condition is called the signal region (SR). In this chapter, the summary of the kinematic differences between the background and the signal processes are shown, together with the descriptions of all of the signal regions used in the analyses.

The direct production of the charginos and neutralinos has many decay modes even if only the modes with at least three leptons are chosen. In this thesis, any processes which include sleptons in the diagrams are not considered, since the slepton mass is supposed to be heavier than the SM weak bosons. The light slepton ( $m_{\tilde{\ell}} \lesssim 100\text{GeV}$ ) is already excluded at the LEP search [83] and at ATLAS electroweak SUSY search with two opposite sign leptons [112]. Thus only the modes with the decay via the SM bosons  $W/Z/h$  is considered. From a rough discussion, the signal processes can be categorised as following two modes

- Decays via on/off-shell  $WZ$ ,
- Decays via on-shell  $Wh$ .

In this thesis, the decay mode via off-shell Higgs is omitted. This is because the contribution of the off-shell Higgs can be small comparing to the off-shell  $Z$  contribution.

In the case of the mass difference between the second lightest neutralino and the lightest neutralino to be greater than  $125\text{GeV}$ , i.e. the SM Higgs boson mass, two modes decaying via on-shell  $WZ$  and  $Wh$  should be mixed. The mixing has already been described in Chap. 1.

Analyses can be divided into two categories. They are noted as Category-A and Category-B. The target of the Category-A is the region with relatively large mass difference between  $\tilde{\chi}_1^\pm/\tilde{\chi}_2^0$  and  $\tilde{\chi}_1^0$ . Detailed discussion will be shown in Sec. 5.3.

On the other hand, the target of the Category-B is the region with compressed mass difference between  $\tilde{\chi}_1^\pm/\tilde{\chi}_2^0$  and  $\tilde{\chi}_1^0$ . The mode for decaying via off-shell  $Z$  is important for the compressed mass region. This discussion will be in Sec. 5.4.

Hereinafter, the lepton symbol  $\ell$  denotes the *light* lepton such as electron and muon.

Table 5.1: Summary of the triggers which are used in this analysis.

Trigger	Detail	Trigger threshold	offline threshold
Single Isolated $e$	EF_e24vhi_medium1	24 GeV	25 GeV
Single Isolated $\mu$	EF_mu24i_tight	24 GeV	25 GeV
Double $e$	EF_2e12Tvh_loose	12, 12 GeV	14, 14 GeV
	EF_e24vh_medium1_e7_medium1	24, 7 GeV	25, 10 GeV
Double $\mu$	EF_2mu13	13, 13 GeV	14, 14 GeV
	EF_mu18_tight_mu8_EFFS	18, 8 GeV	18, 10 GeV
Combined $e\mu$	EF_e12Tvh_medium1_mu8	12, 8 GeV	14, 10 GeV
	EF_mu18_tight_e7_medium1	18, 7 GeV	18, 10 GeV
Triple $e$	EF_e18vh_medium1_2e7T_medium1	18, 7, 7 GeV	20, 9, 9 GeV
Triple $\mu$	3mu6	6, 6, 6 GeV	7, 7, 7 GeV
	mu18_tight_2mu4_EFFS	18, 4, 4 GeV	19, 5, 5 GeV
Combined $e\mu$	EF_2e7T_medium1_mu6	7, 7, 6 GeV	9, 9, 7 GeV
	EF_e7T_medium1_2mu6	7, 6, 6 GeV	9, 7, 7 GeV

## 5.1 Event pre-selection

Event pre-selection is performed by following the standard criteria proposed by the ATLAS SUSY analysis group. Details of the selection criteria are described below.

### 5.1.1 Trigger Selection

It is necessary to set proper triggers for the hadron collider analyses. This analysis uses mainly leptons. Many options of triggers with leptons are prepared, for example, single lepton, di-lepton and tri-lepton triggers, as shown in Tab. 5.1. Trigger menus can overlap each other then the logical “OR” of the triggers should be considered.

Table 5.1 shows the trigger settings for this analysis. The trigger menus written in Tab. 5.1 are formed using the triggers described in Sec. 2.3.

### 5.1.2 Event Quality Cuts

Event quality cuts are defined to reject background events or events suffering from reconstruction or other problems. First, events with jets potentially originating from instrumental effects are rejected. The jets are defined with the problems of the HEC spikes, EM coherent noise, non-collision background and cosmic events, with  $E_T > 20$  GeV and any  $\eta$ , surviving the overlap removal with electrons.

For the same reason, events with the  $E_T^{\text{miss}}$  using the non operational cells in the tile and HEC are rejected. Events including the EM calorimeter and the Tile calorimeter errors are removed.

During the data taking in 2012, the tile calorimeter has a hot spot in the region of  $-0.2 < \eta < 0.1$  and  $2.65 < \phi < 2.75$ . If events with jets pointing to the region, the events are rejected.

For the muons, to suppress the cosmic background and the other source mis-measured muons, events

with the muons with a longitudinal impact parameter  $|z_0| > 1$  mm or a transverse impact parameter  $|d_0| > 0.2$  mm are rejected.

## 5.2 Statistical method

Before the discussion of the signal regions, the variable called  $Z_N$  is introduced, which is used as a statistical indicator of the sensitivity for the analyses. All of the signal regions are defined as to maximise the  $Z_N$  variable.

$Z_N$  is expressed with  $p$ -value (see Sec. 9.2) as following equation:

$$Z_N = \sqrt{2} \operatorname{erf}^{-1}(1 - 2p), \quad (5.1)$$

where the function  $\operatorname{erf}(x)$  is called the error function defined as:

$$\operatorname{erf}(x) = \frac{2}{\sqrt{\pi}} \int_0^x e^{-t^2} dt. \quad (5.2)$$

In the case of Gaussian assumption, the  $Z_N$  represents the scale of the standard deviation  $\sigma$ . In order to exclude models, we can use the one side test for each models. Thus 95% confidence level corresponds to the  $Z_N = 1.64$  [171].

## 5.3 Signal Regions for Category-A

The target scenarios of the Category-A analysis are the region with the mass difference  $\Delta m_{\tilde{\chi}_2^0, \tilde{\chi}_1^0} > 50$  GeV. As described in the introduction of the chapter, three patterns of decay can be considered in this region:

1. decay via off-shell  $Z$  ( $50 \text{ GeV} < \Delta m_{\tilde{\chi}_2^0, \tilde{\chi}_1^0} < 91.2 \text{ GeV}$ )
2. decay via on-shell  $Z$  ( $91.2 \text{ GeV} < \Delta m_{\tilde{\chi}_2^0, \tilde{\chi}_1^0} < 125 \text{ GeV}$ )
3. decay via on-shell  $Z/h$  ( $125 \text{ GeV} < \Delta m_{\tilde{\chi}_2^0, \tilde{\chi}_1^0}$ ).

In the case of third item, the branching ratio is determined from the Higgsino mass parameter  $\mu$  and the  $\tilde{\chi}_2^0$  mixing of the winos and Higgsinos. The expected dominant decay processes are illustrated in Fig. 5.1. However, this analysis assumes the simplified model, where the branching ratio is fixed to 100% for the target decay.

Figure 5.2 shows the Feynman diagrams for the target scenarios of the Category-A. For the scenario with decay via  $WZ$ , the ‘‘binned’’ signal regions are defined to obtain higher significance. This  $WZ$  channel will be described in Sec. 5.3.1. For the scenario with decay via  $Wh$ , three signal regions are optimised taken into account the branching ratio of the Higgs. This  $Wh$  channel will be described in Sec. 5.3.2. Table 5.2 summarises the definition of the signal regions of Category-A. There are four criteria for this category. The region named  $\text{SR}0\tau a$  is a binned signal region for  $WZ$  channel. The regions named  $\text{SR}0\tau b$ ,  $\text{SR}1\tau$  and  $\text{SR}2\tau$  are for the  $Wh$  channel, which are optimised divided by the number of taus.

The single or di-lepton triggers are used. The leptons are reconstructed with the standard selection and isolation, which are described in the chapter of the Particle Reconstruction (Chap. 3). All signal regions are defined to be orthogonal each other. Thus they can be statistically combined in order to get higher statistics.

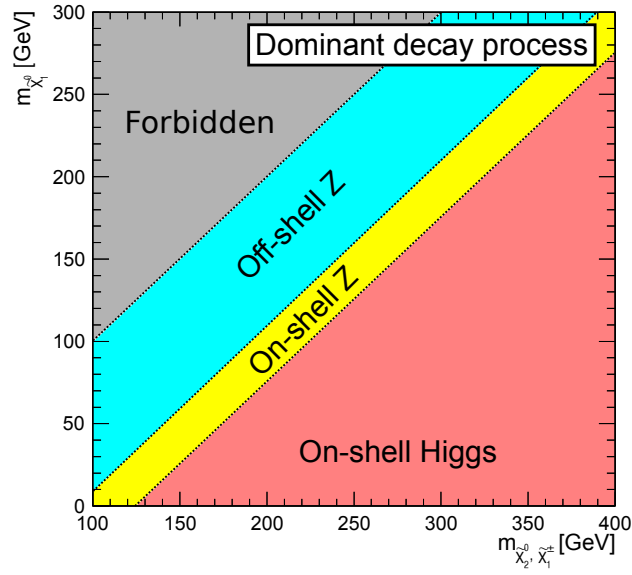


Figure 5.1: Dominant decay processes for direct chargino and neutralino production with high mass sleptons. The region where the chargino mass is smaller than 100 GeV has already been excluded at the LEP search [85].

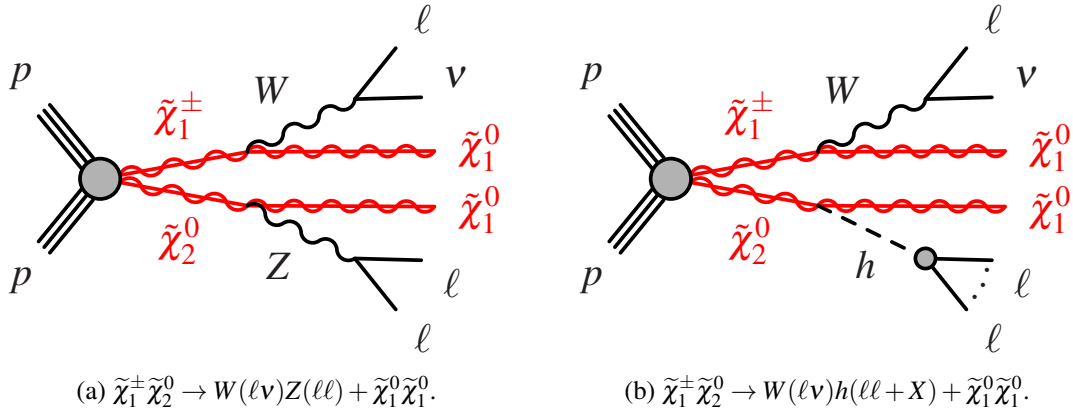


Figure 5.2: Feynman diagram for the WZ/h-mediated scenarios.

Table 5.2: Summary of the signal regions of Category-A.

Singal Region	SR0 $\tau$ a	SR0 $\tau$ b	SR1 $\tau$	SR2 $\tau$
Flavour/sign	$\ell^+ \ell^- \ell'(\ell')$	$\ell^\pm \ell^\pm \ell'^\mp$	$\tau^\pm \ell^\mp \ell'(\ell')^\mp$	$\tau^+ \tau^- \ell$
$b$ -tagged jet	veto	veto	veto	veto
$E_T^{\text{miss}}$	binned	$> 50 \text{ GeV}$	$> 50 \text{ GeV}$	$> 60 \text{ GeV}$
Other	$m_{\text{SFOS}}$ binned $m_T$ binned	$p_T(3^{\text{rd}} \text{ lep}) > 20 \text{ GeV}$ $\min. \Delta\phi_{\ell\ell'} \leq 1.0$	$p_T(2^{\text{nd}} \text{ lep}) > 20 \text{ GeV}$ $\sum p_T(\ell) > 70 \text{ GeV}$ $m_{\ell\tau} < 120 \text{ GeV}$ $m_{ee} Z$ veto	$\sum p_T(\tau) > 110 \text{ GeV}$ $70 < m_{\tau\tau} < 120 \text{ GeV}$
Target model	WZ-mediated	Wh-mediated	Wh-mediated	Wh-mediated

Table 5.3: Summary of the bins in  $m_{\text{SFOS}}$ ,  $m_{\text{T}}$ , and  $E_{\text{T}}^{\text{miss}}$  for SR0 $\tau$ a.

$m_{\text{SFOS}}$	$m_{\text{T}}$	$E_{\text{T}}^{\text{miss}}$	$3\ell$ Z veto	SR bin
12–40	< 80	50–90		1
		> 90		2
	> 80	50–75		3
		> 75		4
40–60	< 80	50–75	yes	5
		> 75		6
	> 80	50–135		7
		> 135		8
60–81.2	< 80	50–75	yes	9
	> 80	50–75		10
	< 110	> 75		11
	> 110	> 75		12
81.2–101.2	< 110	50–90	yes	13
		> 90		14
	> 110	50–135		15
		> 135		16
> 101.2	< 180	50–210		17
	> 180	50–210		18
	< 120	> 210		19
	> 120	> 210		20

### 5.3.1 Decay via $WZ$ scenario

The electroweak SUSY decaying via  $WZ$ -mediated scenario produces three leptons if all of the produced weak bosons decay leptonically. For these scenarios, 20 binned signal regions named SR0 $\tau$ a-bins are defined to get maximum significances for the target grids, as shown in Tab. 5.3. All events with  $b$ -jets are vetoed, and an same-flavour opposite-sign (SFOS) lepton pair is requested. If there are two candidates of SFOS lepton pair in an event, the candidate which has mass closest to the  $Z$  mass (best  $Z$  candidate) is adopted, in order to select the lepton pair from the  $Z$  boson decay. The  $b$ -jet veto reduces the contamination coming from  $t\bar{t}$ . Since the 80%  $b$ -tagging working point is employed [154],  $\sim 95\%$  of the  $t\bar{t}$  is suppressed, while a few % of the signal samples are suppressed. The parameter space is binned in  $m_{\text{SFOS}}$ ,  $m_{\text{T}}$  and  $E_{\text{T}}^{\text{miss}}$ , except the region  $E_{\text{T}}^{\text{miss}} < 50\text{GeV}$ , which is reserved for validation regions. The bins 5, 9, and 13 veto events with  $m_{\ell\ell}$  within 10 GeV of the  $Z$  mass. The  $Z$  veto with  $m_{\ell\ell}$  is for suppressing the background from  $Z \rightarrow \ell\ell\ell$  where one  $\ell$  comes from a converted photon from final state radiation. The masses of  $e^+e^-e$  and  $\mu^+\mu^-e$  which are in the  $Z$  mass window are discarded.

The transverse mass  $m_{\text{T}}$  in Tab. 5.3 is formed using the  $E_{\text{T}}^{\text{miss}}$  and the  $p_{\text{T}}$  of the lepton which do not form the best  $Z$  candidate and the difference azimuthal angle between the  $E_{\text{T}}^{\text{miss}}$  and the lepton  $\Delta\phi_{\ell, E_{\text{T}}^{\text{miss}}}$  as

$$m_{\text{T}} = \sqrt{2p_{\text{T}}(\ell)E_{\text{T}}^{\text{miss}}(1 - \cos\Delta\phi_{\ell, E_{\text{T}}^{\text{miss}}})}, \quad (5.3)$$

where the lepton mass ( $m_e = 511\text{keV}$  and  $m_\mu = 106\text{MeV}$ ) is assumed to be 0 because it is negligible comparing to the  $p_{\text{T}}$  ( $> 10\text{GeV}$ ) and the  $E_{\text{T}}^{\text{miss}}$  ( $> 50\text{GeV}$ ). This variable is usually used to identify  $W \rightarrow \ell\nu$



signals. Whilst the signal has also a  $W$  boson if the mass difference is greater than the  $W$  mass, the shape of the distribution tends to shift higher comparing to the Standard Model processes since the LSP is included in the  $E_T^{\text{miss}}$ . Thus the  $m_T$  binning is useful to detect difference of the shape in the distribution.

The estimated number of events based on the MC background samples are summarised in Tab. 5.4. For the  $WZ$  signal samples, the expected numbers of events in each bin are shown in Figs. 5.3–5.6. The SR0 $\tau$ a-bin1 to 12 require the  $m_{\text{SFOS}}$  less than the  $Z$  mass ( $\sim 91$  GeV). Thus they are sensitive to scenarios where the charginos and neutralinos decaying via off-shell  $W$  and off-shell  $Z$ . The SR0 $\tau$ a-bin13 to 16 require that the  $m_{\text{SFOS}}$  should be  $Z$  mass window ( $91 \text{ GeV} \pm 10 \text{ GeV}$ ). Thus they cover the large region of the scenarios with emitting on-shell  $Z$ . The SR0 $\tau$ a-bin17 to 20 require the high  $m_{\text{SFOS}}$  greater than the  $Z$  mass. Thus they are not sensitive to the scenarios with the on-shell  $Z$ , but sensitive to the scenario with off-shell  $Z$ . The SR0 $\tau$ a-bin19 and 20 are very tight region, so that the numbers of the passed signals are small.

### 5.3.2 Decay via $Wh$ scenario

As including the tau leptons as ‘‘leptons,’’ several patterns of the final states with at least three leptons are considered in the  $Wh$ -mediated scenario, depending on the Higgs decay process as:

- $h \rightarrow WW \rightarrow \ell\nu\ell\nu$
- $h \rightarrow \tau\tau \rightarrow \tau_h\tau_h + \text{missing}$
- $h \rightarrow \tau\tau \rightarrow \ell\ell + \text{missing}$
- $h \rightarrow ZZ \rightarrow \ell\ell\ell\ell$  or  $\ell\ell\nu\nu$
- ...

where  $\ell$  shows the ‘light’ lepton such as electrons or muons.

The branching ratio for near 125 GeV Higgs is shown in Fig. 5.7 [24]. This ratio claims that the modes of decays to  $WW$  and  $\tau\tau$  are promising candidates for search for  $Wh$ -mediated scenario. Therefore there are three signal regions which are optimised for this analysis:

1.  $\tilde{\chi}_1^\pm\tilde{\chi}_2^0 \rightarrow W(\ell\nu)h(WW \rightarrow \ell\nu\ell\nu) + \tilde{\chi}_1^0\tilde{\chi}_1^0$  (no taus mode),
2.  $\tilde{\chi}_1^\pm\tilde{\chi}_2^0 \rightarrow W(\ell\nu)h(\tau\tau \rightarrow \ell\tau_h + \text{missing}) + \tilde{\chi}_1^0\tilde{\chi}_1^0$  (one tau mode),
3.  $\tilde{\chi}_1^\pm\tilde{\chi}_2^0 \rightarrow W(\ell\nu)h(\tau\tau \rightarrow \tau_h\tau_h + \text{missing}) + \tilde{\chi}_1^0\tilde{\chi}_1^0$  (two taus mode).

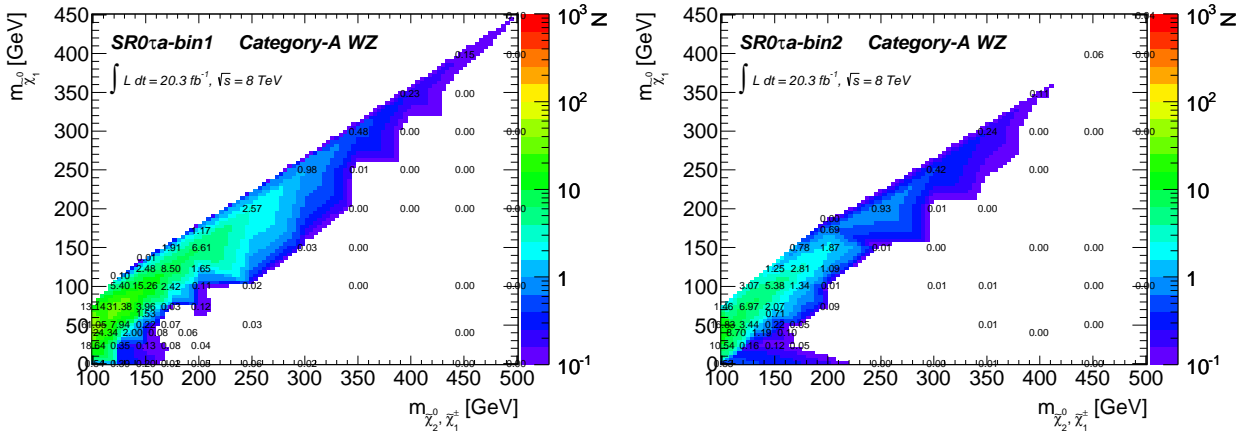
For no taus mode,  $h \rightarrow WW$  to leptonic decay should be dominant, whilst the leptonic decay of  $h \rightarrow \tau\tau$  can make the same final state. For one or two taus mode, the signature from  $h \rightarrow \tau\tau$  is dominant. Figures 5.8 show the Feynman diagram of  $Wh$  scenarios decaying via  $WW$  and  $\tau\tau$ . In the following subsections, the detail of the optimisation for each mode will be discussed.

All signal regions for the  $Wh$  mode are orthogonal and  $b$ -jet veto with 80%  $b$ -tagging working point is applied to reduce  $\sim 95\%$  of the  $t\bar{t}$  contribution.

**Signal Region for no taus mode** The signal region for no taus mode called SR0 $\tau$ b targets the decay via  $Wh$  mode, where Higgs may decay via  $WW$  to electrons or muons. A veto on SFOS lepton pairs is applied to discriminate against the Standard Model  $WZ$  production. The SFOS veto contributes to suppress more than 99% of the SM  $WZ$ ,  $ZZ$  and  $V$ +jets processes, and  $\sim 90\%$  of the  $t\bar{t}+V$ ,  $VVV$  and Higgs contributions. This selection also reduces the SUSY signals, where the 80% of the SUSY is lost. The  $E_T^{\text{miss}} > 50$  GeV is

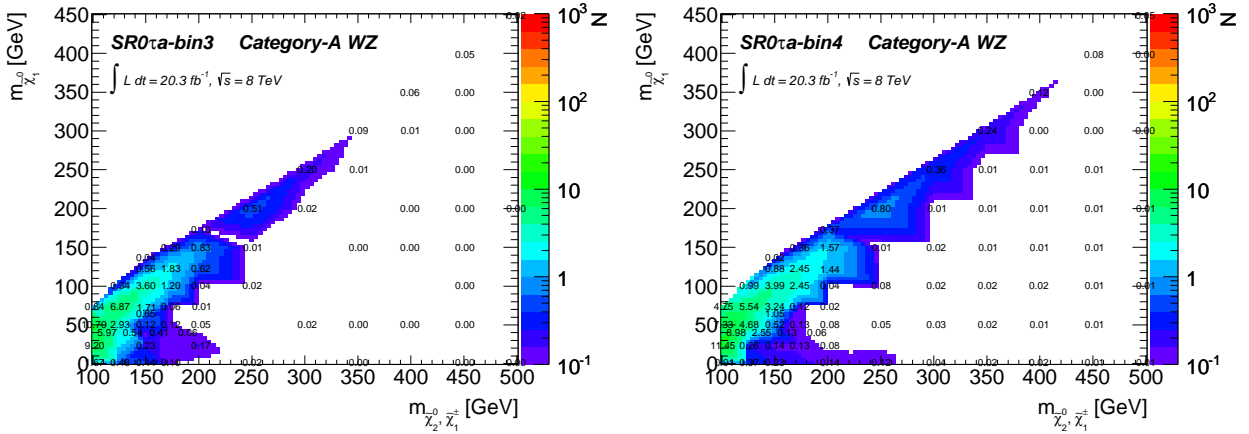
Table 5.4: Numbers of events for the SR0 $\tau\alpha$  binned signal regions. Estimates are based on MC only and uncertainties are statistical only. The irreducible background (noted as SM<sub>irred.</sub>) is the WZ, ZZ,  $\bar{t}t+V$ , triboson VVV (WW, WWZ, WWZ, ZZZ) and the Standard Model Higgs processes, while the reducible backgrounds (noted as SM<sub>red.</sub>) are all others.

SR0 $\tau\alpha$	WZ	ZZ	$\bar{t}t+V$	VVV	Higgs	SM <sub>irred.</sub>	$\bar{t}t$	single $t$	WW	Z+jets	V+ $\gamma$	SM <sub>red.</sub>	$\Sigma$ SM
Bin 1	13.24 $\pm$ 0.60	1.41 $\pm$ 0.04	0.14 $\pm$ 0.03	0.33 $\pm$ 0.03	0.66 $\pm$ 0.02	15.78 $\pm$ 0.61	1.31 $\pm$ 0.39	0.77 $\pm$ 0.55	0.10 $\pm$ 0.05	0.00 $\pm$ 0.00	0.16 $\pm$ 0.09	2.35 $\pm$ 0.68	18.13 $\pm$ 0.91
Bin 2	2.94 $\pm$ 0.26	0.12 $\pm$ 0.01	0.07 $\pm$ 0.01	0.10 $\pm$ 0.01	0.15 $\pm$ 0.01	3.41 $\pm$ 0.26	0.65 $\pm$ 0.32	0.00 $\pm$ 0.00	0.03 $\pm$ 0.02	0.00 $\pm$ 0.00	0.00 $\pm$ 0.00	0.68 $\pm$ 0.32	4.09 $\pm$ 0.42
Bin 3	7.76 $\pm$ 0.45	0.40 $\pm$ 0.02	0.03 $\pm$ 0.01	0.19 $\pm$ 0.02	0.64 $\pm$ 0.03	9.03 $\pm$ 0.45	0.47 $\pm$ 0.33	0.00 $\pm$ 0.00	0.02 $\pm$ 0.02	0.00 $\pm$ 0.00	0.04 $\pm$ 0.04	0.53 $\pm$ 0.33	9.55 $\pm$ 0.56
Bin 4	4.49 $\pm$ 0.31	0.20 $\pm$ 0.02	0.14 $\pm$ 0.03	0.57 $\pm$ 0.04	0.46 $\pm$ 0.02	5.85 $\pm$ 0.31	1.94 $\pm$ 0.65	0.00 $\pm$ 0.00	0.02 $\pm$ 0.02	0.00 $\pm$ 0.00	0.00 $\pm$ 0.00	1.97 $\pm$ 0.65	7.81 $\pm$ 0.72
Bin 5	6.31 $\pm$ 0.38	1.55 $\pm$ 0.04	0.11 $\pm$ 0.04	0.26 $\pm$ 0.02	0.36 $\pm$ 0.02	8.59 $\pm$ 0.39	1.20 $\pm$ 0.40	0.00 $\pm$ 0.00	0.16 $\pm$ 0.06	2.16 $\pm$ 1.25	1.52 $\pm$ 0.33	5.05 $\pm$ 1.35	13.63 $\pm$ 1.41
Bin 6	3.74 $\pm$ 0.27	0.25 $\pm$ 0.02	0.05 $\pm$ 0.01	0.24 $\pm$ 0.02	0.33 $\pm$ 0.02	4.61 $\pm$ 0.28	4.08 $\pm$ 0.94	0.00 $\pm$ 0.00	0.05 $\pm$ 0.03	0.00 $\pm$ 0.00	0.30 $\pm$ 0.14	4.43 $\pm$ 0.95	9.04 $\pm$ 0.99
Bin 7	7.61 $\pm$ 0.39	0.55 $\pm$ 0.03	0.04 $\pm$ 0.01	0.88 $\pm$ 0.05	0.98 $\pm$ 0.05	10.05 $\pm$ 0.40	3.58 $\pm$ 0.92	0.07 $\pm$ 0.05	0.35 $\pm$ 0.12	0.00 $\pm$ 0.00	1.12 $\pm$ 0.26	5.11 $\pm$ 0.97	15.17 $\pm$ 1.05
Bin 8	0.30 $\pm$ 0.06	0.01 $\pm$ 0.00	0.11 $\pm$ 0.05	0.13 $\pm$ 0.02	0.13 $\pm$ 0.02	0.69 $\pm$ 0.08	0.93 $\pm$ 0.46	0.00 $\pm$ 0.00	0.00 $\pm$ 0.00	0.00 $\pm$ 0.00	0.00 $\pm$ 0.00	0.93 $\pm$ 0.46	1.62 $\pm$ 0.47
Bin 9	16.19 $\pm$ 0.74	1.43 $\pm$ 0.04	0.16 $\pm$ 0.03	0.23 $\pm$ 0.02	0.32 $\pm$ 0.02	18.32 $\pm$ 0.74	2.69 $\pm$ 0.75	1.23 $\pm$ 0.71	0.10 $\pm$ 0.06	1.26 $\pm$ 0.89	1.39 $\pm$ 0.27	6.66 $\pm$ 1.39	24.98 $\pm$ 1.57
Bin 10	13.09 $\pm$ 0.63	0.60 $\pm$ 0.03	0.12 $\pm$ 0.03	0.40 $\pm$ 0.03	0.22 $\pm$ 0.01	14.44 $\pm$ 0.63	1.96 $\pm$ 0.62	0.35 $\pm$ 0.35	0.08 $\pm$ 0.05	0.00 $\pm$ 0.00	0.50 $\pm$ 0.19	2.88 $\pm$ 0.74	17.31 $\pm$ 0.97
Bin 11	19.49 $\pm$ 0.80	0.65 $\pm$ 0.03	0.41 $\pm$ 0.05	0.59 $\pm$ 0.03	0.28 $\pm$ 0.01	21.43 $\pm$ 0.81	3.51 $\pm$ 0.91	0.58 $\pm$ 0.58	0.17 $\pm$ 0.10	0.00 $\pm$ 0.00	0.40 $\pm$ 0.09	4.66 $\pm$ 1.09	26.09 $\pm$ 1.35
Bin 12	3.68 $\pm$ 0.35	0.14 $\pm$ 0.01	0.12 $\pm$ 0.03	0.61 $\pm$ 0.04	0.12 $\pm$ 0.01	4.66 $\pm$ 0.35	2.07 $\pm$ 0.62	0.00 $\pm$ 0.00	0.05 $\pm$ 0.04	0.00 $\pm$ 0.00	0.16 $\pm$ 0.16	2.28 $\pm$ 0.65	6.95 $\pm$ 0.73
Bin 13	612.54 $\pm$ 4.79	28.86 $\pm$ 0.19	2.92 $\pm$ 0.12	1.32 $\pm$ 0.04	2.17 $\pm$ 0.03	647.82 $\pm$ 4.80	4.86 $\pm$ 1.01	1.12 $\pm$ 0.56	0.23 $\pm$ 0.09	53.85 $\pm$ 10.18	5.61 $\pm$ 0.51	65.67 $\pm$ 10.26	713.49 $\pm$ 11.32
Bin 14	207.04 $\pm$ 2.77	5.54 $\pm$ 0.09	2.00 $\pm$ 0.08	0.80 $\pm$ 0.03	0.98 $\pm$ 0.02	216.36 $\pm$ 2.78	2.85 $\pm$ 0.69	0.32 $\pm$ 0.32	0.07 $\pm$ 0.07	0.00 $\pm$ 0.00	0.00 $\pm$ 0.00	3.24 $\pm$ 0.76	219.60 $\pm$ 2.88
Bin 15	58.34 $\pm$ 1.37	3.49 $\pm$ 0.06	0.67 $\pm$ 0.05	1.01 $\pm$ 0.04	0.31 $\pm$ 0.01	63.83 $\pm$ 1.37	1.30 $\pm$ 0.49	0.00 $\pm$ 0.00	0.00 $\pm$ 0.00	5.84 $\pm$ 4.13	0.90 $\pm$ 0.34	8.04 $\pm$ 4.17	71.86 $\pm$ 4.39
Bin 16	3.87 $\pm$ 0.39	0.12 $\pm$ 0.01	0.08 $\pm$ 0.01	0.33 $\pm$ 0.02	0.03 $\pm$ 0.00	4.43 $\pm$ 0.39	1.11 $\pm$ 0.08	0.00 $\pm$ 0.00	0.02 $\pm$ 0.02	0.00 $\pm$ 0.00	0.00 $\pm$ 0.00	0.13 $\pm$ 0.08	4.57 $\pm$ 0.40
Bin 17	50.41 $\pm$ 1.28	2.43 $\pm$ 0.06	0.77 $\pm$ 0.08	3.22 $\pm$ 0.08	0.66 $\pm$ 0.02	57.78 $\pm$ 1.29	8.57 $\pm$ 1.28	2.41 $\pm$ 0.85	0.23 $\pm$ 0.08	0.06 $\pm$ 0.06	1.86 $\pm$ 0.37	13.14 $\pm$ 1.58	70.91 $\pm$ 2.04
Bin 18	2.33 $\pm$ 0.29	0.08 $\pm$ 0.01	0.15 $\pm$ 0.04	0.54 $\pm$ 0.03	0.66 $\pm$ 0.02	3.14 $\pm$ 0.29	0.26 $\pm$ 0.26	0.00 $\pm$ 0.00	0.00 $\pm$ 0.00	0.00 $\pm$ 0.00	0.00 $\pm$ 0.00	0.26 $\pm$ 0.26	3.40 $\pm$ 0.39
Bin 19	0.92 $\pm$ 0.17	0.02 $\pm$ 0.01	0.00 $\pm$ 0.00	0.08 $\pm$ 0.01	0.66 $\pm$ 0.02	1.03 $\pm$ 0.17	0.00 $\pm$ 0.00	0.00 $\pm$ 0.00	0.00 $\pm$ 0.00	0.00 $\pm$ 0.00	0.00 $\pm$ 0.00	0.00 $\pm$ 0.00	1.03 $\pm$ 0.17
Bin 20	0.11 $\pm$ 0.06	0.01 $\pm$ 0.00	0.01 $\pm$ 0.01	0.07 $\pm$ 0.01	0.66 $\pm$ 0.02	0.21 $\pm$ 0.06	0.00 $\pm$ 0.00	0.00 $\pm$ 0.00	0.04 $\pm$ 0.04	0.00 $\pm$ 0.00	0.00 $\pm$ 0.00	0.04 $\pm$ 0.04	0.25 $\pm$ 0.07



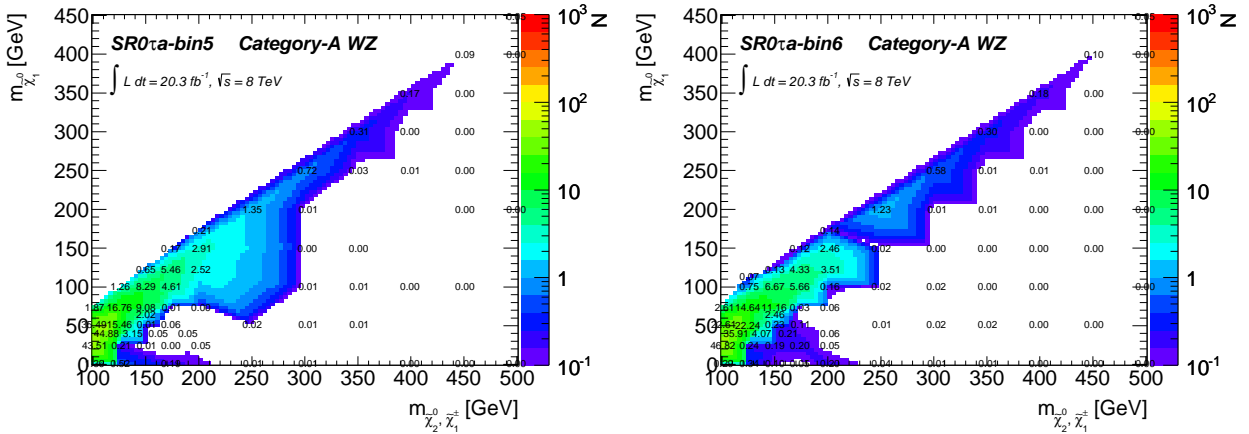
(a) SR0τa-bin1

(b) SR0τa-bin2



(c) SR0τa-bin3

(d) SR0τa-bin4



(e) SR0τa-bin5

(f) SR0τa-bin6

Figure 5.3: Expected numbers of signal events for SR0τa-bin1–6.

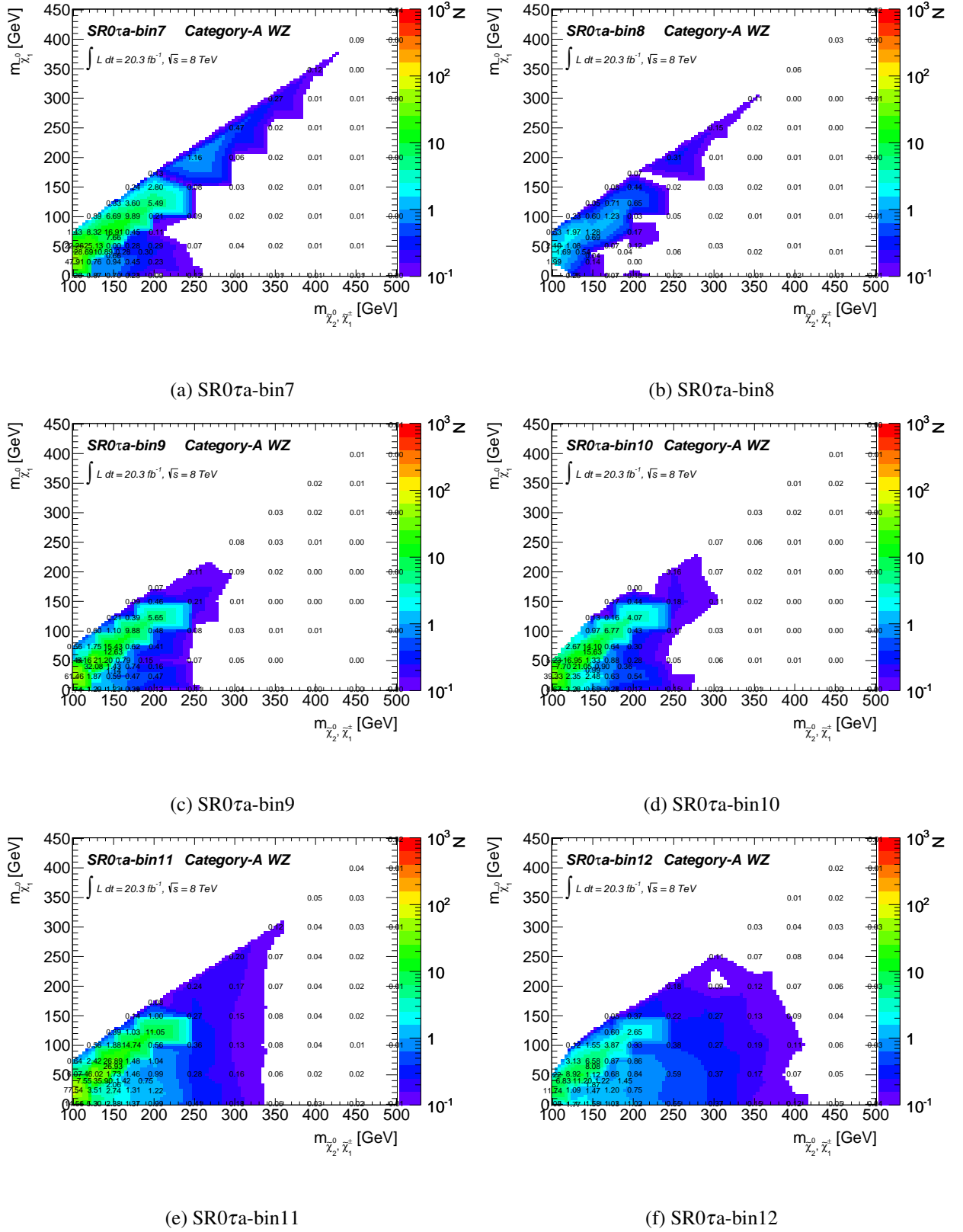
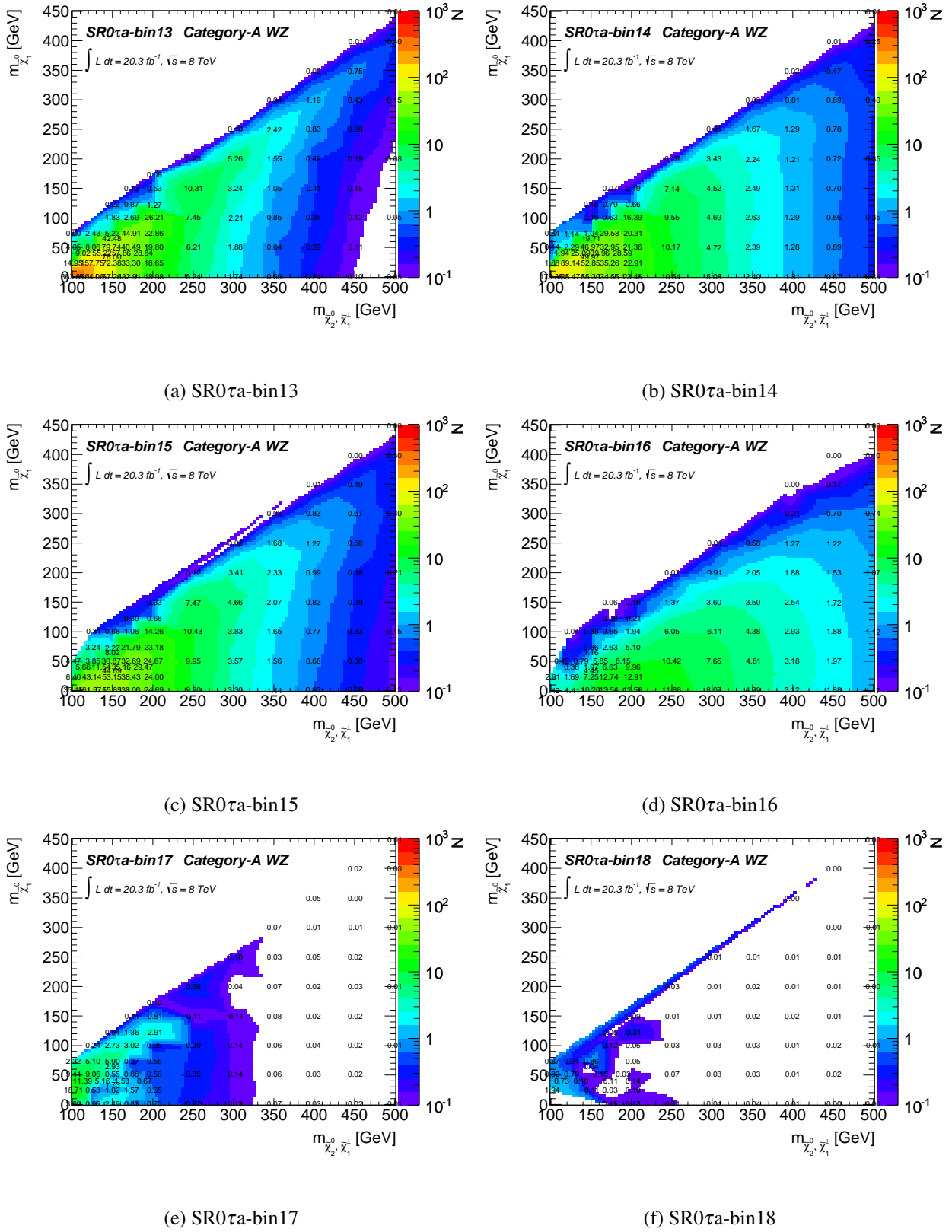
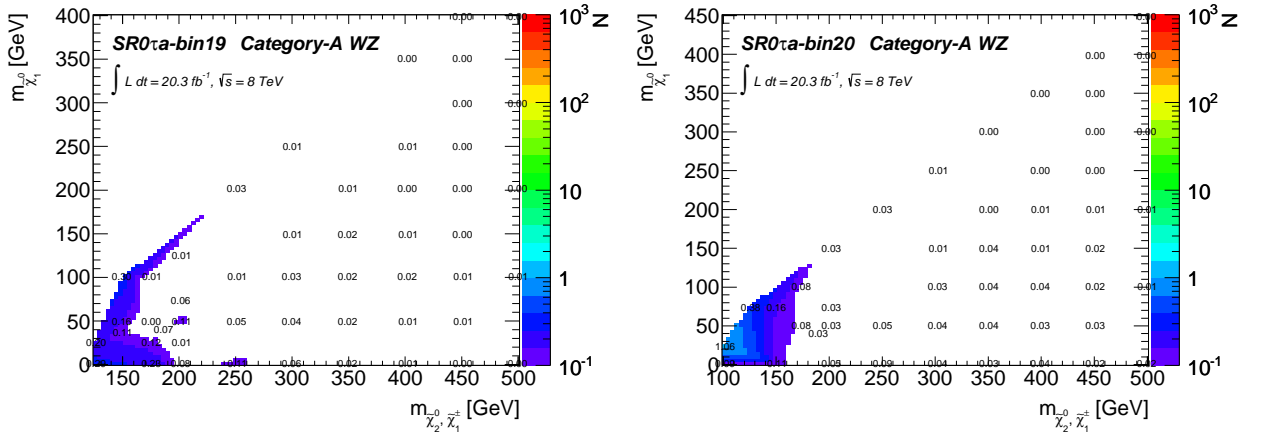


Figure 5.4: Expected numbers of signal events for SR0τa-bin7–12.





(a) SR0τa-bin19

(b) SR0τa-bin20

Figure 5.6: Expected numbers of signal events for SR0τa-bin19–20.

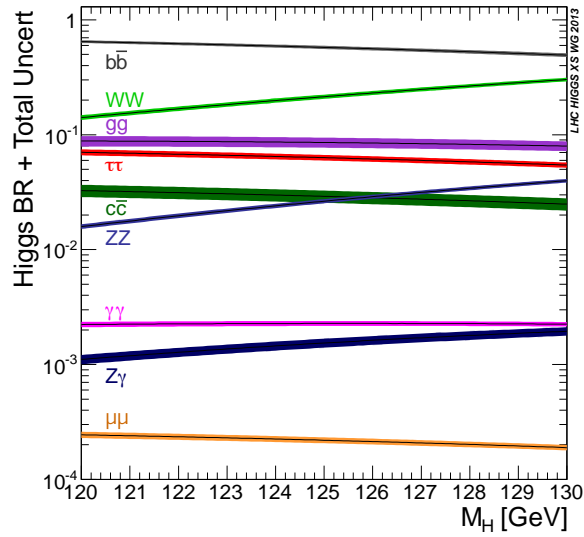


Figure 5.7: Branching ratio for near 125 GeV Higgs [24].

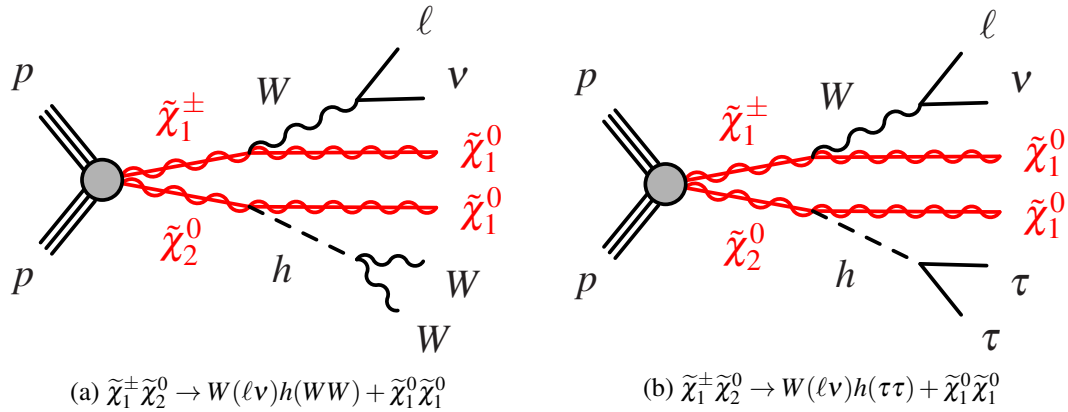


Figure 5.8: Feynman diagrams of  $Wh$  scenarios decaying via  $WW$  and  $\tau\tau$ .

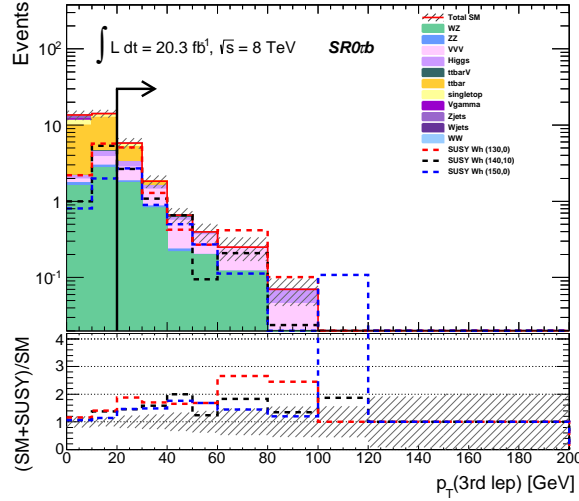


Figure 5.9: Third lepton transverse momentum distribution with three leptons selection, a SFOS lepton pair veto,  $b$ -jet veto and  $E_T^{\text{miss}} > 50$  GeV. Third leptons of the background samples are shifted lower region, hence the selection  $p_T > 20$  GeV has been applied.

required to reduce  $WZ$ ,  $ZZ$  and  $Z$ -jets contamination. The  $E_T^{\text{miss}}$  requirement contributes to reduce 80% of these processes against the events passed the SFOS veto. The low  $E_T^{\text{miss}}$  region is reserved for validation of these background samples.

The transverse momentum of the third lepton is also a useful variable to reduce  $t\bar{t}$  contribution, which has a low  $p_T$  third lepton from leptonic  $b$ -jet decay. Figure 5.9 shows the distribution of the transverse momentum of third lepton with the selection: three leptons selection, a SFOS lepton pair veto,  $b$ -jet veto and  $E_T^{\text{miss}} > 50$  GeV. The selection value is optimised to obtain the highest significance. In this case,  $p_T > 20$  GeV is adopted. It reduces mainly  $t\bar{t}$  contribution ( $\sim 80\%$ ).

The difference of the azimuthal angle ( $\Delta\phi$ ) between opposite sign leptons is calculated for all lepton pairs. The minimum of  $\Delta\phi_{\ell^+\ell^-}$  is plotted with the selection: three leptons selection, a SFOS veto,  $b$ -jet veto,  $E_T^{\text{miss}} > 50$  GeV and  $p_T(\ell_3) > 20$  GeV in Fig. 5.10. In the  $h \rightarrow WW$  decay, conservation of the spin angular momentum and the left handed weak interaction lead to a correlation between the direction of the produced leptons. The  $\Delta\phi$  between opposite sign leptons tends to be lower than the average distribution [172]. According to Fig. 5.10,  $\Delta\phi_{\ell\ell} < 1.0$  is a reasonable selection in order to suppress the SM  $WZ$  background.

**Signal Region for one tau mode** The signal region with two leptons and one hadronic tau is optimised for the SUSY decaying via  $Wh$  mode. The Higgs boson is decaying into di-tau with approximately 6% branching ratio, as shown in Fig. 5.7, which is the highest fraction among those decaying directly into leptons.

In order to suppress the SM contribution from  $WZ$  with  $W \rightarrow \tau\nu$  and  $Z \rightarrow \ell^+\ell^-$ , same-sign lepton pair and an opposite-sign tau is required in the signal region called SR1  $\tau$ . The three lepton pair combinations considered in SR1  $\tau$  are  $e^\pm e^\pm$ ,  $e^\pm \mu^\pm$  and  $\mu^\pm \mu^\pm$ . Although the same-sign requirement on the leptons largely suppresses contribution from  $Z$  decays (roughly 95%), the lepton charge can sometimes be mis-measured for high  $p_T$  electrons, which is so-called charge flip effect. In order to reject the  $Z \rightarrow e^\pm e^\pm$  contribution due to the charge flip effect, the invariant mass of the  $ee$  pairs is calculated. If  $m_{ee}$  is measured to be

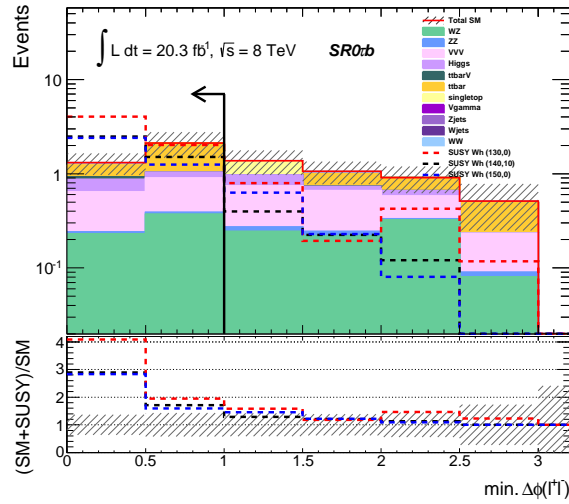


Figure 5.10: Difference of the azimuthal angle between opposite sign leptons. The selection  $\Delta\phi_{\ell\ell} \leq 1.0$  has been applied for SR0 $\tau$ b.

within  $m_Z \pm 10\text{GeV}$ , the event is vetoed. Figure 5.11 shows the invariant mass for same-sign two leptons  $m_{\ell\ell}$  before and after  $Z(ee)$  veto. This selection can suppress 75% of the  $Z(ee)$  contribution, while the signal suppression is only  $\sim 5\%$ . The missing transverse momentum requirement of  $E_T^{\text{miss}} > 50\text{GeV}$  also contribute to suppress the  $Z$ +jets contamination. As well as the other regions, the region with  $E_T^{\text{miss}} < 50\text{GeV}$  is reserved for validation.

The production of SUSY tends to need higher energy comparing to the SM background. In this case, the scalar sum of the transverse momenta tends to be high. This signal region requires the sub-leading lepton  $p_T > 20\text{GeV}$  and the scalar sum of the  $p_T$  for the leading lepton and the sub-leading lepton  $\sum p_T(\ell) > 70\text{GeV}$ . These high  $p_T$  requirement operates as discriminators against  $WZ$  and  $t\bar{t}$ . 80% of  $WZ$  and  $t\bar{t}$  are suppressed, while the signal samples decrease to  $\sim 50\%$ .

It is difficult to distinguish which lepton in the same-sign lepton pair is from Higgs ( $h \rightarrow \tau\tau$ ), then it is assumed that the leading lepton is from  $W$  boson and the sub-leading lepton is from Higgs. If the opposite-sign lepton and tau came from Higgs, their mass should be less than the Higgs mass (125 GeV) because the reconstructed tau and the lepton from a tau should have lower momenta due to the existence of the neutrinos from taus. Thus the requirement of the mass of the sub-leading lepton and the tau less than 120 GeV would suppress the background from the non-Higgs decays.

**Signal Region for two taus mode** The signal region with one lepton and two hadronic taus is optimised for the SUSY decaying via  $Wh$  ( $h \rightarrow \tau_h\tau_h$ ) mode. Although this mode has highest branching ratio, it also has the highest SM contribution due to the hadronic taus.

The  $E_T^{\text{miss}}$  selection is optimised to reduce  $W$ +jets and  $Z(\tau\tau)$ +jets contamination. Since the hadronic taus are reconstructed from jets, the mis-tagged taus have much contribution in this region. Thus the slightly higher  $E_T^{\text{miss}}$  ( $> 60\text{GeV}$ ) than the other regions is required. This selection suppresses 97% of the  $Z$ +jets, 88% of the  $W$ +jets, and 60% of the  $WZ$  and  $t\bar{t}$  contributions.

In this region, opposite-sign tau pair is required to reconstruct Higgs mass. Ideally the mass of the tau lepton pair should be in Higgs mass window, however, the observed mass peak is slightly lower than the



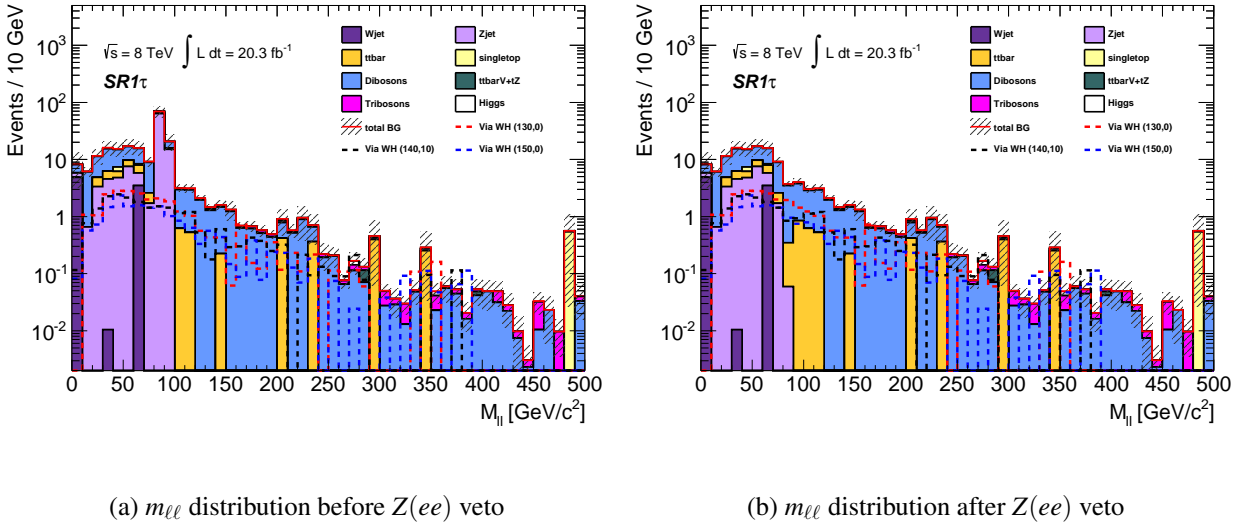


Figure 5.11: The invariant mass for the same-sign leptons before (a) and after (b) applying  $Z(ee)$  veto.

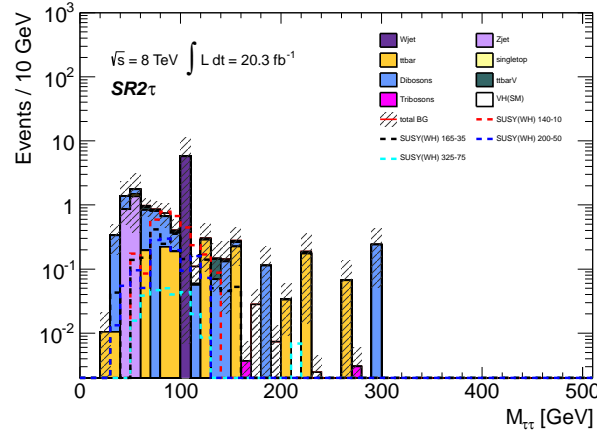


Figure 5.12:  $m_{\tau\tau}$  distribution in  $SR2\tau$  without  $m_{\tau\tau}$  requirement. The Higgs mass window is defined as  $m_{\tau\tau}$  in the mass range from 70 GeV to 120 GeV, which can suppress the SM background processes.

Higgs boson mass value ( $\sim 125$  GeV), as shown in Fig. 5.12. This shift is caused by the missing neutrinos from the tau decays in the mass reconstruction. According to the Fig. 5.12, the redefined Higgs mass window 70–120 GeV requirement is reasonable to suppress the SM background. The mass requirement decreases the SM backgrounds to 21%, whereas it keeps  $\sim 67\%$  of the signals.

From the same reason as the one for signal region  $SR1\tau$ , the scalar sum of  $p_T$  of the two hadronic taus tends to be larger than the SM background contribution because the heavy particles would decay and result in particles with large momentum in final states for SUSY signals. Figure 5.13 shows the distribution of the scalar sum of  $p_T$  of the two hadronic taus. A moderate requirement on the sum of  $p_T$  of the two taus of  $\sum p_T(\tau) > 110$  GeV discriminates well against the SM processes (88% decrease).

The signal yields for the signal regions for  $Wh$  channel are shown in Tab. 5.5. Figures 5.14 show the expected numbers of events in the corresponding signal regions. All signal regions are sensitive to the low mass region of  $Wh$  channel.

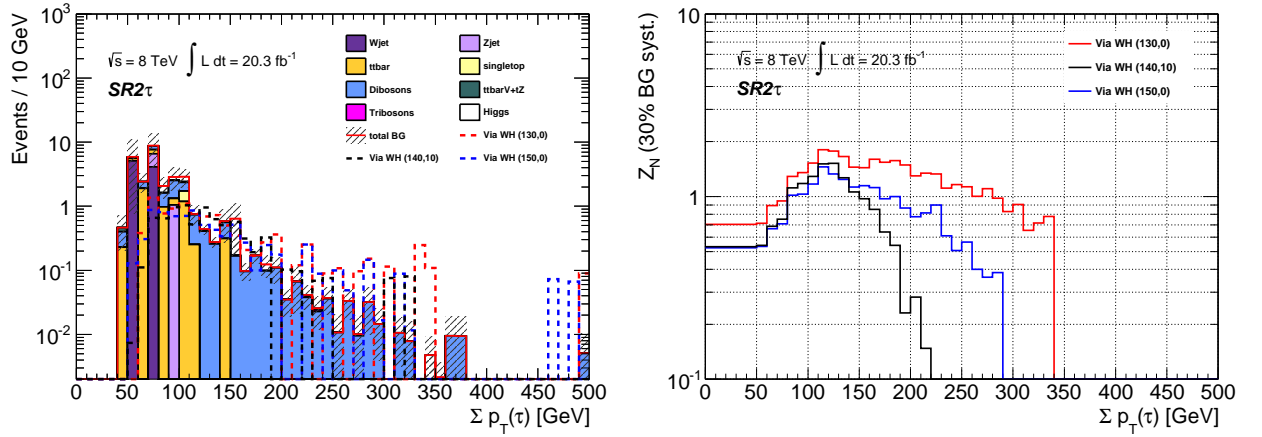
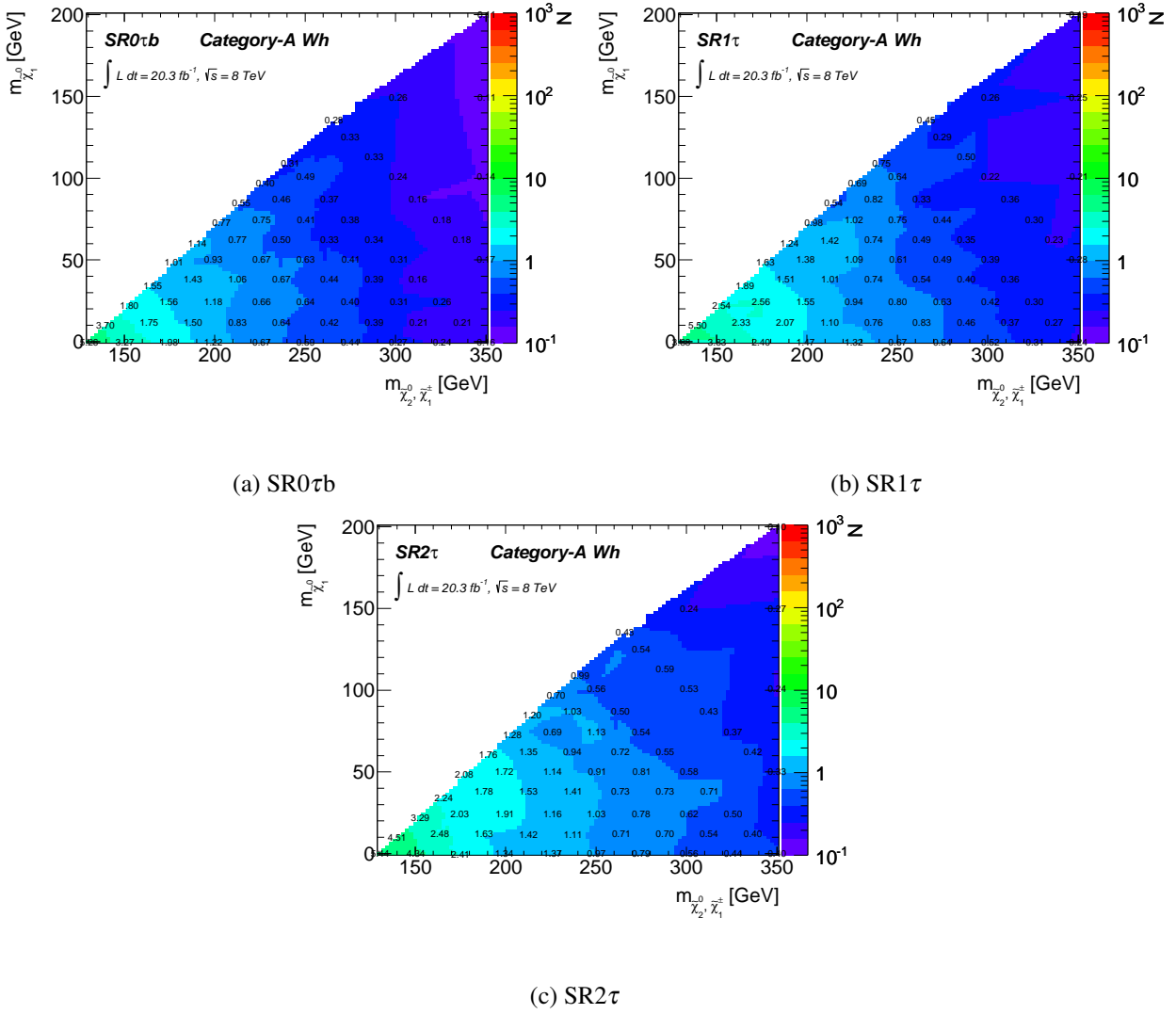
(a) Distribution of the sum of  $p_T$  of the two taus(b)  $Z_N$  variation for the  $\Sigma p_T(\tau)$  selection

Figure 5.13: Distribution and optimisation of the sum of  $p_T$  of the taus. The vertical axis of (b) is  $Z_N$  value with the assumption of the 30% background uncertainty. The optimal selection is  $\Sigma p_T > 110\text{GeV}$ . This selection reduces 88% background processes.

Table 5.5: Numbers of events for the SM processes of the  $SR0\tau b$ ,  $SR1\tau$  and  $SR2\tau$ . Estimates are based on the MC-only and uncertainties are statistical only.

Samples	$SR0\tau b$	$SR1\tau$	$SR2\tau$
$WZ$	$0.7\pm 0.2$	$4.6\pm 0.3$	$2.1\pm 0.2$
$ZZ$	$0.0\pm 0.0$	$0.4\pm 0.0$	$0.1\pm 0.0$
$t\bar{t}+V$	$0.2\pm 0.2$	$0.1\pm 0.1$	$0.0\pm 0.0$
$VVV$	$1.0\pm 0.1$	$0.5\pm 0.0$	$0.0\pm 0.0$
SM Higgs	$0.5\pm 0.1$	$0.3\pm 0.1$	$0.1\pm 0.0$
$\Sigma$ SM irred.	$2.4\pm 0.3$	$5.9\pm 0.4$	$2.3\pm 0.2$
$t\bar{t}$	$1.3\pm 0.3$	$0.6\pm 0.4$	$0.6\pm 0.4$
single $t$	$0.0\pm 0.0$	$0.0\pm 0.0$	$0.0\pm 0.0$
$WW$	$0.1\pm 0.1$	$0.1\pm 0.0$	$0.2\pm 0.1$
$Z$ +jets	$0.0\pm 0.0$	$0.0\pm 0.0$	$0.0\pm 0.0$
$W$ +jets	$0.0\pm 0.0$	$0.0\pm 0.0$	$0.0\pm 0.0$
$V+\gamma$	$0.3\pm 0.3$	$1.5\pm 0.9$	$0.0\pm 0.0$
$VV$ (hadronic)	$0.0\pm 0.0$	$0.0\pm 0.0$	$0.5\pm 0.5$
$\Sigma$ SM red.	$1.7\pm 0.4$	$2.2\pm 1.0$	$1.2\pm 0.6$
$\Sigma$ SM	$4.1\pm 0.5$	$8.1\pm 1.0$	$3.5\pm 0.6$
SUSY via Wh(140,10)	$3.7\pm 0.6$	$5.5\pm 0.8$	$4.5\pm 0.6$
SUSY via Wh(152.5,22.5)	$1.8\pm 0.4$	$2.5\pm 0.4$	$3.3\pm 0.5$

Figure 5.14: Expected numbers of signal events for SR0 $\tau b$  (a), SR1 $\tau$  (b) and SR2 $\tau$  (c).

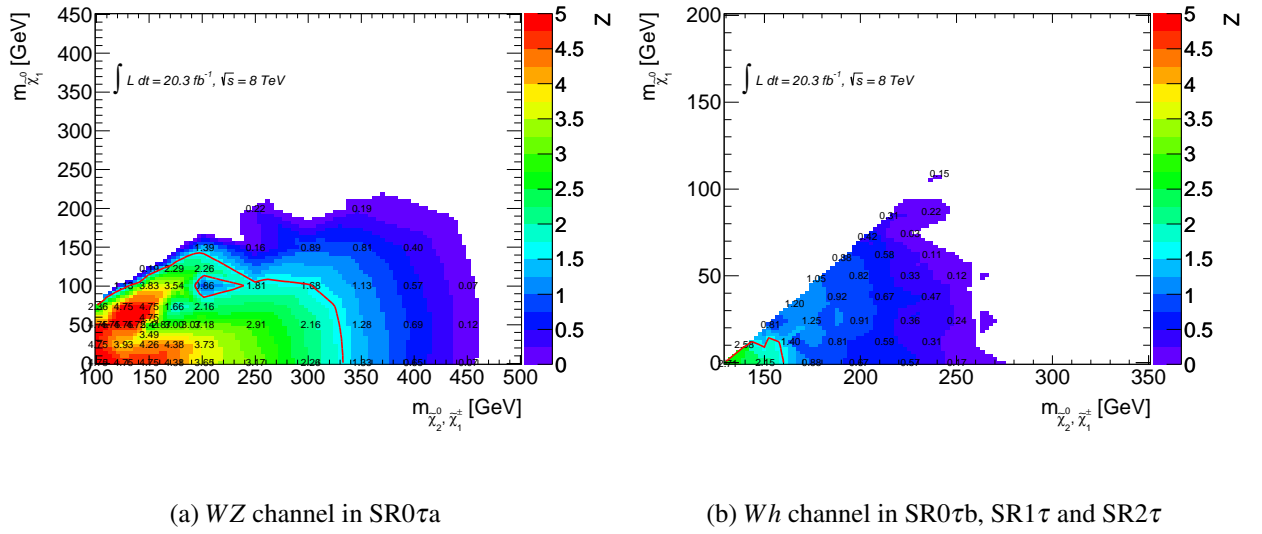


Figure 5.15: Significance for the  $WZ$  channel (a) and  $Wh$  channel (b). These are calculated only with MC samples in the corresponding signal regions of Category-A. The red lines represent the expected exclusion limits with 95% confidence level.

### 5.3.3 Sensitivity for the target scenarios

The sensitivities for the  $WZ$  and  $Wh$  channels with the MC-only estimates are shown in Fig. 5.15a and Fig. 5.15b, respectively.

In Fig. 5.15a, the signal regions in SR0 $\tau$ a are statistically combined. The sensitivity reaches the NLSP mass of approximately 330 GeV and the LSP mass of approximately 100 GeV.

In Fig. 5.15b, the signal regions SR0 $\tau$ b, SR1 $\tau$  and SR2 $\tau$  are statistically combined. The sensitivity reaches the NLSP mass of approximately 150 GeV and the LSP mass of approximately 20 GeV.

## 5.4 Signal Regions for Category-B

The Category-B analysis targets the compressed SUSY decays via  $WZ$ -mediated scenario, especially the mass difference between  $\tilde{\chi}_1^\pm/\tilde{\chi}_2^0$  and  $\tilde{\chi}_1^0$  of  $\Delta m_{\tilde{\chi}_2^0, \tilde{\chi}_1^0} < 50 \text{ GeV}$ . Though  $\tilde{\chi}_1^\pm$  and  $\tilde{\chi}_2^0$  as NLSPs are directly produced by  $pp$ -collision, they cannot decay via on-shell  $W$  and  $Z$  anymore due to their small mass difference. The leptons in final states would have low  $p_T$  comparing to the scenarios with the mass difference of greater than  $Z$  mass. Thus the Category-B analysis uses the lower  $p_T$  requirement in order to keep the acceptance. The tri-lepton triggers are used in this category. The requirement is defined as the leptons' transverse momenta of  $p_T > 7$  and  $5 \text{ GeV}$  for electrons and muons, respectively. In the low  $p_T$  lepton region, the fake background, such as  $W/Z$ +jets, has been further reduced by applying the tighter isolation criteria on the second and third leading lepton as well as the requirement of the high missing transverse momentum, as described in Chap. 3.

The MC samples are prepared for this analysis with the mass differences  $\Delta m_{\tilde{\chi}_2^0, \tilde{\chi}_1^0}$  of 12.5 GeV and 25 GeV. The signal regions are subdivided into two regions in order to maximise the optimisation for each mass difference. The signal region targeting the  $\Delta m_{\tilde{\chi}_2^0, \tilde{\chi}_1^0} = 12.5 \text{ GeV}$  is labelled 'a,' while the other targeting the  $\Delta m_{\tilde{\chi}_2^0, \tilde{\chi}_1^0} = 25 \text{ GeV}$  is labelled 'b.'

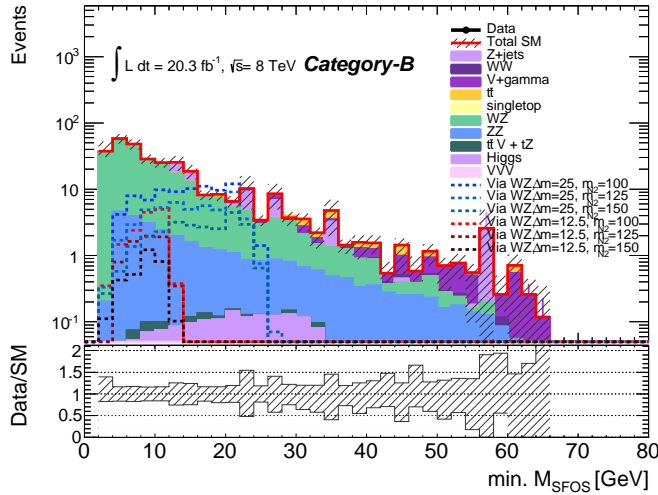


Figure 5.16: The minimum mass of the SFOS lepton pair. The filled histogram represents the SM background distribution, and the dashed lines show the distribution for the corresponding signal samples. The cut-off of the  $\min. m_{\text{SFOS}}$  can be seen in this figure.

In the pre-selection, the SFOS mass threshold is down to 2 GeV, as noted in Sec. 3.8. Due to this, the low mass resonances such as  $J/\psi$  or  $\Upsilon$  contamination greatly increase. To reduce  $J/\psi$  resonances, a veto of the events with minimum mass of the SFOS pair smaller than 4 GeV has been applied. For the  $\Upsilon$  resonances, events with the mass of the SFOS pair which is closest to 9.4 GeV within 1 GeV of the  $\Upsilon$  mass (9.4 GeV) are vetoed.

The most powerful variable for this optimisation is the minimum of the mass for SFOS lepton pair,  $\min. m_{\text{SFOS}}$ , which is related to the mass difference  $\Delta m_{\tilde{\chi}_2^0, \tilde{\chi}_1^0}$ , as

$$\min. m_{\text{SFOS}} \leq \Delta m_{\tilde{\chi}_2^0, \tilde{\chi}_1^0}, \quad (5.4)$$

because the  $\min. m_{\text{SFOS}}$  composes the mass of off-shell  $Z$  from  $\tilde{\chi}_2^0$  decay. Figure 5.16 shows the minimum of  $m_{\text{SFOS}}$  after the event pre-selection. The cut-off of the  $\min. m_{\text{SFOS}}$  depends only on the mass difference  $\Delta m_{\tilde{\chi}_2^0, \tilde{\chi}_1^0}$ . Therefore the ‘a’ and ‘b’ regions should require  $m_{\text{SFOS}}$  less than the mass differences 12.5 GeV and 25 GeV, respectively.

The signal regions of Category-B are summarised in Tab. 5.6. There are two criteria for the scenario named SRSL and SRISR. SRISR requires an Initial State Radiation (ISR)-like jet, which is defined as the leading jet with  $p_T > 50 \text{ GeV}$ , in order to expand the parameter space. SRSL is the standard selection for the Category-B, while it requires jet  $p_T < 50 \text{ GeV}$  to keep orthogonality with SRISR. The detail of the selections will be found in following subsections Sec. 5.4.1 and 5.4.2.

#### 5.4.1 Signal Regions with three low $p_T$ leptons

SRSL is optimised using several kinematic variables such as the tri-lepton invariant mass ( $m_{\ell\ell\ell}$ ) and the transverse mass ( $m_T$ ) of the lepton not forming a SFOS pair with the minimum  $m_{\text{SFOS}}$ . They have reduced di-boson background processes, in particular  $WZ$ . The  $E_T^{\text{miss}}$  threshold is sensitive for reducing fake backgrounds such as  $Z$ +jets process. The threshold of  $E_T^{\text{miss}}$  is set  $E_T^{\text{miss}} > 50 \text{ GeV}$  for both ‘a’ and ‘b’ regions. This  $E_T^{\text{miss}}$  requirement contributes to reduce 80% of the  $Z$ +jets process.

Table 5.6: Summary of the signal regions for Category-B.

Singal Region	SRSLa	SRSLb	SRISRa	SRISRB
Flavour/sign	$\ell^+\ell^-\ell'(\ell')$	$\ell^+\ell^-\ell'(\ell')$	$\ell^+\ell^-\ell'(\ell')$	$\ell^+\ell^-\ell'(\ell')$
$b$ -tagged jet	veto	veto	veto	veto
$\Upsilon$ selection	veto	veto	veto	veto
$E_T^{\text{miss}}$ [GeV]	$> 50$	$> 50$	$> 50$	$> 50$
$p_T(\ell)$	$< 30$	$< 30$	$< 30$	$< 30$
$p_T(1^{\text{st}} \text{ jet})$ [GeV]	$< 50$	$< 50$	$> 50$	$> 50$
$m_{\ell\ell\ell}$ [GeV]	30–60	30–60	–	$< 70$
min. $m_{\text{SFOS}}$ [GeV]	4–15	15–25	5–15	15–25
$m_T$ [GeV]	$< 20$	–	–	–
$\Delta\phi(E_T^{\text{miss}}, 1^{\text{st}} \text{ jet})$	–	–	$> 2.7$	–
$\Delta\phi(E_T^{\text{miss}}, 3\ell)$	–	–	–	$< 2.2$
$p_T(\ell)/p_T(j)$	–	–	$< 0.2$	–
Target $\Delta m(\tilde{\chi}_2^0, \tilde{\chi}_1^0)$	12.5 GeV	25 GeV	12.5 GeV	25 GeV

The signal yields are shown in Tab. 5.7. The expected numbers of events for the signal samples are shown in Figs. 5.17. In SRSLa, there are a few events of the  $\Delta m_{\tilde{\chi}_2^0, \tilde{\chi}_1^0} = 12.5$  GeV samples and the region also have sensitivity to the lightest region of the  $\Delta m_{\tilde{\chi}_2^0, \tilde{\chi}_1^0} = 25$  GeV scenarios. In SRSLb, there are no events of the  $\Delta m_{\tilde{\chi}_2^0, \tilde{\chi}_1^0} = 12.5$  GeV samples and many events of the  $\Delta m_{\tilde{\chi}_2^0, \tilde{\chi}_1^0} = 25$  GeV and 50 GeV scenarios. The  $\Delta m_{\tilde{\chi}_2^0, \tilde{\chi}_1^0} = 12.5$  GeV samples are reduced by mainly  $\Upsilon$  veto, thus the low sensitivity for the region is obtained.

### 5.4.2 Signal Regions with three low $p_T$ leptons and ISR jets

The ISR jets regions, SRISR, have several ISR jet related variables.

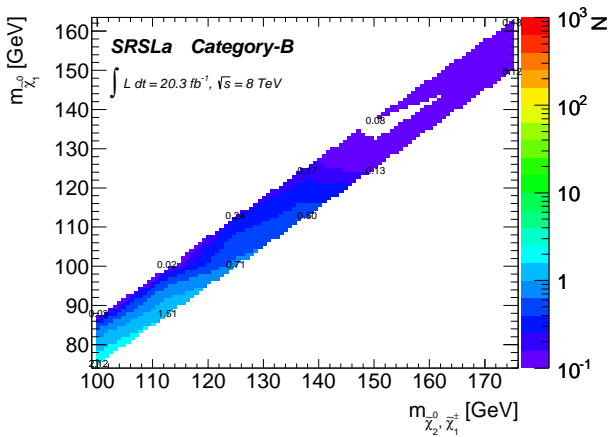
The ISR jet is required to satisfy  $p_T > 50$  GeV. As the  $E_T^{\text{miss}}$  magnitude is strongly correlated with the ISR jet  $p_T$ ,  $E_T^{\text{miss}}$  is also required to be above 50 GeV. The difference of the azimuthal angle  $\Delta\phi$  between the  $E_T^{\text{miss}}$  and the leading jet or the three leptons system are used in the definition of the signal regions. Figure 5.18 shows the schematic diagram of the transverse plane ( $xy$  plane) for the beam pipe with the event with ISR jet and  $\tilde{\chi}_1^\pm \tilde{\chi}_1^0$  direct production. If an ISR jet is produced, the products from the SUSY particle decays should be boosted to the opposite side of the ISR jet. From the considerations,  $\Delta\phi_{E_T^{\text{miss}}, 1^{\text{st}} \text{ jet}}$  and  $\Delta\phi_{E_T^{\text{miss}}, \Sigma\ell}$  are thought to be good discriminators against  $WZ$ ,  $ZZ$  and  $Z$ +jets. Figure 5.19 shows the distributions of the  $\Delta\phi_{E_T^{\text{miss}}, 1^{\text{st}} \text{ jet}}$  and the  $\Delta\phi_{E_T^{\text{miss}}, \Sigma\ell}$  for the events which passed the pre-selection criteria. The SUSY signals have less dependency on the  $\Delta\phi_{E_T^{\text{miss}}, \Sigma\ell}$ , whilst the backgrounds have. To keep the number of events, SRISRa, which targets the mass difference  $\Delta m_{\tilde{\chi}_2^0, \tilde{\chi}_1^0} = 12.5$  GeV, requires only  $\Delta\phi_{E_T^{\text{miss}}, 1^{\text{st}} \text{ jet}} > 2.7$ , while SRISRB, which targets the mass difference  $\Delta m_{\tilde{\chi}_2^0, \tilde{\chi}_1^0} = 25$  GeV, requires only  $\Delta\phi_{E_T^{\text{miss}}, \Sigma\ell} < 2.2$ .

Furthermore, for the SRISRa, the ratio of the leading lepton to the leading jet  $p_T$  is a good discriminator which highlights the behaviour of the soft leptons and ISR jets for the compressed signal points. Thus an upper cut of  $p_T(\ell_1)/p_T(j_1) < 0.2$  is placed on this ratio, which is effective in removing the diboson and  $t\bar{t}$  contribution. These ISR-related variables,  $\Delta\phi_{E_T^{\text{miss}}, 1^{\text{st}} \text{ jet}}$ ,  $\Delta\phi_{E_T^{\text{miss}}, \Sigma\ell}$  and  $p_T(\ell_1)/p_T(j_1)$ , reduces  $\sim 50\%$  of the background and  $\sim 30\%$  of the signals.

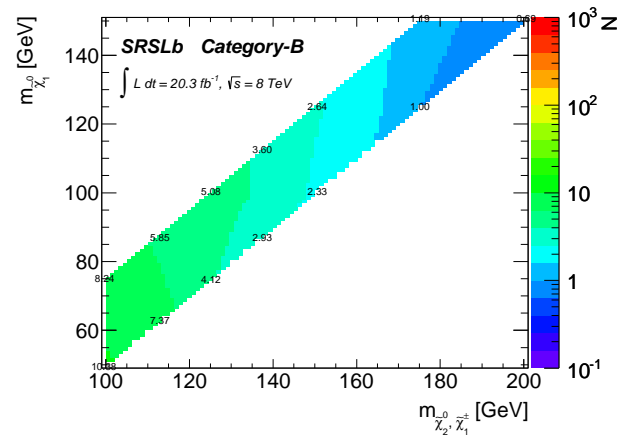
The yields in SRISR is shown in Tab. 5.8. The expected numbers of events for the signal samples are

Table 5.7: Expected yields in SRSL. Estimates are based on the MC-only and uncertainties are statistical only.

Samples	SRSLa	SRSLb
WZ	0.59±0.16	5.02±0.53
ZZ	0.23±0.02	0.66±0.04
$t\bar{t}+V$	0.00±0.00	0.01±0.01
VVV	0.00±0.00	0.02±0.01
Higgs	0.00±0.00	0.04±0.01
$\Sigma$ SM irred.	0.83±0.16	5.75±0.53
$t\bar{t}$	0.00±0.00	0.00±0.00
single $t$	0.00±0.00	0.10±0.10
WW	0.00±0.00	0.00±0.00
Z+jets	0.00±0.00	1.74±1.47
W+jets	0.00±0.00	0.00±0.00
V+ $\gamma$	0.00±0.00	0.14±0.14
J/ $\psi$	0.00±0.00	0.05±0.05
$\Upsilon$	0.00±0.00	0.01±0.01
low-mass DY	0.00±0.00	0.00±0.00
$\Sigma$ SM red.	0.00±0.00	2.03±1.48
$\Sigma$ SM	0.83±0.16	7.78±1.57
SUSY via WZ (100,87.5)	0.03±0.03	0.00±0.00
SUSY via WZ (100,75)	2.12±1.07	8.24±2.03
SUSY via WZ (125,100)	0.71±0.42	5.08±1.13



(a) SRSLa



(b) SRSLb

Figure 5.17: Expected numbers of events in SRSLa (a) and SRSLb (b).

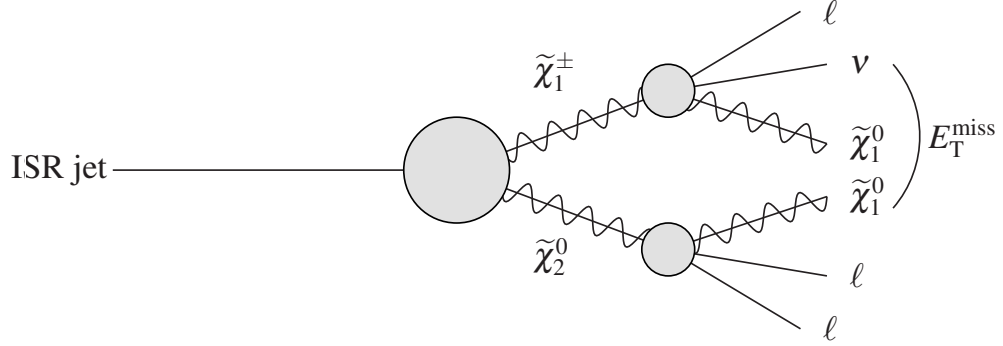
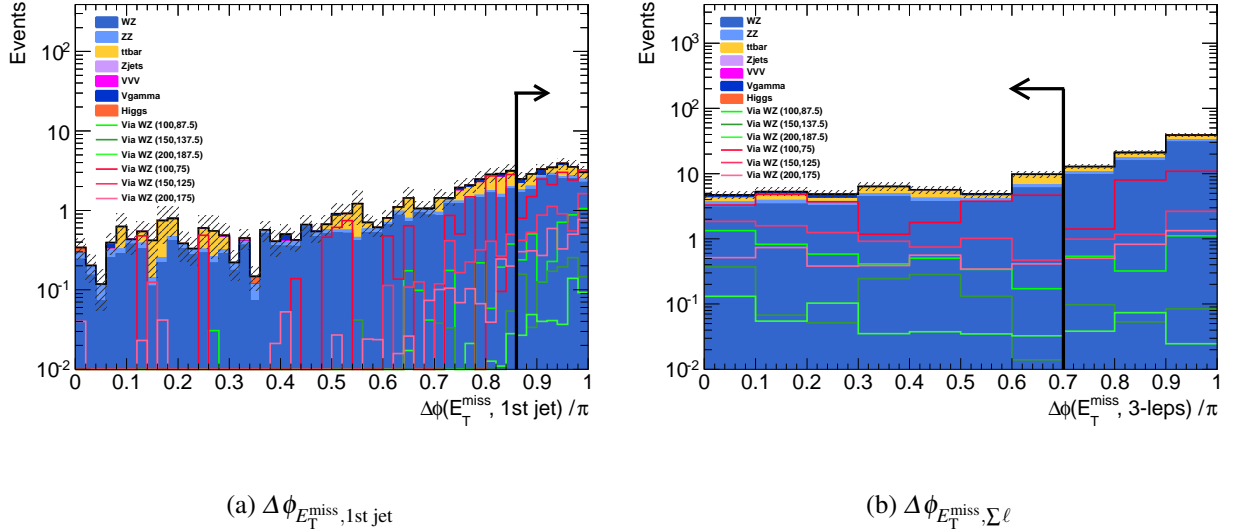
Figure 5.18: Schematic diagram in the transverse plane of the  $pp \rightarrow \text{ISR} + \tilde{\chi}_1^\pm \tilde{\chi}_2^0 (\rightarrow \ell \ell \nu + \tilde{\chi}_1^0 \tilde{\chi}_1^0)$ .

Figure 5.19: Distributions for the ISR related variables after the pre-selection. The difference of the azimuthal angle between  $E_T^{\text{miss}}$  and 1st jet  $\Delta\phi_{E_T^{\text{miss}}, 1\text{st jet}}$  (a) and the difference of the azimuthal angle between  $E_T^{\text{miss}}$  and three lepton system  $\Delta\phi_{E_T^{\text{miss}}, \Sigma\ell}$  (b) are shown. The red lines are the distributions of the SUSY decaying via  $WZ$ -mediated scenario with the mass difference  $\Delta m_{\tilde{\chi}_2^0, \tilde{\chi}_1^0} = 25 \text{ GeV}$  and the green lines are the distributions of the SUSY decaying via  $WZ$ -mediated scenario with the mass difference  $\Delta m_{\tilde{\chi}_2^0, \tilde{\chi}_1^0} = 12.5 \text{ GeV}$ .



Table 5.8: Expected yields in SRISR. Estimates are based on the MC-only and uncertainties are statistical only.

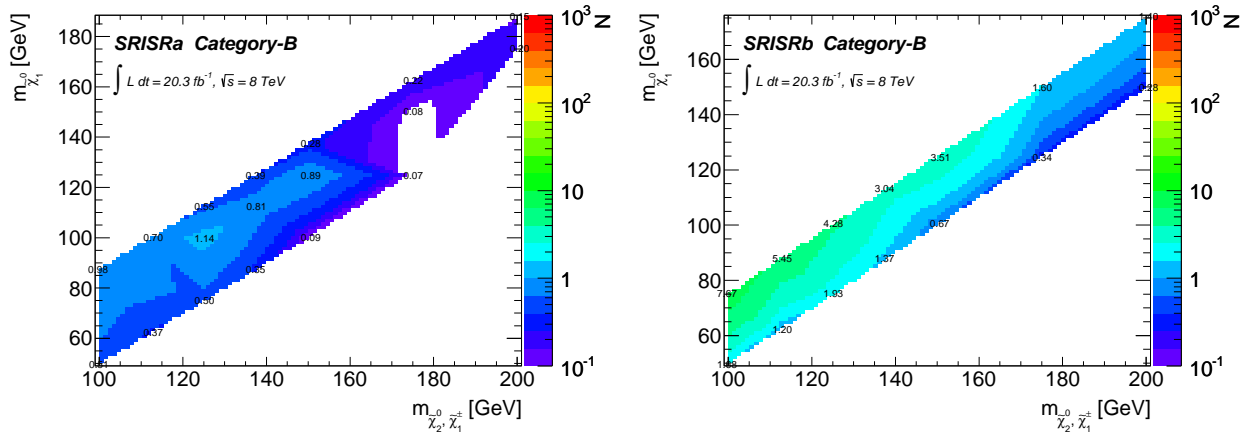
Samples	SRISRa	SRISRb
<i>WZ</i>	0.54±0.17	1.57±0.31
<i>ZZ</i>	0.02±0.01	0.10±0.02
<i>t<math>\bar{t}</math>+V</i>	0.01±0.01	0.01±0.01
<i>VVV</i>	0.00±0.00	0.00±0.00
Higgs	0.00±0.00	0.03±0.01
$\Sigma$ SM irred.	0.58±0.17	1.71±0.31
<i>t<math>\bar{t}</math></i>	0.00±0.00	0.00±0.00
single <i>t</i>	0.00±0.00	0.00±0.00
<i>WW</i>	0.00±0.00	0.03±0.03
<i>Z+jets</i>	0.00±0.00	0.00±0.00
<i>W+jets</i>	0.00±0.00	0.00±0.00
<i>V+<math>\gamma</math></i>	0.00±0.00	0.00±0.00
<i>J/<math>\psi</math></i>	0.00±0.00	0.00±0.00
$\Upsilon$	0.00±0.00	0.00±0.00
low-mass DY	0.00±0.00	0.00±0.00
$\Sigma$ SM red.	0.00±0.00	0.03±0.03
$\Sigma$ SM	0.58±0.17	1.74±0.31
SUSY via <i>WZ</i> (100,87.5)	0.98±0.38	0.00±0.00
SUSY via <i>WZ</i> (100,75)	0.00±0.00	7.67±1.93
SUSY via <i>WZ</i> (125,100)	1.14±0.52	4.28±1.03

shown in Figs. 5.20. In SRISRa, there are a few events of the  $\Delta m_{\tilde{\chi}_2^0, \tilde{\chi}_1^0} = 12.5$  GeV samples. In SRISRb, there are no events of the  $\Delta m_{\tilde{\chi}_2^0, \tilde{\chi}_1^0} = 12.5$  GeV samples and many events of the  $\Delta m_{\tilde{\chi}_2^0, \tilde{\chi}_1^0} = 25$  GeV samples. The  $\Delta m_{\tilde{\chi}_2^0, \tilde{\chi}_1^0} = 12.5$  GeV samples are reduced by mainly  $\Upsilon$  veto, as well as the SRSL analysis. Thus it is difficult to obtain high sensitivity for the  $\Delta m_{\tilde{\chi}_2^0, \tilde{\chi}_1^0} = 12.5$  GeV scenarios.

### 5.4.3 Sensitivity for the target scenarios

The sensitivity which is calculated by the  $Z_N$  method combining all of the signal region in Category-B is shown in Fig. 5.21. The calculation is performed using all of the background MC samples which can be considered, except the *J/ $\psi$*  and  $\Upsilon$  samples. The *J/ $\psi$*  and  $\Upsilon$  samples have large uncertainties due to the low statistics.

The maximum significance is observed at the point of  $(m_{\tilde{\chi}_1^\pm, \tilde{\chi}_2^0}, m_{\tilde{\chi}_1^0}) = (100 \text{ GeV}, 75 \text{ GeV})$  and the sensitivity for the compressed *WZ* channel is expected to extend to the mass point of  $(m_{\tilde{\chi}_1^\pm, \tilde{\chi}_2^0}, m_{\tilde{\chi}_1^0}) = (130 \text{ GeV}, 100 \text{ GeV})$ .



(a) SRISRa

(b) SRISRb

Figure 5.20: Expected numbers of events in SRISRa (a) and SRISRb (b).

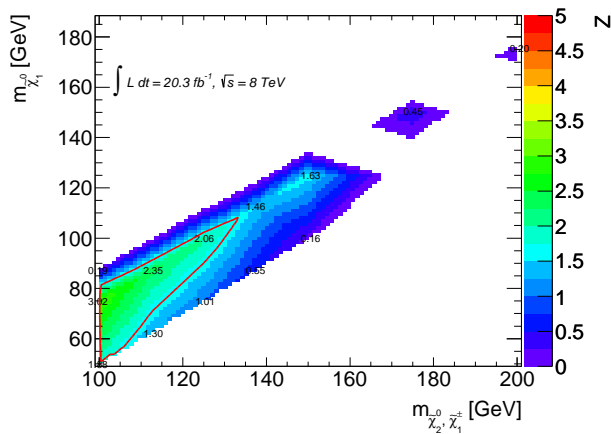


Figure 5.21: Significance for the  $WZ$  compressed scenario. This is calculated only with MC samples by the combination of all signal regions of Category-B.



## Chapter 6

# Background Estimation

Estimation for the contribution of the background processes is the most important part of the analysis. The collision of the high energy protons from the LHC produces many particles. Especially it creates huge amount of hadrons. The signal processes which should be observed are mainly from those with high energy and have three leptons which are from electroweak processes, thus the hadronic processes can be suppressed comparing to the other analyses. Nevertheless, the hadronisation processes can affect such signal processes due to the misidentification of leptons from hadrons with a low probability. Therefore we should consider two sorts of the background sources as following description.

The first one is simply a process which includes at least three ‘real’ leptons. ‘Real’ in this description means the event signature that a true lepton is reconstructed as a lepton. This three-lepton production process cannot be distinguished from the signal processes by the number and sorts of the particles in final states. For this reason, it is called irreducible background. The irreducible background follows the framework of the electroweak theory, which can be calculated by the MC simulation with small uncertainties. Thus the simulated samples can be used to estimate the irreducible background.

The other one is the background with at least one misidentified lepton. The amount of this background can be varied by the condition on the lepton selection criteria, thus it is called reducible background. Many hadronic processes can compose a final state with three leptons and missing transverse energy due to a misidentification. Furthermore, the processes have large cross-sections and large theory uncertainties from QCD. Thus it is not practical to use MC simulation for estimating this background as there are large uncertainties in simulating the misidentification processes, and absolute values of the cross sections. Hence the analysis uses a data-driven method. By using this method, two uncertainties above can be suppressed. The method will be discussed in Sec. 6.2.

### 6.1 Monte Carlo simulation, for well-known background

The background estimation based on Monte Carlo simulated samples are used for irreducible backgrounds. Irreducible background is defined as the Standard Model processes which are indistinguishable from signal due to their same number of leptons in final states as the signal processes. The leptons should be produced from the weak interactions, where the coupling strength and interaction kinematics can be precisely predicted by the Monte Carlo simulation.

The irreducible backgrounds of these analyses have at least three leptons in final states. The Standard Model diboson ( $WZ, ZZ$ ), triboson ( $WWW, WZZ, ZZZ$ ),  $t\bar{t}$ -bosons and the Standard Model Higgs ( $ggH, VH, VBF$  Higgs) production processes are considered as the irreducible backgrounds.

The Monte Carlo samples contain the same reconstructed objects as the real data, thus we can apply same selection criteria as the real data.

Estimation results for the signal regions are shown in Tabs. 5.4, 5.5, 5.7 and 5.8 in Chap. 5.

## 6.2 Estimation for reducible background

The matrix method is the methods to estimate the background contribution of the events including the objects which were mis-identified as leptons.

Particle detectors detect the charged or neutral particles and identify the types of the particles. Even though the detectors are designed to best perform the particle identification, certain fraction of leptons can be mis-identified. Mis-identified leptons mainly come from jets. The method called *matrix method* (MM) utilises the characteristics. Since all of the lepton-like objects have some level of probability to be mis-identified leptons, the matrix method should in principle be applied for all the *fakeable* objects in each event. In this analysis, however, only two objects per event are applied this method for the sake of simplicity. The principle of this method will be described in following sections.

### 6.2.1 Principle of the matrix method

In principle, jets should have different features from real leptons thus the ‘tight’ selection for each object can remove the mis-identified contributions. Applying this selection, however, is not stringent enough to separate real leptons from the mis-identified leptons completely. In the  $pp$  collision at the LHC, the dominant process is the gluon-gluon collision, so that the events would have many reconstructed objects from strong interaction. Precise estimation of the QCD contribution is difficult with the Monte Carlo simulation. The MC uncertainty of QCD is large due to poor prediction for the PDF in LHC and that the perturbation theory breaks down in the low momenta region. This leads QCD mis-modeling when the estimation is implemented with the MC simulation.

#### 6.2.1.1 Simple matrix method for one fake object

The probabilities that real leptons and mis-identified leptons pass the selection are called ‘real efficiency’ and ‘fake rate’ respectively. The numbers of lepton-like objects passed and failed tight selection  $N_T, N_L$  are expressed as following equations with the real efficiency  $\varepsilon$  and the fake rate  $f$  :

$$\begin{cases} N_T = \varepsilon N_R + f N_F \\ N_L = (1 - \varepsilon) N_R + (1 - f) N_F \end{cases}, \quad (6.1)$$

where  $N_R$  and  $N_F$  are the numbers of real and mis-identified (fake) objects. Figure 6.1 illustrates the relation between the real and fake objects.

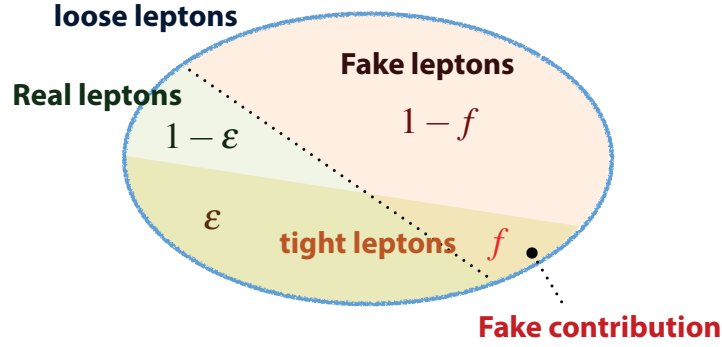


Figure 6.1: Relation among the real leptons, the fake leptons and the leptons passed and failed the tight selection. The figure shows the set of the “loose” leptons surrounded with the blue ellipse, the fake and the real lepton contribution in the “loose” lepton, and the “tight” lepton contribution in “loose” leptons. The fake contribution which should be considered corresponds to the region where the lepton is categorised “tight” and fake.

By using the matrix for these equation, we can get it easily:

$$\begin{pmatrix} N_T \\ N_L \end{pmatrix} = \begin{pmatrix} \varepsilon & f \\ 1 - \varepsilon & 1 - f \end{pmatrix} \begin{pmatrix} N_R \\ N_F \end{pmatrix} = \mathcal{M} \begin{pmatrix} N_R \\ N_F \end{pmatrix}. \quad (6.2)$$

The matrix  $\mathcal{M}$  is called ‘the fake matrix’ in this thesis. The goal of this method is to know the number of fake objects ( $N_F$ ). In the case that the fake matrix is  $2 \times 2$  matrix, the inverse of the fake matrix can be written as

$$\mathcal{M}^{-1} = \frac{1}{\varepsilon - f} \begin{pmatrix} 1 - f & -f \\ \varepsilon - 1 & \varepsilon \end{pmatrix} \quad (6.3)$$

and Eq. (6.2) should be rewritten as follows:

$$\begin{pmatrix} N_R \\ N_F \end{pmatrix} = \mathcal{M}^{-1} \begin{pmatrix} N_T \\ N_L \end{pmatrix}. \quad (6.4)$$

The fake contribution which we like to estimate from the method is the one after the tight selection cut. The  $N_F$  calculated with Eq. (6.4) is the estimated fake contribution just after the baseline lepton cut. The fake contributions after the tight lepton selection could be calculated with the product of  $N_F$  and the fraction  $f$ , which is the probability of the fake leptons to be selected with the tight lepton selection. We set the notation for it  $N_{F \rightarrow T}$ , then,

$$N_{F \rightarrow T} \equiv f N_F = \frac{f}{\varepsilon - f} (\varepsilon N_L - (1 - \varepsilon) N_T). \quad (6.5)$$

In order the formula to be valid,  $(\varepsilon - f)$ , the difference between the real lepton efficiency and the fake rate, should not be close to zero. In the ordinary situation, the fake rate is much smaller than the real efficiency, hence this requirement is fulfilled.

In the discussion so far, we implicitly assumed that only one reconstructed lepton can be fake in each event. It is correct in the case where the number of fake candidate in each event is exactly one.

In order to handle multiple fake contributions, the notation should be simplified. Hence  $(1 - \varepsilon)$  and  $(1 - f)$  are rewritten as follows:

$$\begin{cases} \bar{\varepsilon} = 1 - \varepsilon \\ \bar{f} = 1 - f \end{cases}. \quad (6.6)$$

Then Eq. (6.2) is written simply,

$$\begin{pmatrix} N_T \\ N_L \end{pmatrix} = \begin{pmatrix} \varepsilon & f \\ \bar{\varepsilon} & \bar{f} \end{pmatrix} \begin{pmatrix} N_R \\ N_F \end{pmatrix}. \quad (6.7)$$

This simpler notation helps to understand the matrix method for multiple fake candidates, which is discussed in the next section.

### 6.2.1.2 Matrix method for multiple fake candidates

If we handle more than two fake candidates, it is necessary to consider the fake formulae which takes into account each candidate. In the same manner as the composition of Eq. (6.1), the following equations can be written with the real efficiencies and fake rates as

$$\begin{cases} N_{TT} = \varepsilon_1 \varepsilon_2 N_{RR} + \varepsilon_1 f_2 N_{RF} + f_1 \varepsilon_2 N_{FR} + f_1 f_2 N_{FF} \\ N_{TL} = \varepsilon_1 \bar{\varepsilon}_2 N_{RR} + \varepsilon_1 \bar{f}_2 N_{RF} + f_1 \bar{\varepsilon}_2 N_{FR} + f_1 \bar{f}_2 N_{FF} \\ N_{LT} = \bar{\varepsilon}_1 \varepsilon_2 N_{RR} + \bar{\varepsilon}_1 f_2 N_{RF} + \bar{f}_1 \varepsilon_2 N_{FR} + \bar{f}_1 f_2 N_{FF} \\ N_{LL} = \bar{\varepsilon}_1 \bar{\varepsilon}_2 N_{RR} + \bar{\varepsilon}_1 \bar{f}_2 N_{RF} + \bar{f}_1 \bar{\varepsilon}_2 N_{FR} + \bar{f}_1 \bar{f}_2 N_{FF} \end{cases}. \quad (6.8)$$

In these equations,  $N_{XY}$  ( $X, Y = T, L, R, F$ ) are the number of the events for each composition and  $\varepsilon_i, f_j$  ( $i, j = 1, 2$ ) are the real efficiency and the fake rate respectively. The tag ‘T’ expresses the event that the lepton passed the ‘tight’ selection, ‘L’ expresses the event that the lepton failed the ‘tight’ selection, ‘R’ expresses the event that the lepton is real, and ‘F’ expresses the event the lepton is fake. It is clear that Eq. (6.8) can be rewritten with a matrix,

$$\begin{pmatrix} N_{TT} \\ N_{TL} \\ N_{LT} \\ N_{LL} \end{pmatrix} = \begin{pmatrix} \varepsilon_1 \varepsilon_2 & \varepsilon_1 f_2 & f_1 \varepsilon_2 & f_1 f_2 \\ \varepsilon_1 \bar{\varepsilon}_2 & \varepsilon_1 \bar{f}_2 & f_1 \bar{\varepsilon}_2 & f_1 \bar{f}_2 \\ \bar{\varepsilon}_1 \varepsilon_2 & \bar{\varepsilon}_1 f_2 & \bar{f}_1 \varepsilon_2 & \bar{f}_1 f_2 \\ \bar{\varepsilon}_1 \bar{\varepsilon}_2 & \bar{\varepsilon}_1 \bar{f}_2 & \bar{f}_1 \bar{\varepsilon}_2 & \bar{f}_1 \bar{f}_2 \end{pmatrix} \begin{pmatrix} N_{RR} \\ N_{RF} \\ N_{FR} \\ N_{FF} \end{pmatrix}. \quad (6.9)$$

Total fake contribution to be estimated is the events including leptons passed tight selection, then

$$N_{\text{total Fake}} = N_{RF \rightarrow TT} + N_{FR \rightarrow TT} + N_{FF \rightarrow TT}. \quad (6.10)$$

Note that the  $N_{RR}$  contribution has no fake leptons. Each term that both leptons in the fake events pass the tight selection is easily calculated using their efficiencies and fake rates as

$$\begin{cases} N_{RF \rightarrow TT} = \varepsilon_1 f_2 N_{RF} = \frac{\varepsilon_1 f_2}{(\varepsilon_1 - f_1)(\varepsilon_2 - f_2)} (-\bar{f}_1 \bar{\varepsilon}_2 N_{TT} + \bar{f}_1 \varepsilon_2 N_{TL} + f_1 \bar{\varepsilon}_2 N_{LT} - f_1 \varepsilon_2 N_{LL}) \\ N_{FR \rightarrow TT} = f_1 \varepsilon_2 N_{FR} = \frac{f_1 \varepsilon_2}{(\varepsilon_1 - f_1)(\varepsilon_2 - f_2)} (-\bar{\varepsilon}_1 f_2 N_{TT} + \varepsilon_1 f_2 N_{TL} + \varepsilon_1 \bar{f}_2 N_{LT} - \varepsilon_1 f_2 N_{LL}) \\ N_{FF \rightarrow TT} = f_1 f_2 N_{FF} = \frac{f_1 f_2}{(\varepsilon_1 - f_1)(\varepsilon_2 - f_2)} (\bar{\varepsilon}_1 \bar{\varepsilon}_2 N_{TT} - \bar{\varepsilon}_1 \varepsilon_2 N_{TL} - \varepsilon_1 \bar{\varepsilon}_2 N_{LT} + \varepsilon_1 \varepsilon_2 N_{LL}) \end{cases}. \quad (6.11)$$

The matrix method for three fakes can be calculated in the same manner as the one for two fakes. The

fake matrix  $\mathcal{M}$  for three fakes is  $8 \times 8$  matrix and the equation is as follows:

$$\begin{pmatrix} N_{TTT} \\ N_{TTL} \\ N_{TLT} \\ N_{TLL} \\ N_{LTT} \\ N_{LTL} \\ N_{LLT} \\ N_{LLL} \end{pmatrix} = \begin{pmatrix} \varepsilon_1 \varepsilon_2 \varepsilon_3 & \varepsilon_1 \varepsilon_2 \bar{\varepsilon}_3 & \varepsilon_1 f_2 \varepsilon_3 & \varepsilon_1 f_2 \bar{\varepsilon}_3 & f_1 \varepsilon_2 \varepsilon_3 & f_1 \varepsilon_2 \bar{\varepsilon}_3 & f_1 f_2 \varepsilon_3 & f_1 f_2 \bar{\varepsilon}_3 \\ \varepsilon_1 \varepsilon_2 \bar{\varepsilon}_3 & \varepsilon_1 \varepsilon_2 \bar{\bar{\varepsilon}}_3 & \varepsilon_1 f_2 \bar{\varepsilon}_3 & \varepsilon_1 f_2 \bar{\bar{\varepsilon}}_3 & f_1 \varepsilon_2 \bar{\varepsilon}_3 & f_1 \varepsilon_2 \bar{\bar{\varepsilon}}_3 & f_1 f_2 \bar{\varepsilon}_3 & f_1 f_2 \bar{\bar{\varepsilon}}_3 \\ \varepsilon_1 \bar{\varepsilon}_2 \varepsilon_3 & \varepsilon_1 \bar{\varepsilon}_2 \bar{\varepsilon}_3 & \varepsilon_1 \bar{f}_2 \varepsilon_3 & \varepsilon_1 \bar{f}_2 \bar{\varepsilon}_3 & f_1 \bar{\varepsilon}_2 \varepsilon_3 & f_1 \bar{\varepsilon}_2 \bar{\varepsilon}_3 & f_1 \bar{f}_2 \varepsilon_3 & f_1 \bar{f}_2 \bar{\varepsilon}_3 \\ \varepsilon_1 \bar{\varepsilon}_2 \bar{\varepsilon}_3 & \varepsilon_1 \bar{\varepsilon}_2 \bar{\bar{\varepsilon}}_3 & \varepsilon_1 \bar{f}_2 \bar{\varepsilon}_3 & \varepsilon_1 \bar{f}_2 \bar{\bar{\varepsilon}}_3 & f_1 \bar{\varepsilon}_2 \bar{\varepsilon}_3 & f_1 \bar{\varepsilon}_2 \bar{\bar{\varepsilon}}_3 & f_1 \bar{f}_2 \bar{\varepsilon}_3 & f_1 \bar{f}_2 \bar{\bar{\varepsilon}}_3 \\ \bar{\varepsilon}_1 \varepsilon_2 \varepsilon_3 & \bar{\varepsilon}_1 \varepsilon_2 \bar{\varepsilon}_3 & \bar{\varepsilon}_1 f_2 \varepsilon_3 & \bar{\varepsilon}_1 f_2 \bar{\varepsilon}_3 & \bar{f}_1 \varepsilon_2 \varepsilon_3 & \bar{f}_1 \varepsilon_2 \bar{\varepsilon}_3 & \bar{f}_1 f_2 \varepsilon_3 & \bar{f}_1 f_2 \bar{\varepsilon}_3 \\ \bar{\varepsilon}_1 \varepsilon_2 \bar{\varepsilon}_3 & \bar{\varepsilon}_1 \varepsilon_2 \bar{\bar{\varepsilon}}_3 & \bar{\varepsilon}_1 f_2 \bar{\varepsilon}_3 & \bar{\varepsilon}_1 f_2 \bar{\bar{\varepsilon}}_3 & \bar{f}_1 \varepsilon_2 \bar{\varepsilon}_3 & \bar{f}_1 \varepsilon_2 \bar{\bar{\varepsilon}}_3 & \bar{f}_1 f_2 \bar{\varepsilon}_3 & \bar{f}_1 f_2 \bar{\bar{\varepsilon}}_3 \\ \bar{\varepsilon}_1 \bar{\varepsilon}_2 \varepsilon_3 & \bar{\varepsilon}_1 \bar{\varepsilon}_2 \bar{\varepsilon}_3 & \bar{\varepsilon}_1 \bar{f}_2 \varepsilon_3 & \bar{\varepsilon}_1 \bar{f}_2 \bar{\varepsilon}_3 & \bar{f}_1 \bar{\varepsilon}_2 \varepsilon_3 & \bar{f}_1 \bar{\varepsilon}_2 \bar{\varepsilon}_3 & \bar{f}_1 \bar{f}_2 \varepsilon_3 & \bar{f}_1 \bar{f}_2 \bar{\varepsilon}_3 \\ \bar{\varepsilon}_1 \bar{\varepsilon}_2 \bar{\varepsilon}_3 & \bar{\varepsilon}_1 \bar{\varepsilon}_2 \bar{\bar{\varepsilon}}_3 & \bar{\varepsilon}_1 \bar{f}_2 \bar{\varepsilon}_3 & \bar{\varepsilon}_1 \bar{f}_2 \bar{\bar{\varepsilon}}_3 & \bar{f}_1 \bar{\varepsilon}_2 \bar{\varepsilon}_3 & \bar{f}_1 \bar{\varepsilon}_2 \bar{\bar{\varepsilon}}_3 & \bar{f}_1 \bar{f}_2 \bar{\varepsilon}_3 & \bar{f}_1 \bar{f}_2 \bar{\bar{\varepsilon}}_3 \end{pmatrix} \begin{pmatrix} N_{RRR} \\ N_{RRF} \\ N_{RFR} \\ N_{RFF} \\ N_{FRR} \\ N_{FRF} \\ N_{FFR} \\ N_{FFF} \end{pmatrix}. \quad (6.12)$$

The expression for total fake contribution becomes

$$N_{\text{total Fake}} = N_{RRF \rightarrow TTT} + N_{RFR \rightarrow TTT} + N_{RFF \rightarrow TTT} + N_{FRR \rightarrow TTT} + N_{FRF \rightarrow TTT} + N_{FFR \rightarrow TTT} + N_{FFF \rightarrow TTT}. \quad (6.13)$$

### 6.2.1.3 Simplified matrix method for three leptons analysis

As discussed in the previous section, estimation for triple fake contribution is possible in the three leptons analyses. However if the fake contribution for the lepton with the highest  $p_T$  in the events (leading lepton) is small, we can apply the simplified matrix method.

The leading lepton in each event is assumed to be a real lepton which passes the tight selection. Then we can choose the numbers of events including fake leading lepton as

$$N_{FXX} \equiv 0. \quad (6.14)$$

In this condition, the equivalent expression for Eq. (6.12) can be simplified as:

$$\begin{pmatrix} N_{TTT} \\ N_{TTL} \\ N_{TLT} \\ N_{TLL} \end{pmatrix} = \varepsilon_1 \cdot \begin{pmatrix} \varepsilon_2 \varepsilon_3 & \varepsilon_2 f_3 & f_2 \varepsilon_3 & f_3 f_3 \\ \varepsilon_2 \bar{\varepsilon}_3 & \varepsilon_2 \bar{f}_3 & f_2 \bar{\varepsilon}_3 & f_2 \bar{f}_3 \\ \bar{\varepsilon}_2 \varepsilon_3 & \bar{\varepsilon}_2 f_3 & \bar{f}_2 \varepsilon_3 & \bar{f}_2 f_3 \\ \bar{\varepsilon}_2 \bar{\varepsilon}_3 & \bar{\varepsilon}_2 \bar{f}_3 & \bar{f}_2 \bar{\varepsilon}_3 & \bar{f}_2 \bar{f}_3 \end{pmatrix} \begin{pmatrix} N_{RRR} \\ N_{RRF} \\ N_{RFR} \\ N_{RFF} \end{pmatrix}. \quad (6.15)$$

The coefficient  $\varepsilon_1$  is the real efficiency of the leading lepton which passes the tight selection so that the term  $\varepsilon_1 N_{RXX}$  means the number of events including the leading lepton which is real and passes the tight selection. As we like to estimate the fake contribution where all the three leptons pass the tight selection, we can rewrite the term  $\varepsilon_1 N_{RXX} \equiv N_{XX}$ . Finally we obtained

$$\begin{pmatrix} N_{TTT} \\ N_{TTL} \\ N_{TLT} \\ N_{TLL} \end{pmatrix} = \begin{pmatrix} \varepsilon_2 \varepsilon_3 & \varepsilon_2 f_3 & f_2 \varepsilon_3 & f_3 f_3 \\ \varepsilon_2 \bar{\varepsilon}_3 & \varepsilon_2 \bar{f}_3 & f_2 \bar{\varepsilon}_3 & f_2 \bar{f}_3 \\ \bar{\varepsilon}_2 \varepsilon_3 & \bar{\varepsilon}_2 f_3 & \bar{f}_2 \varepsilon_3 & \bar{f}_2 f_3 \\ \bar{\varepsilon}_2 \bar{\varepsilon}_3 & \bar{\varepsilon}_2 \bar{f}_3 & \bar{f}_2 \bar{\varepsilon}_3 & \bar{f}_2 \bar{f}_3 \end{pmatrix} \begin{pmatrix} N_{RR} \\ N_{RF} \\ N_{FR} \\ N_{FF} \end{pmatrix}, \quad (6.16)$$

which is exactly the same expression as the fake matrix for two fake objects, Eq. (6.9). This analysis uses the lepton triggers, which require at least one reliable isolated lepton, so that it is the reasonable assumption that at least one lepton should be the good quality lepton.



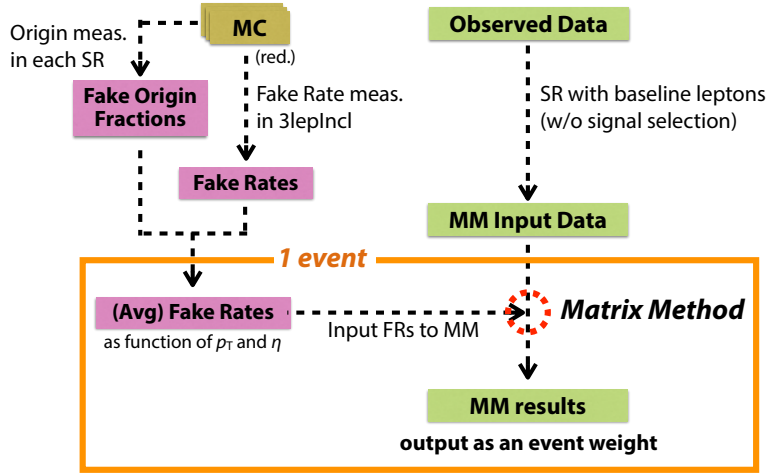


Figure 6.2: Flow diagram of the procedure of the simplified matrix method employed in this analysis. Fake rates are measured separately for the fake origins in the region with the loose selection using the reducible MC samples, such as  $t\bar{t}$  and  $Z$ +jets. Fake origin fractions are measured in each signal region. Then the average fake rate is evaluated using these information. The average fake rate is a function of the  $p_T$ ,  $\eta$  and the flavour. It is used as an input parameter of the matrix method. The input of the matrix method from the observed data is made by applying the selection of the corresponding signal region without the signal selection criteria. The output of the matrix method is recorded as an event weight of the processed event.

## 6.2.2 Matrix Method Procedure

The simplified matrix method described above is implemented event by event. Figure 6.2 shows the flow diagram of the implementation of the simplified matrix method in this analysis.

First, fake rates are measured with the MC samples. Since the fake rates depend on the origins of the fakes, the measurement of the fake rates are performed separately by the origin of the fakes in the region with the loose selection, which requires only the selection that the number of leptons should be three (called three-lepton inclusive region). In the next stage, the fraction of the fake origin is measured using the MC truth information in each region, then the average fake rate is evaluated. This average fake rate  $f$  is composed as a function of the lepton  $p_T$ ,  $\eta$  and the flavour. It is used as an input parameter of the matrix method. The detail of the fake rates is found in the next section, Sec. 6.2.3.

Since the matrix method is a data-driven method, the other input information is an event obtained from the observed data. It is selected using the selection of the signal region without the signal lepton criteria for the second and the third leading leptons. The matrix method is performed event by event. The passed event is categorised by the characteristics of the second and the third leptons as TT, TL, LT, and LL, as described in Sec. 6.2.1. For example, if the second and the third leptons are failed the signal lepton criteria in an event, the event is categorised as LL. In this case, the vector shown in the left side of Eq. (6.16) is  $(N_{TTT}, N_{TTL}, N_{TLT}, N_{TLL}) = (0, 0, 0, 1)$ . The efficiencies  $\varepsilon_i$  ( $i = 1, 2$ ) and the fake rates  $f_i$  ( $i = 1, 2$ ) are obtained from the MC estimation results for the corresponding  $p_T$  and  $\eta$ . The result of the matrix method is handled as a weight of the event. Finally the results are statistically combined as a sum of the event weight:

$$MM_{\text{Tot}}(\text{XR}) = \sum_{e_i \in S(\text{XR})} MM(e_i), \quad (6.17)$$

where  $MM_{\text{Tot}}(\text{XR})$  represents the total value of the matrix method results in the region XR,  $S(\text{XR})$  represents the set of the passed events in the region XR, and  $MM(e_i)$  represents the matrix method results for the event  $e_i$ .

### 6.2.3 Fake Rates

The fake rate is the indispensable ingredients in performing the matrix method. In general, the fake rates are different for lepton flavours, and depend on the transverse momenta and the  $\eta$  position. The other minor dependences are neglected in this analysis. Therefore the fake matrix shown in Eq. (6.15) will be composed of the fake rates which are the function of these variables.

#### 6.2.3.1 Weighted average fake rate

The fake rates are categorised by the lepton flavour ( $\ell = e, \mu, \tau$ (1-prong and 3-prong)) and by four types of the fake origins. They are photon converted lepton (CO), heavy flavour jet (HF), light flavour jet (LF) and the other source. Among the fake origins, the other source is negligible. Thus the mean fake rate is obtained by averaging over these three components with respective weights.

The total fake rate for the fake candidate can be defined as:

$$f_{\text{XR}}^{\ell} = \sum_{i,j} S^i \times R_{\text{XR}}^{ij} \times f^{ij}, \quad (6.18)$$

where XR is the target region,  $i$  and  $j$  are the fake type and the physics process respectively. In this analysis, the fake rates are obtained from MC samples. Details of the variables in Eq. (6.18) are described as follows.

**Fake Rates**  $f^{ij}$  is a fake rate for each fake origin type and for each process. The fake rates are defined by the following equation:

$$\text{fake rate } f = \frac{\# \text{ fake leptons which pass the signal selection}}{\# \text{ total fake candidates}}. \quad (6.19)$$

It is assumed that the fake rate does not depend on the event selection (it is called ‘region’), thus it is measured in the ‘‘three-lepton inclusive region’’ (labeled ‘‘3lepIncl’’), where the statistics are ample to measure the fake rate. The 3lepIncl region is defined as follows:

- Exact three baseline leptons ( $e, \mu$ ) and zero baseline taus are required.
- The leading lepton should pass the signal selection.

The fake rate for tau lepton is measured in the other region labeled ‘‘3lepTau’’ which includes  $e$  or  $\mu$  as the leading lepton and at least one baseline tau. The fake rate measurement has been performed with the MC truth information. The truth information for each lepton is categorised by its origin. The baseline leptons in the target region are classified by the truth information. Then the fake rate as we define as Eq. (6.19) is calculated in each category.

**Fake Origin Fractions**  $R_{\text{XR}}^{ij}$  is a fraction for each fake type and for each process. It is measured with MC truth information in the region. Taking into account three fake types (CO, HF, LF), the fake origin fraction is defined as following equation:

$$R^i = \frac{\# \text{ of } i \text{ fake type candidates}}{\# \text{ of total fake candidates}}. \quad (6.20)$$

Table 6.1: Scale factor measurements are performed for the categories with  $\checkmark$ . Due to the bad purity, the scale factor measurement of the light flavour fakes for electrons and muons and of the heavy flavour fakes for taus cannot be performed. Conversion fakes for electrons are taken into account. For the real efficiency of the taus, the control region cannot be defined due to the effect of the neutrino from the tau decay. The fakes which cannot be measured in the control region are assumed to be consistent with the data and MC prediction within 10% uncertainties.

Origin type	electron	muon	1-prong tau	3-prong tau
Real	$\checkmark$	$\checkmark$	–	–
Conversion	$\checkmark$	–	–	–
Heavy Flavour	$\checkmark$	$\checkmark$	–	–
Light Flavour	–	–	$\checkmark$	$\checkmark$

Whilst it is desirable to measure the fake rate with the data, unfortunately it is impossible. Therefore the measurement is performed with MC samples. This fraction is measured in each target region with the baseline leptons since the denominator of the fake rate is the samples of baseline leptons. As the MC sample has the truth origin information of each lepton, the baseline leptons could be categorised into the origins by simply counting the numbers of baseline leptons.

**Scale Factors**  $S^i$  in Eq. (6.18) is a correction factor for each fake type. Since the fake rates are measured with MC samples, the scale factor is used to correct the MC estimation of the fake rates. They are measured in the control regions with data and MC samples separately by the fake types described below.

#### 6.2.4 Scale Factor Measurement in Control Regions

A correction factor for the selected fake origin type (and also for real efficiency) is measured in each control region by comparison between MC and the collected data. These correction factors are assumed to be independent of selections and any variables. They are simply multiplied to the corresponding fake rates, then it is called scale factors. Furthermore, scale factors are assumed to be constant over the particle  $p_T$ . Distributions are fitted with constant functions. Scale factors are defined as the following equation:

$$S^i = \frac{\text{Fake Rate measured in CR with data}}{\text{Fake Rate measured in CR with MC}} \quad (6.21)$$

Scale factors for fake rates are measured for dominant fake types. For the conversion fakes from electrons, the scale factor is measured in events with a converted photon radiated from a muon in  $Z \rightarrow \mu\mu$  decays. In this control region, the events with the mass of two muons and one electron within  $Z$  mass window are selected to measure fake rate of the electron. For electrons and muons, the control region for heavy flavours is defined. The scale factor is measured in a  $b\bar{b}$ -dominated control sample. It is defined with the selection of only one  $b$ -jet and a baseline lepton, for which the mis-identification probability is measured. The scale factor for fake tau from the light flavour is measured in a  $W$ +jets dominated control sample. It is defined with the selection with one signal muon with  $p_T > 25 \text{ GeV}$  and one tagged  $\tau$ . In summary, the control region measurements are carried out for the specified fake types shown in Tab. 6.1.

The detail of the control regions are described below. Although the applied isolation for electrons and muons are different between Category-A and B, the value of the scale factors might be different. Thus the

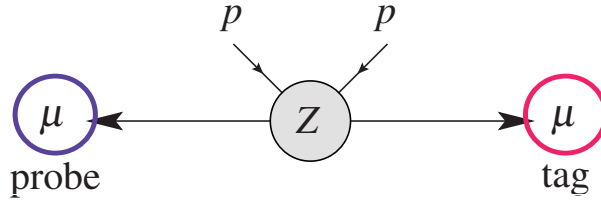


Figure 6.3: Schematic diagram for the tag-and-probe method for the measurement for the real lepton efficiency. The tag lepton should pass the signal selection and the trigger requirement.

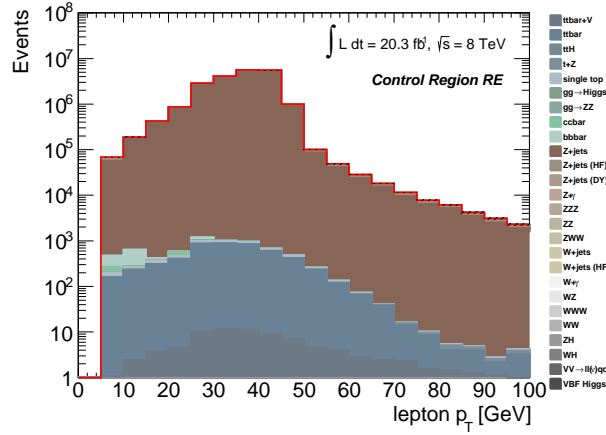


Figure 6.4: Distributions for the *probe* lepton  $p_T$  in the RE control region. The MC results only. The uncertainty is statistical only.

scale factor measurement is performed for each category.

#### 6.2.4.1 Real Electrons and Muons

In order to validate the real efficiency for each lepton, the method known as a *tag-and-probe* method for  $Z$  bosons is used. The procedure of the tag-and-probe method is that a lepton in an event is picked up and tagged if it passes the tight selection as a signal lepton (*tag* lepton) and then the other lepton from  $Z$  is picked up and investigated if it pass the standard signal selection (*probe* lepton), as illustrated in Fig. 6.3. By having the tagged lepton, the identification of the lepton pair is assured then the probe lepton is considered to be a pure real lepton. Hence the selection efficiency of the probe lepton can be interpreted as a real lepton efficiency. The detailed selection criteria are following:

- Require exactly two SFOS baseline leptons in each event
- A lepton should pass the signal selection and the single lepton trigger (*tag* lepton)
- Require the mass of the lepton pair (*tag* lepton and *probe* lepton) within  $m_Z \pm 10\text{GeV}$
- $E_T^{\text{miss}} < 50\text{GeV}$ , where the  $E_T^{\text{miss}}$  requirement contributes to enhance the events from  $Z$ +jets.

For this measurement, all of the expected background samples are used. The main contribution for this measurement is  $Z$ +jets contribution, as shown in Fig. 6.4.

Comparison between the data and MC truth results in this region is performed separately by the lepton flavours. Figures 6.5 show the  $p_T$  dependences of the real efficiencies for electron and muon. The RE

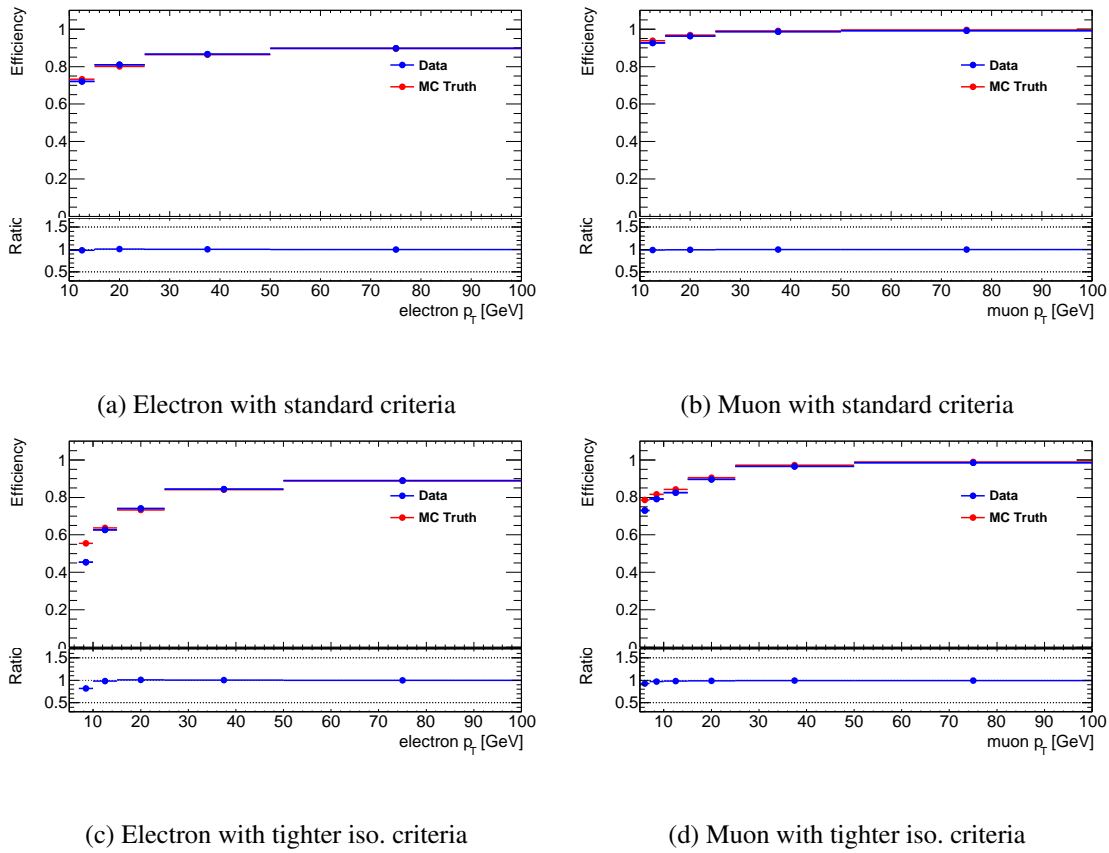


Figure 6.5: The  $p_T$  dependence of the Real Efficiency for each lepton. The “standard” and the “tighter isolation” criteria are described as Sec. 3.4 for electrons and Sec. 3.5 for muons.

Table 6.2: RE scale factors for electrons and muons, as measured separately by the analysis category, Category-A and Category-B.

	$S^{\text{RE}}(e)$	$S^{\text{RE}}(\mu)$	$S^{\text{RE}}(\tau)$
Category-A	$1.00 \pm 0.01$	$1.00 \pm 0.01$	$1.0 \pm 0.1$
Category-B	$1.01 \pm 0.01$	$1.00 \pm 0.01$	–

scale factors for electrons and muons are obtained by fitting in the plot of the  $p_T$  dependence, as shown in Table 6.2. These results show that the scale factor for real efficiencies are consistent with 1.0.

The scale factor measurement for tau leptons is slightly difficult comparing to the scale factors for electrons and muons. The  $Z$  mass reconstructed with tau pair shifts lower and has low resolution due to the neutrinos emitted from the tau decays. Therefore we cannot choose the exact region of  $Z$  mass window then we set the RE scale factor for tau leptons is 1.0, with the uncertainty of 10%.

#### 6.2.4.2 Conversion Fakes of Electrons

Conversion fake is the contribution from the photon conversion, as illustrated in Fig. 6.6. The energy of the leptons from photon conversion is typically low, thus one of the conversion leptons can be missed and the other takes most of the energy from the photon ( $p_T(\ell_{\text{conv}}) \sim p_T(\gamma_{\text{conv}})$ ). The conversion fake is dominant in electron channel. The contribution for the muon and tau channels is considered to be zero.

In order to enhance the conversion fake, the three lepton mass  $m_{\mu\mu e}$  within  $Z$  mass window can be used. The schematic diagram of the control region is shown in Fig. 6.7. The detail of the control region for conversion fakes defined as follows:

- Exactly two signal muons and one baseline electron
- At least one signal muon should pass the lepton trigger
- Three lepton mass should be in the  $Z$  mass window :  $m_{\mu\mu e} \in m_Z \pm 10\text{GeV}$
- $b$ -jets vetoed
- $E_T^{\text{miss}} < 30\text{GeV}$

where  $b$ -veto is to suppress the process with heavy flavour jets and the  $E_T^{\text{miss}}$  requirement is to keep orthogonal from the signal regions.

Figure 6.8 shows the dominant processes in the CO control region estimated by all of the MC samples. In this region, it is clear that the dominant contribution is  $Z$ +jets. The scale factor is calculated with the same manner as the calculation of the scale factor for real efficiencies. Figure 6.9 shows  $p_T$  dependence of the conversion electrons. Then the scale factor for conversion fake are determined by fitting a constant function in the  $p_T$  distribution. The results are shown in Tab. 6.3. For Category-A, the scale factor is consistent with 1.0. On the other hand, the Category-B result shows that it is large discrepancy between the MC prediction and the observed data. It would be the contribution of the low  $p_T$  leptons.

#### 6.2.4.3 Heavy Flavour Fakes of Electrons and Muons

The fake contribution from heavy flavour jets ( $b$  or  $c$ ) is the dominant fake contribution for this analysis. The heavy flavour fake is mainly from the mis-identification of the lepton from the heavy flavour jet cone.

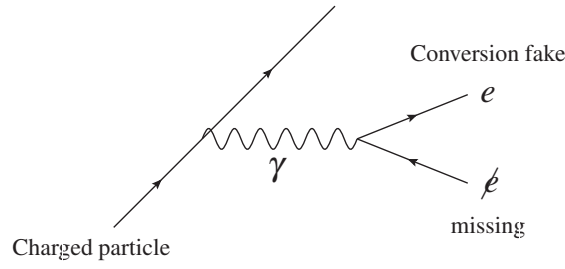


Figure 6.6: Origin of the conversion fakes

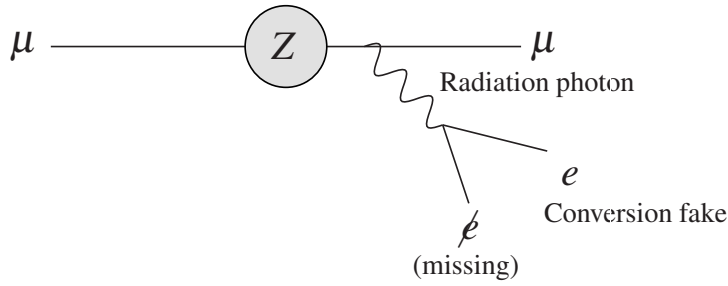


Figure 6.7: Schematic diagram of the target of the conversion fake control region.

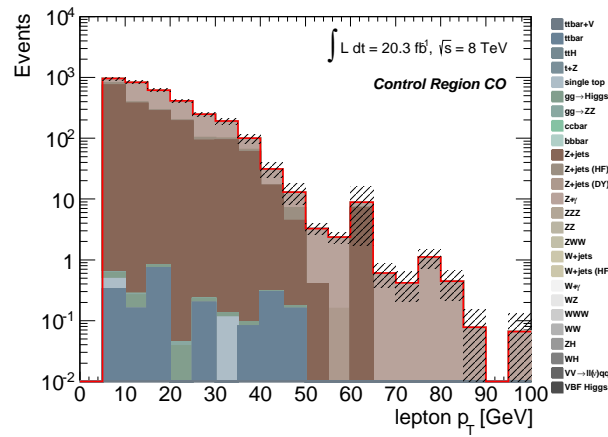
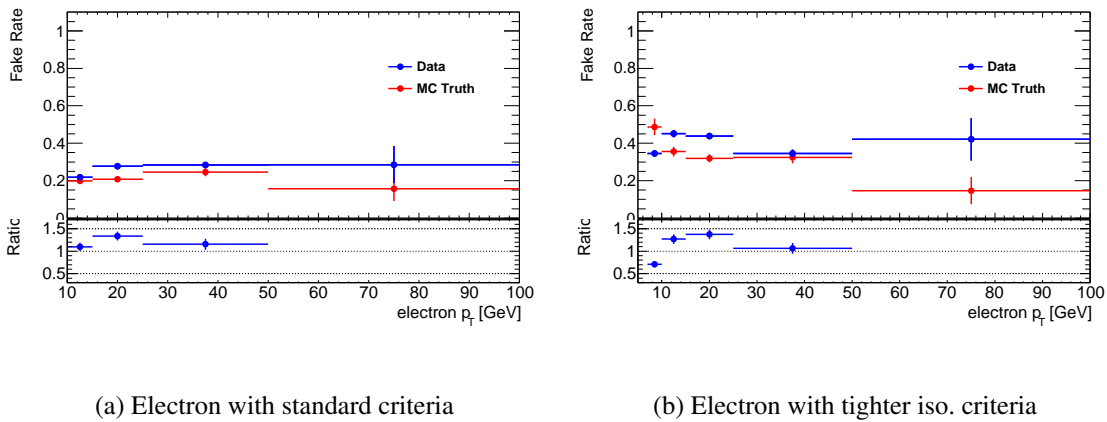


Figure 6.8: Distributions for the *probe* lepton  $p_T$  in the CO control region.



(a) Electron with standard criteria

(b) Electron with tighter iso. criteria

Figure 6.9: The  $p_T$  dependence of the conversion fake rate for electrons. The “standard” and the “tighter isolation” criteria are described in Sec. 3.4.

Table 6.3: CO scale factors for electrons and muons, as measured separately by the analysis category, Category-A and Category-B.

	$s^{\text{CO}}(e)$	$s^{\text{CO}}(\mu)$	$s^{\text{CO}}(\tau)$
Category-A	$1.14 \pm 0.12$	–	–
Category-B	$1.41 \pm 0.06$	–	–

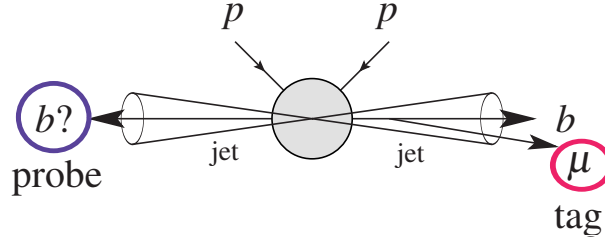


Figure 6.10: Schematic diagram for the control region for the heavy flavour fakes.

The idea of the control region definition is based on detecting the pair produced heavy flavour jets. If one jet is tagged as  $b$ -jet, the other jet tends to be the heavy flavour jets due to the flavour conservation. In this analysis, single or multiple lepton triggers are employed. To keep consistency in the triggers, the control region requires passing a muon trigger for the tag muon. The schematic diagram for the control region is shown in Fig. 6.10. The control region setting is as follows:

- One muon overlapped  $b$ -tagged jet pass the signal selection without overlap removal
- The signal muon should pass trigger ( $tag$  muon)
- Exactly one  $b$ -tagged jet
- The other lepton which is not overlapping with any jets or the other leptons with the cone distance  $\Delta R > 0.3$  ( $probe$  lepton)
- $E_T^{\text{miss}} < 60 \text{ GeV}$ , to suppress  $t\bar{t}$  di-lepton mode
- $m_T(\text{probe lepton}) < 50 \text{ GeV}$
- Mass of  $tag$  muon and  $probe$  muon should be out of  $Z$  mass window ( $m_Z \pm 10 \text{ GeV}$ )

The  $E_T^{\text{miss}}$  requirement contributes to suppress  $t\bar{t}$  contribution, which can have two real high  $p_T$  leptons if the both  $W$  boson decays into leptons. The transverse mass for  $probe$  lepton requirement can suppress the lepton from  $W$  in the process of  $W$ +jets. Therefore the dominant process can be the QCD contribution mainly from  $b\bar{b}$  and  $c\bar{c}$ .

In fact, the distribution for the control region for the heavy flavour jets is  $b\bar{b}$  dominating, as shown in Fig. 6.11. Although it looks good purity in this region, the  $b\bar{b}$  process is going down as the lepton  $p_T$  is getting higher. At the same time, the  $t\bar{t}$  contribution is getting larger. The  $t$  quark decays immediately into  $b$  quark and  $W$  boson, which decays leptonically or hadronically. Thus the processes including  $t$  quark contributes this control region with  $b$  quark and real lepton. If the process is dominantly in this region, the heavy flavour fake contribution cannot be measured anymore. Therefore, to suppress the  $t$  quark contribution, the subtraction of the events with the other origin objects is performed with MC truth information. The results are shown in Fig. 6.12. These figures shows the distribution after the subtraction.



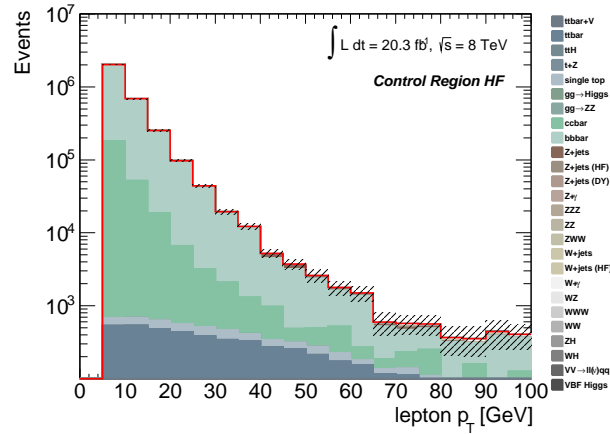


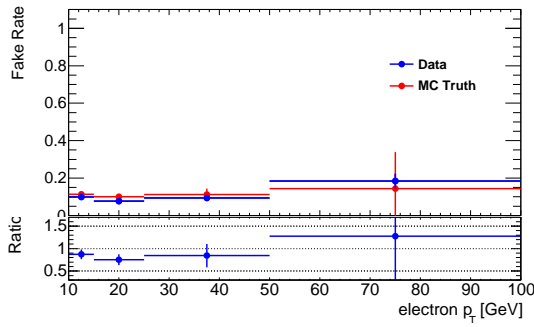
Figure 6.11: Distributions for the lepton  $p_T$  in the HF control region.

Table 6.4: HF scale factors for electrons and muons, as measured separately by the analysis category, Category-A and Category-B.

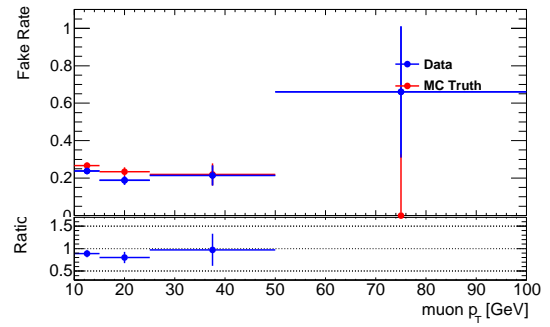
	$S^{\text{HF}}(e)$	$S^{\text{HF}}(\mu)$	$S^{\text{HF}}(\tau)$
Category-A	$0.72 \pm 0.05$	$0.87 \pm 0.09$	$1.0 \pm 0.1$
Category-B	$0.88 \pm 0.09$	$0.88 \pm 0.06$	–

In the high  $p_T$  region ( $\sim 100\text{GeV}$ ), the fake rates for electron and muon are still high after the subtraction. This is because the region enhances the di-jet processes with the lepton trigger in order to avoid the trigger bias. Thus it is hard to dispel the influence of the uncertainty of the di-jet MC samples. The influence is taken into account in the scale factor uncertainties with the conservative systematic uncertainty.

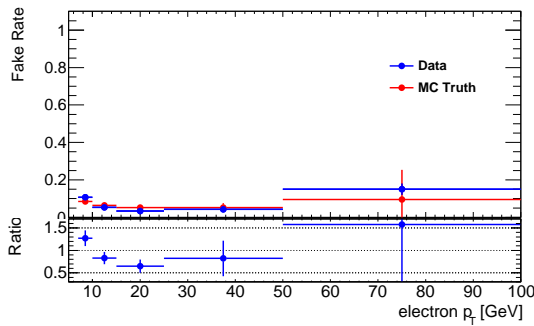
The fitting results for the scale factors are shown in Tab. 6.5. The scale factors are slightly low comparing to 1.0. For taus, the scale factor is set to 1.0 with 10% uncertainty.



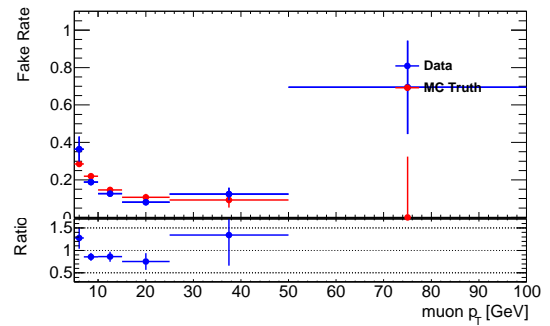
(a) Electrons with standard criteria



(b) Muons with standard criteria



(c) Electrons with tighter iso. criteria



(d) Muons with tighter iso. criteria

Figure 6.12: The  $p_T$  dependence of the HF leptons ( $e, \mu$ ) after the MC truth subtraction.

#### 6.2.4.4 Light Flavour fakes of Taus

For tau lepton, the contribution of the light flavour fakes is dominant. It is possible to form the control region for light flavour fakes of taus. The control region is defined to enhance the  $W(\mu\nu)$ +jets process. The emitted jets are the candidate of the tau fakes, as shown in Fig. 6.13. The control region for taus can be defined as follows:

- One signal muon should pass the single muon trigger (*tag* lepton)
- Exactly one baseline tau (*probe* lepton)
- $m_T(\text{tag}) > 60\text{ GeV}$ , to select  $W$
- $b$ -jet vetoed
- $\Delta R(\text{tag}, \text{probe}) > 0.3$
- $\sum \cos \Delta \phi = \cos(\Delta \phi(E_T^{\text{miss}}, \text{probe})) + \cos(\Delta \phi(E_T^{\text{miss}}, \text{tag})) < -0.15$ , where  $\sum \cos \Delta \phi$  is claimed as a good discriminator for  $Z \rightarrow \tau\tau$  [173].

The last requirement is validated in the measurement of the  $Z \rightarrow \tau\tau$  cross section with the ATLAS detector [173]. This variable calculated with  $Z \rightarrow \tau\tau$  samples tends to have peak near zero, and tends to be positive region. Thus this discriminator contributes to select  $W$ +jets processes, as shown in Fig. 6.14.

The results are provided separately for the 1-prong and 3-prong taus. Figures 6.15 show the  $p_T$  distribution of the LF fake rates. These figure show that the LF fake rates for taus are very low. The fitting results are found in Tab. 6.5. It is very difficult to define light flavour enhanced region for electrons and muons with an isolated lepton. In addition, it is not dominant fake for electron and muon. Thus for electrons and muons, the scale factors are set to 1.0 with the 10% uncertainties.

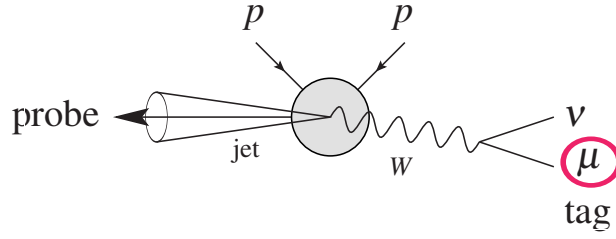


Figure 6.13: Schematic diagram for the control region for the light flavour fake taus.

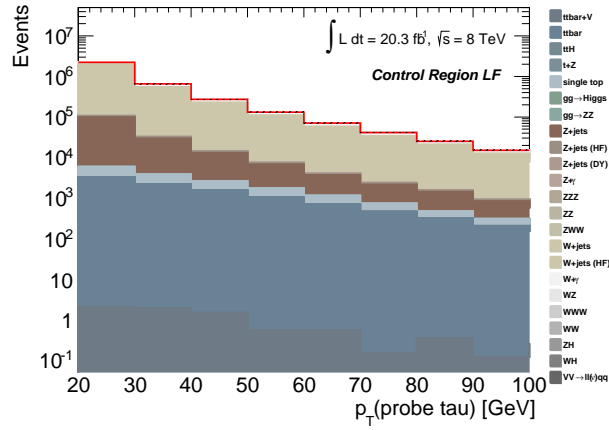
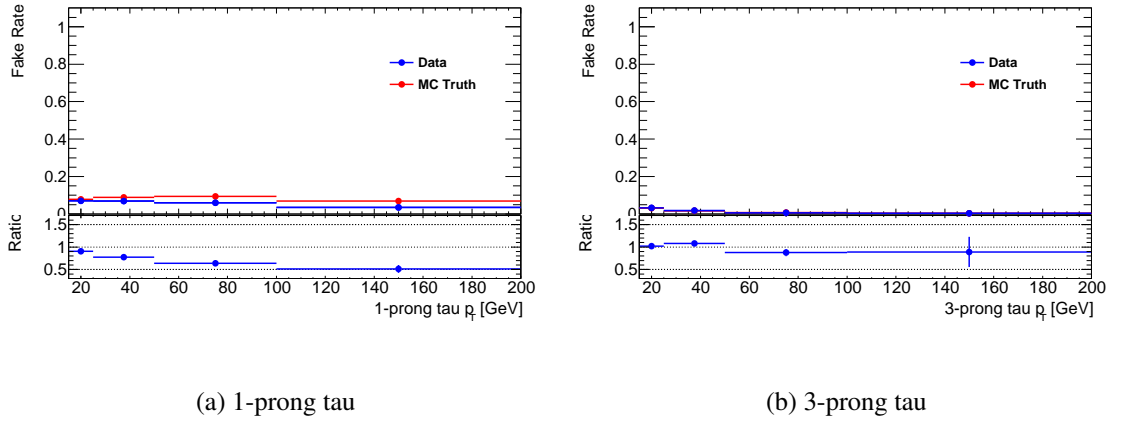
Figure 6.14: Distribution for the tau  $p_T$  in the LF control region.Figure 6.15: The  $p_T$  dependence for the LF taus.

Table 6.5: LF scale factors for electrons and muons, as measured separately by the analysis category, Category-A and Category-B.

	$S^{\text{LF}}(e)$	$S^{\text{LF}}(\mu)$	$S^{\text{LF}}(\tau_1)$	$S^{\text{LF}}(\tau_3)$
Category-A	$1.0 \pm 0.1$	$1.0 \pm 0.1$	$0.84 \pm 0.01$	$1.02 \pm 0.02$
Category-B	$1.0 \pm 0.1$	$1.0 \pm 0.1$	–	–



## Chapter 7

# Uncertainties

In this analysis, The uncertainties are classified in that on the irreducible background and the reducible background, and are estimated separately. The uncertainties on the irreducible background modelling are estimated with several studies of the detector performances, the MC generators and the theoretical sources. They are measured by varying a given systematic uncertainty between utmost edge of  $\pm 1\sigma$ , more detail will be described in Sec. 7.1. The uncertainties on the reducible background modelling are estimated with the matrix method. The statistical uncertainties of the collected data and the MC samples, and the uncertainties from the method itself are taken into account. Detail will be discussed in Sec. 7.2. The estimated uncertainties are statistically combined with the square root of the quadratic sum of the uncertainties as

$$\sigma_{\text{sys,tot}} = \sqrt{\sum_{\text{kind of syst.}} \sigma_i^2}, \quad (7.1)$$

where  $\sigma_{\text{sys,tot}}$  is the total uncertainty. Since uncertainties tend to be asymmetric, the  $\sigma_{\text{sys,tot}}$  is calculated separately for the positive or negative contribution with respect to the corresponding central value.

### 7.1 Uncertainties on the irreducible backgrounds

The irreducible background is estimated by MC simulation. The uncertainty for the MC related estimation includes the uncertainty of the reconstructed energy, efficiencies of the reconstruction and the identification, and the MC generation. The detailed description are summarised below.

**Monte Carlo Statistics** The uncertainties from Monte Carlo statistics. Since the signal regions except the SR0 $\tau$ a-bins applies very tight selections, the statistical uncertainties tend to be dominant sources of the uncertainties. The absolute statistical uncertainties in Category-A are estimated to be 10–20% for WZ/ZZ, 50–60% for  $t\bar{t}+V$ , 10–20% for VVV and 10–20% for Higgs. On the other hand, because of the tighter regions than that of Category-A, the absolute statistical uncertainties in Category-B are 20–80% for WZ, 20–30% for ZZ, 60–90% for  $t\bar{t}+V$  and 40–90% for VVV and  $\sim 100\%$  for Higgs. While some samples have much high uncertainties, the samples have less contribution. Thus total statistical uncertainties are estimated to be below  $\sim 30\%$ .

**Jets** The uncertainties related jets are considered for the JES [147], the JER [148] and Jet Vertex Fraction cut (JVF cut) [150], as described in Sec. 3.6. The uncertainty arisen from the JES is estimated

by applying energy scaling for jets with  $15\text{ GeV} < p_T < 7\text{ TeV}$  and  $|\eta| < 4.5$ . This uncertainty is also applied to the corresponding components of the  $E_T^{\text{miss}}$ . The uncertainty arisen from the JER is estimated by smearing  $p_T$  of each jet according to a Gaussian distribution, with unit mean and a width given by a  $p_T$  and  $\eta$ -dependent resolution function. The contribution of the uncertainties are small comparing to the other sources because the analyses focus on the leptons.

In Category-A, these uncertainties are estimated to be less than 5% for all MC samples except the JER for  $ZZ$  in  $\text{SR}0\tau b$  ( $\sim 10\%$ ) and for  $VVV$  and Higgs in  $\text{SR}2\tau b$  ( $\sim 10\%$ ).

In Category-B, the JES uncertainties are expected to be 10–25% for  $ZZ$  in the ISR signal regions and less than 5% for the other samples. The JER are expected to be  $\sim 10\%$  for all samples and the JVF uncertainties are negligible ( $< 1\%$ ). Category-B has selections for jets, thus the uncertainties related jets would be large comparing to the Category-A analyses.

**Electrons** The uncertainties with electrons are considered for the Electron Energy Scale (EES) [121], the Electron Energy Resolution (EER) [121] and the Electron Scale Factor (ESF) [135], as described in Sec. 3.4. The EES uncertainty is parametrised by  $E_T$  and  $\eta$ . This is validated with the events with  $Z \rightarrow ee$  and  $J/\psi \rightarrow ee$  in data. It is applied to both the relevant objects in the event and to the corresponding components of the  $E_T^{\text{miss}}$ . Since the estimations of the EES and EER are very precisely less than  $\sim 1\%$  and better than 10% [121], respectively, the EES and EER uncertainties are expected to be less than 1% for all samples.

The ESF estimation is based on reconstruction and identification efficiency measurements from  $J/\psi$  and  $Z$  events [135]. The uncertainty on the electron identification is estimated to be  $\sim 5\%$ . The uncertainties for the signal regions are estimated to be less than 5% for all samples, which is estimated from the identification uncertainty.

**Muons** The uncertainties related to muons are considered from the Muon Energy Scale (MES) [174] of the ID track and the MS track. The MES is measured using the MC simulated samples of  $j/\psi \rightarrow \mu\mu$  and  $Z \rightarrow \mu\mu$  and is validated with the observed data in 2012. The muon momentum is corrected using the scale factors (MES) parametrised by  $\eta$  and  $\phi$  in ID and MS. The systematic uncertainties for MES have been calculated by varying the dimuon masses  $\pm 5\text{ GeV}$  in ID and MS separately. The uncertainty is expected to be much smaller than the other sources,  $\sim 1\%$ , for all samples.

**Taus** The uncertainties related to taus are considered from the Tau Energy Scale (TES) [156]. This is parametrised by the  $p_T$ ,  $\eta$  and  $N^{\text{track}}$ -dependant function on the true taus. The scale factors are measured using the MC simulated  $Z \rightarrow \tau\tau$  samples with the same manner as the measurement of the JES [175]. Only in  $\text{SR}1\tau$  and  $\text{SR}2\tau$ , the TES uncertainty is considered. This is expected to be 5% for all samples in both region, except the  $t\bar{t}+V$  sample in  $\text{SR}2\tau$ . Since the  $t\bar{t}+V$  processes have very few generated events ( $\sim 10^2$ ), large TES uncertainty of the  $t\bar{t}+V$  in  $\text{SR}2\tau$  is estimated ( $\sim 40\%$ ). However, the contribution of the  $t\bar{t}+V$  is very small (expected 0.023 events), the relative uncertainty is small.

The uncertainty on the tau identification efficiency is also considered [156]. The contribution is estimated to be 5% for all samples in  $\text{SR}1\tau$  and 10% for all samples in  $\text{SR}2\tau$ .

***b*-tagging efficiency** The uncertainty of *b*-tagging algorithm in the MC samples is taken into account by varying the scale factor of the *b*-tagging efficiency. The *b*-tagging efficiency is measured by comparing the MC samples and the observed data in 2012 [176]. The estimated uncertainties are 20–30% for  $t\bar{t}+V$  samples in all of the signal regions, and are negligible for the other samples.

**Missing Transverse Energy** The  $E_T^{\text{miss}}$  uncertainty comes from the  $E_T^{\text{miss}}$  soft term, which is from pile-up contribution. It is estimated by adjusting the energy scale (5%) and resolution of this term. This uncertainty is negligible for all of the SM samples studied. The other sources of the  $E_T^{\text{miss}}$  uncertainty is included in the other uncertainties, such as electrons, muons and jets.

**Luminosity** The luminosity uncertainty for the data taken in 2012 is 2.8% [177].

**Trigger** The correction factors for one lepton triggers are estimated and are consistent with 1.0 within the uncertainties, as described in Sec. 2.3. In this analysis, the correction factors for the triggers are not applied. The effects arisen from the correction factors are taken into account as systematic uncertainties. Since the three-lepton triggers are employed in this analysis, the uncertainty from the trigger efficiency of 5% is adequate.

**Pile-up** The MC samples have been generated to reproduce the phenomena with pile-up effects using the ATLAS tunes [167–169]. The modelling of the pile-up in the MC samples is validated comparing to the observed data in 2012. The uncertainty from the modelling of the pile-up is evaluated varying the scale factors by  $\pm 3\%$ . The contributions of the pile-up are  $\sim 10\%$  for all samples.

**MC Cross Section** The uncertainty in the MC cross-sections for the backgrounds employed in this analysis is 30% for  $t\bar{t}+V$  [178, 179], 5% for  $ZZ$  [180], 7% for  $WZ$  [181] and a conservative 100% for the triboson samples. The  $WZ$  and  $ZZ$  cross-sections are normalised to the SM prediction and the uncertainty taken from SM calculations [182], which are excellent agreement with the ATLAS  $WZ$  and  $ZZ$  cross-section measurements [180, 181]. For the Higgs samples, a conservative 20% uncertainty is applied for  $VH$  and VBF production, whilst a 100% uncertainty is evaluated to  $t\bar{t}H$  and  $ggH$  production. They are based on the studies of the  $VH$  production channel [183].

**MC Generator** The uncertainty from the MC generator employed to simulate the irreducible diboson backgrounds is evaluated by comparing the acceptance of the selections of the signal regions in the POWHEG and MC@NLO samples. They are estimated to be 10–20% in Category-A and  $\sim 20\%$  in Category-B.

For the  $t\bar{t}+V$  background, the MADGRAPH generator is compared to the ALPGEN generator. This is estimated to be  $\sim 80\%$  for Category-A except the binned signal regions and Category-B signal regions. For the Category-A binned signal regions, the generator uncertainty is 10–40%.

**PDF** The PDF uncertainties are calculated with the full eigenset of the CT10 PDF set for  $ZZ$  and  $WZ$ . For the  $t\bar{t}+V$  samples, the PDF uncertainty is already included in the cross-section uncertainty. For the Category-A signal regions, the PDF uncertainty is expected to be less than 1%. For the Category-B signal regions, it is expected to be  $\sim 3\%$ .



## 7.2 Uncertainties on the reducible backgrounds

The uncertainties on the reducible backgrounds are evaluated from the matrix method described in Sec. 6.2. The matrix method employs many input information, such as the real efficiencies, the fake rates and the fake origin fractions from the MC samples and the data taken at the ATLAS detector. These contributions are evaluated separately by implementing the matrix method with varying systematics sources with  $1\sigma$  up or down, as shown below.

**Data Statistics** The amount of the observed data in ATLAS with  $\sqrt{s} = 8\text{TeV}$  in 2012 is a source of the statistical uncertainty on the reducible backgrounds. In the matrix method estimates, the selection of the baseline leptons are applied. It is looser selection than the nominal selection for the leptons (signal leptons). Hence the amount of events is expected much larger than the nominal requirements. The expected statistical uncertainties are shown in Tab. 7.4 for Category-A and Tab. 7.5 for Category-B.

**Real Efficiency and Fake Rates** The real efficiency and the fake rates are measured with MC simulated samples in the three-lepton inclusive region with the truth information. The uncertainties for them are due to the statistics of the three lepton inclusive region. Statistical uncertainties for the real efficiency is estimated as approximately 1–5% for Category-A and 1–15% for Category-B. The difference between them is from the isolation efficiencies and  $p_T$  requirement.

**Fake Origin Fraction** The fake origin fraction is evaluated in each region, as described in Sec. 6.2.3. The statistical uncertainty of it is relatively higher than that of real efficiency or fake rates because of the small statistics in the region. For Category-A, absolute uncertainty is approximately 50% in each region. On the other hand, Category-B analysis applied tight selection comparing to the Category-A analysis. As a result, absolute uncertainties of 30–100% for SRSL and 40–100% for SRISR are obtained.

**Dependencies for Fake Rates and Real Efficiency** The fake rates used in these analyses are parametrised in the flavours,  $p_T$ ,  $\eta$  and tau prongs. The other dependencies are tested and taken into account as the systematics uncertainties.

In Category-A, dependencies of the results on the  $E_T^{\text{miss}}$ , the  $m_T$ , the mass of same-flavour opposite-sign lepton pair are tested, as shown in Tabs. 7.1 and 7.2. Whereas some large dependencies are observed for light flavour muons, the overall effects on the final uncertainty is small because the large uncertainties are observed in the channel which has less contribution in the reducible background.

For Category-B analysis, the statistical uncertainty of the fake origin fraction is much higher compared to Category-A analysis. Table 7.3 shows the  $E_T^{\text{miss}}$  and  $m_T$  dependences in the Category-B analysis with the statistical uncertainty for the corresponding fake rate. Although several dependences are large as well as Category-A, the statistical uncertainties are much higher than those. Thus as a result, the dependencies for these variables can be assumed to be sufficiently smaller than the contribution of the statistical uncertainties.

**Scale Factor for Fake Rate** The scale factors are measured in control regions, as described in Sec. 6.2.4. During this measurement, the high purities in the control regions are assumed. The assumption

Table 7.1: Absolute systematic uncertainties on the matrix method efficiencies and fake rates due to the  $E_T^{\text{miss}}$  and  $m_T$  dependences in the Category-A analysis. In the table, the following notation is used: RE: real efficiency, HF: heavy flavour jet, LF: light flavour jet, CO: converted photon, QJ: quark jet, GJ: gluon jet.

Category-A Fake Type	$E_T^{\text{miss}}$ dependence			$m_T$ dependence		
	Top (%)	VV (%)	Z (%)	Top (%)	VV (%)	Z (%)
electron RE	1	1–10	3–27	1–2	2–3	4–15
electron CO	1–10	8–13	4–7	1–4	2–13	2–7
electron HF	0.2–1.2	3–11	5–9	0–1	1–4	2–8
electron LF	0.4–5.8	1–15	5–8	1–2	1–15	4–6
muon RE	0.2–1.4	0–17	5–14	1–2	2–7	2–19
muon HF	1–2	5–20	3–6	0–2	5–11	2–6
muon LF	3–4	8–38	5–13	2–3	7–45	4–14
tau RE	0.1–0.3	0.3–1.3	0.4–2.9	1–2	1–4	0–2
tau CO	0.1	0.3–1.1	0.3–0.5	0.1	0.3–1.1	0.2–1.0
tau HF	0.1	1–6	0.4–2.2	0.1	0.4–7.4	1–3
tau QJ	0.1–0.2	0.3–1.0	0.2–1.2	0.1–0.2	0.2–0.9	1
tau GJ	0.1–0.3	0.2–2.9	0.6–1.4	0.1–0.4	0.1–3.1	0.2–1.9

Table 7.2: Absolute systematic uncertainties on the matrix method efficiencies and fake rates due to the  $m_{\text{SFOS}}$  dependence in the Category-A analysis. In the table, the following notation is used: RE: real efficiency, HF: heavy flavour jet, LF: light flavour jet, CO: converted photon.

Fake Type	Top category (%)	VV category (%)	Z category (%)
electron RE	1–5	3–14	2–8
electron CO	1–4	4–14	4–9
electron HF	1–3	1–4	2–8
electron LF	0–7	2–15	3–12
muon RE	0–4	1–18	1–4
muon HF	1–6	5–13	3–12
muon LF	2–31	5–18	4–15

Table 7.3: Absolute uncertainties on the matrix method efficiencies and fake rates due to the  $E_T^{\text{miss}}$  and  $m_T$  dependences in the Category-B analysis. Statistical uncertainties are also shown in this table. In the table, the following notation is used: RE: real efficiency, HF: heavy flavour jet, LF: light flavour jet, CO: converted photon.

Category-B Fake Type	$E_T^{\text{miss}}$ dependence			$m_T$ dependence			Stat. (%)
	Top (%)	VV (%)	Z (%)	Top (%)	VV (%)	Z (%)	
electron RE	0.4–4	0.1–3	0.5–8.2	0–3	0–7	0.8–1.5	1.4–15
electron CO	6–94	2–16	0.3–3.5	4–20	4–19	0.8–8.4	4.5–21
electron HF	2–31	8–43	0–15	5–9	5–74	1–19	11–101
electron LF	1–10	2–177	8–19	7–42	0–15	5–10	13–57
muon RE	0–13	0.1–2	0.1–16	0.4–3	0–4	0–15	1.5–13
muon HF	3–19	9–30	1–71	1–16	2–11	5–13	7–27
muon LF	3–99	6–15	5–13	7–69	4–47	5–13	7–118

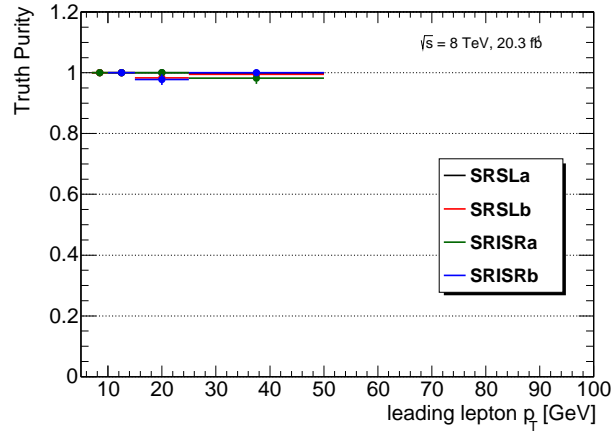


Figure 7.1: Leading lepton purity for Category-B estimated with MC background samples. The uncertainties are statistical only.

is well satisfied within a few %. Conservative uncertainties which are calculated by the uncertainty from the SF measurement and additionally the difference between the scale factor and 1.0 are applied.

**Method Simplification** The matrix method used in this analysis is simplified in order to keep the statistics of the input data elements. As described in Sec. 6.2.1.3, it is ensured by the high purity of the leading lepton that the simplified matrix method works well in the three lepton analyses.

Rough estimates of the uncertainty will be shown below. Four dimensional vectors  $\mathbf{T}$ ,  $\mathbf{L}$ ,  $\mathbf{R}$  and  $\mathbf{F}$  are defined as following equation which satisfied the matrix method expression for three leptons as Eq. 6.12:

$$\begin{pmatrix} \mathbf{T} \\ \mathbf{L} \end{pmatrix} = \begin{pmatrix} \varepsilon_1 \mathcal{M}_2 & f_1 \mathcal{M}_2 \\ \bar{\varepsilon}_1 \mathcal{M}_2 & \bar{f}_1 \mathcal{M}_2 \end{pmatrix} \begin{pmatrix} \mathbf{R} \\ \mathbf{F} \end{pmatrix}, \quad (7.2)$$

where  $\mathcal{M}_2$  shows the fake matrix for 2nd or 3rd leptons. The simplified matrix method uses the expression with the assumption  $\mathbf{F} \sim 0$ . If the purity  $I$  is given and is simply assumed as  $I = \mathbf{R}/(\mathbf{R} + \mathbf{F})$ , the corrected matrix method expression is obtained from the upper side of Eq. (7.2),

$$\mathbf{T} \sim \left(1 + \frac{f_1 \bar{I}}{\varepsilon_1 I}\right) \cdot \varepsilon_1 \mathcal{M}_2 \mathbf{R}, \quad (7.3)$$

where  $\bar{I} = 1 - I$ . In the simplified matrix method which is used in this analysis, only the first term is taken into account. The second term is the correction factor  $f_1 \bar{I}/\varepsilon_1 I$ . The leading lepton real efficiency and fake rates are  $\sim 90\%$  and  $\sim 20\%$ , respectively, and the purity of each region is estimated greater than 95%, as shown in Figure 7.1. If we use these parameters, the absolute uncertainty of the method can be estimated as approximately 1%. Then the uncertainty from this method could be neglected, since the statistical uncertainties are much larger.

### 7.2.1 Uncertainties on the reducible background for signal regions

The estimation results for uncertainties on the reducible background of signal regions can be found in Tab. 7.4 and 7.5. In signal regions of Category-A, the uncertainties from the statistics and the fake fractions are dominant. The total uncertainties are estimated as 10–30%.

Table 7.4: Uncertainties for reducible background in signal regions in Category-A.

	SR0 $\tau$ a	SR0 $\tau$ b	SR1 $\tau$	SR2 $\tau$
Expected Events	136.5	1.48	4.30	4.86
Statistics	+4, -4%	+25, -25%	+14, -14%	+13, -13%
Fake Fractions	+14, -10%	+6, -5%	+8, -8%	+4, -4%
$E_T^{\text{miss}}$ dependence	+7, -7%	+5, -5%	+2, -2%	+2, -2%
$m_{\ell\ell}$ dependence	+18, -17%	-	+8, -8%	-
$m_T$ dependence	+7, -7%	+5, -5%	+2, -2%	+2, -2%
$\eta$ dependence	+5, -4%	+4, -4%	+1, -1%	+1, -1%
Scale Factors	+5, -4%	+4, -4%	+1, -1%	+1, -1%
Total	+24, -21%	+33, -33%	+19, -19%	+14, -14%

Table 7.5: Uncertainties for reducible background in signal regions in Category-B.

	SRSLa	SRSLb	SRISRa	SRISRb
Expected Events	2.8	9.7	0.09	1.4
Statistics	+44, -44%	+23, -23%	+78, -78%	+67, -67%
Fake Fraction	+7, -41%	+7, -15%	+0, -0%	+8, -24%
Real Efficiency	+2, -1%	+7, -10%	+5, -6%	+6, -7%
Electron FR	+19, -27%	+13, -15%	+18, -17%	+9, -20%
Muon FR	+21, -38%	+14, -18%	+6, -6%	+25, -18%
Scale Factors	+4, -4%	+8, -8%	+16, -16%	+2, -2%
Total	+53, -76%	+33, -38%	+82, -82%	+73, -77%

On the other hand, the uncertainties on the reducible background of the signal regions of Category-B are much larger. The tight selections are applied in these regions, thus the statistical uncertainties are dominant, 40–80%.

### 7.3 Summary of Total Uncertainties for Signal Regions

Dominant uncertainties are summarised in Tab. 7.6 for Category-A and Tab. 7.7 for Category-B. For no taus regions in Category-A, uncertainties on the irreducible background are dominant because of the less fake contribution. For the binned signal regions SR0 $\tau$ a, the uncertainty is  $\sim 12\%$ . In SR0 $\tau$ b, the total uncertainty is 33%, where the theoretical uncertainties such as cross-sections are dominant. In SR1 $\tau$ , the total uncertainty is 18%. The dominant sources of the uncertainties are the cross-sections and the statistical uncertainty on the reducible background. In SR2 $\tau$ b, the contribution of the tau fakes is dominant uncertainty and the total uncertainty is 13%.

For the Category-B regions, the statistical uncertainty is the dominant source. In SRSLa/b, the reducible background is the largest contribution thus the uncertainty on the reducible background dominates the total uncertainty. The total uncertainties of 51% and 24% are expected in SRSLa and SRSLb, respectively. For the ISR regions, the reducible background has been much suppressed. Thus the statistical uncertainty and the theoretical uncertainty on the irreducible background are dominant. The total uncertainties of 30% and

Table 7.6: Dominant systematic uncertainties on background estimates in the various signal regions in Category-A.

Uncertainty of channels	SR0 $\tau$ a	SR0 $\tau$ b	SR1 $\tau$	SR2 $\tau$
Statistics on the reducible background	0.4–28.5%	13.7%	8.4%	12.2%
Statistics on the irreducible background	0.8–25.8%	8.3%	4.9%	3.1%
Muon mis-identification probability	0.1–23.8%	2.2%	< 1%	–
Electron mis-identification probability	0.3–9.5%	1.3%	< 1%	–
Tau mis-identification probability	–	–	7.7%	5.4%
Generator	3.2–35.1%	11.4%	3.1%	< 1%
Cross section	4.2–25.1%	37.1%	8.5%	3.0%
Total	10–15%	33%	18%	13%

Table 7.7: Dominant systematic uncertainties on background estimates in the various signal regions in Category-B.

Uncertainty of channels	SRSLa	SRSLb	SRISRa	SRISRB
Statistics on the reducible background	34%	14%	11%	30%
Statistics on the irreducible background	4%	3%	25%	10%
Muon mis-identification probability	27%	11%	< 1%	10%
Electron mis-identification probability	23%	10%	2%	9%
Generator	2%	4.7%	12%	7%
Cross section	2%	2%	5.7%	3.5%
Total	51%	24%	30%	35%

35% are expected in SRISRa and SRISRB, respectively.

## Chapter 8

# Validation of the Background Modelling

In order to confirm that the background modelling with the matrix method successfully describe the background level in signal regions, two types of validations are carried out.

One is called MC closure test, which is the test of the matrix method using the MC samples as an input. This test aims to check the self consistency of the method. This will be described in Sec. 8.1.

The other is the validation with data. To keep orthogonal from the signal regions, the new region called the validation regions are defined for the test. The validation region is the region close to the signal region where we expect similar event characteristics to the signal region, but with small signal contamination. Further information and the results are shown in Sec. 8.2.

### 8.1 Validation with the MC closure test

In order to validate the performance of the simplified matrix method, the MC closure test has been performed. In this test, the fake lepton contributions are estimated via two approaches and are compared to see if the results agree with each other. The one approach simply estimates the amount of fake leptons using the truth information in the MC, the other uses the simplified matrix method where the better statistical precision is expected. The main contributions for signal regions are heavy flavour jets such as  $b$  or  $c$ -jet contribution, therefore, the test has been performed with  $t\bar{t}$  sample. In addition, the test has been performed with  $Z$ +jets samples to validate the light flavour contribution.

The MC closure test for  $t\bar{t}$  has been implemented in the “three lepton inclusive region” (3lepIncl; see Sec. 6.2.3), as shown in Fig. 8.1. The uncertainties are only statistical. There is good agreement between the matrix method estimate and the MC prediction. Figures 8.2 show the results of MC closure test with the  $Z$ +jets samples in the 3lepIncl region vetoed  $b$ -jets. The  $b$ -jets veto contributes to reduce heavy flavour contamination. The  $Z$ +jets test is for the validation for the light flavour fakes. The region within the  $Z$  mass window ( $m_Z \pm 10 \text{ GeV}$ ) has discrepancy between MC and the matrix method estimates with  $\sim 2\sigma$ . In the  $Z$  mass region, the fake rates are different from the other region. Since the fake rates are parametrised by  $p_T$  and  $\eta$ , the mass contribution is not taken into account. Taking notice of the low mass and low  $p_T$  region, where there is no on-shell  $Z$ , the matrix method reproduces the MC prediction precisely. Thus the simplified matrix method is reliable to apply the  $Z$ +jets (light flavour) background.

As a result, the MC closure test shows that the simplified matrix method itself is correct method as

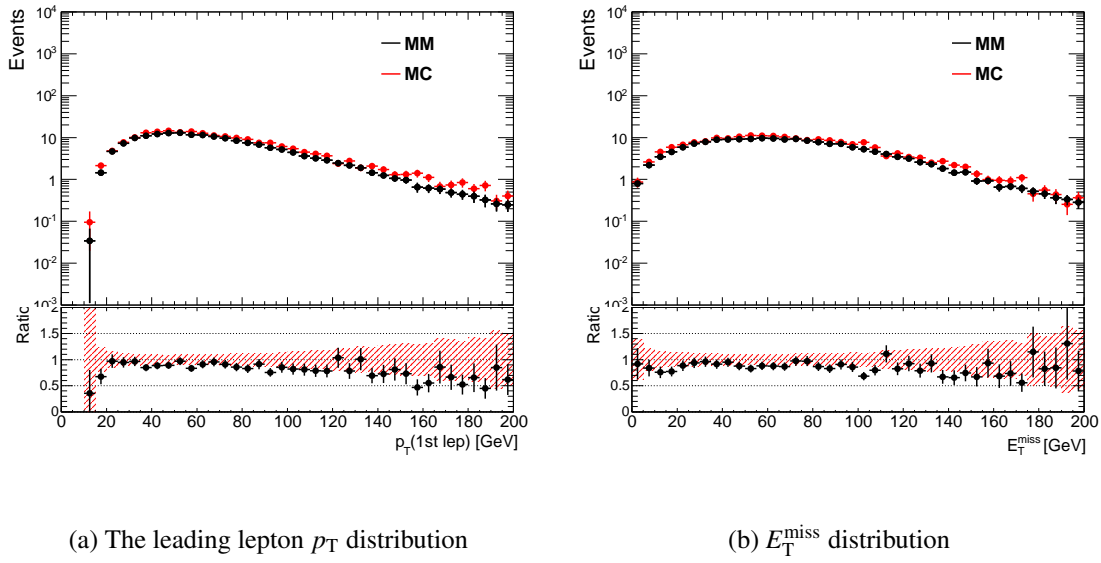


Figure 8.1: Results from MC closure test performed with  $t\bar{t}$  sample in the 3 lepton inclusive region.

estimation of the fake contribution. In this test, all inputs are from MC samples. Thus, to complete the validation, the test with inputs from data and fake rates from MC is necessary. The tests are performed in the validation regions.

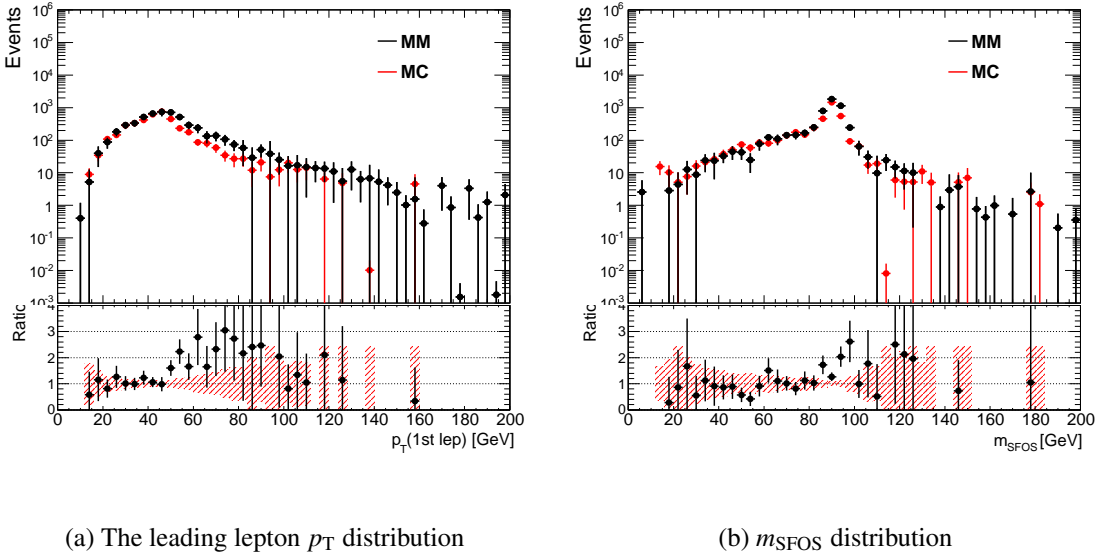


Figure 8.2: Results from MC closure test performed with  $Z + \text{jets}$  sample in the 3 lepton inclusive region.

## 8.2 Validation Regions

The regions which are close but orthogonal from the signal regions are defined. The definition of the validation regions are based on the requirements of the  $E_T^{\text{miss}}$  and the number of  $b$ -jets, as shown in Fig. 8.3. The detail of the definition is summarised in Tab. 8.1 and Tab. 8.2. Two types of the validation regions are defined. One is labeled “a,” which selects the low  $E_T^{\text{miss}}$  region comparing to the target signal region. The  $E_T^{\text{miss}}$  requirements are 35–50 GeV for Category-A and 0–30 GeV for Category-B. In these regions, the target processes are the SM di-boson processes and  $V + \text{jets}$ . In the VRSLa in Category-B, the requirement for the leading lepton  $p_T$  is  $p_T < 30 \text{ GeV}$ . The signal regions have  $p_T < 30 \text{ GeV}$  requirement, so that it is reliable to validate in this region. The other validation region in Category-B have less statistics in the low  $p_T$  region, hence, there are no requirement for the leading lepton  $p_T$ . The regions labeled “b” require exactly one  $b$ -tagged jet. Only to keep orthogonality from the signal regions, the requirement of at least one  $b$ -jets is reasonable. However, we could not control the final states with three leptons and three  $b$ -jets up to the present. In this analysis, the  $b$ -jets should be vetoed, then it is adequate to require exactly one  $b$ -jet for validation region in order to avoid the problem in the three lepton and three  $b$ -jets final states. The target of this region is heavy flavour jet processes, such as  $t\bar{t}$  and single top production. As the requirements are adequate to suppress the di-jet processes, the  $b\bar{b}$  and  $c\bar{c}$  processes are negligible.



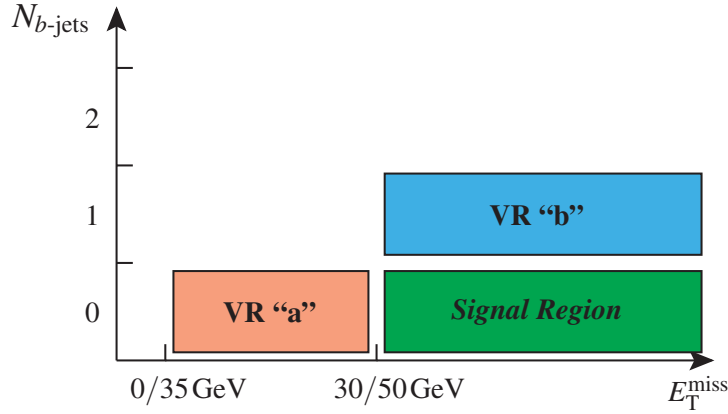


Figure 8.3: The strategy of the definition of the validation regions. The categories of the validation region ‘a’ and ‘b’ are defined as the low  $E_T^{\text{miss}}$  regions and the one  $b$  regions, respectively. The low  $E_T^{\text{miss}}$  region ‘a’ requires similar selections with low  $E_T^{\text{miss}}$  requirement. The one  $b$  region ‘b’ requires similar selections with exactly one  $b$ -jet.

Table 8.1: Validation Region Definition for Category-A.

VRs	VR0 $\tau$ noZa	VR0 $\tau$ Za	VR0 $\tau$ noZb	VR0 $\tau$ Zb	VR1 $\tau$ a	VR1 $\tau$ b	VR2 $\tau$ a	VR2 $\tau$ b
Flavour/sign	$\ell^+\ell^-\ell^{(\prime)}$	$\ell^+\ell^-\ell^{(\prime)}$	$\ell^+\ell^-\ell^{(\prime)}$	$\ell^+\ell^-\ell^{(\prime)}$	$\ell^\pm\ell^\pm\tau$	$\ell^\pm\ell^\pm\tau$	$\ell\tau\tau$	$\ell\tau\tau$
$N(b\text{-jet})$	0	0	1	1	0	1	0	1
Z bosons	veto	request	veto	request	–	–	–	–
$E_T^{\text{miss}}$ [GeV]	35–50	35–50	> 50	> 50	35–50	> 50	35–50	> 50
Target process	$WZ^*, Z^*Z^*, Z^*+jets$	$WZ, Z+jets$	$t\bar{t}$	$WZ$	$WZ, Z+jets$	$t\bar{t}$	$W/Z+jets$	$t\bar{t}$

Table 8.2: Validation Region Definition for Category-B.

VRs	VRSLa	VRSLb	VRISRa	VRISRb
Flavour/sign	$lll$	$lll$	$lll$	$lll$
$N(b\text{-jet})$	0	1	0	1
$N(\text{ISR-like jet})$	0	0	$\geq 1$	$\geq 1$
Z bosons	veto	–	veto	veto
$E_T^{\text{miss}}$ [GeV]	< 30	> 30	30–50	> 50
$p_T(1\text{st lep})$	< 30	–	–	–
Target process	$WZ, Z+jets$	$t\bar{t}$	$WZ, Z+jets$	$t\bar{t}$

### 8.3 Validation with Data

The results of the background expectation and the data in the validation regions are shown in Tab. 8.3 for Category-A and Tab. 8.4 for Category-B. The results include the statistical and systematic uncertainties. The systematic uncertainties are described in detail in Chap. 7. The validation is summarised in Tab. 8.5. The symbols representing *good* (all bins within  $1\sigma$  uncertainties), *not available* and *the data observed out of  $1\sigma$  uncertainties*, are defined. All of the validations have worked well except a small number of regions: the numbers of events within VR0 $\tau$ noZa and VRISRb, the leading lepton  $p_T$  distributions for VR0 $\tau$ noZa, VR1 $\tau$ a/b, VRSLb and VRISRa/b, the sub-leading lepton  $p_T$  distribution for VRISRa/b, the  $E_T^{\text{miss}}$  distribution for VR0 $\tau$ Zb, the  $m_T$  distribution for VR0 $\tau$ noZa, and the  $m_{\text{SFOS}}$  distribution for VRISRb.

The deviations of the numbers of events within VR0 $\tau$ noZa and VRISRb are roughly estimated to  $CL_b = 0.88$  and  $0.15$ . These are less than  $2\sigma$  deviation, thus they should be the statistical fluctuation.

Some kinematic distributions for the validation regions are shown in Figs. 8.4–8.15, whereas the validation is performed with the variables shown in Tab. 8.5. For Category-A validation regions, as shown in Figs. 8.4–8.11, the distributions of the lepton or the tau  $p_T$  and the specific variable such as  $E_T^{\text{miss}}$  or  $m_T$  are shown. In the region with tau contribution, VR1 $\tau$  and VR2 $\tau$ , the fake contribution is dominant. This is because the tau fake rates are higher than the other leptons'. The small deviations from data and estimation are observed in VR0 $\tau$ noZa in the lower region of the sub-leading lepton  $p_T$  and the  $m_T$  distributions. Only the specific bins have  $2\sigma$  deviation, thus they would be regarded as statistical fluctuations.

For Category-B validation regions, as shown in Figs. 8.12–8.15, the distribution of the lepton  $p_T$  and the several variables such as  $E_T^{\text{miss}}$ ,  $m_T$  and  $\min. m_{\text{SFOS}}$ . Almost all regions show good agreements between estimates and the observed data, except the lepton distributions in the VRISRa and the distributions in VRISRb. For the VRISRa, the bad purity of 80% is observed in the leading lepton  $p_T$  region of  $p_T < 30\text{GeV}$ . Then the rough calculation of the effect using Eq. (7.3) would be  $\sim 30\%$ .

As a result, the observed data agree with the background modeling with the simplified matrix method and MC prediction for all validation regions.



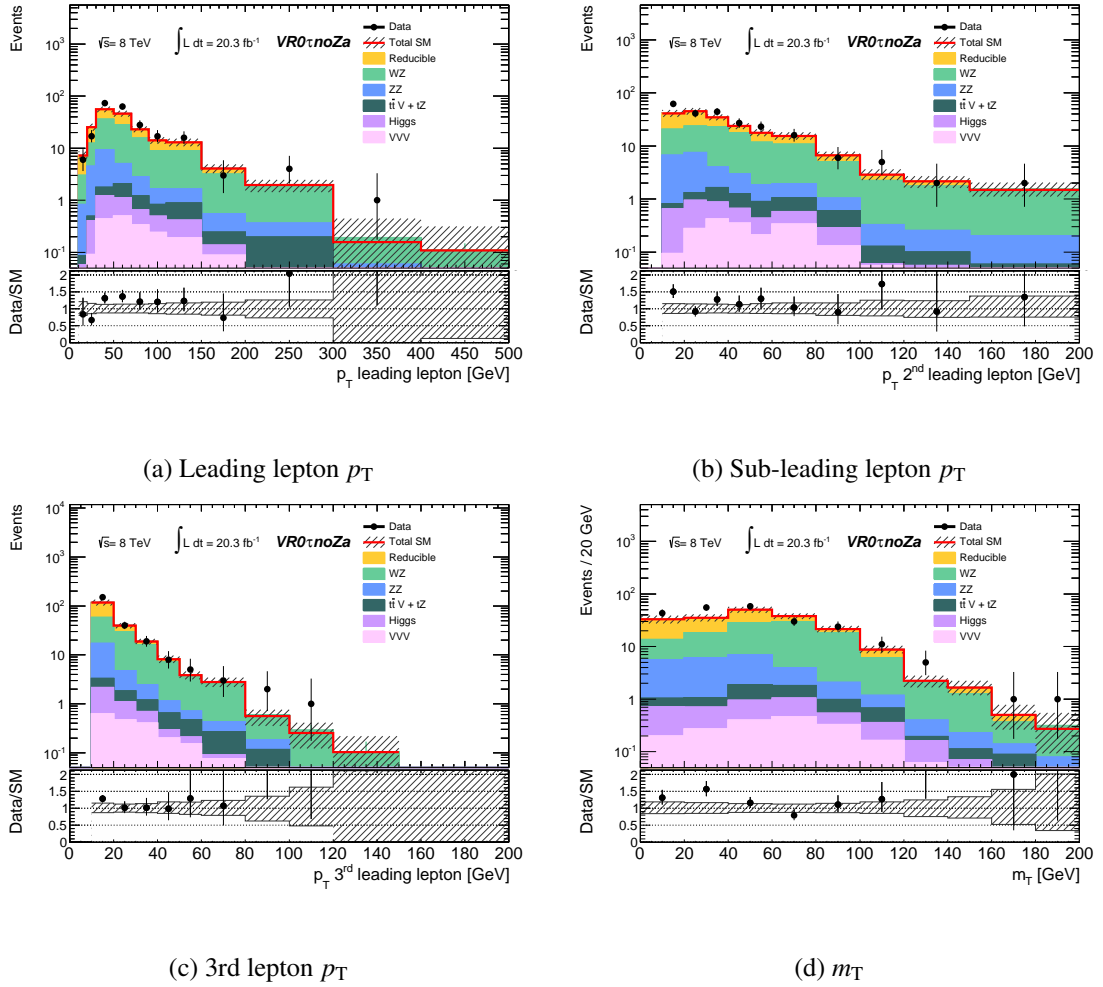
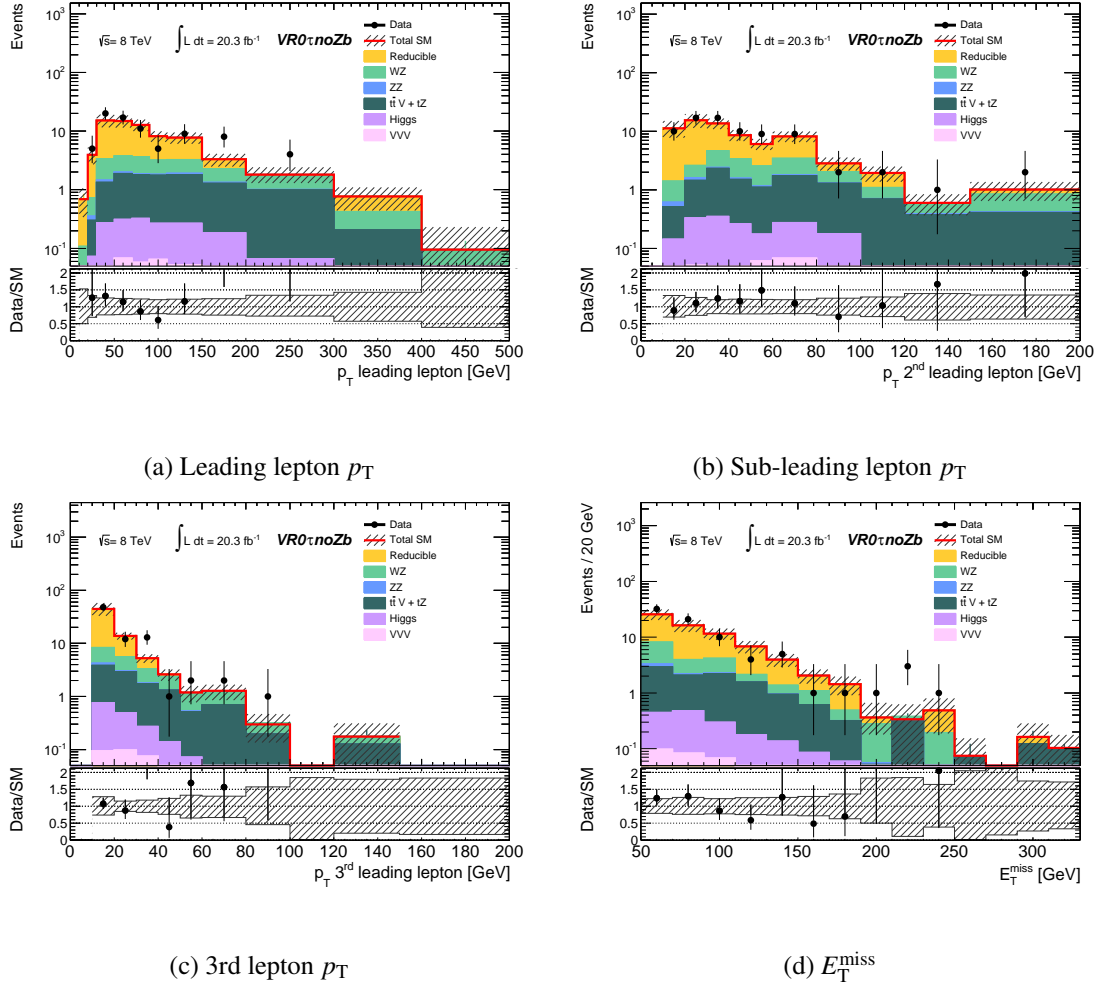


Figure 8.4: Distributions in  $VR0\tau noZa$ .

Figure 8.5: Distributions in  $VR0\tau noZb$ .

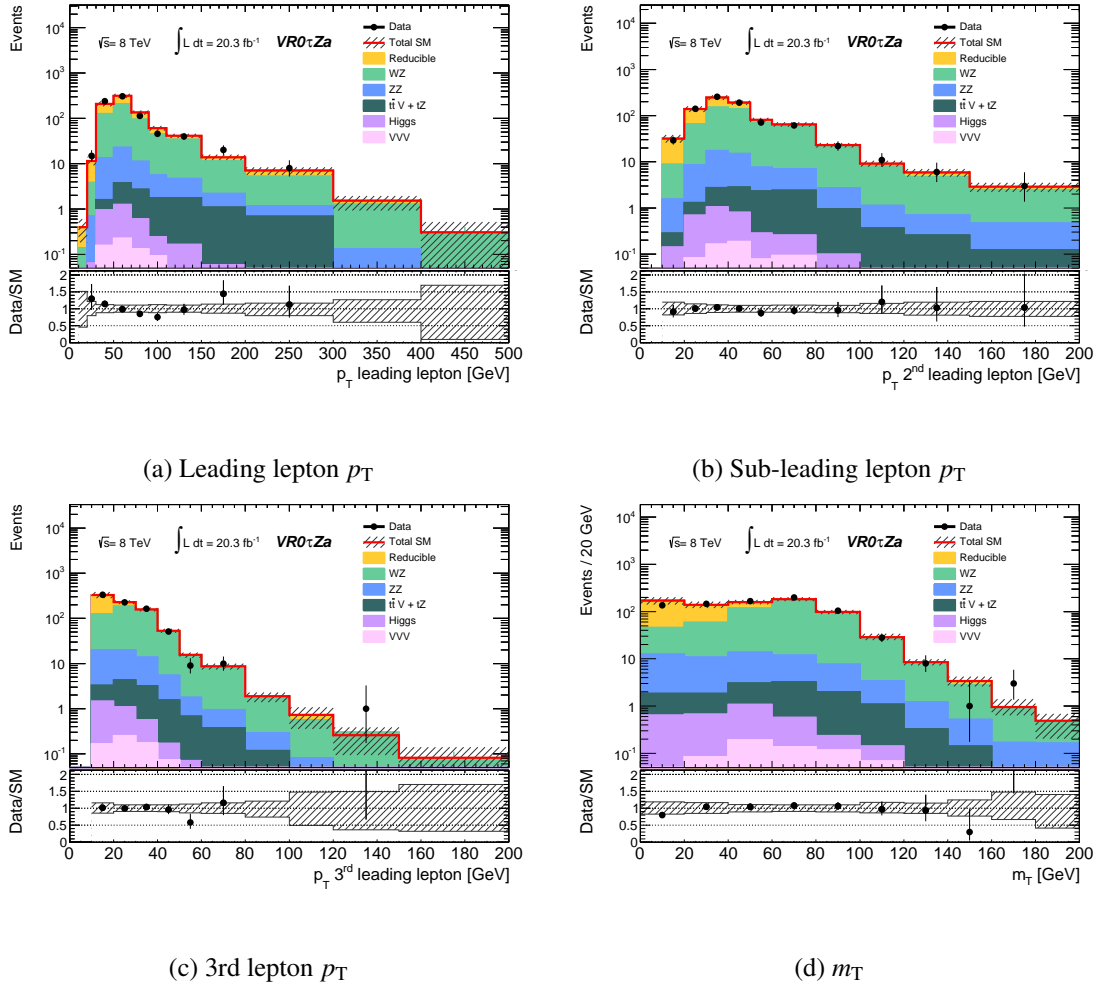


Figure 8.6: Distributions in  $VR0\tau Z_a$ .

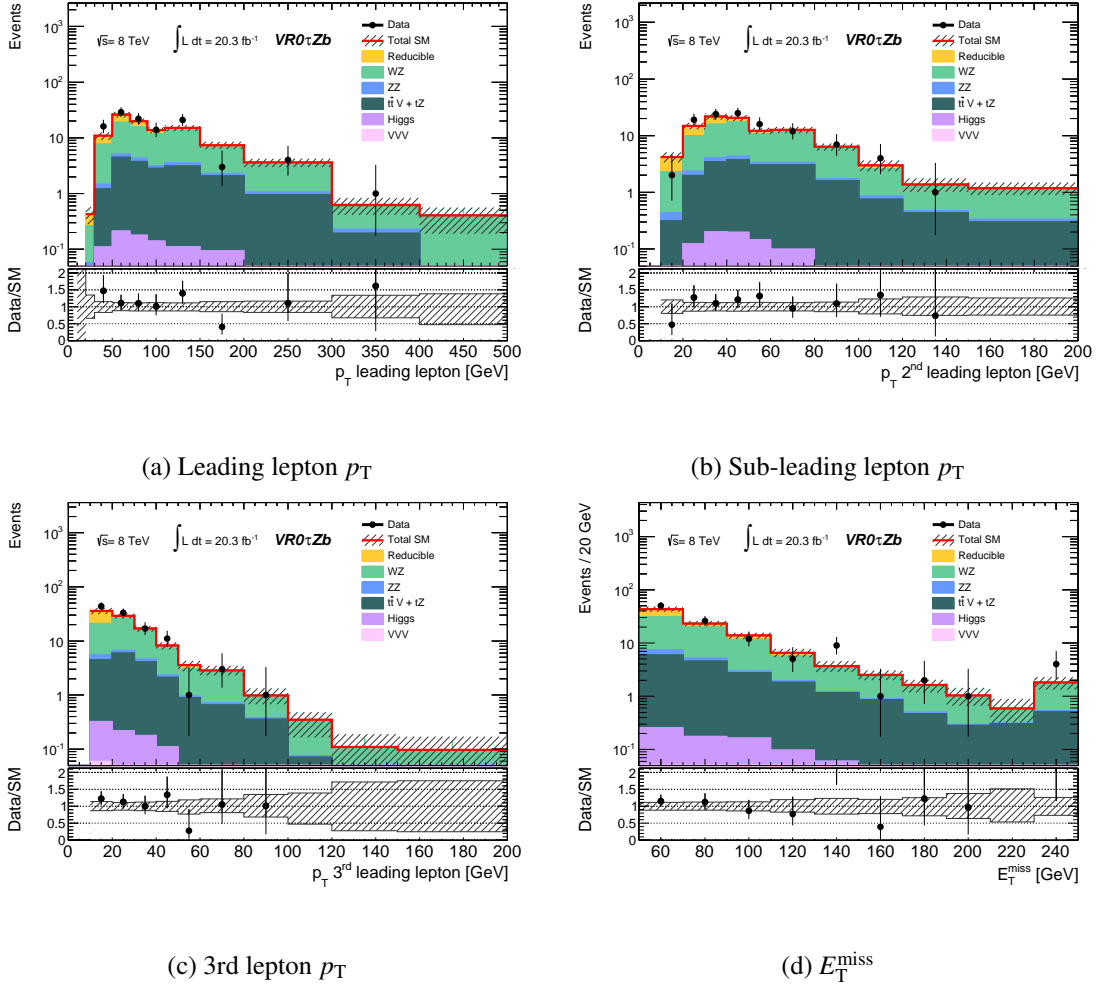
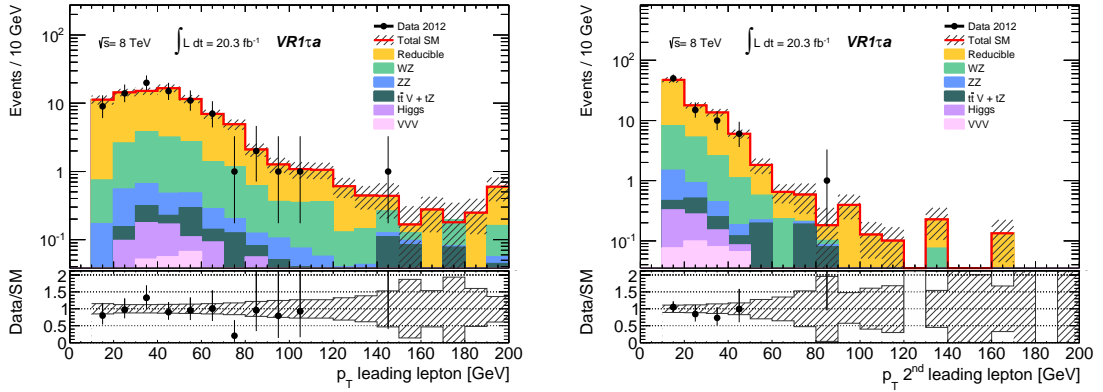
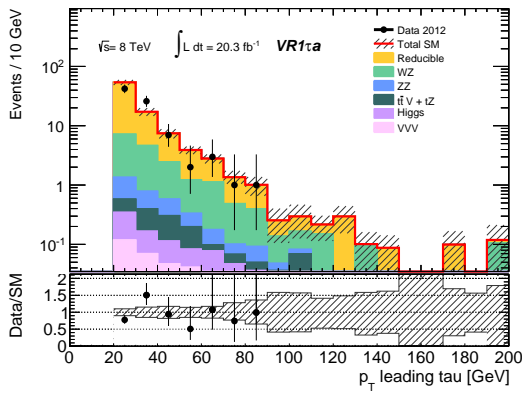


Figure 8.7: Distributions in VR0τZb.

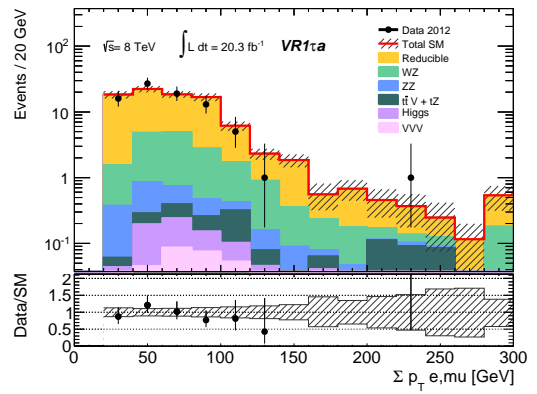


(a) Leading lepton  $p_T$

(b) Sub-leading lepton  $p_T$



(c) Leading tau  $p_T$



(d)  $\sum p_T(\ell)$

Figure 8.8: Distributions in VR1  $\tau a$ .



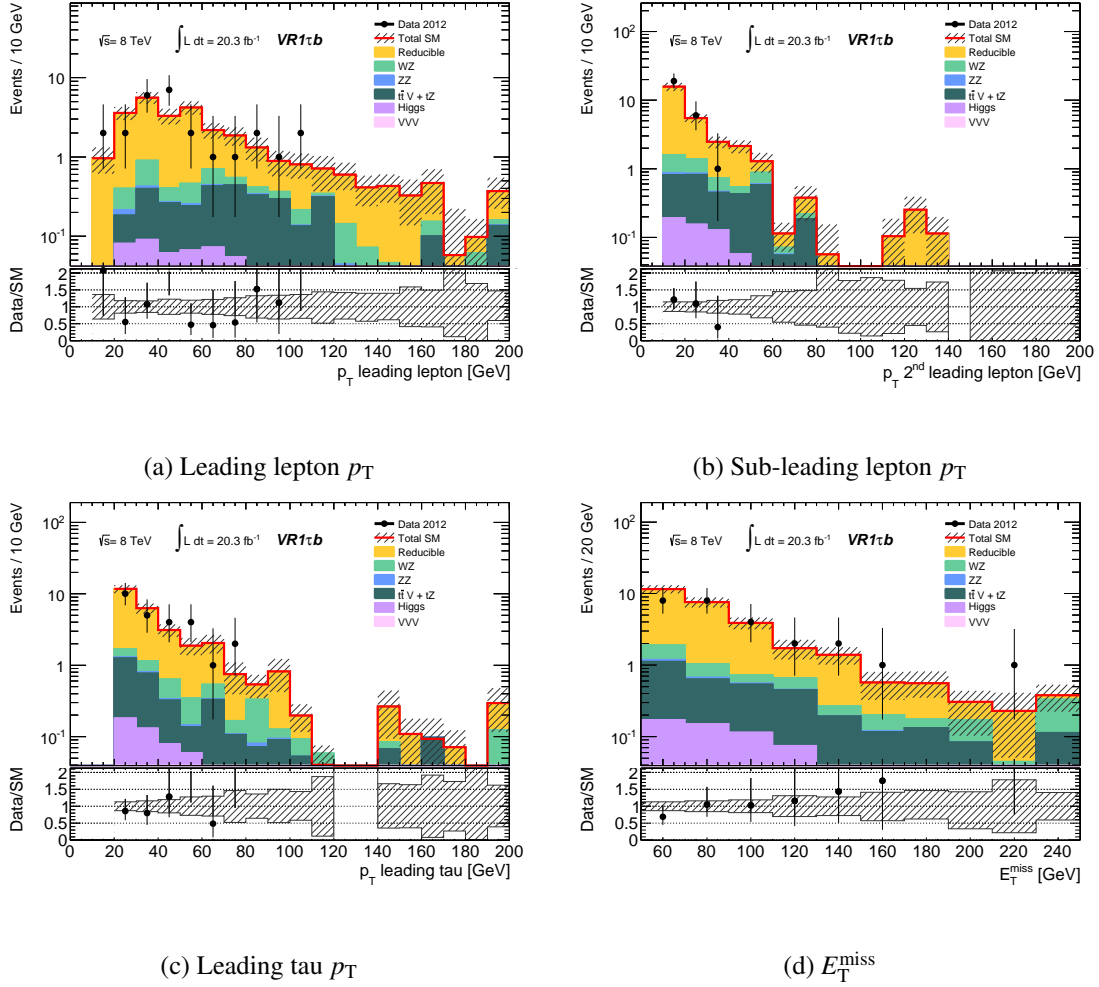
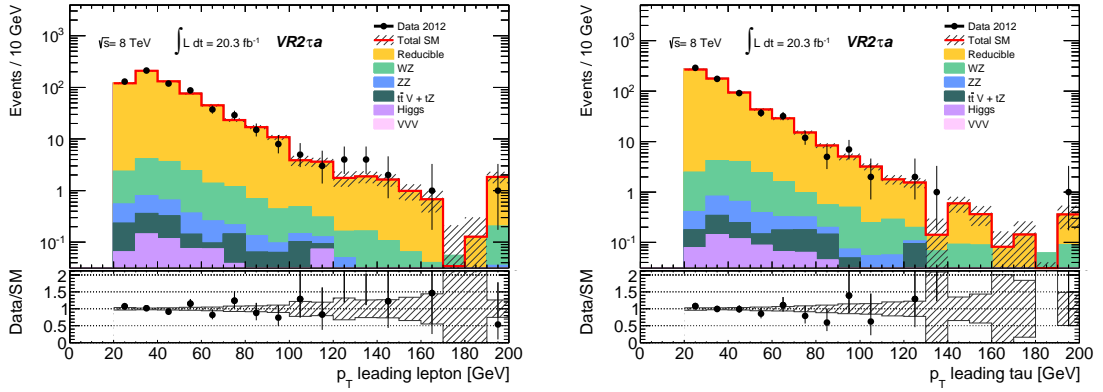
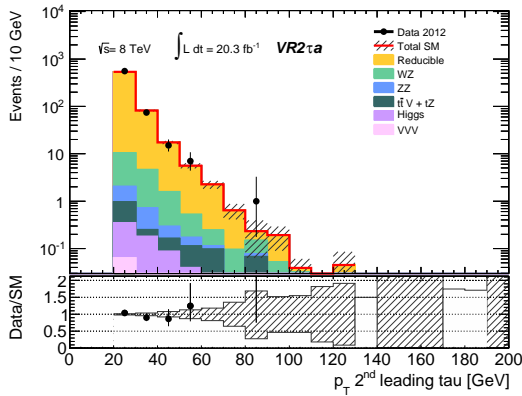


Figure 8.9: Distributions in VR1 $\tau$ b.

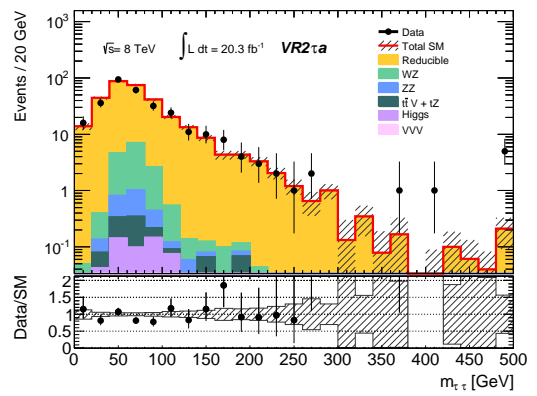


(a) Leading lepton  $p_T$

(b) Leading tau  $p_T$



(c) Sub-leading tau  $p_T$



(d)  $m_{\tau\tau}$

Figure 8.10: Distributions in  $VR2\tau a$ .

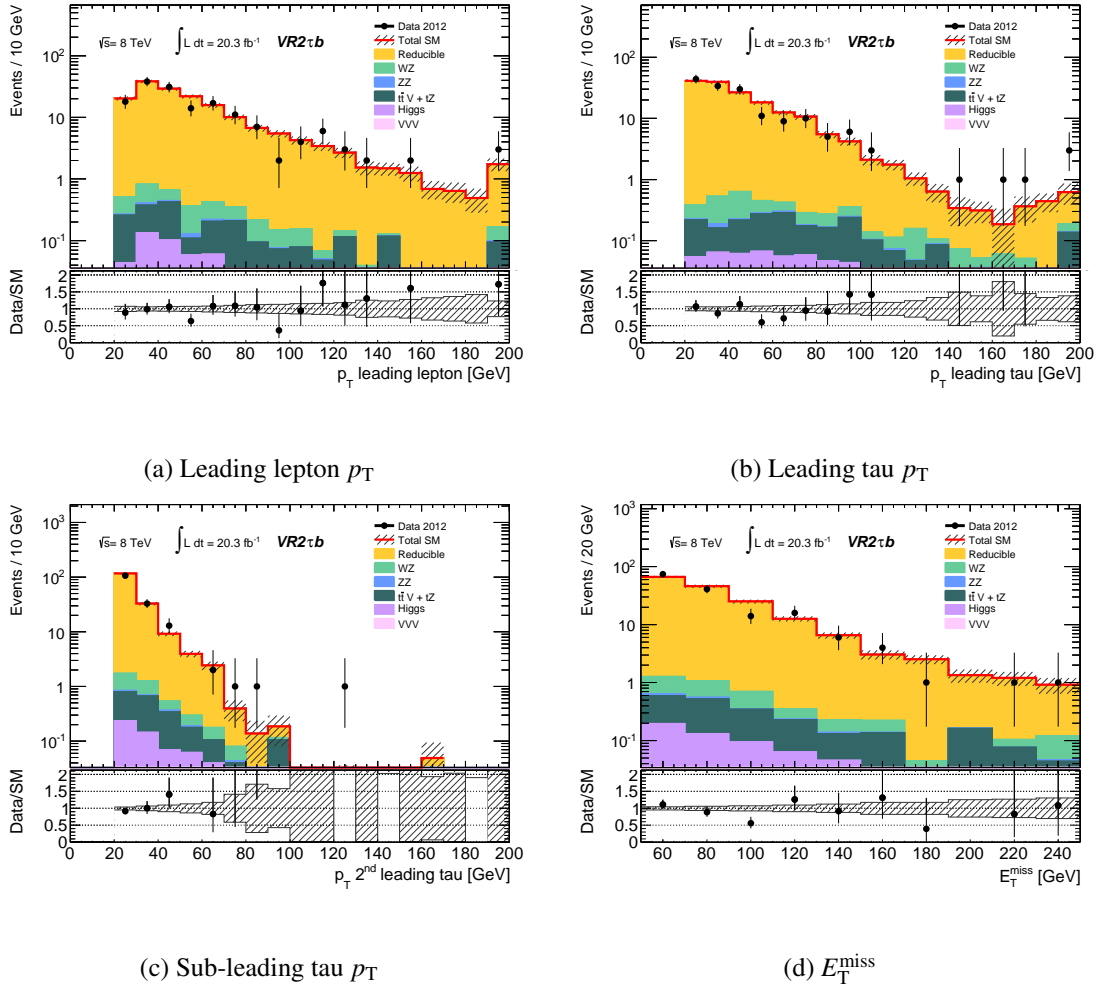


Figure 8.11: Distributions in VR2 $\tau$ b.

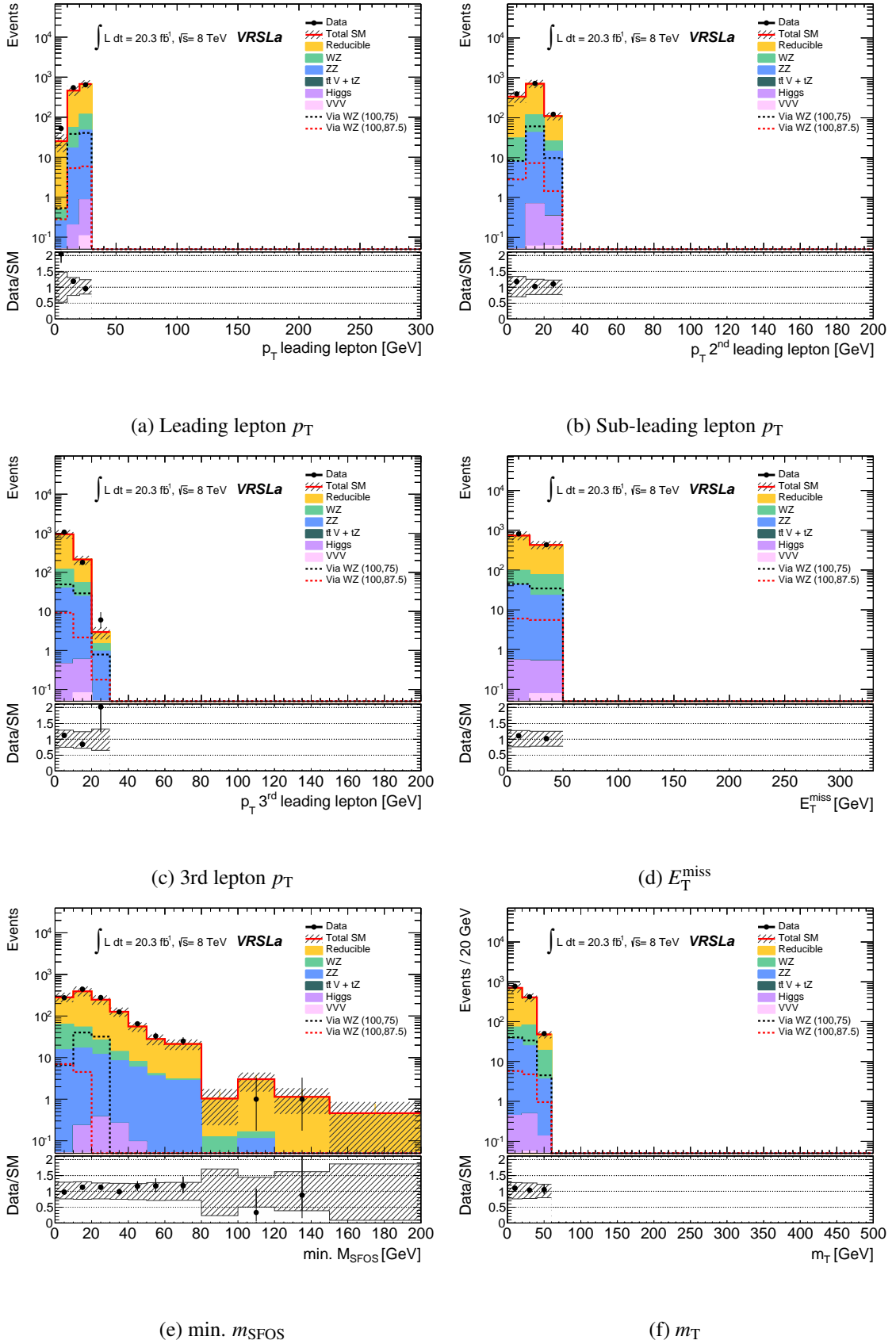


Figure 8.12: Distributions in VRSLa.

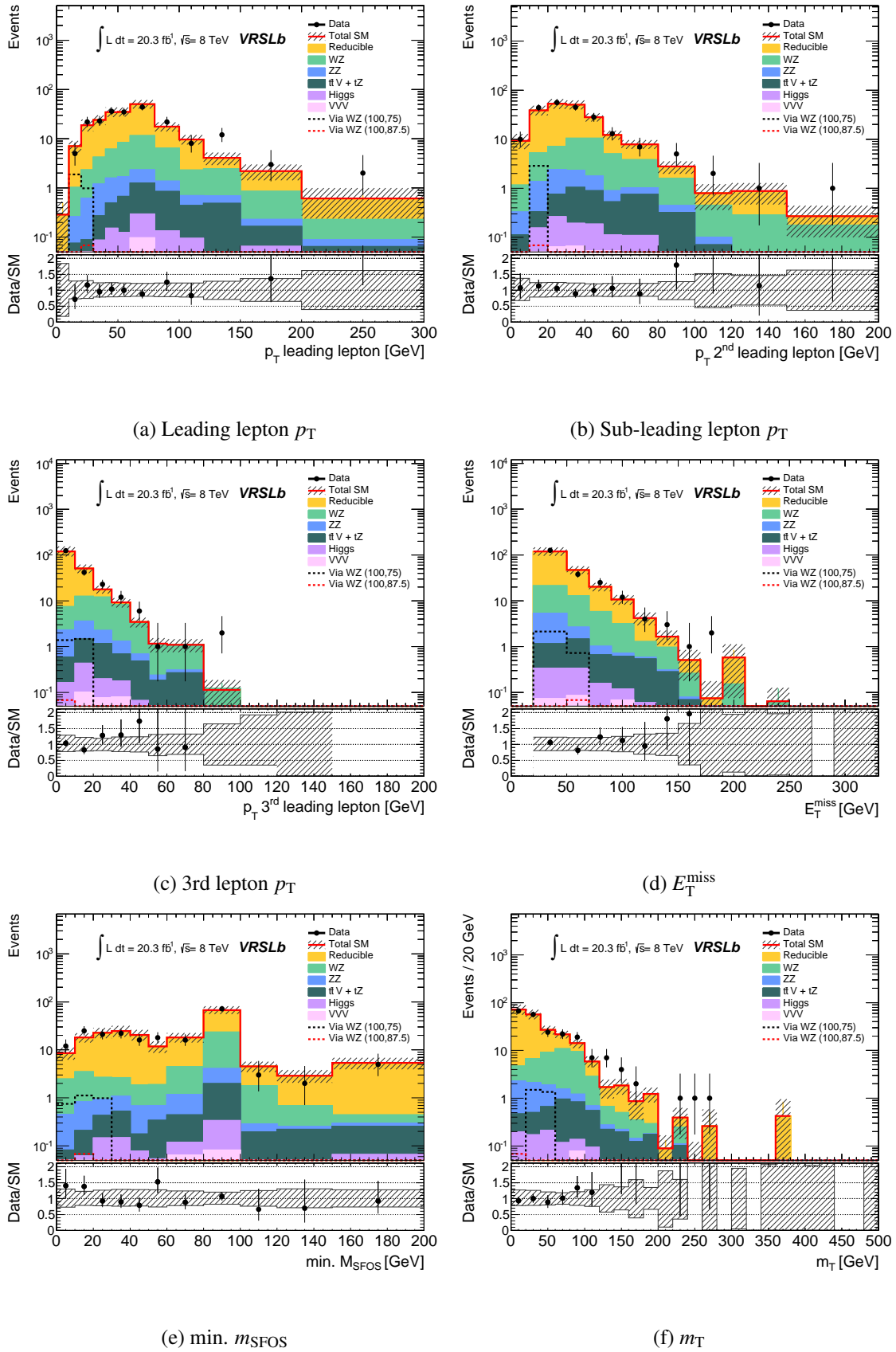


Figure 8.13: Distributions in VRSLb.

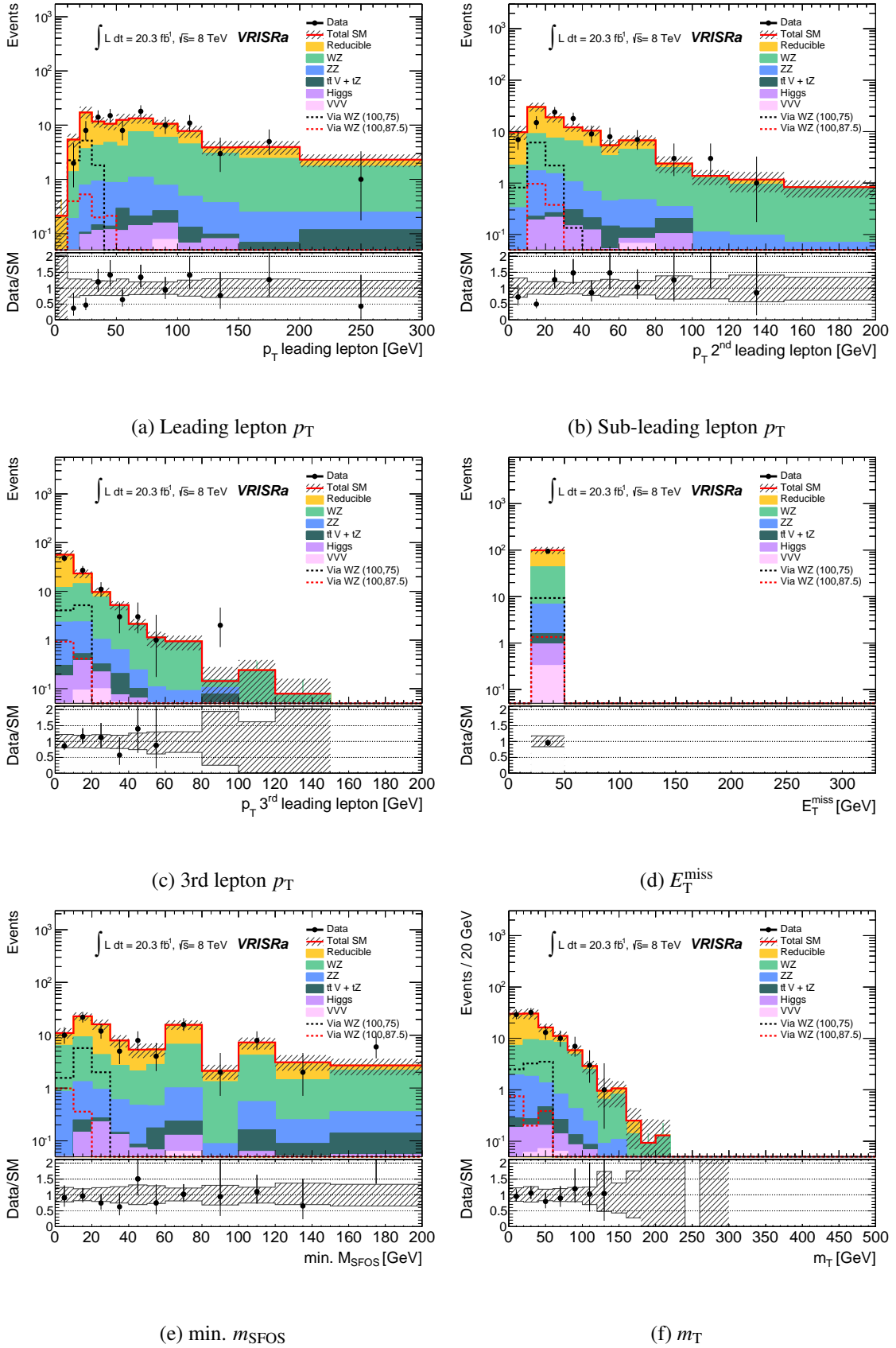


Figure 8.14: Distributions in VRISRa.

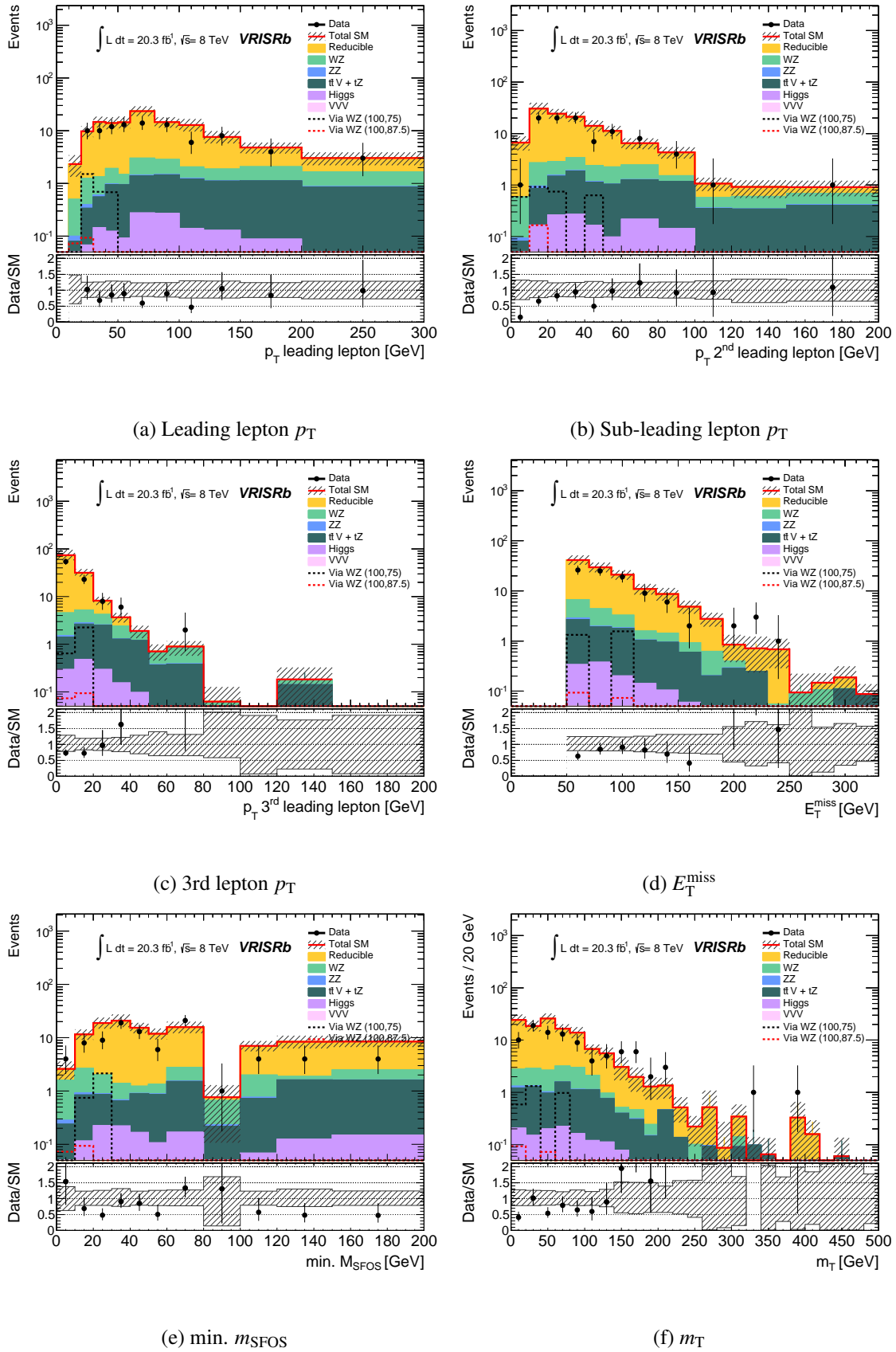


Figure 8.15: Distributions in VRISRb.

## Chapter 9

# Results and Interpretation

A blind analysis, in which the data in the signal regions are blinded until reliable background modelling is achieved, is performed in this analysis in order to prevent an artificial bias against the data. Only in the validation regions, the background modeling has been scrutinised with the data, whereas the data in signal regions are blinded. Since the validation of the background modelling in the validation regions are satisfactory, the signal regions are unblinded. In Sec. 9.1, the amount of observed data in each region and some distributions are reported. In Sec. 9.2, the statistical method of the interpretation is described. Finally, the interpretations are given in the model-independent and the model-dependent forms.

### 9.1 Observed data

Observed data in the signal regions are shown in Tab. 9.1 for  $WZ/h$ -mediated scenario signal regions ( $SR0\tau_a$ ,  $SR0\tau_b$ ,  $SR1\tau$  and  $SR2\tau$ ) in Category-A, and Tab. 9.2 for compressed  $WZ$ -mediated scenario signal regions ( $SRSL$ ,  $SRISR$ ) in Category-B. Statistic and systematic uncertainties on the background estimation described in Chap. 7 are taken into account for all results. Figures 9.1–9.7 show the corresponding distributions for  $SR0\tau_b$  (Fig. 9.1),  $SR1\tau$  (Fig. 9.2),  $SR2\tau$  (Fig. 9.3),  $SRSLa$  (Fig. 9.4),  $SRSLb$  (Fig. 9.5),  $SRISRa$  (Fig. 9.6) and  $SRISRb$  (Fig. 9.7). Whereas some regions have excesses with nearly  $2\sigma$  deviation, no significant deviation from the SM expectation has been observed.

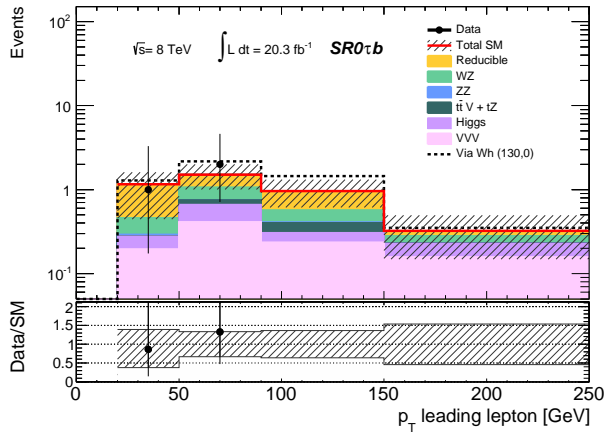


Table 9.1: Expected SM background events and observed events in data in the binned signal regions for Category-A for  $WZ/h$ -mediated scenario (SR0 $\tau$ a, SR0 $\tau$ b, SR1 $\tau$ , SR2 $\tau$ ). Statistic and systematic uncertainties on the background estimation are taken into account. Some regions have excess from the SM expectation, the statistical significance of those will be discussed in the next section.

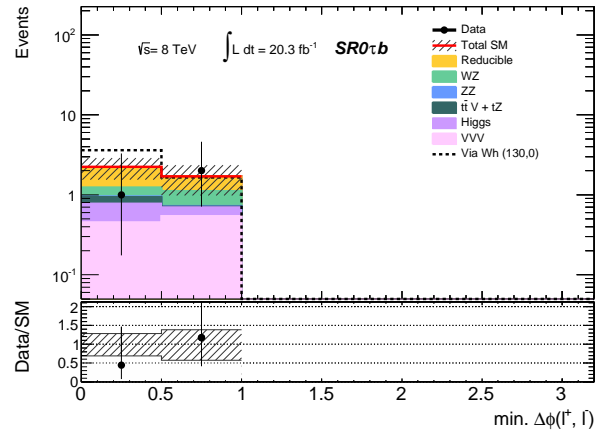
SRs	Irreducible bg.	Reducible bg.	Total SM	Data
SR0 $\tau$ a-bin1	15.8 <sup>+3.6</sup> <sub>-3.4</sub>	6.7 <sup>+2.4</sup> <sub>-2.4</sub>	23 <sup>+4</sup> <sub>-4</sub>	36
SR0 $\tau$ a-bin2	3.4 <sup>+1.4</sup> <sub>-1.4</sub>	0.8 <sup>+0.4</sup> <sub>-0.4</sub>	4.2 <sup>+1.5</sup> <sub>-1.5</sub>	5
SR0 $\tau$ a-bin3	9.0 <sup>+1.7</sup> <sub>-1.7</sub>	1.6 <sup>+0.7</sup> <sub>-0.8</sub>	10.6 <sup>+1.8</sup> <sub>-1.8</sub>	9
SR0 $\tau$ a-bin4	5.9 <sup>+1.3</sup> <sub>-1.3</sub>	2.66 <sup>+1.04</sup> <sub>-0.99</sub>	8.5 <sup>+1.7</sup> <sub>-1.6</sub>	9
SR0 $\tau$ a-bin5	8.6 <sup>+1.8</sup> <sub>-1.8</sub>	4.3 <sup>+1.6</sup> <sub>-1.4</sub>	12.9 <sup>+2.4</sup> <sub>-2.3</sub>	11
SR0 $\tau$ a-bin6	4.6 <sup>+1.7</sup> <sub>-1.6</sub>	2.0 <sup>+0.8</sup> <sub>-0.8</sub>	6.6 <sup>+1.9</sup> <sub>-1.8</sub>	13
SR0 $\tau$ a-bin7	10.1 <sup>+1.7</sup> <sub>-1.7</sub>	4.0 <sup>+1.5</sup> <sub>-1.4</sub>	14.1 <sup>+2.2</sup> <sub>-2.2</sub>	15
SR0 $\tau$ a-bin8	0.69 <sup>+0.32</sup> <sub>-0.31</sub>	0.40 <sup>+0.27</sup> <sub>-0.26</sub>	1.1 <sup>+0.4</sup> <sub>-0.4</sub>	1
SR0 $\tau$ a-bin9	18.3 <sup>+3.3</sup> <sub>-3.1</sub>	4.1 <sup>+1.3</sup> <sub>-1.2</sub>	22.4 <sup>+3.6</sup> <sub>-3.4</sub>	28
SR0 $\tau$ a-bin10	14.4 <sup>+2.6</sup> <sub>-2.7</sub>	1.9 <sup>+0.9</sup> <sub>-0.8</sub>	16.4 <sup>+2.8</sup> <sub>-2.8</sub>	24
SR0 $\tau$ a-bin11	21 <sup>+4</sup> <sub>-4</sub>	5.7 <sup>+2.1</sup> <sub>-1.9</sub>	27 <sup>+5</sup> <sub>-5</sub>	29
SR0 $\tau$ a-bin12	4.7 <sup>+1.4</sup> <sub>-1.4</sub>	0.9 <sup>+0.5</sup> <sub>-0.4</sub>	5.5 <sup>+1.5</sup> <sub>-1.4</sub>	8
SR0 $\tau$ a-bin13	648 <sup>+67</sup> <sub>-66</sub>	68 <sup>+21</sup> <sub>-19</sub>	715 <sup>+70</sup> <sub>-68</sub>	714
SR0 $\tau$ a-bin14	216 <sup>+33</sup> <sub>-33</sub>	2.2 <sup>+1.9</sup> <sub>-2.0</sub>	219 <sup>+33</sup> <sub>-33</sub>	214
SR0 $\tau$ a-bin15	64 <sup>+13</sup> <sub>-13</sub>	1.2 <sup>+0.6</sup> <sub>-0.6</sub>	65 <sup>+13</sup> <sub>-13</sub>	63
SR0 $\tau$ a-bin16	4.4 <sup>+1.7</sup> <sub>-1.5</sub>	0.14 <sup>+0.25</sup> <sub>-0.27</sub>	4.6 <sup>+1.7</sup> <sub>-1.5</sub>	3
SR0 $\tau$ a-bin17	58 <sup>+8</sup> <sub>-7</sub>	11.3 <sup>+3.5</sup> <sub>-3.2</sub>	69 <sup>+9</sup> <sub>-8</sub>	60
SR0 $\tau$ a-bin18	3.1 <sup>+1.4</sup> <sub>-1.4</sub>	0.27 <sup>+0.20</sup> <sub>-0.20</sub>	3.4 <sup>+1.4</sup> <sub>-1.4</sub>	1
SR0 $\tau$ a-bin19	1.0 <sup>+0.4</sup> <sub>-0.4</sub>	0.17 <sup>+0.16</sup> <sub>-0.15</sub>	1.2 <sup>+0.4</sup> <sub>-0.4</sub>	0
SR0 $\tau$ a-bin20	0.21 <sup>+0.14</sup> <sub>-0.14</sub>	0.08 <sup>+0.11</sup> <sub>-0.10</sub>	0.29 <sup>+0.18</sup> <sub>-0.17</sub>	0
SR0 $\tau$ b	2.4 <sup>+1.1</sup> <sub>-1.1</sub>	1.5 <sup>+0.4</sup> <sub>-0.4</sub>	3.8 <sup>+1.2</sup> <sub>-1.2</sub>	3
SR1 $\tau$	5.9 <sup>+0.9</sup> <sub>-0.8</sub>	4.3 <sup>+0.8</sup> <sub>-0.8</sub>	10.3 <sup>+1.2</sup> <sub>-1.2</sub>	13
SR2 $\tau$	2.4 <sup>+0.3</sup> <sub>-0.3</sub>	4.9 <sup>+0.7</sup> <sub>-0.7</sub>	7.2 <sup>+0.7</sup> <sub>-0.8</sub>	5

Table 9.2: Expected SM background events and observed events in data in the signal regions for Category-B (SRSL, SRISR). Statistical and systematic uncertainties on the background estimation are taken into account. The data amount of all signal regions completely agree with the SM expectation.

SRs	Irreducible bg.	Reducible bg.	Total SM	Data
SRSLa	0.82 <sup>+0.48</sup> <sub>-0.33</sub>	2.8 <sup>+1.5</sup> <sub>-2.2</sub>	3.7 <sup>+1.5</sup> <sub>-2.2</sub>	4
SRSLb	5.7 <sup>+1.5</sup> <sub>-1.2</sub>	9.7 <sup>+3.1</sup> <sub>-3.6</sub>	15.4 <sup>+3.3</sup> <sub>-3.8</sub>	15
SRISRa	0.58 <sup>+0.20</sup> <sub>-0.19</sub>	0.09 <sup>+0.08</sup> <sub>-0.08</sub>	0.67 <sup>+0.22</sup> <sub>-0.22</sub>	1
SRISRb	1.7 <sup>+0.4</sup> <sub>-0.4</sub>	1.4 <sup>+1.0</sup> <sub>-1.1</sub>	3.1 <sup>+1.1</sup> <sub>-1.2</sub>	3

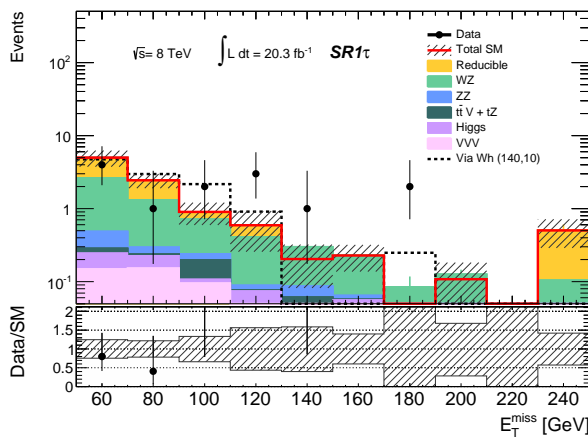


(a) Leading lepton  $p_T$

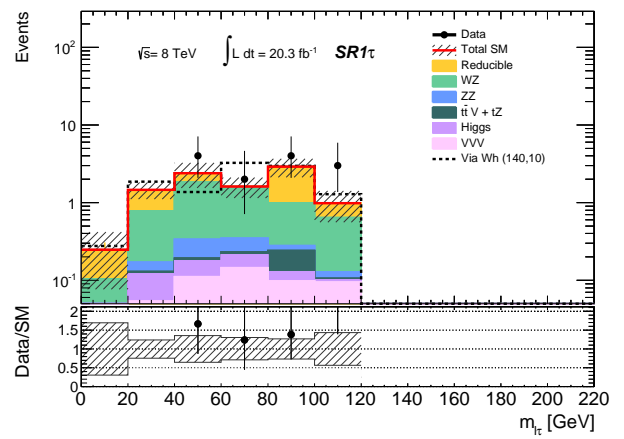


(b)  $\min. \Delta\phi_{\ell^+\ell^-}$

Figure 9.1: Distributions for  $SR0\tau b$ .



(a)  $E_T^{\text{miss}}$



(b)  $m_{\ell\tau}$

Figure 9.2: Distributions for  $SR1\tau$ .

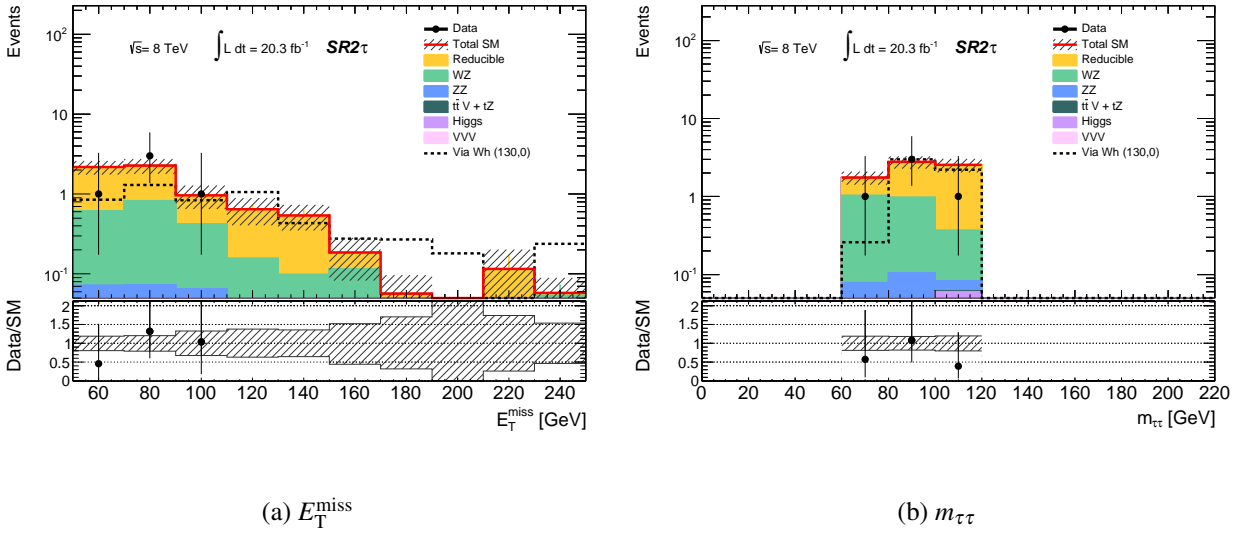


Figure 9.3: Distributions for SR2 $\tau$ .

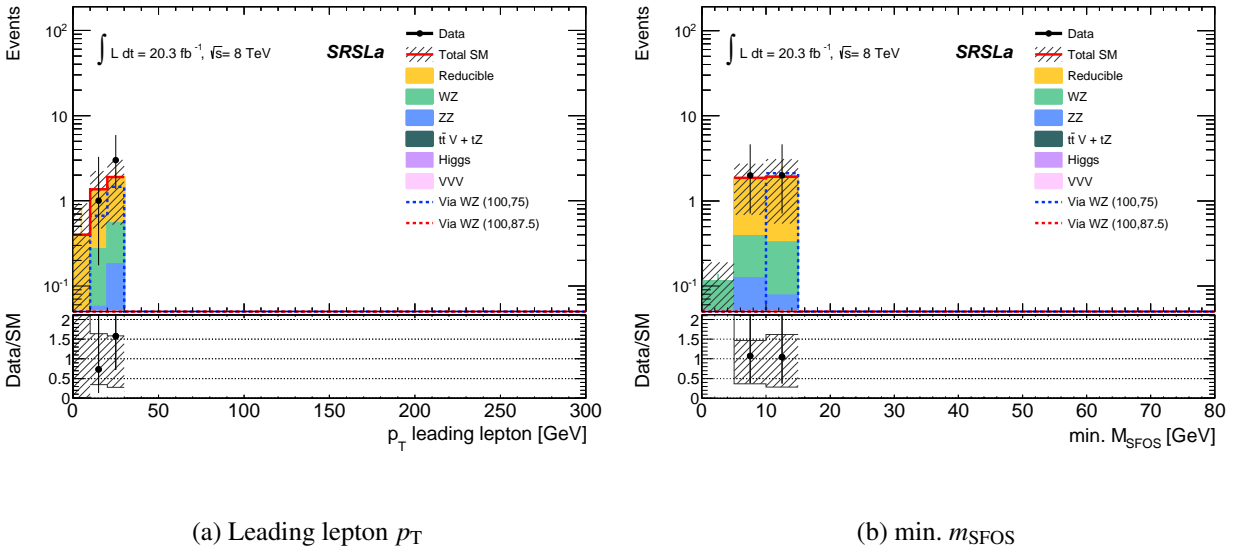
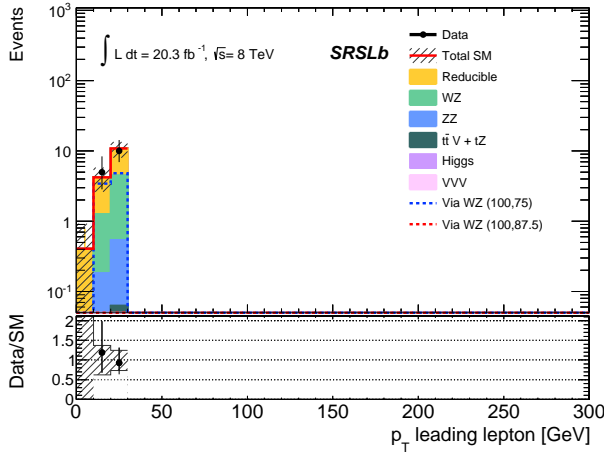
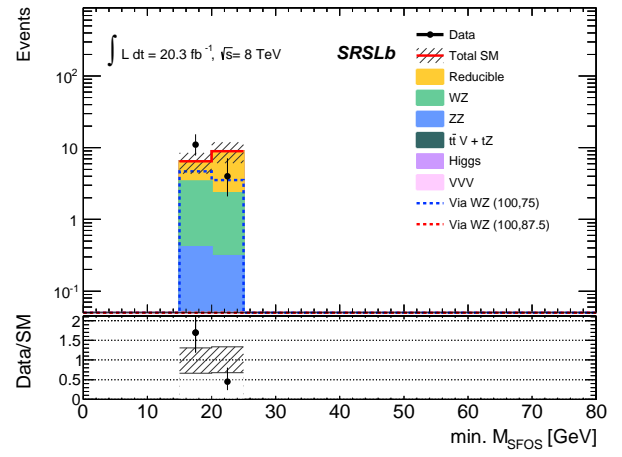


Figure 9.4: Distributions for SRSLa.

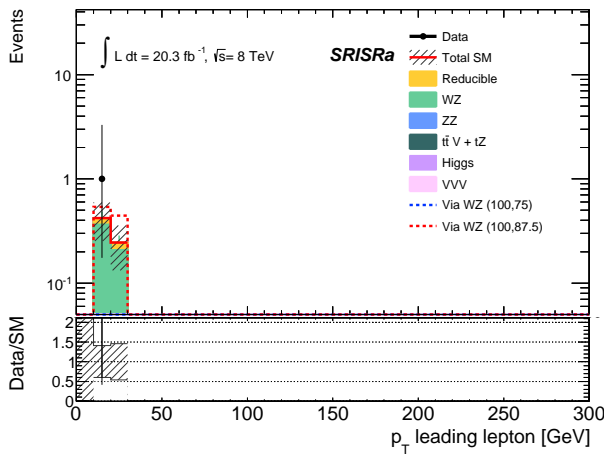


(a) Leading lepton  $p_T$

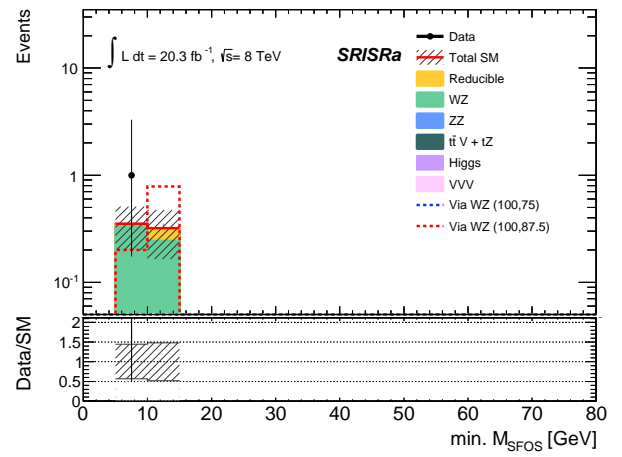


(b) min.  $m_{SFOS}$

Figure 9.5: Distributions for SRSLb.



(a) Leading lepton  $p_T$



(b) min.  $m_{SFOS}$

Figure 9.6: Distributions for SRISRa.

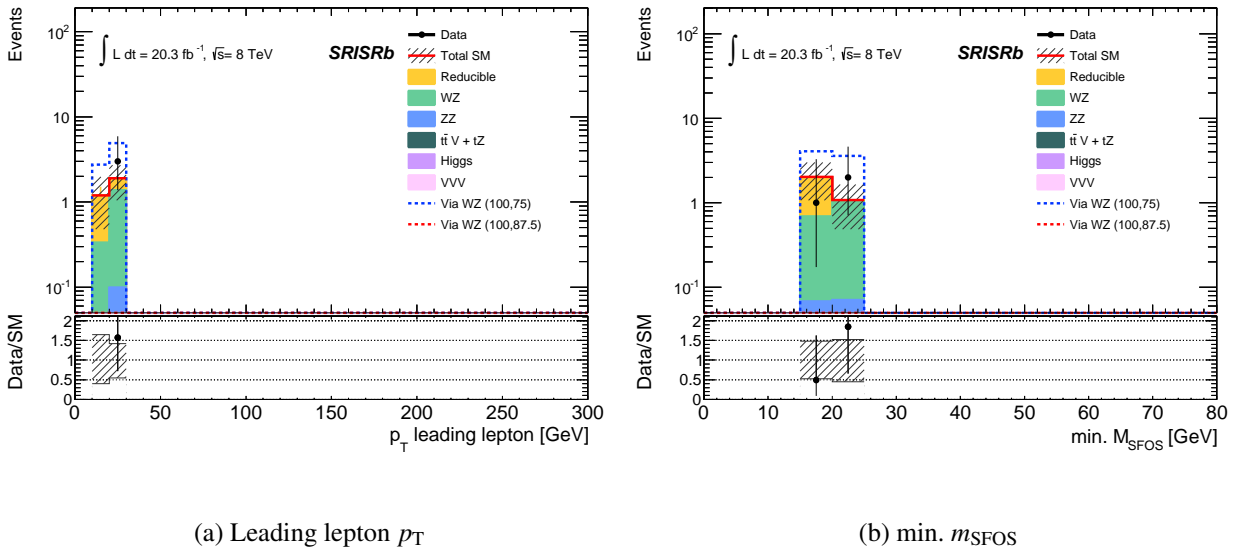


Figure 9.7: Distributions for SRISRb.

## 9.2 Statistical Interpretation of Results

As there is no significant excess in all signal regions, the assumed signal models should be limited. In this section, the exclusion limits for the models are described.

The compatibility with the Standard Model, exclusion limits on the visible cross sections and the exclusions are assessed with the profile log-likelihood ratio tests [171, 184]. This is following the ATLAS standard method for exclusion limit setting. The likelihood  $L(n_S)$  parametrises all uncertainties given in Chap. 7 and is defined as

$$L(n_S|\mu, b, \theta) = P(n_S|\lambda_S(\mu, b, \theta)) \times P_{\text{sys}}(\theta^0, \theta). \quad (9.1)$$

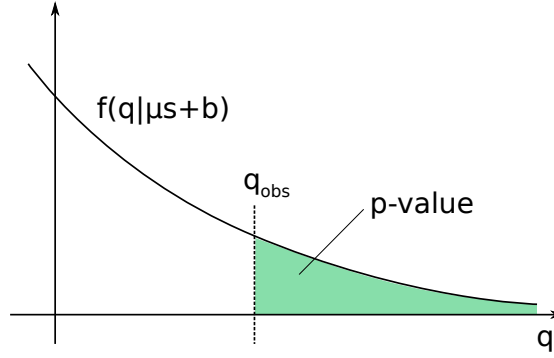
The parameter  $n_S$  represents the number of observed events in data,  $P(n_S)$  is a Poisson distribution modelling the expected event count in the signal regions. The  $\lambda_S$  is the Poisson expectation depending on the background prediction  $b$ . The  $\mu$  is the SUSY signal strength parameter, where  $\mu = 0$  corresponds to the situation where the SUSY signal does not exist, and  $\mu = 1$  corresponds to the situation where the signal expectation is the nominal value of the model under consideration. The parameter  $\theta$  shows the systematic uncertainties as nuisance parameters. The  $P_{\text{sys}}$  represents the constraints on systematic uncertainties. The  $\theta^0$  is the nominal values of the systematic uncertainties around which the parameter  $\theta$  can be varied, for example when maximising the likelihood.  $P_{\text{sys}}$  is the product of Gaussian distributions with  $\sigma = 1$ ,

$$P_{\text{sys}}(\theta^0, \theta) = \prod_{j \in S} G(\theta_j^0 - \theta_j), \quad (9.2)$$

where the  $G(x)$  is the Gaussian function and  $S$  is the full set of systematic uncertainties.

To test the hypothesis, the profile log-likelihood ratio is considered:

$$q_\mu = -2 \ln \lambda(\mu) = -2 \ln \frac{L(\mu, \hat{\theta})}{L(\hat{\mu}, \hat{\theta})}, \quad (9.3)$$

Figure 9.8: Illustration of the  $p$ -value.

where  $\hat{\theta}$  is the value of  $\theta$  that maximised the likelihood  $L$  for the specified  $\mu$  (local maximum), and  $\hat{\mu}$  and  $\hat{\theta}$  represent the values that maximised the likelihood  $L$  (global maximum). Thus the relation of  $L(\hat{\mu}, \hat{\theta}) > L(\mu, \hat{\theta})$  is always satisfied. The  $\lambda(\mu)$  is called the profile likelihood ratio. The profile log-likelihood ratio  $q_\mu$  represents the power of the likelihood for the specific  $\mu$  and is positive value. The high  $q_\mu$  value represents that there is large discrepancy between the observed data and the SM prediction. The quantity of the level of disagreement is computed as the  $p$ -value, which is understood as the probability of the situation  $q_\mu > q_\mu^{\text{obs}}$ :

$$p_\mu = \int_{q_\mu^{\text{obs}}}^{\infty} f(q_\mu | \mu s + b) dq_\mu, \quad (9.4)$$

where the function  $f(q_\mu | \mu s + b)$  represents the probability density function of the  $q_\mu$  under the assumption of the signal strength  $\mu$ . The  $p$ -value is illustrated in Fig. 9.8. The functions for the model-independent and the model-dependent limit setting are described in the corresponding sections below.

### 9.2.1 Model-independent limits

The model-independent limits is set without any assumptions about the signal models. This is then calculated with the amounts of events of observed data and the SM prediction.

If the case of the background only is considered,  $\mu \equiv 0$ , then

$$q_0 = \begin{cases} -2 \ln \lambda(0) & \hat{\mu} \geq 0, \\ 0 & \hat{\mu} < 0, \end{cases} \quad (9.5)$$

where the  $\hat{\mu}$  should be positive, because the SUSY signal should not be observed as negative contribution. To quantify the level of disagreement between the data and the hypothesis of  $\mu = 0$ , the  $p$ -value is calculated using the  $q_0$  value as

$$p_0 = \int_{q_0^{\text{obs}}}^{\infty} f(q_0 | b) dq_0, \quad (9.6)$$

where the function  $f(q_0 | b)$  represents the probability density function of the  $q_0$  under assumption of the background-only hypothesis. The  $p_0$  represents the level of the difference between data and known background. This includes no assumption for the signals. It is called the discovery  $p_0$  value.

For the upper limit setting, Eq. (9.3) should be redefined because the data with  $\hat{\mu} > \mu$  would not give

any information for the upper limit. Therefore, the  $q_\mu$  should be defined as

$$q_\mu = \begin{cases} -2 \ln \lambda(\mu) & \hat{\mu} \leq \mu, \\ 0 & \hat{\mu} > \mu. \end{cases} \quad (9.7)$$

Taking into account the SUSY signal case,  $\hat{\mu} < 0$  should not be considered. Since the SUSY provides the positive contribution, the signal strength for the maximum likelihood value  $\hat{\mu}$  should be positive. Thus the following test statistic  $q_\mu$  should be used to set upper limits as

$$q_\mu = \begin{cases} -2 \ln \frac{L(\mu, \hat{\theta}(\mu))}{L(0, \hat{\theta}(0))} & \hat{\mu} < 0, \\ -2 \ln \frac{L(\mu, \hat{\theta}(\mu))}{L(\hat{\mu}, \hat{\theta})} & 0 \leq \hat{\mu} \leq \mu, \\ 0 & \hat{\mu} > \mu. \end{cases} \quad (9.8)$$

The  $p$ -value calculation uses the same manner as Eq. (9.4). The upper limit on the number of new physics signals is derived as a  $\mu$  value at the corresponding  $p$ -value. The  $S^{95}$  denotes the 95% confidence level (CL) upper limits on the number of signals (the corresponding  $p$ -value is  $p_\mu = 0.05$ ). The 95% CL limit on the visible cross-section  $\langle \epsilon \sigma \rangle^{95}$  is simply derived using Eq. (2.1) as

$$\langle \epsilon \sigma \rangle^{95} = \frac{S^{95}}{\int \mathcal{L} dt}, \quad (9.9)$$

where the denominator is the integrated luminosity. They are calculated using the expected and the observed numbers of events.

The  $CL_b$  is the quantity of the deviation from the background only hypothesis. It is evaluated using the assumption of the number of signals as  $S^{95} (= \mu^{95})$ , thus

$$CL_b = 1 - p_{\mu^{95}}, \quad \text{such that } p_{\mu^{95}} = \int_{q_{\mu^{95}}^{\text{obs}}}^{\infty} f(q_{\mu^{95}}|b) dq_{\mu^{95}}. \quad (9.10)$$

Table 9.3 and Table 9.4 are the results of the quantities of the compatibility of the observed data with the SM background for the signal regions. The tables show the expected and the observed numbers of events, 95% upper limits on the number of events and the visible cross section,  $CL_b$  and the discovery  $p_0$  value. For the Category-A, the maximum significance of the background-only hypothesis is observed in the SR0 $\tau$ a-bin1 of  $1.98\sigma$  and next  $1.76\sigma$  in SR0 $\tau$ a-bin6 and  $1.44\sigma$  in SR0 $\tau$ a-bin10, while in the other region less than  $1\sigma$  deviations are observed. Therefore, there are no significant deviation from the expectation in the signal regions. For the Category-B, there are no excess in all of the signal regions.

Table 9.3: Compatibility of the observed data with the SM background for the signal regions in Category-A. The expected and observed number of events are shown, along with the 95% CL upper limits on the number of signal events  $S^{95}$ , as well as the limit on the visible cross-section  $\langle \epsilon\sigma \rangle^{95}$ . The  $CL_b$  is the confidence level observed for the background only hypothesis. The  $p_0$  is the discovery  $p$ -value of the background only hypothesis. The  $\sigma$  is shown as the significance of the background only hypothesis.

	$N_{\text{exp}}$	$N_{\text{obs}}$	$S_{\text{obs}}^{95}$	$S_{\text{exp}}^{95}$	$\langle \epsilon\sigma \rangle_{\text{obs}}^{95} [\text{fb}]$	$\langle \epsilon\sigma \rangle_{\text{exp}}^{95} [\text{fb}]$	$CL_b$	$p_0$	$\sigma$
SR0 $\tau$ a-bin1	$23_{-4}^{+4}$	36	26	$14_{-4}^{+6}$	1.29	$0.70_{-0.19}^{+0.30}$	0.96	0.02	1.98
SR0 $\tau$ a-bin2	$4.2_{-1.5}^{+1.5}$	5	6.8	$6.2_{-1.8}^{+3.0}$	0.34	$0.31_{-0.09}^{+0.15}$	0.60	0.38	0.31
SR0 $\tau$ a-bin3	$10.6_{-1.8}^{+1.8}$	9	7.3	$8.3_{-2.4}^{+3.9}$	0.36	$0.41_{-0.12}^{+0.19}$	0.35	0.50	
SR0 $\tau$ a-bin4	$8.5_{-1.6}^{+1.7}$	9	8.0	$7.7_{-2.2}^{+3.7}$	0.39	$0.38_{-0.11}^{+0.18}$	0.55	0.44	0.15
SR0 $\tau$ a-bin5	$12.9_{-2.3}^{+2.4}$	11	7.9	$9.0_{-2.7}^{+4.2}$	0.39	$0.45_{-0.13}^{+0.21}$	0.34	0.50	
SR0 $\tau$ a-bin6	$6.6_{-1.8}^{+1.9}$	13	14.1	$8.1_{-2.3}^{+3.7}$	0.69	$0.40_{-0.11}^{+0.18}$	0.93	0.04	1.76
SR0 $\tau$ a-bin7	$14.1_{-2.2}^{+2.2}$	15	10.4	$9.5_{-2.7}^{+4.4}$	0.51	$0.47_{-0.13}^{+0.22}$	0.58	0.41	0.22
SR0 $\tau$ a-bin8	$1.1_{-0.4}^{+0.4}$	1	3.5	$3.6_{-1.3}^{+2.2}$	0.17	$0.18_{-0.06}^{+0.11}$	0.47	0.50	
SR0 $\tau$ a-bin9	$22.4_{-3.4}^{+3.6}$	28	17.5	$12.6_{-3.5}^{+5.7}$	0.86	$0.62_{-0.17}^{+0.28}$	0.80	0.18	0.92
SR0 $\tau$ a-bin10	$16.4_{-2.8}^{+2.8}$	24	18.1	$11.2_{-3.1}^{+5.1}$	0.89	$0.55_{-0.15}^{+0.25}$	0.91	0.08	1.44
SR0 $\tau$ a-bin11	$27_{-5}^{+5}$	29	15	$13.7_{-3.9}^{+5.9}$	0.76	$0.68_{-0.19}^{+0.29}$	0.60	0.39	0.29
SR0 $\tau$ a-bin12	$5.5_{-1.4}^{+1.5}$	8	9.1	$6.9_{-2.0}^{+3.3}$	0.45	$0.34_{-0.10}^{+0.16}$	0.77	0.20	0.83
SR0 $\tau$ a-bin13	$715_{-68}^{+70}$	714	134	$134_{-34}^{+46}$	6.58	$6.61_{-1.68}^{+2.26}$	0.49	0.50	
SR0 $\tau$ a-bin14	$219_{-33}^{+33}$	214	64.5	$67_{-17}^{+23}$	3.18	$3.31_{-0.86}^{+1.12}$	0.45	0.50	
SR0 $\tau$ a-bin15	$65_{-13}^{+13}$	63	28	$30_{-7}^{+11}$	1.38	$1.46_{-0.36}^{+0.52}$	0.45	0.50	
SR0 $\tau$ a-bin16	$4.6_{-1.5}^{+1.7}$	3	4.8	$6.0_{-1.8}^{+2.9}$	0.23	$0.30_{-0.09}^{+0.15}$	0.31	0.50	
SR0 $\tau$ a-bin17	$69_{-8}^{+9}$	60	17	$22_{-6}^{+8}$	0.84	$1.07_{-0.30}^{+0.39}$	0.22	0.50	
SR0 $\tau$ a-bin18	$3.4_{-1.4}^{+1.4}$	1	3.6	$5.0_{-1.5}^{+2.6}$	0.18	$0.25_{-0.08}^{+0.13}$	0.22	0.50	
SR0 $\tau$ a-bin19	$1.2_{-0.4}^{+0.4}$	0	2.4	$3.6_{-1.3}^{+2.2}$	0.12	$0.18_{-0.07}^{+0.11}$	0.20	0.50	
SR0 $\tau$ a-bin20	$0.29_{-0.17}^{+0.18}$	0	2.2	$2.6_{-1.0}^{+1.9}$	0.11	$0.13_{-0.05}^{+0.09}$	0.37	0.50	
SR0 $\tau$ b	$3.8_{-1.2}^{+1.2}$	3	5.0	$5.7_{-1.7}^{+2.8}$	0.25	$0.28_{-0.08}^{+0.14}$	0.38	0.50	
SR1 $\tau$	$10.3_{-1.2}^{+1.2}$	13	10.6	$8.2_{-2.4}^{+3.9}$	0.52	$0.40_{-0.12}^{+0.19}$	0.75	0.22	0.77
SR2 $\tau$	$7.2_{-0.8}^{+0.7}$	5	5.2	$6.8_{-2.0}^{+3.4}$	0.25	$0.34_{-0.10}^{+0.17}$	0.23	0.50	

Table 9.4: Compatibility of the observed data with the SM background for the signal regions in Category-B. The expected and observed numbers of events are shown, along with the 95% CL upper limits on the number of signal events  $S^{95}$ , as well as the limit on the visible cross-section  $\langle \epsilon\sigma \rangle^{95}$ . The  $CL_b$  is the confidence level observed for the background only hypothesis. The  $p_0$  is the discovery  $p$ -value of the background-only hypothesis.

Signal channel	$N_{\text{exp}}$	$N_{\text{obs}}$	$S_{\text{obs}}^{95}$	$S_{\text{exp}}^{95}$	$\langle \epsilon\sigma \rangle_{\text{obs}}^{95} [\text{fb}]$	$CL_b$	$p_0$
SRSLa	$3.7_{-2.2}^{+1.5}$	4	8.3	$8.2_{-2.2}^{+1.7}$	0.41	0.59	0.47
SRSLb	$15.4_{-3.8}^{+3.3}$	15	12.6	$12.6_{-3.0}^{+5.2}$	0.62	0.50	0.5
SRISRa	$0.67_{-0.22}^{+0.22}$	1	4.0	$3.8_{-0.3}^{+0.6}$	0.20	0.69	0.36
SRISRb	$1.4_{-1.1}^{+1.0}$	3	6.1	$6.0_{-1.3}^{+2.1}$	0.30	0.54	0.5



### 9.2.2 Model-dependent limits

The model-dependent limit setting is following so-called  $CL_s$  method [185]. This method uses the log-likelihood ratio between the SUSY signal plus background ( $L_{s+b}$ ,  $\mu = 1$ ) and background-only ( $L_b$ ,  $\mu = 0$ ), defined as following equation

$$q = -2 \ln \frac{L_{s+b}}{L_b} = -2 \ln \frac{L(\mu = 1, \hat{\theta}(1))}{L(\mu = 0, \hat{\theta}(0))}. \quad (9.11)$$

Using the  $q$  as a test statistic, the quantities  $p_{s+b}$  and  $p_b$  are defined as

$$p_{s+b} = P(q \geq q_{\text{obs}} | s+b) = \int_{q_{\text{obs}}}^{\infty} f(q|s+b) dq, \quad (9.12)$$

$$p_b = P(q \leq q_{\text{obs}} | b) = \int_{-\infty}^{q_{\text{obs}}} f(q|b) dq, \quad (9.13)$$

where the  $f(q|s+b)$  and  $f(q|b)$  are the probability density functions for signal plus background and background-only hypotheses, respectively. Their relation is illustrated in Fig. 9.9. Then the quantity called  $CL_s$  is defined as

$$CL_s = \frac{p_{s+b}}{1 - p_b}. \quad (9.14)$$

The exclusion limit corresponding 95% CL is obtained from the formula  $CL_s < 0.05$ . After applying the  $CL_s$  method to the SUSY scenarios decaying via  $WZ$  and  $Wh$  channels, the exclusion limits with 95% CL are obtained in Figs. 9.10 for Category-A analysis and Fig. 9.11 for Category-B analysis. In each category, the signal regions are orthogonal then they can be statistically combined. The yellow bands in these figures represent the  $1\sigma$  bands of the background uncertainties. If the background estimation is precisely performed, the yellow bands should be narrow.

From the Category-A analyses, the channel of the simplified model for SUSY decays via on-shell  $WZ$  with  $m_{\tilde{\chi}_1^\pm, \tilde{\chi}_2^0} < 360 \text{ GeV}$  for  $m_{\tilde{\chi}_1^0} = 0 \text{ GeV}$  is excluded. For the off-shell  $WZ$  channel, the observed limit is weaker than the expected limit with approximately  $2\sigma$  in the small  $\Delta m_{\tilde{\chi}_2^0, \tilde{\chi}_1^0}$  region due to the larger amount of observed events in SR0 $\tau$ a-bin1 than expected. For the  $Wh$  channel, the exclusion limit is set up to  $m_{\tilde{\chi}_1^\pm, \tilde{\chi}_2^0} \sim 150 \text{ GeV}$ .

From the Category-B analyses, the compressed mass region of  $m_{\tilde{\chi}_1^\pm, \tilde{\chi}_2^0} < 110 \text{ GeV}$  and  $m_{\tilde{\chi}_1^0}$  between 60 GeV and 80 GeV is excluded.

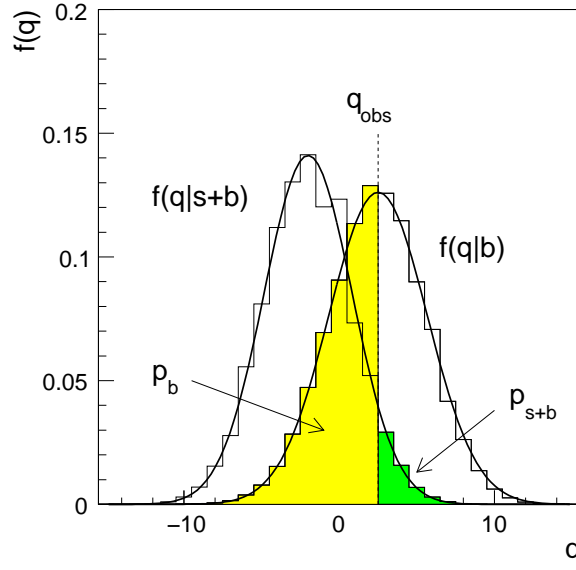
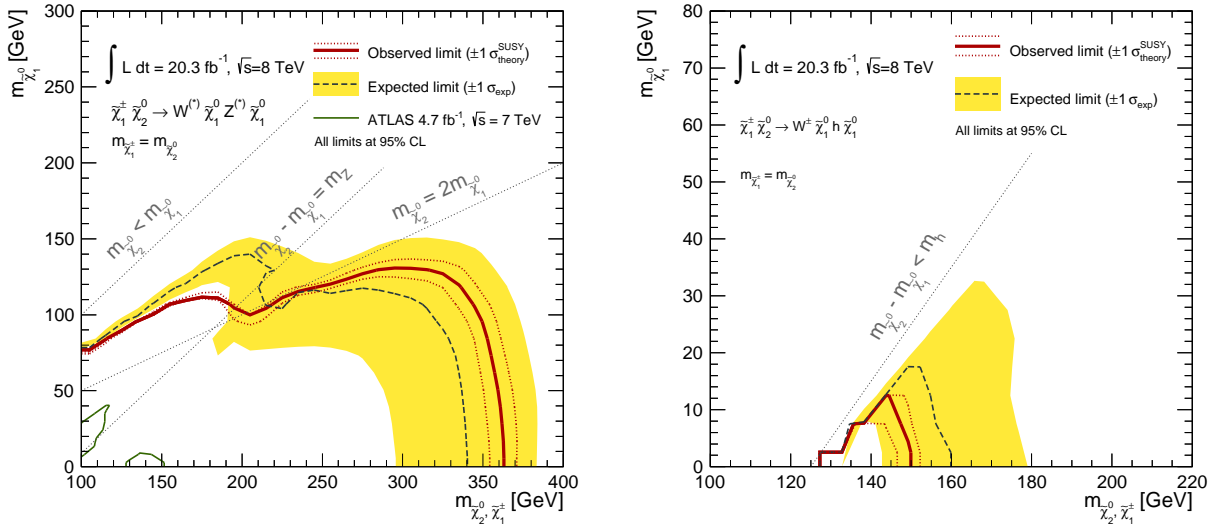


Figure 9.9: Example of distributions of the test variable  $q$  under the signal plus background and background-only hypotheses [186].



(a) Simplified model for SUSY decays via  $WZ$

(b) Simplified model for SUSY decays via  $Wh$

Figure 9.10: Exclusion limit contours for the simplified models for SUSY scenarios decay via  $WZ$  (a) and  $Wh$  (b). All signal regions of Category-A are statistically combined. In figures, the region surrounded by the red solid lines are the observed exclusion limits with 95% CL. The red dashed lines represent the  $\pm 1\sigma$  movable regions by the theory uncertainties. Similarly, the region surrounded by the black dashed lines are the expected exclusion limits with 95% CL. The yellow regions represent the  $\pm 1\sigma$  uncertainties. The exclusion limit of the results of ATLAS  $\sqrt{s} = 7$  TeV Analyses is also shown as green lines in (a) [187].

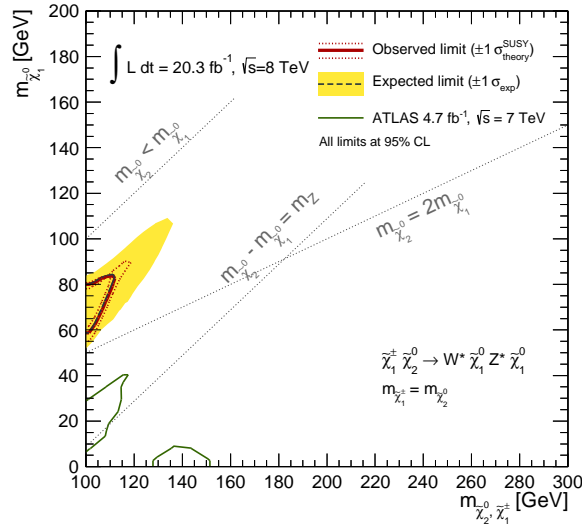


Figure 9.11: Exclusion limit contour for the simplified model for SUSY scenario decay via  $WZ$  with the results of Category-B. All signal regions of Category-B are statistically combined. In the figure, the region surrounded by the red solid lines are the observed exclusion limits with 95% CL. The red dashed lines represent the  $\pm 1\sigma$  movable regions by the theory uncertainties. Similarly, the region surrounded by the black dashed lines are the expected exclusion limits with 95% CL. The yellow region represents the  $\pm 1\sigma$  uncertainties. The exclusion limit of the results of ATLAS  $\sqrt{s} = 7$  TeV Analyses is also shown as green lines [187].

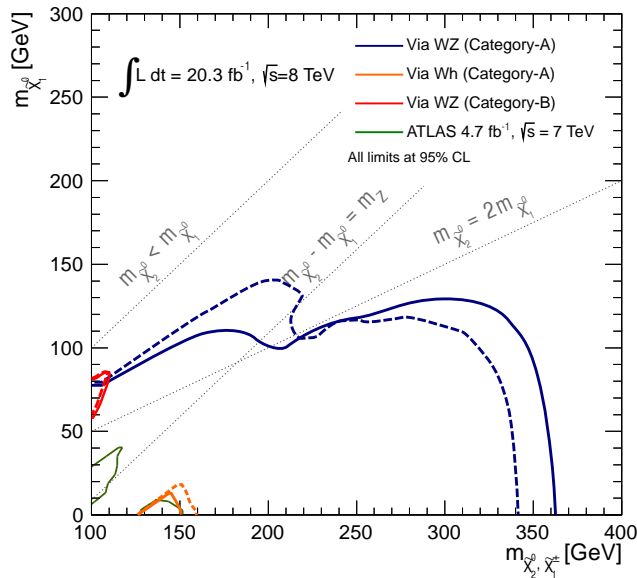


Figure 9.12: Summary plot for the exclusion limits for all analyses which described in this thesis. The dashed lines show the expected exclusion limits for the corresponding analyses, and the solid lines show the observed exclusion limits for the corresponding analyses. Since analyses of  $WZ$  scenario with Category-A and Category-B are not orthogonal, they cannot be combined statistically. The observed exclusion limit of the results of the ATLAS 7 TeV analysis is also shown [187]. All lines indicate the upper limits with 95% confidence level.

## 9.3 Discussion

In this section, the interpretation for the results and the prospects for the analysis of the search are discussed. Discussions for the following topics are shown:

- comparison between our results and the CMS results
- improvement of the analyses
- interpretation of the excesses
- limit for the dark matter
- muon  $g - 2$  interpretation
- signal acceptance (prospect for LHC Run-2)
- fake suppression at the optimisation stage (prospect for LHC Run-2)

### 9.3.1 Comparison to the CMS analyses

This thesis has reported the results of mass region of wino-NLSP and bino-LSP plane with the scenarios of the direct production of charginos and neutralinos decaying via  $WZ$  or  $Wh$ . The CMS collaboration [107] has also reported the results of these scenarios. The results are shown in Fig. 9.13. The criteria of searches for charginos and neutralinos via  $WZ$  decaying scenario are based on two decay modes. One is the mode in final states with two leptons and two jets, and the other is the mode in final states with three leptons, as same as our analysis. The three-lepton analysis uses the  $E_T^{\text{miss}}$ -bin  $\times$   $m_{\text{SFOS}}$ -bin  $\times$   $m_T$ -bin =  $3 \times 4 \times 3$  binned signal regions [188]. The two-lepton and two-jet analysis is applied the requirement of the  $W$  and  $Z$  mass, which are reconstructed from two jets and two SFOS leptons, respectively. For the  $Wh$  scenario, the results are based on the analyses with the events with three leptons, and with one lepton and two  $b$ -jets [188]. The analysis with three leptons targets to detect signals from the decay:  $\tilde{\chi}_1^\pm \tilde{\chi}_1^0 \rightarrow W \tilde{\chi}_1^0 h \tilde{\chi}_1^0 \rightarrow \ell \nu WW(\text{leptonically}) + \tilde{\chi}_1^0 \tilde{\chi}_1^0$  or  $\ell \nu \tau \tau + \tilde{\chi}_1^0 \tilde{\chi}_1^0$ . In the CMS analyses, up to one hadronical decaying tau is required, while in our analysis two hadronical decaying taus are taken into account. The analysis with one lepton and two  $b$ -jets analysis is based on the decay mode:  $\tilde{\chi}_1^\pm \tilde{\chi}_1^0 \rightarrow W \tilde{\chi}_1^0 h \tilde{\chi}_1^0 \rightarrow \ell \nu b \bar{b} + \tilde{\chi}_1^0 \tilde{\chi}_1^0$ . Tagging two  $b$ -jets is required and their mass should be in the Higgs mass window (100–150 GeV).

As a result, the exclusion limits for charginos and neutralinos are set by CMS as follows:

$$m_{\tilde{\chi}_1^\pm, \tilde{\chi}_2^0} > 280 \text{ GeV under } m_{\tilde{\chi}_1^0} = 0 \text{ GeV (} WZ \text{ scenario),}$$

$$m_{\tilde{\chi}_1^\pm, \tilde{\chi}_2^0} > 200 \text{ GeV under } m_{\tilde{\chi}_1^0} = 0 \text{ GeV (} Wh \text{ scenario),}$$

as shown in Fig. 9.13. The CMS has recorded  $19.5 \text{ fb}^{-1}$  of the data, which is close agreement with the amount of the data recorded in ATLAS,  $20.3 \text{ fb}^{-1}$ . According to the results, Fig. 9.10a and Fig. 9.13a, the  $WZ$  expected limits are consistent within  $1\sigma$  band. However, the observed limits are rather different between them. The CMS result claim that the region with the large difference of mass between  $\tilde{\chi}_2^0$  and  $\tilde{\chi}_1^0$  are less stringent than the expected because of the excesses in the signal regions with  $m_T > 160 \text{ GeV}$  and  $75 < m_{\text{SFOS}} < 105 \text{ GeV}$  [188]. The behaviour is very interesting because the ATLAS result shown in Fig. 9.10a shows the opposite tendency.

The  $Wh$  results in ATLAS and CMS, as shown in Fig. 9.10b and Fig. 9.13b, respectively, show the large deviation between them. However, the CMS result has already been combined not only the multi-lepton

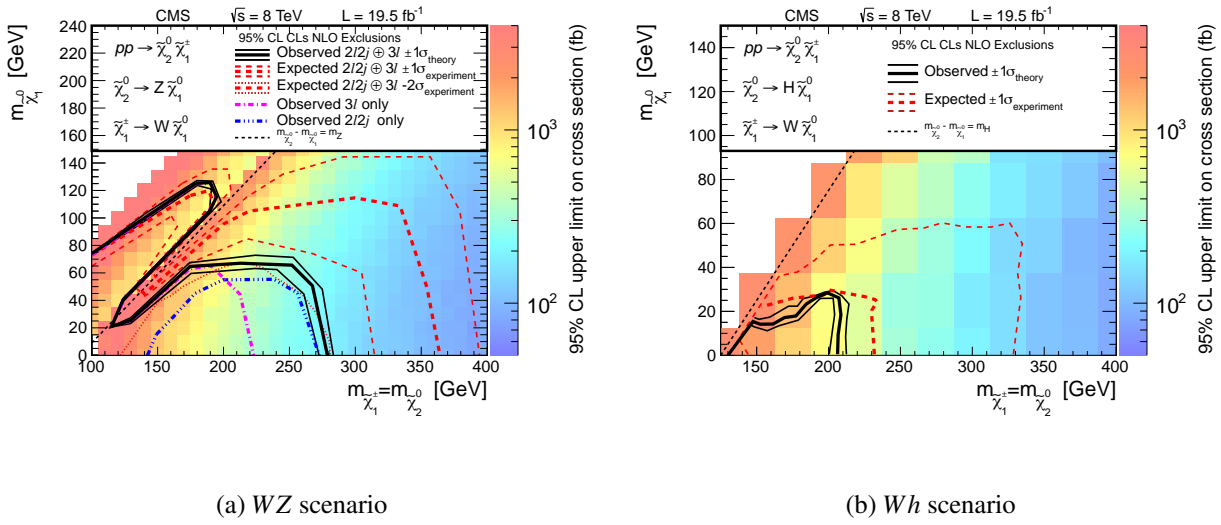


Figure 9.13: Exclusion limits for charginos and neutralinos decaying via  $WZ/h$  in CMS [188].

results but also two  $b$ -jet analyses. The ATLAS result for the  $Wh$  analysis with  $h \rightarrow b\bar{b}$  has prepared as shown in Fig. 9.14. This result in the yellow band clearly shows that the uncertainties are large. Thus the results from the both analyses are consistent within  $1\sigma$  uncertainty. Since the large uncertainties are mainly coming from the statistics of the data, the precise limits would be obvious from the analyses with the data taken in LHC Run-2.

### 9.3.2 Improvement of the analyses

In Category-A, the binned signal region  $SR0\tau a$  contributes to obtain high sensitivity in the  $WZ$  scenarios. The exclusion limit with 95% CL is much improved comparing to the ATLAS 7 TeV analysis [187]. Since the integrated luminosity of this analysis ( $20.3 \text{ fb}^{-1}$ ) is approximately five times larger than the ATLAS 7 TeV analysis ( $4.7 \text{ fb}^{-1}$ ), the significance is simply expected to increase approximately twice. The result of  $WZ$  scenario, as shown in Fig. 9.10a, represents that the much high sensitivity has been obtained in this analysis.

The Category-B is the first attempt to investigate the region with the small difference between the masses of the second lightest neutralino  $\tilde{\chi}_2^0$  and the lightest neutralino  $\tilde{\chi}_1^0$ . Loosening the lepton  $p_T$  requirement has been very challenging because the background has been expected to increase significantly. In this analysis, the requirement of the ISR-like jets contributes to separate signals and backgrounds. In particular, ISR-related variables, the ratio of the transverse momenta of the leading lepton and the leading jet,  $p_T(\ell)/p_T(j)$ , and the difference of the azimuthal angle  $\Delta\phi_{E_T^{\text{miss}}, \Sigma\ell}$  and  $\Delta\phi_{j, E_T^{\text{miss}}}$ , contribute to obtain high significance. The ratio of the  $p_T(\ell)$  and the  $p_T(j)$  and the difference between the azimuthal angles of the leading jet and the missing transverse momentum  $\Delta\phi_{j, E_T^{\text{miss}}}$  have been used as discriminators in several analyses studied hitherto. The difference between the azimuthal angles of the missing transverse momentum and the three-lepton system  $\Delta\phi_{E_T^{\text{miss}}, \Sigma\ell}$  is a characteristic discriminator of this analysis. The discrimination powers have already been shown in Figs. 5.19.

The fake estimation with the matrix method has been investigated with great effort in this analysis,

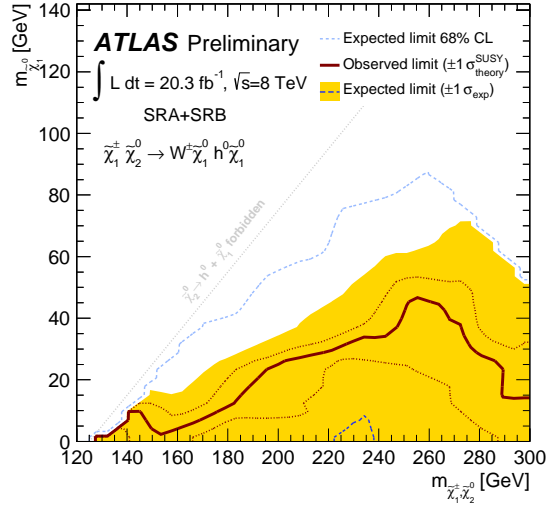


Figure 9.14: Preliminary exclusion limit for  $Wh$  (decaying to  $\ell\nu b\bar{b}$ ) scenario in ATLAS [189].

especially in Category-B where the mis-identified efficiencies are expected to be much higher than the region with the requirement of the high  $p_T$  leptons. To suppress the contribution from the fake backgrounds, the tighter isolation criteria (as described Sec. 3.4 for electrons and Sec. 3.5 for muons) are applied for the second and the third leptons. This leads to make the fake background contribution a half comparing to the standard isolation criteria. The tighter isolation criteria was not applied to the leading leptons because of the acceptance. In fact, the purity of the leading lepton is almost 100%, whereas that of the second and the third leptons are less than 70%. The maps of the fake rates and the real efficiencies are made as the  $p_T$  and  $|\eta|$  plane. This contributes the precise estimation for the fake rates. In the low  $p_T$  region, the fake rates and the real efficiencies vary dramatically. Thus it is important to define the  $p_T$  bins according to the size of the variations of the fake rates and the real efficiencies. In this analysis, the fake rates and the real efficiencies in the low  $p_T$  region have fine bins and the fake origin fractions have rough bins due to the low statistics in signal regions.

### 9.3.3 Interpretation for “via sleptons” scenario and a pMSSM model

This thesis has focused to study the SUSY scenarios with the assumption where the sleptons have their masses heavier than the NLSP, since the sleptons have been excluded with the mass lighter than 300 GeV with the LSP mass  $m_{\tilde{\chi}_1^0} = 0$  GeV, as described in Sec. 1.5. However, as shown in Fig. 1.16, the parameter space with the difference between masses of the sleptons and the LSP  $\Delta m_{\tilde{\ell}, \tilde{\chi}_1^0} < 50$  GeV has not been excluded even for the slepton masses less than 300 GeV. The “via sleptons” scenario assumes that the slepton masses are  $m_{\tilde{\ell}_L} = (m_{\tilde{\chi}_2^0} + m_{\tilde{\chi}_1^0})/2$ , thus the second lightest neutralino  $\tilde{\chi}_2^0$  decays into on-shell slepton and the lepton, and the lightest chargino  $\tilde{\chi}_1^\pm$  decays into on-shell slepton and the neutrino. The emitted slepton decays into the lepton and the LSP. The Feynman diagram for the scenario with the chargino and the neutralino decaying via sleptons is shown in Fig. 9.15.

The simplified model for the slepton scenario is adopted, where the selectron, the smuon and the stau are assumed to have compressed mass spectra, thus they are not distinguished. All signal regions are used for the interpretation of the slepton scenario. The results are shown in Fig. 9.16. While  $WZ/h$  scenarios

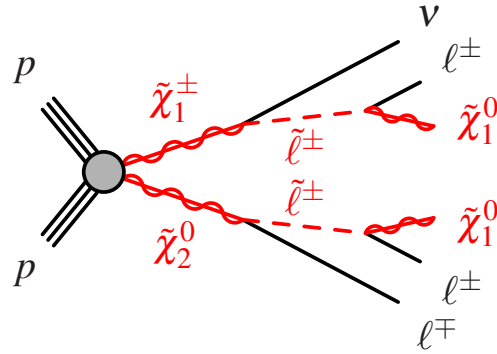


Figure 9.15: Feynman diagram for the “via slepton” scenario. The slepton mass is assumed to be the middle of masses between the second lightest neutralino and the lightest neutralino,  $(m_{\tilde{\chi}_2^0} + m_{\tilde{\chi}_1^0})/2$ .

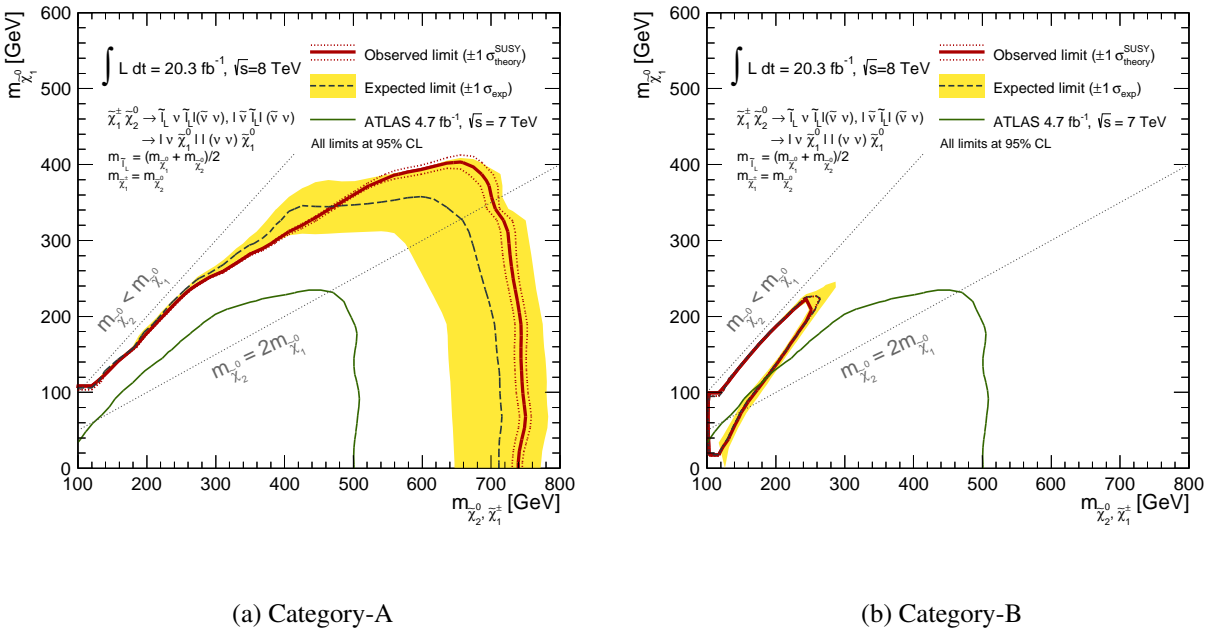


Figure 9.16: Interpretation for “via sleptons” scenario. The left-handed slepton masses are assumed to be  $m_{\tilde{l}_L} = (m_{\tilde{\chi}_2^0} + m_{\tilde{\chi}_1^0})/2$ . The exclusion limits are calculated with Category-A signal regions (a) and Category-B signal regions (b). In figures, the region surrounded by the red solid lines are the observed exclusion limits with 95% CL. The red dashed lines represent the  $\pm 1\sigma$  movable regions by the theory uncertainties. Similarly, the region surrounded by the black dashed lines are the expected exclusion limits with 95% CL. The yellow regions represent the  $\pm 1\sigma$  uncertainties. The result of ATLAS 7 TeV analysis [187] is also shown.

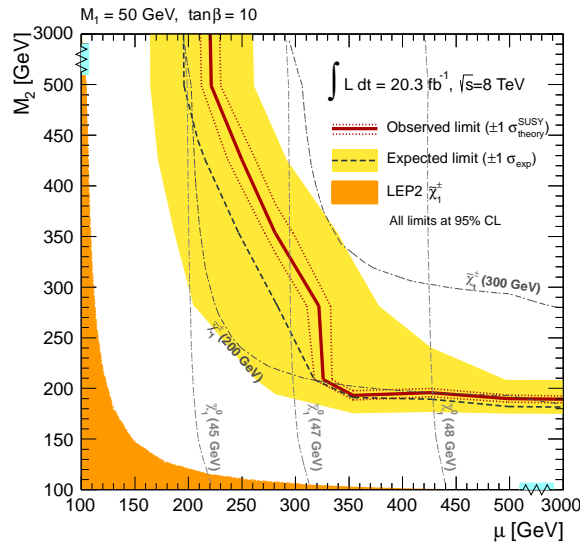


Figure 9.17: Interpretation for pMSSM with high mass sleptons  $m_{\tilde{\ell}} = 3$  TeV. The category-A signal regions are used. The parameters  $M_1$  and  $\tan\beta$  are fixed at 50 GeV and 50, respectively. The region filled the orange colour represents the exclusion region by the LEP searches [85].

are similar phenomena to the Standard Model  $WZ/h$  processes, the slepton scenario has less background processes. Thus the exclusion limit for this scenario is much stronger than the  $WZ/h$  scenarios. The limit reaches the lightest chargino mass of 720 GeV at the LSP mass of 0 GeV by the Category-A analysis, as shown in Fig. 9.16a. The Category-B signal regions are sensitive to the compressed region of the slepton scenario. The region where the difference between  $m_{\tilde{\chi}_1^\pm, \tilde{\chi}_2^0}$  and  $m_{\tilde{\chi}_1^0}$  is 20 GeV has been excluded with the Category-B signal regions, as shown in Fig. 9.16b.

The pMSSM model, as described in Sec. 1.3.2, is also taken into account. The pMSSM parameters are the  $U(1)$  gaugino mass parameter  $M_1$ , the  $SU(2)$  gaugino mass parameter  $M_2$ , the Higgsino mass parameter  $\mu$ , the ratio of the VEV of the two Higgs fields  $\tan\beta$ , the mass parameters of the left and right handed sleptons and the mass parameter of the CP-odd Higgs  $m_A$ . The parameters  $M_1$ ,  $\tan\beta$  and all slepton masses are fixed at 50 GeV, 50 and 3 TeV, respectively. In this parameter space, decays via  $WZ/h$  are dominant. The Higgs branching fractions are assumed to be the SM-like. However, the branching fraction of the decay mode  $h \rightarrow \tilde{\chi}_1^0 \tilde{\chi}_1^0$  rises to considerable value in the lower  $\mu$ . For example, if the  $\mu$  decreases to 200 GeV, the branching fraction of  $h \rightarrow \tilde{\chi}_1^0 \tilde{\chi}_1^0$  rises to  $\sim 20\%$ . The result with the Category-A analysis for the pMSSM scenario is given with the  $\mu$ - $M_2$  plane in Fig. 9.17. As a result, the parameter space with the lightest chargino mass of  $< \sim 200$  GeV is excluded with 95% confidence level. The result is approximately twice stronger than the LEP results [85].

### 9.3.4 Excesses in $SR0\tau a$

In the compressed mass region, which corresponds to the light blue region of Fig. 5.1, the observed exclusion limit is much weaker than the expected limit in Fig. 9.10a. The dominant origin of the discrepancy is the excess in the  $SR0\tau a$ -bin1, where the low  $m_{\text{SFOS}}$  (12–40 GeV),  $m_T$  ( $< 80$  GeV) and  $E_T^{\text{miss}}$  (50–90 GeV) are required. The distributions for the leading lepton  $p_T$  and the  $E_T^{\text{miss}}$  in  $SR0\tau a$ -bin1 are



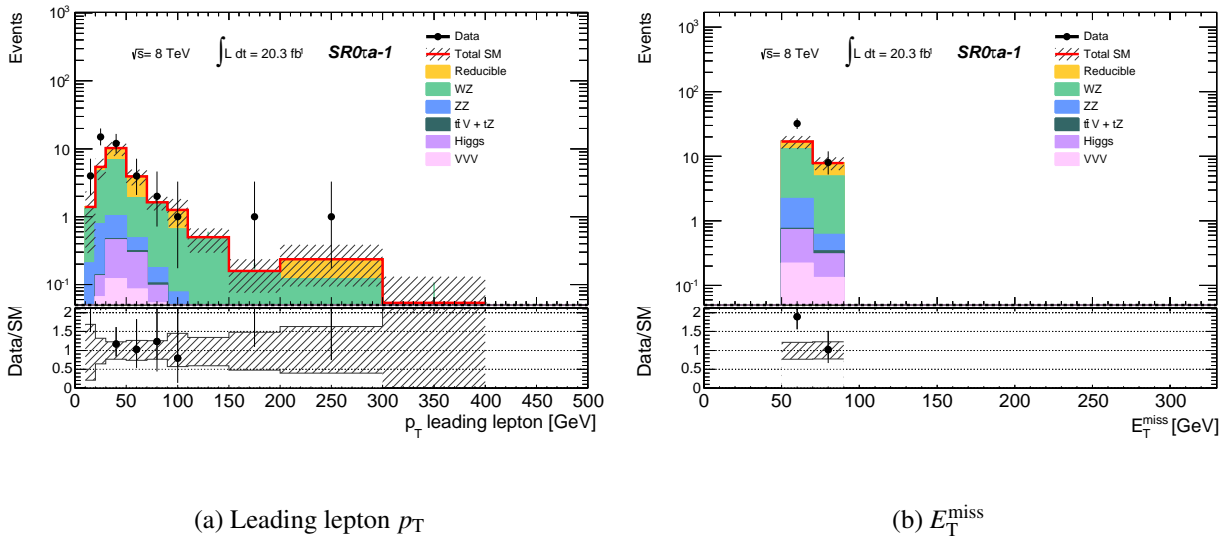


Figure 9.18: Distributions for the leading lepton  $p_T$  (a) and the  $E_T^{\text{miss}}$  (b) in the SR0 $\tau$ a-bin1. Excess was observed in the low  $p_T$  and  $E_T^{\text{miss}}$  region.

shown in Figs. 9.18. The SUSY with the compressed mass spectra tends to create the low  $p_T$  leptons. The  $E_T^{\text{miss}}$  of the SUSY signals tends to shift larger region, which does not reproduced in Figure 9.18b. This could be considered as caused by the fluctuation in the fake contribution.

### 9.3.5 Dark matter limits

The interpretation for the dark matter candidates will be described. As explained in Sec. 1.4, the Higgsino mass term  $|\mu|$  is assumed to be larger than the bino and the wino mass terms  $M_1, M_2$ . Thus the NLSP and the LSP are wino-like and bino-like neutralinos, respectively. The relic abundance of the bino tends to be higher than the observed relic abundance by the Planck collaboration [21],

$$\Omega_{\text{DM}} h^2 = 0.1197 \pm 0.0022, \quad (9.15)$$

where  $\Omega_{\text{DM}}$  represents the cold dark matter density and  $h$  represents the Hubble constant with the unit of 100 km/s/Mpc. The relic densities of the various LSP dark matter and the various mass of the dark matter are calculated. Figure 9.19 shows the calculation results with the pMSSM model [190]. Blue points, purple crosses and red squares represent the bino, wino and Higgsino dark matter cases. The green dashed line represents the observed relic density by Planck. Blue points mainly distribute the region with the relic abundance of  $\sim 10^2$ , which is much larger than the observed relic abundance. Therefore, if the bino is the dark matter (the LSP), annihilation processes are necessary to suppress the relic density of the bino.

Many processes to suppress the relic density are proposed hitherto, for example, the Higgs resonance and bino-wino coannihilation [191]. The Higgs resonance case assumes that two LSPs  $\tilde{\chi}_1^0$  are annihilated into the lightest Higgs  $\tilde{\chi}_1^0 \tilde{\chi}_1^0 \rightarrow h$ . The suppressing power is thus maximum in the close region to the half of the Higgs mass ( $\sim 63$  GeV). If the bino exists in this mass region, the relic density satisfies the relation observed at Planck.

For the bino-wino coannihilation scenarios [192], the difference of the masses between bino (LSP) and wino (NLSP)  $\Delta m_{\tilde{\chi}_2^0, \tilde{\chi}_1^0}$  should be small, as shown in Fig. 9.20. The black solid and dashed lines repre-

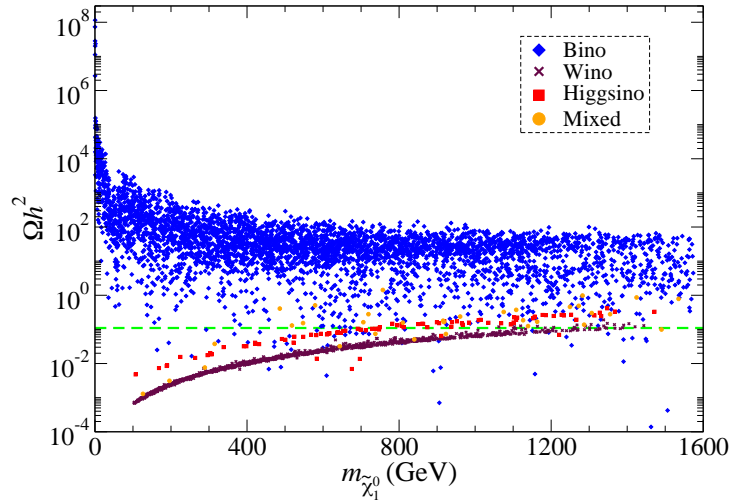


Figure 9.19: 2D distribution for the relic density of the dark matter for each model [190]. Blue points represent the bino dark matter case. The purple crosses represent the wino dark matter case. Red squares represent the Higgsino dark matter case. Orange points represent the case with the mixed bino, wino and Higgsinos. Green dashed line represents the observed relic density by Planck [21]. Many of the blue points (bino cases) distribute the region with larger relic density than the observed value. On the other hand, the purple crosses (wino cases) distribute the region with less relic density than the observed value. Some Higgsino cases, the red squares, distribute the region with equivalent relic density to the observed value.

sent the reasonable regions to explain the observed relic density. The red region shows the region with larger relic density than the observed value at Planck. The blue region has been already excluded by LEP searches [85], and the orange region has been excluded by our analysis. In our results, the region with mass difference  $\Delta m_{\tilde{\chi}_2^0, \tilde{\chi}_1^0} > 25 \text{ GeV}$  is excluded in the second lightest neutralino mass of  $m_{\tilde{\chi}_2^0} \sim 100 \text{ GeV}$ , as shown in Fig. 9.20b. The figure also shows the favourable lines for the Higgs resonance and the bino-wino coannihilation scenarios with the results of this analysis. Whereas the  $Wh$  scenario has small exclusion region, the Higgs annihilation scenario has been excluded up to the mass of 360 GeV where the  $WZ$  simplified model is assumed. On the other hand, the bino-wino coannihilation scenario has not been excluded by this analysis, although the Category-B analysis focuses on the region.

### 9.3.6 Muon $g - 2$ interpretation

As described in Chap. 1, the muon anomalous magnetic moment  $(g - 2)_\mu$  has  $\sim 3\sigma$  deviation from the SM prediction. The theories have been proposed which can explain the deviation with the quantum correction of the SUSY particles. The non-universal gaugino masses scenario with the latest SUSY constraint [47] is an example. Figure 9.21 shows the calculated results of the favourable region to explain the deviation of the muon  $g - 2$ . The calculation is based on the latest SUSY constraints as [47]

$$\begin{aligned}
 123 \text{ GeV} &\leq m_h \leq 127 \text{ GeV}, \\
 0.8 \times 10^{-9} &\leq BR(B_s \rightarrow \mu\mu) \leq 6.2 \times 10^{-9} \text{ [193]}, \\
 2.99 \times 10^{-4} &\leq BR(b \rightarrow s\gamma) \leq 3.87 \times 10^{-4} \text{ [194]}, \\
 0.15 &\leq \frac{BR(B_u \rightarrow \tau\nu_\tau)_{\text{MSSM}}}{BR(B_u \rightarrow \tau\nu_\tau)_{\text{SM}}} \leq 2.41 \text{ [194]},
 \end{aligned}$$

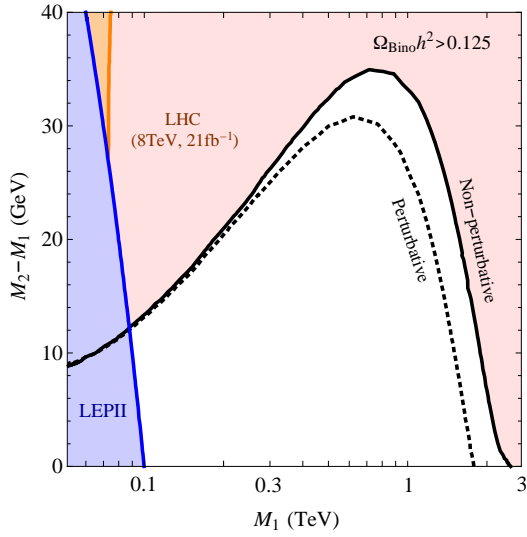
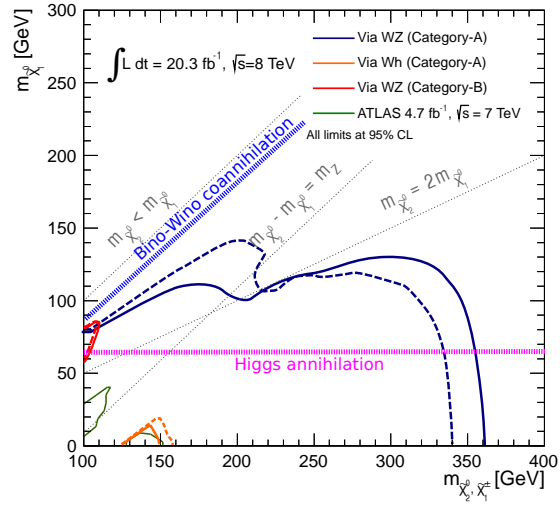
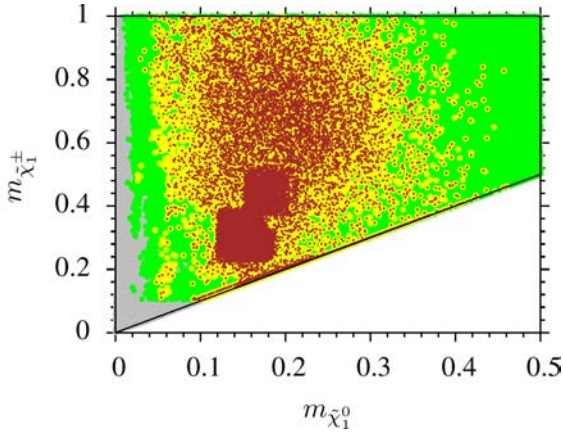
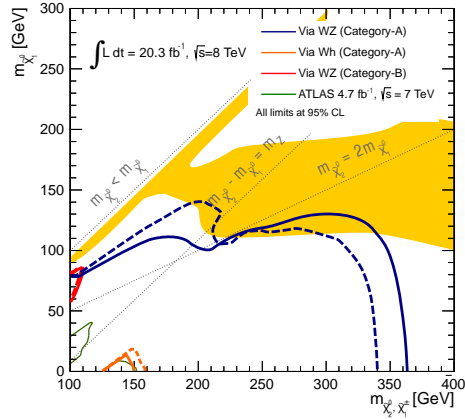
(a) Coannihilation region in  $M_1-\Delta m_{2,1}$  plane [192](b) Annihilation region in  $M_1-M_2$  plane.

Figure 9.20: Coannihilation region between bino and wino with the bino dark matter scenario in the  $M_1-\Delta m_{M_2, M_1}$  plane [192] (a) and  $M_1-M_2$  plane (b). (a) also shows the results of LEP2 and the Category-A analyses. (b) shows the favourable regions of the bino-wino coannihilation and the Higgs resonance scenarios and the exclusion limit curves obtained on this analysis.

(a)  $M_1-M_2$  plane [47]

(b) Overlaid view of the limit curves and favourable region

Figure 9.21: Calculated results for the region where the muon  $g-2$  deviation can explain within  $1\sigma$ . The plot with  $M_1-M_2$  plane is shown in (a) [47], and the overlaid view of the exclusion limit curves obtained from this analysis and the favourable region from (a) (yellow region) is shown in (b). Green points in (a) represent the region satisfying the  $B$ -physics constraints [193, 194]. Brown points in (a) represent the region satisfying the relic abundance of the dark matter corresponding  $0.001 < \Omega_{\text{DM}} h^2 < 1$  [47].

$$\begin{aligned}
m_{\tilde{g}} &\geq 1.4 \text{ TeV (for } m_{\tilde{g}} \sim m_{\tilde{q}}), \\
m_{\tilde{g}} &\geq 1 \text{ TeV (for } m_{\tilde{g}} \ll m_{\tilde{q}}), \\
m_A &\geq 700 \text{ GeV (for } \tan \beta \simeq 48).
\end{aligned}$$

In Fig. 9.21, green points satisfy all of the constraints from  $B$ -physics results. Yellow points represent the region where muon  $g-2$  can be explained within  $1\sigma$  deviation, which is subset of the green points. Brown points satisfy the loose requirement of the neutralino relic abundance,  $0.001 < \Omega_{\text{DM}} < 1$ , which is subset of the yellow points. The region covers the mass of the lightest neutralino from  $\sim 100 \text{ GeV}$  to  $\sim 300 \text{ GeV}$  in the lower  $\tilde{\chi}_1^\pm$  mass region. On the other hand, the exclusion limit of  $WZ$  scenario shown in Fig. 9.21b covers the mass of the LSP up to  $100 \text{ GeV}$  with the second lightest neutralino mass of  $< 350 \text{ GeV}$ . Thus the exclusion limit reaches the region where the muon  $g-2$  deviation favours. However, most of the favourable region shown in Fig. 9.21b remains out of the exclusion reach.

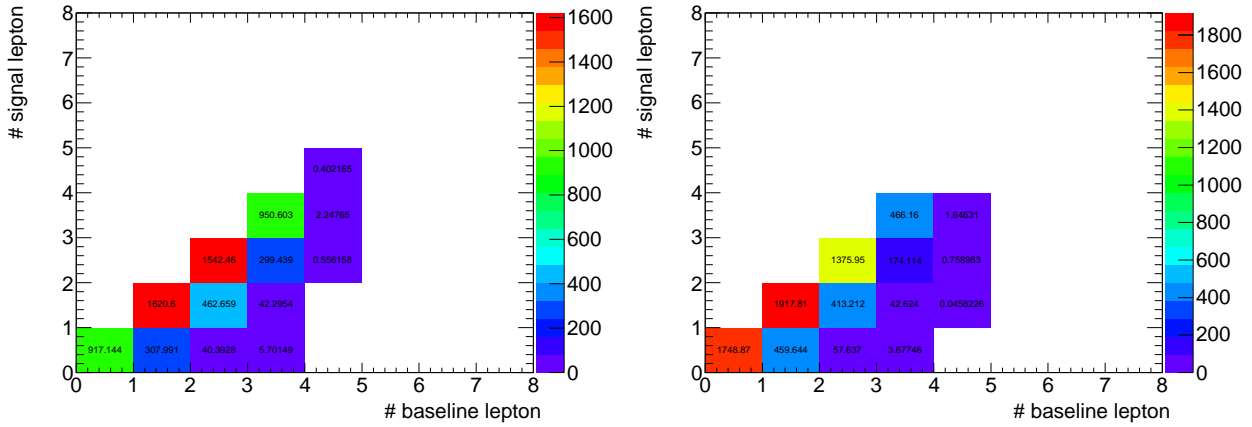
The muon  $g-2$  anomaly includes the contribution of the smuon or the muon sneutrino, thus the slepton masses should be light. In this calculation, the slepton masses in the range between  $200 \text{ GeV}$  and  $600 \text{ GeV}$  are allowed. These sleptons have not been excluded in this analysis.

### 9.3.7 Signal acceptances in the $WZ$ compressed region

The Category-B analysis focuses the region where  $\Delta m_{\tilde{\chi}_2^0, \tilde{\chi}_1^0} \leq 50 \text{ GeV}$ . This region tends to have low  $p_T$  leptons from the SUSY signals. Sometimes such low  $p_T$  leptons could not be detected due to the detector acceptance. Investigation of the number of the undetected leptons with the signal samples is useful to know the signal acceptance. Figures 9.22 show the 2D plots of the number of baseline leptons versus the number of signal leptons for the SUSY signals. The samples filtered to have leptonically decaying  $W$  and  $Z$  are employed. The signal leptons are defined as the leptons passing the standard criteria (see Sec. 3.4 and Sec. 3.5). In this thesis, the channel including exactly three baseline leptons and exactly three signal leptons (hereinafter referred to as “3S3B”; the channel with  $n$  signal leptons and  $m$  baseline leptons is hereinafter referred to as “ $nSmB$ ”) has been analysed in order to simplify the fake estimation with the matrix method. According to Figs. 9.22, the fraction of two lepton final states gets larger than that of three lepton final states as the difference of mass between NLSP and LSP gets smaller. Thus investigating 2S2B can be interesting in order to obtain larger statistics. The difficulty of the analysis in 2S2B is that the  $Z \rightarrow \ell\ell$  contribution should be much larger than that of the 3S3B. Figure 9.23 show the 2D plot for expected main backgrounds,  $WZ$  and  $Z$ +jets. The contribution of the  $WZ$  and  $Z$ +jets in 2S2B channel are much larger (10 times and  $10^3$  times, respectively) than the contribution in the 3S3B region, whereas the SUSY signal increases 2–6 times larger than the 3S3B. The selection of the three baseline and signal leptons, therefore, contributes to suppress these backgrounds. Hence the 3S3B region has advantage even though the signals are reduced because of the failure of real leptons in the lepton identification.

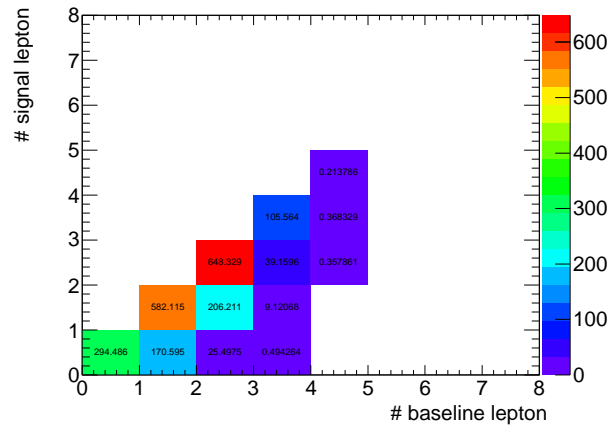
A possible candidate to keep SUSY signals is found in the final states 2S3B in Fig. 9.22 and Fig. 9.23. The number of signals in 2S3B is half of that of the 3S3B, as shown in Fig. 9.22. Thus if the analysis in 2S3B is performed, the statistics of signals would increase to roughly 1.5 times larger than current analysis. To perform this, estimation of the total amount of the fake contribution from the simplified matrix method Eq. (6.10), Eq. (6.11) and Eq. (6.13) should be modified as

$$N_{\text{total Fake}} = N_{\text{RRF} \rightarrow \text{TTL}}^{\text{simplified}} + N_{\text{RFR} \rightarrow \text{TTL}}^{\text{simplified}} + N_{\text{RFF} \rightarrow \text{TTL}}^{\text{simplified}}, \quad (9.16)$$



(a) SUSY WZ (100,50)

(b) SUSY WZ (100,75)



(c) SUSY WZ (100,87.5)

Figure 9.22: 2D plots of the numbers of baseline and signal leptons. The pre-selection and  $b$ -veto are applied. Triggers are not applied.

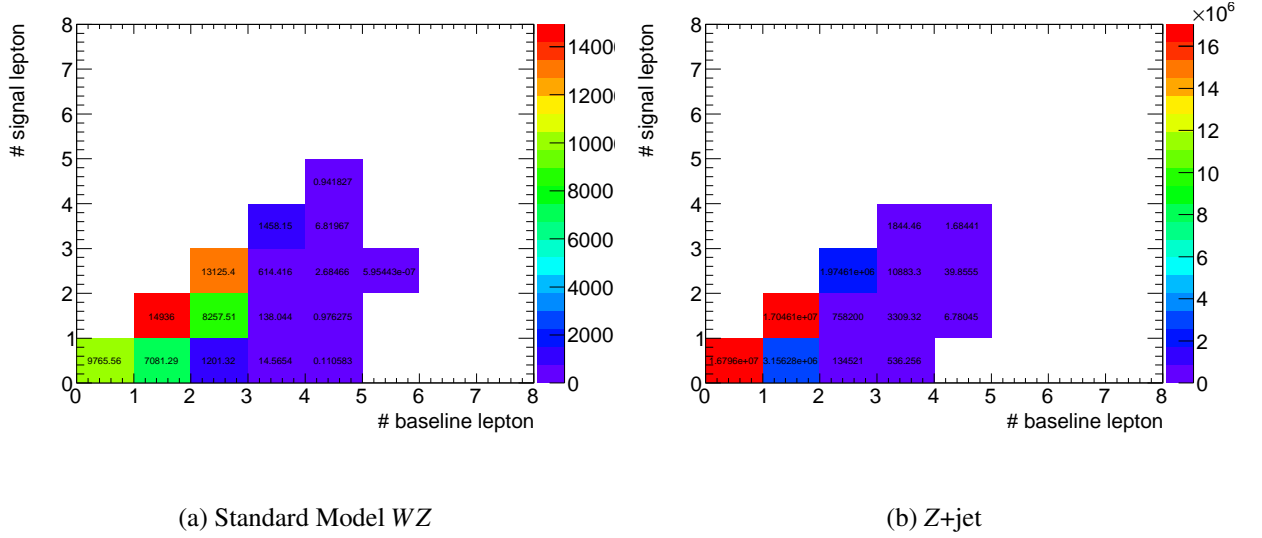


Figure 9.23: 2D plots of the numbers of baseline and signal leptons. The pre-selection,  $Z$ -veto and  $b$ -veto are applied. Triggers are not applied.

$$\text{where } \begin{cases} N_{\text{RRF} \rightarrow \text{TTL}}^{\text{simplified}} = \frac{\varepsilon_2 \bar{f}_3 + \bar{\varepsilon}_2 f_3}{2} N_{\text{RRF}} \\ N_{\text{RFR} \rightarrow \text{TTL}}^{\text{simplified}} = \frac{f_2 \bar{\varepsilon}_3 + \bar{f}_2 \varepsilon_3}{2} N_{\text{RFR}} \\ N_{\text{RFF} \rightarrow \text{TTL}}^{\text{simplified}} = \frac{f_2 \bar{f}_3 + \bar{f}_2 f_3}{2} N_{\text{RFF}} \end{cases} \quad (9.17)$$

In Eq. (9.17),  $N_{\text{RRF}}$ ,  $N_{\text{RFR}}$  and  $N_{\text{RFF}}$  are calculated using Eq. (6.15). An important thing in exploring 2S3B channel is the suppression power of backgrounds such as  $Z$ +jets and  $t\bar{t}$ . For example, the  $Z$ +jets has two real leptons in the final states, thus this is a candidate of the main background in 2S2B channel. The candidates of the discriminating variables are selecting different-flavour same-sign signal lepton pair and the selection of the minimal  $m_{\text{SFOS}}$ . In particular, the minimal  $m_{\text{SFOS}}$  for baseline leptons is a powerful discriminator in 2S3B channel contrary to the 2S2B channel, where the minimal  $m_{\text{SFOS}}$  should be wrong since one lepton is missing. The 2S3B and 3S3B are orthogonal thus they can be statistically combined. Hence the new channel could be useful in increasing the signal statistics. It is necessary to optimise the lepton identification criteria for this new channel because it is strongly depending on the lepton identification criteria. It is required that the optimisation should be performed comprehensively for all channels.

### 9.3.8 Fake suppression in the optimisation stage

The sensitivity would be critically damaged to include the fake estimation results with the low lepton  $p_{\text{T}}$  regions. Figure 5.21, which is the expected sensitivity with the MC only study, argues that the analysis has sensitivity to exclude up to  $m_{\tilde{\chi}_1^\pm, \tilde{\chi}_2^0} = 130 \text{ GeV}$  under the difference of mass  $\Delta m_{\tilde{\chi}_2^0, \tilde{\chi}_1^0}$ . On the other hand, the signal yields shown in Tab. 9.2 claim that the fake contribution is dominant for several channels and the expected exclusion limit shown in Figure 9.11 is up to  $m_{\tilde{\chi}_1^\pm, \tilde{\chi}_2^0} = 110 \text{ GeV}$  under the difference of mass  $\Delta m_{\tilde{\chi}_2^0, \tilde{\chi}_1^0} = 25 \text{ GeV}$ , which is much weaker than that in Fig. 5.21. Thus the fake suppression would be essential for the compressed  $WZ$  scenario.

At the optimisation stage, only the MC estimates are performed. It would be risky because the fake contribution is not taken into account by the MC estimates. For the Category-B analysis, the tighter iso-

lution criteria are required. However, the fake contribution cannot be reduced down to the level of the irreducible background.

The same issue exists in the  $Wh$  channel of Category-A. Reconstructed taus have had numerous fake contribution. Thus it would be proper to apply *tight* selection for taus, whereas the *medium* selection has been applied in the Category-A analyses.

The other solution would be to take into account the fake contribution in the optimisation stage. Usually the estimation with the matrix method takes much time, thus it has been performed only after the optimisation. However, the fake estimation with the matrix method in the early stage can be useful to suppress the fake contribution in the region where the fake contribution is not negligible. To do this, the signal regions including less contribution of the fake can be defined. This would reduce the uncertainties on the reducible background, thus the significance would get larger.

## Chapter 10

# Conclusion

This thesis presented a search for direct production of charginos and neutralinos in proton-proton collisions with the  $20.3 \text{ fb}^{-1}$  data taken in 2012 at the ATLAS detector. In this search, the lightest charginos and second lightest neutralinos are assumed to be wino-like and have degenerate mass spectra  $m_{\tilde{\chi}_1^\pm} = m_{\tilde{\chi}_2^0}$  and the lightest neutralino is assumed to be bino-like.

The  $\tilde{\chi}_1^\pm \tilde{\chi}_2^0$  decay channels via  $WZ/h$  are investigated. In these channels, the final states would include three leptons and the missing transverse momentum. The analysis is performed in the two categories, Category-A and Category-B. The binned signal region is adopted to obtain high sensitivity for  $WZ$  channel in Category-A. For the  $Wh$  channel, using taus contributes to expand the signal acceptance. Category-B targets the  $WZ$  channel with the compressed mass spectra ( $\Delta m_{\tilde{\chi}_2^0, \tilde{\chi}_1^0} < 50 \text{ GeV}$ ). The requirements of the low  $p_T$  leptons and ISR-like jets are employed.

The background suppression is improved in this analysis. In the Category-B, the ISR specific variables,  $p_T(\ell)/p_T(j)$ ,  $\Delta\phi_{j, E_T^{\text{miss}}}$  and  $\Delta\phi_{E_T^{\text{miss}}, \Sigma\ell}$ , have been employed. The fake estimation of the analysis has been performed using the simplified matrix method. The binning of the fake rates with  $p_T$  and  $\eta$  contributes to reproduce the reducible backgrounds precisely even in the region with the low  $p_T$  leptons.

No significant deviations from the Standard Model have been observed. The exclusion limits for  $WZ/h$  channels for the simplified models are set using the profile log-likelihood ratio method. The two-dimensional exclusion limits,  $m_{\tilde{\chi}_1^\pm, \tilde{\chi}_2^0}$  versus  $m_{\tilde{\chi}_1^0}$ , are already shown in Sec. 9.2. Figures 10.1 show the  $m_{\tilde{\chi}_1^\pm, \tilde{\chi}_2^0}$  one-dimensional limits for  $WZ$  and  $Wh$  channels with the results from the ATLAS 7 TeV analysis [187]. The  $m_{\tilde{\chi}_1^\pm}$  less than  $103.5 \text{ GeV}$  has already been excluded with 95% CL at the LEP search [85]. According to the ATLAS 7 TeV analysis, the  $m_{\tilde{\chi}_1^\pm, \tilde{\chi}_2^0}$  from  $120 \text{ GeV}$  to  $160 \text{ GeV}$  was excluded in the  $WZ$  channel. This analysis reports the exclusion limits have significantly extended up to the  $m_{\tilde{\chi}_1^\pm, \tilde{\chi}_2^0}$  of  $360 \text{ GeV}$ , as shown in Fig. 10.1a. This is a significant improvement and is the most strongest limit setting at present. For the  $Wh$  channel, there were no limits in the ATLAS 7 TeV analyses, however, this analysis has set the limits of the  $m_{\tilde{\chi}_1^\pm, \tilde{\chi}_2^0}$  from  $125 \text{ GeV}$  to  $150 \text{ GeV}$  for the first time, as shown in Fig. 10.1b.

The analysis in Category-B has set exclusion limit as  $m_{\tilde{\chi}_1^\pm, \tilde{\chi}_2^0} < 110 \text{ GeV}$  to the compressed mass region  $\Delta m_{\tilde{\chi}_2^0, \tilde{\chi}_1^0} < 50 \text{ GeV}$ . The large contribution of fakes are observed in this region. The fake contribution has been estimated precisely, then the total background estimates agree with the data.

The limits for a dark matter model and a model which can explain the deviation of the muon  $g-2$  with the SUSY are discussed. For the dark matter model, the Higgs annihilation scenario has been excluded with



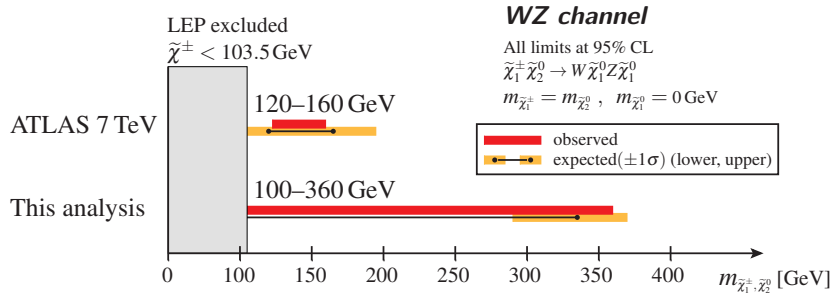
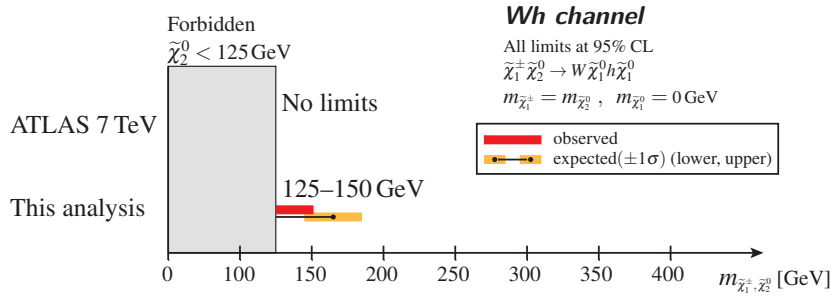
(a) *WZ* channel(b) *Wh* channel

Figure 10.1: Comparison of the observed and expected limits for *WZ* channel (a) and *Wh* channel (b) between the results from this analysis and the analyses with  $\sqrt{s} = 7$  TeV data taken in ATLAS [187]. Red bands and black lines show the observed and the expected exclusion limits. The yellow bands shows the  $\pm 1\sigma$  uncertainties on the expected limits. The limits for the LSP mass of 0 GeV are shown.

the NLSP mass below 350 GeV in the *WZ* simplified model, while the bino-wino coannihilation scenario has not been excluded. For the muon  $g - 2$ , the exclusion limit has reach the favourable region in the *WZ* simplified model.

The prospects for the improvement of the study have been discussed. The signal yield would be improved by using the region with exactly two signal leptons. The requirement of three baseline leptons is hopeful candidate to suppress the backgrounds, such as  $Z$ -jets. The second is the estimates for the fake contribution. This is essential for *Wh* channel and the region with the small mass difference.

# Acknowledgement

First, I am deeply grateful to my supervisor, Prof. Osamu Jinnouchi. Without his support, this study would not have been completed. Although I have faced many troubles since I started this study, he has given advice at any time. His valued advice were entirely useful to continue the study. I would also thank our group in Tokyo Tech: M. Hirose, N. E. Pettersson, K. Motohashi, K. Todome, D. Yamaguchi, D. M. Hayakawa, Y. T. Homma and the other members. Especially M. Hirose and N. E. Pettersson have given opportunities for useful discussions and comments for my work (suggestion about the analysis method, comments for English phrase, and so on).

My studies at Tokyo Tech was supported by many members belonging our department. I am greatly thankful to Prof. M. Kuze, who is also a member of the ATLAS Collaboration. He has given many helpful advice about the research in ATLAS, sometimes encouraged me, and has helped the research life at Tokyo Tech and at CERN. His comments were relevant, so that they were very useful for me (related to not only my work, but some interesting topics). I am very grateful to Prof. T.-A. Shibata. He has educated me about the point of view and the interest of Particle Physics in my first year of the research life, and also trained my English. The experience in the first year has much inspired me to continue to study Particle Physics. I would also thank to Prof. N. Kawai and the members of his group, who have helped me the life in the group room.

I would like to thank members of the ATLAS electroweak SUSY analysis group: C. J. Potter, I. Santoyo Castillo, C. Y. Shehu (*Univ. of Sussex*), Z. Gecse (*Univ. of British Columbia*), A. Petridis (*Stockholm Univ.*), S. Farrell (*UC Irvine*), B. Schneider (*Universität Bern*) and A. Kourkoumeli-Charalampidi (*Aristotle Univ. of Thessaloniki*). Whereas I was the first member of the group from my institute, the members have given many useful advice about common tools or methods. In particular, S. Farrell and I. Santoyo Castillo helped with respect to the fake estimates based on their experiences. Without such many of supports, I would not obtain great results of the fake estimation. Many thanks for the difficult meeting arrangements among the U.S., the U.K. and Japan. Also, I owe C. Y. Shehu and A. Kourkoumeli-Charalampidi for discussing Category-B analysis.

My work of the detector performance study was supported by S. J. McMahon (*RAL*), S. Oda and J. Tojo (*Kyushu Univ.*). I would like to thank them for any supports.

During this study, I have stayed at CERN for a total of two years. Special thanks to Prof. Osamu Jinnouchi and all other members of the ATLAS Japan group for giving the great environment. In particular, at CERN, I have been supported my study by S. Asai, N. Kanaya, J. Tanaka, Y. Yamaguchi, S. Yamamoto, and T. Yamanaka (*Univ. of Tokyo*).

With respect to living at CERN, I would like to thank my friends who lived together with me for two

years. Thanks to T. Nobe (*Tokyo Tech*), Y. Ninomiya, T. Okuyama and T. Dohmae (*Univ. of Tokyo*) and other friends staying at CERN. And also, I am grateful to our landlord, A. Pace (*CERN*), who helped many difficulty of our daily life at CERN.

This study was supported from the Center of Excellence Program by MEXT, Japan through the ‘Nano science and Quantum Physics’ Project of the Tokyo Institute of Technology. I would thank the leader Prof. S. Saito and the secretariat.

Finally, to my family, I would like to express my heartfelt gratitude. Financial and mental supports were given willingly until now. Most of all, I really want to thank to my family for accepting and supporting my *odd* research life. Additionally, my mental supports were also given by some pieces of music. I am thankful to composers and players of all ages and countries for composing and playing the musical masterpieces.

# Bibliography

- [1] M. Gell-Mann, *A Schematic Model of Baryons and Mesons*, Phys. Lett. **8** (1964) 214–215.
- [2] M. Y. Han and Y. Nambu, *Three Triplet Model with Double SU(3) Symmetry*, Phys. Rev. **139** (1965) B1006–B1010.
- [3] S. Weinberg, *A Model of Leptons*, Phys.Rev.Lett. **19** (1967) 1264–1266.
- [4] A. Salam, *Weak and Electromagnetic Interactions*, Conf.Proc. **C680519** (1968) 367–377.
- [5] S. Glashow, J. Iliopoulos, and L. Maiani, *Weak Interactions with Lepton-Hadron Symmetry*, Phys.Rev. **D2** (1970) 1285–1292.
- [6] C. N. Yang and R. L. Mills, *Conservation of Isotopic Spin and Isotopic Gauge Invariance*, Phys. Rev. **96** (1954) 191–195. <http://link.aps.org/doi/10.1103/PhysRev.96.191>.
- [7] T. Nakano and K. Nishijima, *Charge Independence for V-particles*, Progress of Theoretical Physics **10** (1953) 581–582.
- [8] M. Gell-Mann, *The interpretation of the new particles as displaced charge multiplets*, Il Nuovo Cimento **4** no. 2, (1956) 848–866. <http://dx.doi.org/10.1007/BF02748000>.
- [9] F. Englert and R. Brout, *Broken Symmetry and the Mass of Gauge Vector Mesons*, Physical Review Letters **13** (1964) 321–323.
- [10] P. W. Higgs, *Broken Symmetries and the Masses of Gauge Bosons*, Physical Review Letters **13** (1964) 508–509.
- [11] L. Alvarez-Gaume and J. Ellis, *Eyes on a prize particle*, Nat Phys **7** no. 1, (2011) 2–3. <http://dx.doi.org/10.1038/nphys1874>.
- [12] Y. Nambu and G. Jona-Lasinio, *Dynamical Model of Elementary Particles Based on an Analogy with Superconductivity. I*, Phys. Rev. **122** (1961) 345–358. <http://link.aps.org/doi/10.1103/PhysRev.122.345>.
- [13] ATLAS Collaboration, *Observation of a new particle in the search for the Standard Model Higgs boson with the ATLAS detector at the LHC*, Phys. Lett. **B 716** (2012) 1–29, arXiv:1207.7214 [hep-ex].

- [14] CMS Collaboration, *Observation of a new boson at a mass of 125 GeV with the CMS experiment at the LHC*, Phys. Lett. **B 716** (2012) 30–61, arXiv:1207.7235 [hep-ex].
- [15] *Measurements of the Higgs boson production and decay rates and coupling strengths using pp collision data at  $\sqrt{s} = 7$  and 8 TeV in the ATLAS experiment*, Tech. Rep. ATLAS-CONF-2015-007, CERN, Geneva, Mar, 2015. <https://cds.cern.ch/record/2002212>.
- [16] K. Begeman, A. Broeils, and R. Sanders, *Extended rotation curves of spiral galaxies: Dark haloes and modified dynamics*, Mon.Not.Roy.Astron.Soc. **249** (1991) 523.
- [17] Supernova Search Team Collaboration, A. G. Riess et al., *Observational evidence from supernovae for an accelerating universe and a cosmological constant*, Astron.J. **116** (1998) 1009–1038, arXiv:astro-ph/9805201 [astro-ph].
- [18] Supernova Cosmology Project Collaboration, S. Perlmutter et al., *Measurements of  $\Omega$  and  $\Lambda$  from 42 high redshift supernovae*, Astrophys.J. **517** (1999) 565–586, arXiv:astro-ph/9812133 [astro-ph].
- [19] WMAP Collaboration, G. Hinshaw et al., *Nine-Year Wilkinson Microwave Anisotropy Probe (WMAP) Observations: Cosmological Parameter Results*, Astrophys. J .Suppl. **208** (2013) 19, arXiv:1212.5226 [astro-ph.CO].
- [20] Planck Collaboration, P. Ade et al., *Planck 2015 results. XIV. Dark energy and modified gravity*, arXiv:1502.01590 [astro-ph.CO].
- [21] Planck Collaboration, P. Ade et al., *Planck 2015 results. XIII. Cosmological parameters*, arXiv:1502.01589 [astro-ph.CO].
- [22] Planck Collaboration, J. A. Tauber et al., *Planck pre-launch status: The Planck mission*, A&A **520** (2010) A1. <http://dx.doi.org/10.1051/0004-6361/200912983>.
- [23] S. Hannestad, A. Mirizzi, G. G. Raffelt, and Y. Y. Y. Wong, *Neutrino and axion hot dark matter bounds after WMAP-7*, Journal of Cosmology and Astroparticle Physics **8** (2010) 1, arXiv:1004.0695.
- [24] Particle Data Group Collaboration, K. A. Olive et al., *Review of Particle Physics*, Chin. Phys. **C38** (2014) 090001.
- [25] G. W. Bennett et al., *Measurement of the Negative Muon Anomalous Magnetic Moment to 0.7 ppm*, Phys. Rev. Lett. **92** (2004) 161802. <http://link.aps.org/doi/10.1103/PhysRevLett.92.161802>.
- [26] K. Hagiwara, R. Liao, A. D. Martin, D. Nomura, and T. Teubner,  *$(g - 2)_\mu$  and  $\alpha(M_Z^2)$  re-evaluated using new precise data*, J.Phys. **G38** (2011) 085003, arXiv:1105.3149 [hep-ph].
- [27] T. Aoyama, M. Hayakawa, T. Kinoshita, and M. Nio, *Complete Tenth-Order QED Contribution to the Muon  $g-2$* , Phys.Rev.Lett. **109** (2012) 111808, arXiv:1205.5370 [hep-ph].

- [28] K. Fujikawa, B. W. Lee, and A. I. Sanda, *Generalized Renormalizable Gauge Formulation of Spontaneously Broken Gauge Theories*, Phys. Rev. D **6** (1972) 2923–2943.  
<http://link.aps.org/doi/10.1103/PhysRevD.6.2923>.
- [29] A. Czarnecki, B. Krause, and W. J. Marciano, *Electroweak Corrections to the Muon Anomalous Magnetic Moment*, Phys. Rev. Lett. **76** (1996) 3267–3270.  
<http://link.aps.org/doi/10.1103/PhysRevLett.76.3267>.
- [30] M. Knecht, M. Perrottet, E. de Rafael, and S. Peris, *Electroweak Hadronic Contributions to the muon  $g - 2$* , Journal of High Energy Physics **2002** no. 11, (2002) 003.  
<http://stacks.iop.org/1126-6708/2002/i=11/a=003>.
- [31] A. Czarnecki, W. J. Marciano, and A. Vainshtein, *Refinements in electroweak contributions to the muon anomalous magnetic moment*, Phys. Rev. D **67** (2003) 073006.  
<http://link.aps.org/doi/10.1103/PhysRevD.67.073006>.
- [32] KLOE Collaboration, F. Ambrosino et al., *Measurement of  $\sigma(e^+e^- \rightarrow \pi^+\pi^-\gamma(\gamma))$  and the dipion contribution to the muon anomaly with the KLOE detector*, Phys.Lett. **B670** (2009) 285–291, arXiv:0809.3950 [hep-ex].
- [33] KLOE Collaboration, F. Ambrosino et al., *Measurement of  $\sigma(e^+e^- \rightarrow \pi^+\pi^-)$  from threshold to  $0.85\text{ GeV}^2$  using Initial State Radiation with the KLOE detector*, Phys.Lett. **B700** (2011) 102–110, arXiv:1006.5313 [hep-ex].
- [34] B. Aubert et al., *Precise Measurement of the  $e^+e^- \rightarrow \pi^+\pi^-(\gamma)$  Cross Section with the Initial State Radiation Method at BABAR*, Phys. Rev. Lett. **103** (2009) 231801.  
<http://link.aps.org/doi/10.1103/PhysRevLett.103.231801>.
- [35] H. Miyazawa, *Baryon Number Changing Currents*, Prog. Theor. Phys. **36** (6) (1966) 1266–1276.
- [36] P. Ramond, *Dual Theory for Free Fermions*, Phys. Rev. **D 3** (1971) 2415–2418.
- [37] Y. A. Gol’fand and E. P. Likhtman, *Extension of the Algebra of Poincare Group Generators and Violation of  $p$  Invariance*, JETP Lett. **13** (1971) 323–326.
- [38] A. Neveu and J. H. Schwarz, *Factorizable dual model of pions*, Nucl. Phys. **B 31** (1971) 86–112.
- [39] A. Neveu and J. H. Schwarz, *Quark Model of Dual Pions*, Phys. Rev. **D 4** (1971) 1109–1111.
- [40] J. Gervais and B. Sakita, *Field theory interpretation of supergauges in dual models*, Nucl. Phys. **B 34** (1971) 632–639.
- [41] D. V. Volkov and V. P. Akulov, *Is the Neutrino a Goldstone Particle?*, Phys. Lett. **B 46** (1973) 109–110.
- [42] J. Wess and B. Zumino, *A Lagrangian Model Invariant Under Supergauge Transformations*, Phys. Lett. **B 49** (1974) 52–54.

- [43] J. Wess and B. Zumino, *Supergauge Transformations in Four-Dimensions*, Nucl. Phys. **B 70** (1974) 39–50.
- [44] R. Haag, J. T. opuszaski, and M. Sohnius, *All possible generators of supersymmetries of the S-matrix*, Nuclear Physics B **88** no. 2, (1975) 257 – 274.  
<http://www.sciencedirect.com/science/article/pii/0550321375902795>.
- [45] H. Murayama and A. Pierce, *Not even decoupling can save minimal supersymmetric SU(5)*, Phys.Rev. **D65** (2002) 055009, arXiv:hep-ph/0108104 [hep-ph].
- [46] Super-Kamiokande Collaboration Collaboration, K. Abe et al., “*Search for Proton Decay via  $p \rightarrow \nu K^+$  using 260 kiloton-year data of Super-Kamiokande*”, Phys.Rev. **D90** (2014) 072005, arXiv:1408.1195 [hep-ex].
- [47] I. Gogoladze, F. Nasir, Q. Shafi, and C. S. Un, *Nonuniversal Gaugino Masses and Muon  $g-2$* , Phys. Rev. **D90** no. 3, (2014) 035008, arXiv:1403.2337 [hep-ph].
- [48] M. Endo, K. Hamaguchi, S. Iwamoto, and T. Yoshinaga, *Muon  $g - 2$  vs LHC in Supersymmetric Models*, JHEP **1401** (2014) 123, arXiv:1303.4256 [hep-ph].
- [49] S. Dimopoulos and H. Georgi, *Softly Broken Supersymmetry and SU(5)*, Nucl.Phys. **B193** (1981) 150.
- [50] S. P. Martin, *A Supersymmetry primer*, Adv.Ser.Direct.High Energy Phys. **21** (2010) 1–153, arXiv:hep-ph/9709356 [hep-ph].
- [51] D. J. H. Chung, L. L. Everett, G. L. Kane, S. F. King, J. D. Lykken, and L.-T. Wang, *The Soft supersymmetry breaking Lagrangian: Theory and applications*, Phys. Rept. **407** (2005) 1–203, arXiv:hep-ph/0312378 [hep-ph].
- [52] P. Van Nieuwenhuizen, *Supergravity*, Phys. Rept. **68** (1981) 189–398.
- [53] H. Pagels and J. R. Primack, *Supersymmetry, Cosmology and New TeV Physics*, Phys. Rev. Lett. **48** (1982) 223.
- [54] S. Weinberg, *Cosmological Constraints on the Scale of Supersymmetry Breaking*, Phys. Rev. Lett. **48** (1982) 1303.
- [55] G. F. Giudice, M. A. Luty, H. Murayama, and R. Rattazzi, *Gaugino mass without singlets*, JHEP **12** (1998) 027, arXiv:hep-ph/9810442 [hep-ph].
- [56] L. Randall and R. Sundrum, *Out of this world supersymmetry breaking*, Nucl. Phys. **B557** (1999) 79–118, arXiv:hep-th/9810155 [hep-th].
- [57] ATLAS Collaboration, G. Aad et al., *Search for charginos nearly mass degenerate with the lightest neutralino based on a disappearing-track signature in  $pp$  collisions at  $\sqrt{s}=8$  TeV with the ATLAS detector*, Phys. Rev. **D88** no. 11, (2013) 112006, arXiv:1310.3675 [hep-ex].

- [58] C. R. Nappi and B. A. Ovrut, *Supersymmetric Extension of the  $SU(3) \times SU(2) \times U(1)$  Model*, Phys. Lett. **B113** (1982) 175.
- [59] L. Alvarez-Gaume, M. Claudson, and M. B. Wise, *Low-Energy Supersymmetry*, Nucl. Phys. **B207** (1982) 96.
- [60] M. Dine and A. E. Nelson, *Dynamical supersymmetry breaking at low-energies*, Phys. Rev. **D48** (1993) 1277–1287, arXiv:hep-ph/9303230 [hep-ph].
- [61] M. Dine, A. E. Nelson, and Y. Shirman, *Low-energy dynamical supersymmetry breaking simplified*, Phys. Rev. **D51** (1995) 1362–1370, arXiv:hep-ph/9408384 [hep-ph].
- [62] M. Dine, A. E. Nelson, Y. Nir, and Y. Shirman, *New tools for low-energy dynamical supersymmetry breaking*, Phys. Rev. **D53** (1996) 2658–2669, arXiv:hep-ph/9507378 [hep-ph].
- [63] T. Moroi, H. Murayama, and M. Yamaguchi, *Cosmological constraints on the light stable gravitino*, Phys. Lett. **B303** (1993) 289–294.
- [64] ATLAS Collaboration, *Search for supersymmetry in final states with jets, missing transverse momentum and a Z boson at  $\sqrt{s} = 8$  TeV with the ATLAS detector*, ATLAS-CONF-2012-152, ATLAS-COM-CONF-2012-185 (2012). <https://cds.cern.ch/record/1493491/>.
- [65] J. Alwall, P. Schuster, and N. Toro, *Simplified Models for a First Characterization of New Physics at the LHC*, Phys.Rev. **D79** (2009) 075020, arXiv:0810.3921 [hep-ph].
- [66] A. Djouadi, J.-L. Kneur, and G. Moultaka, *SuSpect: A Fortran code for the supersymmetric and Higgs particle spectrum in the MSSM*, Comput. Phys. Commun. **176** (2007) 426–455, arXiv:hep-ph/0211331 [hep-ph].
- [67] A. Djouadi et al., *The Minimal supersymmetric standard model: Group summary report*, arXiv:hep-ph/9901246 [hep-ph].
- [68] ATLAS Collaboration, G. Aad et al., *Search for new phenomena in final states with large jet multiplicities and missing transverse momentum at  $\sqrt{s} = 8$  TeV proton-proton collisions using the ATLAS experiment*, JHEP **1310** (2013) 130, arXiv:1308.1841 [hep-ex].
- [69] CMS Collaboration, S. Chatrchyan et al., *Search for new physics in the multijet and missing transverse momentum final state in proton-proton collisions at  $\sqrt{s} = 8$  TeV*, JHEP **1406** (2014) 055, arXiv:1402.4770 [hep-ex].
- [70] M. Spira, *Higgs and SUSY particle production at hadron colliders*, pp. , 217–226. 2002. arXiv:hep-ph/0211145 [hep-ph]. [http://www-library.desy.de/preparch/desy/proc/proc02-02/Proceedings/pl.1c/spira\\_pr.pdf](http://www-library.desy.de/preparch/desy/proc/proc02-02/Proceedings/pl.1c/spira_pr.pdf).
- [71] W. Beenakker, R. Hopker, M. Spira, and P. M. Zerwas, *Squark and gluino production at hadron colliders*, Nucl. Phys. **B492** (1997) 51–103, arXiv:hep-ph/9610490 [hep-ph].



- [72] W. Beenakker, M. Kramer, T. Plehn, M. Spira, and P. M. Zerwas, *Stop production at hadron colliders*, Nucl. Phys. **B515** (1998) 3–14, arXiv:hep-ph/9710451 [hep-ph].
- [73] W. Beenakker, M. Klasen, M. Kramer, T. Plehn, M. Spira, and P. M. Zerwas, *The Production of charginos / neutralinos and sleptons at hadron colliders*, Phys. Rev. Lett. **83** (1999) 3780–3783, arXiv:hep-ph/9906298 [hep-ph]. [Erratum: Phys. Rev. Lett.100,029901(2008)].
- [74] T. Plehn, *Measuring the MSSM Lagrangean*, Czech. J. Phys. **55** (2005) B213–B220, arXiv:hep-ph/0410063 [hep-ph].
- [75] ATLAS Collaboration, *Search for direct-slepton and direct-chargino production in final states with two opposite-sign leptons, missing transverse momentum and no jets in 20/fb of pp collisions at  $\sqrt{s} = 8$  TeV with the ATLAS detector*, Tech. Rep. ATLAS-CONF-2013-049, ATLAS-COM-CONF-2013-050, 2013.
- [76] K. Howe and P. Saraswat, *Excess Higgs Production in Neutralino Decays*, JHEP **1210** (2012) 065, arXiv:1208.1542 [hep-ph].
- [77] ALEPH Collaboration, D. Decamp et al., *ALEPH: A detector for electron-positron annihilations at LEP*, Nucl.Instrum.Meth. **A294** (1990) 121–178.
- [78] ALEPH Collaboration, D. Buskulic et al., *Performance of the ALEPH detector at LEP*, Nucl.Instrum.Meth. **A360** (1995) 481–506.
- [79] DELPHI Collaboration, P. Aarnio et al., *The DELPHI detector at LEP*, Nucl.Instrum.Meth. **A303** (1991) 233–276.
- [80] DELPHI Collaboration, P. Abreu et al., *Performance of the DELPHI detector*, Nucl.Instrum.Meth. **A378** (1996) 57–100.
- [81] OPAL Collaboration, K. Ahmet et al., *The OPAL detector at LEP*, Nucl.Instrum.Meth. **A305** (1991) 275–319.
- [82] L3 Collaboration, *The Construction of the L3 Experiment*, Nucl.Instrum.Meth. **A289** (1990) 35–102.
- [83] LEPSUSYWG, ALEPH, DELPHI, L3 and OPAL experiments, *Searches for sleptons at LEP*, note LEPSUSYWG/04-01.1 (2004). <http://lepsusy.web.cern.ch/lepsusy/Welcome.html>.
- [84] LEPSUSYWG, ALEPH, DELPHI, L3 and OPAL experiments, *Searches for stops and sbottoms at LEP*, note LEPSUSYWG/04-02.1 (2004). <http://lepsusy.web.cern.ch/lepsusy/Welcome.html>.
- [85] LEPSUSYWG, ALEPH, DELPHI, L3 and OPAL experiments, *Searches for charginos with large  $m_0$  at LEP*, note LEPSUSYWG/01-03.1 (2001). <http://lepsusy.web.cern.ch/lepsusy/Welcome.html>.

- [86] LEPSUSYWG, ALEPH, DELPHI, L3 and OPAL experiments, *Searches for charginos at small mass difference at LEP*, note LEPSUSYWG/02-04.1 (2002).  
<http://lepsusy.web.cern.ch/lepsusy/Welcome.html>.
- [87] LEPSUSYWG, ALEPH, DELPHI, L3 and OPAL experiments, *Searches for heavy stable charged particles at LEP*, note LEPSUSYWG/02-05.1 (2002).  
<http://lepsusy.web.cern.ch/lepsusy/Welcome.html>.
- [88] LEPSUSYWG, ALEPH, DELPHI, L3 and OPAL experiments, *Interpretation in constrained MSSM and limit on the LSP mass at LEP*, note LEPSUSYWG/04-07.1 (2004).  
<http://lepsusy.web.cern.ch/lepsusy/Welcome.html>.
- [89] LEPSUSYWG, ALEPH, DELPHI, L3 and OPAL experiments, *LSP mass limit in mSUGRA at LEP*, note LEPSUSYWG/02-06.2 (2002). <http://lepsusy.web.cern.ch/lepsusy/Welcome.html>.
- [90] LEPSUSYWG, ALEPH, DELPHI, L3 and OPAL experiments, *Searches for SUSY with two photons at LEP*, note LEPSUSYWG/04-09.1 (2004).  
<http://lepsusy.web.cern.ch/lepsusy/Welcome.html>.
- [91] LEPSUSYWG, ALEPH, DELPHI, L3 and OPAL experiments, *Searches for SUSY with single photon at LEP*, note LEPSUSYWG/04-10.1 (2004).  
<http://lepsusy.web.cern.ch/lepsusy/Welcome.html>.
- [92] LEPSUSYWG, ALEPH, DELPHI, L3 and OPAL experiments, *Searches for GMSB signals with sleptons as NLSP at LEP*, note LEPSUSYWG/02-09.2 (2002).  
<http://lepsusy.web.cern.ch/lepsusy/Welcome.html>.
- [93] LEPSUSYWG, ALEPH, DELPHI, L3 and OPAL experiments, *Searches for R-parity violated SUSY signals with LLE couplings at LEP*, note LEPSUSYWG/02-10.1 (2002).  
<http://lepsusy.web.cern.ch/lepsusy/Welcome.html>.
- [94] CDF Collaboration, T. Affolder et al., *Search for scalar top and scalar bottom quarks in  $p\bar{p}$  collisions at  $\sqrt{s} = 1.8$  TeV*, Phys.Rev.Lett. **84** (2000) 5704–5709, arXiv:hep-ex/9910049 [hep-ex].
- [95] DØ Collaboration, V. Abazov et al., *A search for the scalar top quark in  $p\bar{p}$  collisions at  $\sqrt{s} = 1.8$  TeV*, Phys.Rev.Lett. **88** (2002) 171802, arXiv:hep-ex/0108018 [hep-ex].
- [96] J. R. Ellis, K. Enqvist, and D. V. Nanopoulos, *A Very Light Gravitino in a No Scale Model*, Phys.Lett. **B147** (1984) 99.
- [97] CDF Collaboration, F. Abe et al., *Observation of top quark production in  $p\bar{p}$  collisions*, Phys.Rev.Lett. **74** (1995) 2626–2631, arXiv:hep-ex/9503002 [hep-ex].
- [98] DØ Collaboration, S. Abachi et al., *Observation of the top quark*, Phys.Rev.Lett. **74** (1995) 2632–2637, arXiv:hep-ex/9503003 [hep-ex].

- [99] CDF Collaboration, F. Abe et al., *The CDF Detector: An Overview*, Nucl.Instrum.Meth. **A271** (1988) 387–403.
- [100] V. Abazov et al., *The upgraded  $D\bar{D}$  detector*, Nuclear Instruments and Methods in Physics Research Section A: Accelerators, Spectrometers, Detectors and Associated Equipment **565** no. 2, (2006) 463 – 537. <http://www.sciencedirect.com/science/article/pii/S0168900206010357>.
- [101] CDF,  $D\bar{D}$  Collaboration, M. Jaffre, *SUSY searches at the Tevatron*, EPJ Web Conf. **28** (2012) 09006, arXiv:1202.0712 [hep-ex].
- [102] CDF Collaboration, M. Gold, J. Strologas, M. Vogel, et al., *Search for trilepton Supersymmetry at the Collider Detector at Fermilab*, CDF Public Note no. 10636, (2011). [http://www-cdf.fnal.gov/physics/exotic/r2a/20110826.trilepton\\_6fb/](http://www-cdf.fnal.gov/physics/exotic/r2a/20110826.trilepton_6fb/).
- [103] CDF,  $D\bar{D}$  Collaboration, V. Buescher et al., *Combination of CDF and  $D\bar{D}$  limits on a gauge mediated SUSY model using diphoton and missing transverse energy channel*, arXiv:hep-ex/0504004 [hep-ex].
- [104] W. Beenakker, R. Hopker, and M. Spira, *PROSPINO: A Program for the production of supersymmetric particles in next-to-leading order QCD*, arXiv:hep-ph/9611232 [hep-ph].
- [105] L. Evans and P. Bryant, *LHC Machine*, JINST **3** (2008) S08001.
- [106] ATLAS Collaboration, G. Aad et al., *The ATLAS Experiment at the CERN Large Hadron Collider*, JINST **3** (2008) S08003.
- [107] CMS Collaboration, S. Chatrchyan et al., *The CMS experiment at the CERN LHC*, JINST **3** (2008) S08004.
- [108] CMS Collaboration, S. Chatrchyan et al., *Search for supersymmetry in hadronic final states with missing transverse energy using the variables  $\alpha_T$  and  $b$ -quark multiplicity in  $pp$  collisions at  $\sqrt{s} = 8$  TeV*, Eur.Phys.J. **C73** no. 9, (2013) 2568, arXiv:1303.2985 [hep-ex].
- [109] CMS Collaboration, V. Khachatryan et al., *Searches for supersymmetry using the  $M_{T2}$  variable in hadronic events produced in  $pp$  collisions at 8 TeV*, JHEP **05** (2015) 078, arXiv:1502.04358 [hep-ex].
- [110] ATLAS Collaboration, G. Aad et al., *ATLAS Run 1 searches for direct pair production of third-generation squarks at the Large Hadron Collider*, arXiv:1506.08616 [hep-ex].
- [111] ATLAS Collaboration, *ATLAS SUSY Public Results*,. <https://twiki.cern.ch/twiki/bin/view/AtlasPublic/SupersymmetryPublicResults>.
- [112] ATLAS Collaboration, G. Aad et al., *Search for direct production of charginos, neutralinos and sleptons in final states with two leptons and missing transverse momentum in  $pp$  collisions at  $\sqrt{s} = 8$  TeV with the ATLAS detector*, JHEP **1405** (2014) 071, arXiv:1403.5294 [hep-ex].

- [113] CMS Collaboration, *CMS SUSY Public Results*,  
<https://twiki.cern.ch/twiki/bin/view/CMSPublic/PhysicsResultsSUS>.
- [114] ATLAS Collaboration. <https://www.atlas.ch>.
- [115] K. Schindl, *The injector chain for the LHC*,  
[http://sl-div.web.cern.ch/sl-div/publications/chamx99/PAPERS/KS1\\_5.PDF](http://sl-div.web.cern.ch/sl-div/publications/chamx99/PAPERS/KS1_5.PDF).
- [116] J. Haffner, *The CERN accelerator complex./Complexe des accélérateurs du CERN*,  
<http://cds.cern.ch/record/1621894>. General Photo.
- [117] ATLAS Collaboration, *Luminosity Public Results*,  
<https://twiki.cern.ch/twiki/bin/view/AtlasPublic/LuminosityPublicResults>.
- [118] G. Aad et al., *ATLAS pixel detector electronics and sensors*, Journal of Instrumentation **3** no. 07, (2008) P07007. <http://stacks.iop.org/1748-0221/3/i=07/a=P07007>.
- [119] ATLAS TRT Collaboration, E. Abat et al., *The ATLAS Transition Radiation Tracker (TRT) proportional drift tube: Design and performance*, JINST **3** (2008) P02013.
- [120] ATLAS Collaboration, *Particle Identification Performance of the ATLAS Transition Radiation Tracker*, Tech. Rep. ATLAS-CONF-2011-128, CERN, Geneva, Sep, 2011.  
<https://cds.cern.ch/record/1383793>.
- [121] ATLAS Collaboration, G. Aad et al., *Electron and photon energy calibration with the ATLAS detector using LHC Run 1 data*, Eur.Phys.J. **C74** no. 10, (2014) 3071, arXiv:1407.5063 [hep-ex].
- [122] A. Yamamoto et al., *The ATLAS central solenoid*, Nucl. Instrum. Meth. **A584** (2008) 53–74.
- [123] A. Yamamoto et al., *Progress in ATLAS central solenoid magnet*, IEEE Trans. Appl. Supercond. **10** (2000) 353–356.
- [124] ATLAS Collaboration, P. Jenni, M. Nordberg, M. Nessi, and K. Jon-And, *ATLAS Forward Detectors for Measurement of Elastic Scattering and Luminosity*. Technical Design Report. CERN, Geneva, 2008. <https://cds.cern.ch/record/1095847>.
- [125] ATLAS Collaboration, *Luminosity Determination Using the ATLAS Detector*, Tech. Rep. ATLAS-CONF-2010-060, CERN, Geneva, Jul, 2010. <https://cds.cern.ch/record/1281333>.
- [126] ATLAS Collaboration, *ATLAS detector and physics performance: Technical Design Report, 1*. Technical Design Report ATLAS. CERN, Geneva, 1999.  
<https://cds.cern.ch/record/391176>.
- [127] ATLAS Collaboration, *Expected performance of the ATLAS experiment: detector, trigger and physics*. CERN, Geneva, 2009. <https://cds.cern.ch/record/1125884>.
- [128] R. Achenbach et al., *The ATLAS level-1 calorimeter trigger*, JINST **3** (2008) P03001.

- [129] ATLAS Collaboration, *Performance of the ATLAS Electron and Photon Trigger in p-p Collisions at  $\sqrt{s} = 7$  TeV in 2011*, Tech. Rep. ATLAS-CONF-2012-048, CERN, Geneva, May, 2012. <https://cds.cern.ch/record/1450089>.
- [130] G. Aad et al., *Performance of the ATLAS muon trigger in pp collisions at  $\sqrt{s} = 8$  TeV*, The European Physical Journal C **75** no. 3, (2015). <http://dx.doi.org/10.1140/epjc/s10052-015-3325-9>.
- [131] T. Cornelissen, M. Elsing, S. Fleischmann, W. Liebig, E. Moyses, and A. Salzburger, *Concepts, Design and Implementation of the ATLAS New Tracking (NEWT)*, Tech. Rep. ATL-SOFT-PUB-2007-007. ATL-COM-SOFT-2007-002, CERN, Geneva, Mar, 2007.
- [132] ATLAS Collaboration, *Performance of the ATLAS Inner Detector Track and Vertex Reconstruction in the High Pile-Up LHC Environment*, Tech. Rep. ATLAS-CONF-2012-042, ATLAS-COM-CONF-2012-014, 2012.
- [133] ATLAS Collaboration, *Performance of primary vertex reconstruction in proton-proton collisions at  $\sqrt{s} = 7$  TeV in the ATLAS experiment*, Tech. Rep. ATLAS-CONF-2010-069, CERN, Geneva, Jul, 2010. <https://cds.cern.ch/record/1281344>.
- [134] ATLAS Collaboration, *Tracking studies for b-tagging with 900 GeV collision data with the ATLAS detector*, Tech. Rep. ATLAS-CONF-2010-003, CERN, Geneva, Jun, 2010. <https://cds.cern.ch/record/1273190>.
- [135] ATLAS Collaboration, *Electron efficiency measurements with the ATLAS detector using the 2012 LHC proton-proton collision data*, Tech. Rep. ATLAS-CONF-2014-032, CERN, Geneva, Jun, 2014. <http://cds.cern.ch/record/1706245>.
- [136] ATLAS Collaboration, W. Lampl, S. Laplace, D. Lelas, P. Loch, H. Ma, S. Menke, S. Rajagopalan, D. Rousseau, S. Snyder, and G. Unal, *Calorimeter Clustering Algorithms: Description and Performance*, Tech. Rep. ATL-LARG-PUB-2008-002. ATL-COM-LARG-2008-003, CERN, Geneva, Apr, 2008.
- [137] R. Fruhwirth, *Application of Kalman filtering to track and vertex fitting*, Nucl.Instrum.Meth. **A262** (1987) 444–450.
- [138] A. Hocker et al., *TMVA - Toolkit for Multivariate Data Analysis*, PoS **ACAT** (2007) 040, [arXiv:physics/0703039](https://arxiv.org/abs/physics/0703039) [PHYSICS].
- [139] M. Cacciari, G. P. Salam, and G. Soyez, *The Anti- $k_t$  jet clustering algorithm*, JHEP **0804** (2008) 063, [arXiv:0802.1189](https://arxiv.org/abs/hep-ph/0802.1189) [hep-ph].
- [140] ATLAS Collaboration, T. Barillari et al., *Local hadronic calibration*,. <http://cds.cern.ch/record/1112035>.
- [141] S. D. Ellis and D. E. Soper, *Successive combination jet algorithm for hadron collisions*, Phys.Rev. **D48** (1993) 3160–3166, [arXiv:hep-ph/9305266](https://arxiv.org/abs/hep-ph/9305266) [hep-ph].

- [142] Y. L. Dokshitzer, G. Leder, S. Moretti, and B. Webber, *Better jet clustering algorithms*, JHEP **9708** (1997) 001, arXiv:hep-ph/9707323 [hep-ph].
- [143] M. Wobisch and T. Wengler, *Hadronization corrections to jet cross-sections in deep inelastic scattering*, arXiv:hep-ph/9907280 [hep-ph].
- [144] M. Cacciari, G. P. Salam, and G. Soyez, *The Catchment Area of Jets*, JHEP **0804** (2008) 005, arXiv:0802.1188 [hep-ph].
- [145] G. Corcella, I. Knowles, G. Marchesini, S. Moretti, K. Odagiri, et al., *HERWIG 6: An Event generator for hadron emission reactions with interfering gluons (including supersymmetric processes)*, JHEP **0101** (2001) 010, arXiv:hep-ph/0011363 [hep-ph].
- [146] ATLAS Collaboration, G. Aad et al., *Jet energy measurement with the ATLAS detector in proton-proton collisions at  $\sqrt{s} = 7$  TeV*, Eur.Phys.J. **C73** no. 3, (2013) 2304, arXiv:1112.6426 [hep-ex].
- [147] ATLAS Collaboration, *Jet energy scale and its systematic uncertainty for jets produced in proton-proton collisions at  $\sqrt{s} = 7$  TeV and measured with the ATLAS detector*, Tech. Rep. ATLAS-CONF-2010-056, CERN, Geneva, Jul, 2010. <https://cds.cern.ch/record/1281329>.
- [148] ATLAS Collaboration, *Jet energy resolution and selection efficiency relative to track jets from in-situ techniques with the ATLAS Detector Using Proton-Proton Collisions at a Center of Mass Energy  $\sqrt{s} = 7$  TeV*, Tech. Rep. ATLAS-CONF-2010-054, CERN, Geneva, Jul, 2010. <http://cds.cern.ch/record/1281311>.
- [149] ATLAS Collaboration, *Data-driven determination of the energy scale and resolution of jets reconstructed in the ATLAS calorimeters using dijet and multijet events at  $\sqrt{s} = 8$  TeV*, Tech. Rep. ATLAS-CONF-2015-017, CERN, Geneva, Apr, 2015. <https://cds.cern.ch/record/2008678>.
- [150] ATLAS Collaboration, *Tagging and suppression of pileup jets with the ATLAS detector*, Tech. Rep. ATLAS-CONF-2014-018, CERN, Geneva, May, 2014. <https://cds.cern.ch/record/1700870>.
- [151] ATLAS Collaboration, *Pile-up subtraction and suppression for jets in ATLAS*, Tech. Rep. ATLAS-CONF-2013-083, CERN, Geneva, Aug, 2013. <https://cds.cern.ch/record/1570994>.
- [152] ATLAS Collaboration, *Commissioning of the ATLAS high-performance b-tagging algorithms in the 7 TeV collision data*, Tech. Rep. ATLAS-CONF-2011-102, CERN, Geneva, Jul, 2011.
- [153] ATLAS Collaboration, *Performance of Impact Parameter-Based b-tagging Algorithms with the ATLAS Detector using Proton-Proton Collisions at  $\sqrt{s} = 7$  TeV*, Tech. Rep. ATLAS-CONF-2010-091, CERN, Geneva, Oct, 2010. <https://cds.cern.ch/record/1299106>.

- [154] ATLAS Collaboration, *Calibration of the performance of b-tagging for c and light-flavour jets in the 2012 ATLAS data*, Tech. Rep. ATLAS-CONF-2014-046, CERN, Geneva, Jul, 2014.  
<https://cds.cern.ch/record/1741020>.
- [155] ATLAS Collaboration, G. Aad et al., *Identification and energy calibration of hadronically decaying tau leptons with the ATLAS experiment in pp collisions at  $\sqrt{s} = 8$  TeV*, arXiv:1412.7086 [hep-ex].
- [156] ATLAS Collaboration, *Performance of the Reconstruction and Identification of Hadronic Tau Decays with ATLAS*, Tech. Rep. ATLAS-CONF-2011-152, CERN, Geneva, Nov, 2011.  
<https://cds.cern.ch/record/1398195>.
- [157] ATLAS Collaboration, *Performance of Missing Transverse Momentum Reconstruction in ATLAS with 2011 Proton-Proton Collisions at  $\sqrt{s} = 7$  TeV*, Tech. Rep. ATLAS-CONF-2012-101, CERN, Geneva, Jul, 2012. <https://cds.cern.ch/record/1463915>.
- [158] T. Sjostrand, S. Mrenna, and P. Z. Skands, *PYTHIA 6.4 Physics and Manual*, JHEP **0605** (2006) 026, arXiv:hep-ph/0603175 [hep-ph].
- [159] J. Alwall, P. Demin, S. de Visscher, R. Frederix, M. Herquet, et al., *MadGraph/MadEvent v4: The New Web Generation*, JHEP **0709** (2007) 028, arXiv:0706.2334 [hep-ph].
- [160] P. Nason, *A New method for combining NLO QCD with shower Monte Carlo algorithms*, JHEP **0411** (2004) 040, arXiv:hep-ph/0409146 [hep-ph].
- [161] M. L. Mangano, M. Moretti, F. Piccinini, R. Pittau, and A. D. Polosa, *ALPGEN, a generator for hard multiparton processes in hadronic collisions*, JHEP **0307** (2003) 001, arXiv:hep-ph/0206293 [hep-ph].
- [162] S. Frixione and B. R. Webber, *The MC@NLO 3.2 event generator*, arXiv:hep-ph/0601192 [hep-ph].
- [163] J. Pumplin et al., *New generation of parton distributions with uncertainties from global QCD analysis*, JHEP **07** (2002) 012, arXiv:hep-ph/0201195.
- [164] H.-L. Lai et al., *New parton distributions for collider physics*, Phys. Rev. **D 82** (2010) 074024, arXiv:1007.2241 [hep-ph].
- [165] GEANT4 Collaboration, S. Agostinelli et al., *GEANT4: A Simulation toolkit*, Nucl. Instrum. Meth. **A506** (2003) 250–303.
- [166] ATLAS Collaboration, G. Aad et al., *The ATLAS Simulation Infrastructure*, Eur. Phys. J. **C70** (2010) 823–874, arXiv:1005.4568 [physics.ins-det].
- [167] ATLAS Collaboration, *New ATLAS event generator tunes to 2010 data*, Tech. Rep. ATL-PHYS-PUB-2011-008, CERN, Geneva, Apr, 2011.

- [168] ATLAS Collaboration, *Summary of ATLAS Pythia 8 tunes*, ATL-PHYS-PUB-2012-003 (2012).  
<https://cdsweb.cern.ch/record/1474107>.
- [169] P. Z. Skands, *Tuning Monte Carlo Generators: The Perugia Tunes*, Phys.Rev. **D82** (2010) 074018,  
arXiv:1005.3457 [hep-ph].
- [170] M. Bähr, S. Gieseke, M. A. Gigg, D. Grellscheid, K. Hamilton, O. Latunde-Dada, S. Plätzer,  
P. Richardson, M. H. Seymour, A. Sherstnev, and B. R. Webber, *Herwig++ physics and manual*,  
The European Physical Journal C **58** no. 4, (2008) 639–707.  
<http://dx.doi.org/10.1140/epjc/s10052-008-0798-9>.
- [171] G. Cowan, K. Cranmer, E. Gross, and O. Vitells, *Asymptotic formulae for likelihood-based tests of  
new physics*, The European Physical Journal C **71** no. 2, (2011).  
<http://dx.doi.org/10.1140/epjc/s10052-011-1554-0>.
- [172] ATLAS Collaboration, G. Aad et al., *Determination of spin and parity of the Higgs boson in the  
 $WW^* \rightarrow e\nu\mu\nu$  decay channel with the ATLAS detector*, Eur. Phys. J. **C75** no. 5, (2015) 231,  
arXiv:1503.03643 [hep-ex].
- [173] ATLAS Collaboration, G. Aad et al., *Measurement of the Z to tau tau Cross Section with the ATLAS  
Detector*, Phys. Rev. **D84** (2011) 112006, arXiv:1108.2016 [hep-ex].
- [174] ATLAS Collaboration, G. Aad et al., *Measurement of the muon reconstruction performance of the  
ATLAS detector using 2011 and 2012 LHC protonproton collision data*, Eur. Phys. J. **C74** no. 11,  
(2014) 3130, arXiv:1407.3935 [hep-ex].
- [175] ATLAS Collaboration, *Reconstruction, Energy Calibration, and Identification of Hadronically  
Decaying Tau Leptons*, ATLAS-CONF-2011-077, ATLAS-COM-CONF-2011-057 (2011).  
<https://cds.cern.ch/record/1353226>.
- [176] ATLAS Collaboration, *Calibration of b-tagging using dileptonic top pair events in a combinatorial  
likelihood approach with the ATLAS experiment*, ATLAS-CONF-2014-004,  
ATLAS-COM-CONF-2014-003 (2014). <https://cds.cern.ch/record/1664335>.
- [177] ATLAS Collaboration, G. Aad et al., *Improved luminosity determination in pp collisions at  $\sqrt{s} = 7$   
TeV using the ATLAS detector at the LHC*, Eur.Phys.J. **C73** no. 8, (2013) 2518, arXiv:1302.4393  
[hep-ex].
- [178] A. Kardos, Z. Trocsanyi, and C. Papadopoulos, *Top quark pair production in association with a  
Z-boson at NLO accuracy*, Phys. Rev. **D85** (2012) 054015, arXiv:1111.0610 [hep-ph].
- [179] J. M. Campbell and R. K. Ellis,  *$t\bar{t}W^{+-}$  production and decay at NLO*, JHEP **07** (2012) 052,  
arXiv:1204.5678 [hep-ph].
- [180] ATLAS Collaboration, *Measurement of the total ZZ production cross section in proton-proton  
collisions at  $\sqrt{s} = 8$  TeV in  $20\text{ fb}^{-1}$  with the ATLAS detector*, ATLAS-CONF-2013-020.  
<http://cdsweb.cern.ch/record/1525555>.



- [181] ATLAS Collaboration, *A Measurement of WZ Production in Proton-Proton Collisions at  $\sqrt{s} = 8$  TeV with the ATLAS Detector*, ATLAS-CONF-2013-021.  
<http://cdsweb.cern.ch/record/1525557>.
- [182] J. M. Campbell, R. K. Ellis, and C. Williams, *Vector boson pair production at the LHC*, JHEP **07** (2011) 018, arXiv:1105.0020 [hep-ph].
- [183] S. Dittmaier et al., *Handbook of LHC Higgs Cross Sections: 2. Differential Distributions*, arXiv:1201.3084 [hep-ph].
- [184] M. Baak, G. Besjes, D. Cte, A. Koutsman, J. Lorenz, et al., *HistFitter software framework for statistical data analysis*, Eur.Phys.J. **C75** no. 4, (2015) 153, arXiv:1410.1280 [hep-ex].
- [185] A. L. Read, *Presentation of search results: the  $CL_s$  technique*, Journal of Physics G: Nuclear and Particle Physics **28** no. 10, (2002) 2693.  
<http://stacks.iop.org/0954-3899/28/i=10/a=313>.
- [186] G. Cowan, K. Cranmer, E. Gross, and O. Vitells, *Asymptotic formulae for likelihood-based tests of new physics*, European Physical Journal C **71** (2011) 1554, arXiv:1007.1727 [physics.data-an].
- [187] ATLAS Collaboration, G. Aad et al., *Search for direct production of charginos and neutralinos in events with three leptons and missing transverse momentum in  $\sqrt{s} = 7$  TeV pp collisions with the ATLAS detector*, Phys.Lett. **B718** (2013) 841–859, arXiv:1208.3144 [hep-ex].
- [188] CMS Collaboration, V. Khachatryan et al., *Searches for electroweak production of charginos, neutralinos, and sleptons decaying to leptons and W, Z, and Higgs bosons in pp collisions at 8 TeV*, Eur. Phys. J. **C74** no. 9, (2014) 3036, arXiv:1405.7570 [hep-ex].
- [189] ATLAS Collaboration, *Search for chargino and neutralino production in final states with one lepton, two b-jets consistent with a Higgs boson, and missing transverse momentum with the ATLAS detector in  $20.3 \text{ fb}^{-1}$  of  $\sqrt{s} = 8$  TeV pp collisions*, Tech. Rep. ATLAS-CONF-2013-093, CERN, Geneva, Aug, 2013. <https://cds.cern.ch/record/1595756>.
- [190] H. Baer, A. D. Box, and H. Summy, *Neutralino versus axion/axino cold dark matter in the 19 parameter SUGRA model*, JHEP **10** (2010) 023, arXiv:1005.2215 [hep-ph].
- [191] S. Henrot-Versillé, R. Lafaye, T. Plehn, M. Rauch, D. Zerwas, S. Plaszczynski, B. Rouillé d’Orfeuil, and M. Spinelli, *Constraining Supersymmetry using the relic density and the Higgs boson*, Phys. Rev. **D89** no. 5, (2014) 055017, arXiv:1309.6958 [hep-ph].
- [192] K. Harigaya, K. Kaneta, and S. Matsumoto, *Gaugino coannihilations*, Phys. Rev. **D89** no. 11, (2014) 115021, arXiv:1403.0715 [hep-ph].
- [193] CDF Collaboration, T. Aaltonen et al., *Search for  $B_s^0 \rightarrow \mu^+ \mu^-$  and  $B_d^0 \rightarrow \mu^+ \mu^-$  decays with  $2 \text{ fb}^{-1}$  of  $p\bar{p}$  collisions*, Phys. Rev. Lett. **100** (2008) 101802, arXiv:0712.1708 [hep-ex].

- [194] Heavy Flavor Averaging Group Collaboration, E. Barberio et al., *Averages of  $b$ -hadron and  $c$ -hadron Properties at the End of 2007*, arXiv:0808.1297 [hep-ex].



## **Appendix A**

# **Monte Carlo Samples**

### **A.1 The Standard Model MC samples**

The lists for the MC samples of the backgrounds which are used in the analysis are given in Tabs. A.1–A.7.

Table A.1: The diboson samples used for the analyses.

Process	Generator	filter	$\sigma$ [pb]	k-factor	filter eff.	$\int \mathcal{L} dt$ [fb $^{-1}$ ]
$ZZ \rightarrow eeee$	POWHEG	$e/\mu$	0.08	1.0	0.91	15767.9
$ZZ \rightarrow \mu\mu\mu\mu$	POWHEG	$e/\mu$	0.08	1.0	0.91	15680.7
$ZZ \rightarrow \tau\tau\tau\tau$	POWHEG	$e/\mu$	0.08	1.0	0.11	36813.5
$ZZ \rightarrow ee\mu\mu$	POWHEG	$e/\mu$	0.18	1.0	0.83	11018.7
$ZZ \rightarrow ee\tau\tau$	POWHEG	$e/\mu$	0.18	1.0	0.58	10760.7
$ZZ \rightarrow \mu\mu\tau\tau$	POWHEG	$e/\mu$	0.18	1.0	0.59	10669.5
$ZZ \rightarrow ee\tau\tau$	POWHEG	$e/\mu/\tau$	0.18	1.0	0.084	7487.0
$ZZ \rightarrow \mu\mu\tau\tau$	POWHEG	$e/\mu/\tau$	0.18	1.0	0.082	7427.3
$ZZ \rightarrow \tau\tau\tau\tau$	POWHEG	$e/\mu/\tau$	0.08	1.0	0.324	12045.4
$WZ \rightarrow e^+vee$	POWHEG	$e/\mu$	1.41	1.122	0.29	408.6
$WZ \rightarrow e^+\nu\mu\mu$	POWHEG	$e/\mu$	0.94	1.122	0.35	512.6
$WZ \rightarrow e^+\nu\tau\tau$	POWHEG	$e/\mu$	0.17	1.122	0.17	2325.6
$WZ \rightarrow \mu^+vee$	POWHEG	$e/\mu$	1.40	1.122	0.29	412.4
$WZ \rightarrow \mu^+\nu\mu\mu$	POWHEG	$e/\mu$	0.95	1.122	0.35	505.4
$WZ \rightarrow \mu^+\nu\tau\tau$	POWHEG	$e/\mu$	0.17	1.122	0.17	2300.6
$WZ \rightarrow \tau^+vee$	POWHEG	$e/\mu$	1.40	1.122	0.14	336.2
$WZ \rightarrow \tau^+\nu\mu\mu$	POWHEG	$e/\mu$	0.94	1.122	0.18	395.5
$WZ \rightarrow \tau^+\nu\tau\tau$	POWHEG	$e/\mu$	0.17	1.122	0.06	1683.5
$WZ \rightarrow e^-vee$	POWHEG	$e/\mu$	0.98	1.144	0.30	570.7
$WZ \rightarrow e^-\nu\mu\mu$	POWHEG	$e/\mu$	0.64	1.144	0.35	736.3
$WZ \rightarrow e^-\nu\tau\tau$	POWHEG	$e/\mu$	0.11	1.144	0.16	3697.9
$WZ \rightarrow \mu^-vee$	POWHEG	$e/\mu$	0.94	1.144	0.30	596.2
$WZ \rightarrow \mu^-\nu\mu\mu$	POWHEG	$e/\mu$	0.65	1.144	0.35	722.8
$WZ \rightarrow \mu^-\nu\tau\tau$	POWHEG	$e/\mu$	0.11	1.144	0.16	3685.5
$WZ \rightarrow \tau^-vee$	POWHEG	$e/\mu$	0.94	1.144	0.15	479.5
$WZ \rightarrow \tau^-\nu\mu\mu$	POWHEG	$e/\mu$	0.64	1.144	0.19	557.2
$WZ \rightarrow \tau^-\nu\tau\tau$	POWHEG	$e/\mu$	0.11	1.144	0.06	2648.3
$WZ \rightarrow e^+\nu\tau\tau$	POWHEG	$e/\mu/\tau$	0.17	1.122	0.163	2382.4
$WZ \rightarrow \mu^+\nu\tau\tau$	POWHEG	$e/\mu/\tau$	0.17	1.122	0.164	2367.0
$WZ \rightarrow \tau^+vee$	POWHEG	$e/\mu/\tau$	1.40	1.122	0.053	228.2
$WZ \rightarrow \tau^+\nu\mu\mu$	POWHEG	$e/\mu/\tau$	0.94	1.122	0.058	309.5
$WZ \rightarrow \tau^+\nu\tau\tau$	POWHEG	$e/\mu/\tau$	0.17	1.122	0.198	498.1
$WZ \rightarrow e^-\nu\tau\tau$	POWHEG	$e/\mu/\tau$	0.11	1.144	0.151	3912.0
$WZ \rightarrow \mu^-\nu\tau\tau$	POWHEG	$e/\mu/\tau$	0.11	1.144	0.152	3882.4
$WZ \rightarrow \tau^-vee$	POWHEG	$e/\mu/\tau$	0.94	1.144	0.057	310.5
$WZ \rightarrow \tau^-\nu\mu\mu$	POWHEG	$e/\mu/\tau$	0.64	1.144	0.066	396.4
$WZ \rightarrow \tau^-\nu\tau\tau$	POWHEG	$e/\mu/\tau$	0.11	1.144	0.183	819.7
$W(\rightarrow e\nu) + \gamma$	SHERPA	–	163.11	1.0	1.0	11.0
$W(\rightarrow \mu\nu) + \gamma$	SHERPA	–	162.74	1.0	1.0	11.0
$W(\rightarrow \tau\nu) + \gamma$	SHERPA	–	162.00	1.0	1.0	11.0
$Z(\rightarrow ee) + \gamma$	SHERPA	–	32.26	1.0	1.0	37.1
$Z(\rightarrow \mu\mu) + \gamma$	SHERPA	–	32.32	1.0	1.0	37.1
$Z(\rightarrow \tau\tau) + \gamma$	SHERPA	–	32.33	1.0	1.0	30.9

Table A.2: The triboson MC samples used for the analyses.

Process	$\sigma$ [fb]	k-factor	$\int \mathcal{L} dt$ [fb $^{-1}$ ]
<i>WWW</i>	5.10	1.5	6533
<i>ZWW</i>	1.55	1.5	21500
<i>ZZZ</i>	0.33	1.5	101000

Table A.3: The  $t\bar{t}$ +boson samples used for the analyses.

Process	Generator	$\sigma$ [pb]	k-factor	$\int \mathcal{L} dt$ [fb $^{-1}$ ]
$t\bar{t}W(\ell\nu)$ with 0 partons	ALPGEN	$2.7 \times 10^{-2}$	1.255	443.4
$t\bar{t}W(\ell\nu)$ with 1 parton	ALPGEN	$1.8 \times 10^{-2}$	1.255	443.0
$t\bar{t}W(\ell\nu)$ with 2 partons	ALPGEN	$9.5 \times 10^{-3}$	1.255	421.0
$t\bar{t}W(\ell\nu)$ with 3 partons	ALPGEN	$6.5 \times 10^{-3}$	1.255	366.1
$t\bar{t}W(qq)$ with 0 partons	ALPGEN	$5.4 \times 10^{-2}$	1.255	440.1
$t\bar{t}W(qq)$ with 1 parton	ALPGEN	$3.7 \times 10^{-2}$	1.255	432.9
$t\bar{t}W(qq)$ with 2 partons	ALPGEN	$1.9 \times 10^{-2}$	1.255	415.5
$t\bar{t}W(qq)$ with 3 partons	ALPGEN	$1.3 \times 10^{-2}$	1.255	390.4
$t\bar{t}Z(\nu\nu)$ with 0 partons	ALPGEN	$1.1 \times 10^{-2}$	1.277	740.0
$t\bar{t}Z(\nu\nu)$ with 1 parton	ALPGEN	$1.0 \times 10^{-2}$	1.277	390.0
$t\bar{t}Z(\nu\nu)$ with 2 partons	ALPGEN	$6.9 \times 10^{-3}$	1.277	226.0
$t\bar{t}Z(\nu\nu)$ with 3 partons	ALPGEN	$5.0 \times 10^{-3}$	1.277	236.3
$t\bar{t}Z(\ell\ell)$ with 0 partons	ALPGEN	$7.9 \times 10^{-3}$	1.277	496.6
$t\bar{t}Z(\ell\ell)$ with 1 parton	ALPGEN	$7.7 \times 10^{-3}$	1.277	511.7
$t\bar{t}Z(\ell\ell)$ with 2 partons	ALPGEN	$5.3 \times 10^{-3}$	1.277	443.8
$t\bar{t}Z(\ell\ell)$ with 3 partons	ALPGEN	$4.0 \times 10^{-3}$	1.277	393.7
$t + Z(\ell\ell)$ <i>Wt</i> -channel	MADGRAPH	$4.1 \times 10^{-3}$	1.0	24212.8
$t + Z(\ell\ell)$ <i>st</i> -channel	MADGRAPH	0.03	1.0	3214.4
$t\bar{t}WW$	MADGRAPH	$9.19 \times 10^{-4}$	1.34	10880
(S) $t\bar{t}W$	MADGRAPH	0.10	1.18	3270.1
(S) $t\bar{t}W$ with 1 jet	MADGRAPH	0.05	1.18	6376.7
(S) $t\bar{t}W$ with 2 jets	MADGRAPH	0.04	1.18	8202.4
(S) $t\bar{t}Z$	MADGRAPH	0.07	1.34	4409.8
(S) $t\bar{t}Z$ with 1 jet	MADGRAPH	0.05	1.34	6581.2
(S) $t\bar{t}Z$ with 2 jets	MADGRAPH	0.04	1.34	7501.7

Table A.4: The top-quark samples used for the analyses.

Process	Generator	$\sigma$ [pb]	k-factor	filter eff.	$\int \mathcal{L} dt$ [fb $^{-1}$ ]
$t\bar{t}$ not all-hadronic	POWHEG	252.89	1.0	0.54	545.6
$Wt$	MC@NLO	20.66	1.08	1.0	78.9
$t$ -channel $e\nu$	ACERMC	8.60	1.10	1.0	31.6
$t$ -channel $\mu\nu$	ACERMC	8.60	1.10	1.0	31.6
$t$ -channel $\tau\nu$	ACERMC	8.60	1.10	1.0	31.6
$s$ -channel $e\nu$	MC@NLO	0.56	1.07	1.0	278.9
$s$ -channel $\mu\nu$	MC@NLO	0.56	1.07	1.0	278.9
$s$ -channel $\tau\nu$	MC@NLO	0.56	1.07	1.0	278.7

Table A.5:  $Z/\gamma^*$ +jets samples used for the analyses.

Process	$Z \rightarrow ee$		$Z \rightarrow \mu\mu$		$Z \rightarrow \tau\tau$	
	$\sigma$ [pb]	$\int \mathcal{L} dt$ [fb $^{-1}$ ]	$\sigma$ [pb]	$\int \mathcal{L} dt$ [fb $^{-1}$ ]	$\sigma$ [pb]	$\int \mathcal{L} dt$ [fb $^{-1}$ ]
Z+jets with 0 partons	848.29	7.8	848.31	7.8	848.24	7.8
Z+jets with 1 parton	207.21	6.4	207.46	6.4	207.48	6.4
Z+jets with 2 partons	69.44	5.8	69.39	5.8	69.18	5.9
Z+jets with 3 partons	18.36	6.0	18.40	6.0	18.30	6.0
Z+jets with 4 partons	4.64	6.5	4.61	6.5	4.66	6.4
Z+jets with 5 partons	1.42	7.1	1.41	7.1	1.39	7.2
Z+jets low mass with 0 partons	4154.56	0.2	4154.44	0.2	4154.44	0.2
Z+jets low mass with 1 parton	129.99	2.3	129.93	2.3	129.92	2.3
Z+jets low mass with 2 partons	63.05	7.5	63.01	7.5	63.00	7.5
Z+jets low mass with 3 partons	13.50	10.7	13.43	10.8	13.53	10.7
Z+jets low mass with 4 partons	3.09	11.7	3.11	11.7	3.10	70.5
Z+jets low mass with 5 partons	0.83	96.2	0.83	96.2	0.83	96.6
Z+bb with 0 partons	9.49	15.8	9.49	15.8	9.48	15.8
Z+bb with 1 parton	3.82	21.0	3.79	21.1	3.81	21.0
Z+bb with 2 partons	1.34	33.5	1.35	33.5	1.35	33.3
Z+bb with 3 partons	0.58	7.8	0.60	8.3	0.58	8.6
Z+cc with 0 partons	17.83	33.9	17.84	33.6	17.84	33.6
Z+cc with 1 parton	8.51	30.5	8.49	31.2	8.50	31.2
Z+cc with 2 partons	3.58	30.7	3.58	32.2	3.59	32.1
Z+cc with 3 partons	1.39	28.8	1.39	28.9	1.38	29.0

Table A.6:  $W$ +jets samples used for the analyses.

Process	$W \rightarrow e\nu$		$W \rightarrow \mu\nu$		$W \rightarrow \tau\nu$	
	$\sigma$ [pb]	$\int \mathcal{L} dt$ [fb $^{-1}$ ]	$\sigma$ [pb]	$\int \mathcal{L} dt$ [fb $^{-1}$ ]	$\sigma$ [pb]	$\int \mathcal{L} dt$ [fb $^{-1}$ ]
$W$ +jets with 0 partons	9300.36	0.4	9296.48	0.4	9299.11	0.4
$W$ +jets with 1 parton	2047.68	1.2	2049.06	1.2	2050.20	1.2
$W$ +jets with 2 partons	619.05	6.1	618.67	6.1	618.64	6.1
$W$ +jets with 3 partons	167.62	6.0	167.44	6.0	167.43	6.0
$W$ +jets with 4 partons	42.63	5.9	42.67	6.0	42.59	5.9
$W$ +jets with 5 partons	12.99	5.4	13.05	5.0	13.19	4.9

Table A.7: The Standard Model Higgs production samples used for the analyses.

Process	higgs decay	Generator	$\sigma$ [pb]	filter eff.	$\int \mathcal{L} dt$ [fb $^{-1}$ ]
$ggF$		POWHEGPYTHIA 8	$4.41 \times 10^{-1}$	0.491	2311
$VBF$	$H \rightarrow WW^* \rightarrow \ell\nu\ell\nu$	POWHEG	$3.56 \times 10^{-2}$	0.507	16600
$WH$		PYTHIA	$1.50 \times 10^{-1}$	0.105	1270
$ZH$		PYTHIA	$8.90 \times 10^{-3}$	1.000	2250
$t\bar{t} + H$		PYTHIA	$2.80 \times 10^{-2}$	1.000	6700

## A.2 New Physics MC samples

The lists for the MC samples of the new physics models which are used in the analysis are given in Tab. A.8. For the signal samples, as described in Chap. 1, the cross section depends on the produced gaugino mass,  $M_2$  in this thesis. Samples are generated with 10000 or 20000 events. They are filtered by the generator to include three leptons. For example, the SUSY  $Wh$  samples have no  $b\bar{b}$  decays due to the filter.



Table A.8: List of the SUSY signal MC simulated samples

Process	Generator	$m_{\tilde{\chi}_1^\pm, \tilde{\chi}_2^0}$ [GeV]	$\sigma$ [pb]	$\sigma$ uncert. [%]
WZ all leptonic	HERWIG++	100.0	11.48423	7.51
	HERWIG++	112.5	7.32643	7.26
	HERWIG++	125.0	4.91089	6.88
	HERWIG++	137.5	3.42271	7.01
	HERWIG++	150.0	2.45269	6.70
	HERWIG++	162.5	1.80696	6.75
	HERWIG++	175.0	1.35264	6.60
	HERWIG++	187.5	1.03514	6.40
	HERWIG++	200.0	0.80224	6.48
	HERWIG++	250.0	0.32327	6.88
	HERWIG++	300.0	0.14815	6.70
	HERWIG++	350.0	0.07440	7.15
	HERWIG++	400.0	0.03962	7.76
	HERWIG++	450.0	0.02197	8.36
	HERWIG++	500.0	0.01253	8.35
Wh all leptonic	HERWIG++	130.0	3.78567	6.71
	HERWIG++	140.0	2.85306	6.85
	HERWIG++	150.0	2.19063	6.45
	HERWIG++	152.5	2.04910	6.44
	HERWIG++	162.5	1.60242	6.46
	HERWIG++	175.0	1.20506	6.56
	HERWIG++	177.5	1.14028	6.55
	HERWIG++	187.5	0.92145	6.41
	HERWIG++	190.0	0.87627	6.45
	HERWIG++	200.0	0.71445	6.30
	HERWIG++	202.5	0.67903	6.34
	HERWIG++	212.5	0.56066	6.31
	HERWIG++	215.0	0.28790	6.40
	HERWIG++	225.0	0.44647	6.69
	HERWIG++	227.5	0.42559	6.52
	HERWIG++	237.5	0.35750	6.67
	HERWIG++	240.0	0.34289	6.45
	HERWIG++	250.0	0.28790	6.31
	HERWIG++	262.5	0.23413	6.68
	HERWIG++	265.0	0.22568	6.93
	HERWIG++	275.0	0.19275	7.23
	HERWIG++	287.5	0.15894	6.86
	HERWIG++	300.0	0.13173	6.93
	HERWIG++	312.5	0.11000	6.98
	HERWIG++	325.0	0.09231	7.06
HERWIG++	337.5	0.07738	7.19	
HERWIG++	350.0	0.06623	7.31	

# List of Figures

- 1.1 Illustration of the Higgs potential [11].  $\text{Re}(\phi)$  and  $\text{Im}(\phi)$  represent  $\phi_3$  and  $\phi_4$  in Eq. (1.18). 5
- 1.2 Result of the measurement of the Yukawa coupling constant from the ATLAS experiment [15]. The blue dashed line shows the fitting results. . . . . 7
- 1.3 The rotation velocity of the matters around the NGC6503 galaxy [16]. The data are fitted with the three parameters: the visible components like stars (dashed curve), the gas (interstellar medium; dotted curve), and the dark matter (dash-dot curve). The contribution of the dark matter is approximately seven times larger than the contribution of the stars at the 20 kpc distance. . . . . 8
- 1.4 Examples of the diagram of the one-loop quantum corrections for a fermion (a) and for a sfermion (b). . . . . 11
- 1.5 Feynman diagrams for the  $\tilde{\chi}_1^\pm \tilde{\chi}_2^0$  production via  $s$ -channel (a) and via  $t$ -channel (b). In figures,  $W^*$  and  $\tilde{q}^*$  represent the off-shell  $W$  boson and the off-shell squark, respectively. If the squarks have heavy mass spectra, the  $s$ -channel production mode (a) is dominant and the  $t$ -channel production mode (b) is strongly suppressed because of the heavy squark mass. 17
- 1.6 Cross sections for pair production of SUSY particles as a function of their mass at the LHC for a centre-of-mass energy of 8 TeV [24, 70–74]. The cross section of the direct production of charginos and neutralinos is several orders of magnitude smaller than the production of coloured SUSY particles. . . . . 17
- 1.7 Decay process for  $\tilde{\chi}_1^\pm$  and  $\tilde{\chi}_2^0$  via SM bosons. There are four possible decay modes: (a)  $\tilde{W}^\pm \rightarrow W^\pm + \tilde{B}$ , (b)  $\tilde{W}^0 \rightarrow h + \tilde{H}^0$ , (c)  $\tilde{H}^0 \rightarrow h + \tilde{B}$ , and (d)  $\tilde{H}^0 \rightarrow Z + \tilde{H}^0$ . In the case where all squarks, gluinos and sleptons are much heavier than the SM bosons, charginos and neutralinos decays via the SM bosons are dominant processes.  $\tilde{H}$  represents one of the Higgs super-partner expressed in gauge eigenstates  $(\tilde{H}_d^-, \tilde{H}_u^+, \tilde{H}_d^0, \tilde{H}_u^0)$ . . . . . 18
- 1.8 Wino-like  $\tilde{\chi}_2^0$  decay via SM boson mediated scenario. The black point shows the mixing. Since mixing of neutral gauginos and Higgsinos is needed twice to decay via  $Z$  shown in (a), the process can be suppressed if the mass difference is greater than Higgs mass because only one mixing is needed to decay via Higgs shown in (b). . . . . 19
- 1.9 Branching ratio of a neutral wino NLSP to a Higgs and a bino LSP as a function of  $\mu$  and  $\tan\beta$ , for the wino mass term  $M_2$  of 175 GeV and the Higgs mass of 125 GeV. The branching ratio is computed using tree-level neutralino masses and mixing, with the input  $M_1 = 0$  [76]. . . . . 19

1.10	Results of searches for stops and sbottoms at LEP (ALEPH, DELPHI, L3 and OPAL) [84]. The figures are also shown the first results of searches in Tevatron (CDF and DØ) [94, 95]. The $\theta$ represents the mixing angle between left-handed and right-handed squarks, $\tilde{q}_1 = \tilde{q}_L \cos \theta + \tilde{q}_R \sin \theta$ . The blue region is an exclusion limit with $\theta = 56^\circ$ and the red region is an exclusion limit with $\theta = 0^\circ$ (left-handed like squark). . . . .	21
1.11	Exclusion limits at LEP for the right-handed selectrons (red), smuons (green) and staus (blue). The exclusion limits are calculated at 95% confidence level [83]. The $\mu$ and $\tan \beta$ parameters are assumed to be 200 GeV and 1.5, respectively. . . . .	22
1.12	Exclusion limits at LEP for no-scale supergravity model (shown as “LNZ”) as a plane of gravitino and neutralino (bino-like) masses [91]. . . . .	23
1.13	Observed and expected exclusion limits in the sneutrino and stop masses plot at DØ (red lines) [101]. The previous results from LEP2 (green region), DØ (purple and black lines) and CDF (blue line) are also shown. . . . .	24
1.14	Chargino exclusion limits at CDF for mSUGRA (a) and GMSB (b) scenarios. The red lines show the theoretical prediction using PROSPINO [104]. . . . .	24
1.15	Exclusion limits for the gluino pair production at CMS (a) and the stop pair production at ATLAS (b). . . . .	25
1.16	Exclusion limits for directly pair produced left-handed (a) and right-handed (b) sleptons in ATLAS [112]. . . . .	26
2.1	Location of the LHC and the ATLAS detector. . . . .	28
2.2	LHC injection complex, drawn by Julie Haffner [116] . . . . .	28
2.3	Peak luminosity per day in 2012 [117]. . . . .	29
2.4	Total Integrated Luminosity and Data Quality in 2012 [117]. . . . .	29
2.5	The image of the whole ATLAS detector [106]. . . . .	30
2.6	Overview of the Inner Detector [106]. . . . .	32
2.7	A pixel module located on barrel part [106]. . . . .	32
2.8	A SCT module located in the barrel part [106]. . . . .	33
2.9	Whole view of the Calorimeter [106] . . . . .	34
2.10	A photo of the accordion structure of the EM calorimeter [106] . . . . .	35
2.11	A module of EM calorimeter, located on near $\eta = 0$ [106]. . . . .	36
2.12	A module of the tile calorimeter [106]. . . . .	37
2.13	Whole view of the Muon Detector [106]. . . . .	38
2.14	Sketch of the MDT chamber. Three spacer bars separate between two drift tube multi-layers [106]. . . . .	39
2.15	ATLAS magnet system [106] . . . . .	40
2.16	Trigger Flow of the L1 trigger [106]. EM shows the electron/photon trigger menus. . . . .	41
3.1	Wedge-shaped illustration of the ATLAS detector with the particle passing [114]. . . . .	46
3.2	Space-points distribution and track candidates [131]. This is an example of $t\bar{t}$ event display with the cross section of the ATLAS ID (Pixel and SCT) barrel part. . . . .	47

3.3	The primary and secondary track reconstruction efficiency in minimum bias Monte Carlo samples [132]. . . . .	48
3.4	Non-primary fraction in minimum bias Monte Carlo simulation results [132]. . . . .	49
3.5	Impact Parameters definition in $xy$ plane (a) and $rz$ plane (b). . . . .	50
3.6	Comparison results among the $k_t$ (left-top), Cambridge/Aachen (right-top), SISCone (left-bottom) and Anti- $k_t$ (right-bottom) algorithms with a sample parton-level event generated with HERWIG [145], together with $\sim 10^4$ random soft clusters [139]. The anti- $k_t$ algorithm is stable behaviour against the many soft cluster effects. . . . .	57
3.7	JVF value distribution for hard-scatter jets and pile-up jets with $20\text{GeV} < p_T < 50\text{GeV}$ and $ \eta  < 2.4$ in $Z$ +jets simulated samples [151]. . . . .	58
4.1	Signal grids and their cross-sections for $WZ/h$ -mediated scenarios. . . . .	66
5.1	Dominant decay processes for direct chargino and neutralino production with high mass sleptons. The region where the chargino mass is smaller than $100\text{GeV}$ has already been excluded at the LEP search [85]. . . . .	70
5.2	Feynman diagram for the $WZ/h$ -mediated scenarios. . . . .	70
5.3	Expected numbers of signal events for SR0 $\tau$ a-bin1–6. . . . .	74
5.4	Expected numbers of signal events for SR0 $\tau$ a-bin7–12. . . . .	75
5.5	Expected numbers of signal events for SR0 $\tau$ a-bin13–18. . . . .	76
5.6	Expected numbers of signal events for SR0 $\tau$ a-bin19–20. . . . .	77
5.7	Branching ratio for near $125\text{GeV}$ Higgs [24]. . . . .	77
5.8	Feynman diagrams of $Wh$ scenarios decaying via $WW$ and $\tau\tau$ . . . . .	77
5.9	Third lepton transverse momentum distribution with three leptons selection, a SFOS lepton pair veto, $b$ -jet veto and $E_T^{\text{miss}} > 50\text{GeV}$ . Third leptons of the background samples are shifted lower region, hence the selection $p_T > 20\text{GeV}$ has been applied. . . . .	78
5.10	Difference of the azimuthal angle between opposite sign leptons. The selection $\Delta\phi_{\ell\ell} \leq 1.0$ has been applied for SR0 $\tau$ b. . . . .	79
5.11	The invariant mass for the same-sign leptons before (a) and after (b) applying $Z(ee)$ veto. . . . .	80
5.12	$m_{\tau\tau}$ distribution in SR2 $\tau$ without $m_{\tau\tau}$ requirement. The Higgs mass window is defined as $m_{\tau\tau}$ in the mass range from $70\text{GeV}$ to $120\text{GeV}$ , which can suppress the SM background processes. . . . .	80
5.13	Distribution and optimisation of the sum of $p_T$ of the taus. The vertical axis of (b) is $Z_N$ value with the assumption of the 30% background uncertainty. The optimal selection is $\sum p_T > 110\text{GeV}$ . This selection reduces 88% background processes. . . . .	81
5.14	Expected numbers of signal events for SR0 $\tau$ b (a), SR1 $\tau$ (b) and SR2 $\tau$ (c). . . . .	82
5.15	Significance for the $WZ$ channel (a) and $Wh$ channel (b). These are calculated only with MC samples in the corresponding signal regions of Category-A. The red lines represent the expected exclusion limits with 95% confidence level. . . . .	83
5.16	The minimum mass of the SFOS lepton pair. The filled histogram represents the SM background distribution, and the dashed lines show the distribution for the corresponding signal samples. The cut-off of the min. $m_{\text{SFOS}}$ can be seen in this figure. . . . .	84

5.17	Expected numbers of events in SRSLa (a) and SRSLb (b). . . . .	86
5.18	Schematic diagram in the transverse plane of the $pp \rightarrow \text{ISR} + \tilde{\chi}_1^\pm \tilde{\chi}_2^0 (\rightarrow \ell\ell\nu + \tilde{\chi}_1^0 \tilde{\chi}_1^0)$ . . .	87
5.19	Distributions for the ISR related variables after the pre-selection. The difference of the azimuthal angle between $E_T^{\text{miss}}$ and 1st jet $\Delta\phi_{E_T^{\text{miss}}, 1\text{st jet}}$ (a) and the difference of the azimuthal angle between $E_T^{\text{miss}}$ and three lepton system $\Delta\phi_{E_T^{\text{miss}}, \Sigma\ell}$ (b) are shown. The red lines are the distributions of the SUSY decaying via $WZ$ -mediated scenario with the mass difference $\Delta m_{\tilde{\chi}_2^0, \tilde{\chi}_1^0} = 25 \text{ GeV}$ and the green lines are the distributions of the SUSY decaying via $WZ$ -mediated scenario with the mass difference $\Delta m_{\tilde{\chi}_2^0, \tilde{\chi}_1^0} = 12.5 \text{ GeV}$ . . . . .	87
5.20	Expected numbers of events in SRISRa (a) and SRISRb (b). . . . .	89
5.21	Significance for the $WZ$ compressed scenario. This is calculated only with MC samples by the combination of all signal regions of Category-B. . . . .	89
6.1	Relation among the real leptons, the fake leptons and the leptons passed and failed the tight selection. The figure shows the set of the “loose” leptons surrounded with the blue ellipse, the fake and the real lepton contribution in the “loose” lepton, and the “tight” lepton contribution in “loose” leptons. The fake contribution which should be considered corresponds to the region where the lepton is categorised “tight” and fake. . . . .	93
6.2	Flow diagram of the procedure of the simplified matrix method employed in this analysis. Fake rates are measured separately for the fake origins in the region with the loose selection using the reducible MC samples, such as $t\bar{t}$ and $Z$ +jets. Fake origin fractions are measured in each signal region. Then the average fake rate is evaluated using these information. The average fake rate is a function of the $p_T$ , $\eta$ and the flavour. It is used as an input parameter of the matrix method. The input of the matrix method from the observed data is made by applying the selection of the corresponding signal region without the signal selection criteria. The output of the matrix method is recorded as an event weight of the processed event. . . . .	96
6.3	Schematic diagram for the tag-and-probe method for the measurement for the real lepton efficiency. The tag lepton should pass the signal selection and the trigger requirement. . . .	99
6.4	Distributions for the <i>probe</i> lepton $p_T$ in the RE control region. The MC results only. The uncertainty is statistical only. . . . .	99
6.5	The $p_T$ dependence of the Real Efficiency for each lepton. The “standard” and the “tighter isolation” criteria are described as Sec. 3.4 for electrons and Sec. 3.5 for muons. . . . .	100
6.6	Origin of the conversion fakes . . . . .	102
6.7	Schematic diagram of the target of the conversion fake control region. . . . .	102
6.8	Distributions for the <i>probe</i> lepton $p_T$ in the CO control region. . . . .	102
6.9	The $p_T$ dependence of the conversion fake rate for electrons. The “standard” and the “tighter isolation” criteria are described in Sec. 3.4. . . . .	102
6.10	Schematic diagram for the control region for the heavy flavour fakes. . . . .	103
6.11	Distributions for the lepton $p_T$ in the HF control region. . . . .	104
6.12	The $p_T$ dependence of the HF leptons ( $e, \mu$ ) after the MC truth subtraction. . . . .	105
6.13	Schematic diagram for the control region for the light flavour fake taus. . . . .	107
6.14	Distribution for the tau $p_T$ in the LF control region. . . . .	107

6.15	The $p_T$ dependence for the LF taus. . . . .	107
7.1	Leading lepton purity for Category-B estimated with MC background samples. The uncertainties are statistical only. . . . .	114
8.1	Results from MC closure test performed with $t\bar{t}$ sample in the 3 lepton inclusive region. . .	118
8.2	Results from MC closure test performed with $Z$ + jets sample in the 3 lepton inclusive region.	119
8.3	The strategy of the definition of the validation regions. The categories of the validation region ‘a’ and ‘b’ are defined as the low $E_T^{\text{miss}}$ regions and the one $b$ regions, respectively. The low $E_T^{\text{miss}}$ region ‘a’ requires similar selections with low $E_T^{\text{miss}}$ requirement. The one $b$ region ‘b’ requires similar selections with exactly one $b$ -jet. . . . .	120
8.4	Distributions in VR0 $\tau$ noZa. . . . .	123
8.5	Distributions in VR0 $\tau$ noZb. . . . .	124
8.6	Distributions in VR0 $\tau$ Za. . . . .	125
8.7	Distributions in VR0 $\tau$ Zb. . . . .	126
8.8	Distributions in VR1 $\tau$ a. . . . .	127
8.9	Distributions in VR1 $\tau$ b. . . . .	128
8.10	Distributions in VR2 $\tau$ a. . . . .	129
8.11	Distributions in VR2 $\tau$ b. . . . .	130
8.12	Distributions in VRSLa. . . . .	131
8.13	Distributions in VRSLb. . . . .	132
8.14	Distributions in VRISRa. . . . .	133
8.15	Distributions in VRISRb. . . . .	134
9.1	Distributions for SR0 $\tau$ b. . . . .	137
9.2	Distributions for SR1 $\tau$ . . . . .	137
9.3	Distributions for SR2 $\tau$ . . . . .	138
9.4	Distributions for SRSLa. . . . .	138
9.5	Distributions for SRSLb. . . . .	139
9.6	Distributions for SRISRa. . . . .	139
9.7	Distributions for SRISRb. . . . .	140
9.8	Illustration of the $p$ -value. . . . .	141
9.9	Example of distributions of the test variable $q$ under the signal plus background and background-only hypotheses [186]. . . . .	145
9.10	Exclusion limit contours for the simplified models for SUSY scenarios decay via $WZ$ (a) and $Wh$ (b). All signal regions of Category-A are statistically combined. In figures, the region surrounded by the red solid lines are the observed exclusion limits with 95% CL. The red dashed lines represent the $\pm 1\sigma$ movable regions by the theory uncertainties. Similarly, the region surrounded by the black dashed lines are the expected exclusion limits with 95% CL. The yellow regions represent the $\pm 1\sigma$ uncertainties. The exclusion limit of the results of ATLAS $\sqrt{s} = 7$ TeV Analyses is also shown as green lines in (a) [187]. . . . .	145

- 9.11 Exclusion limit contour for the simplified model for SUSY scenario decay via  $WZ$  with the results of Category-B. All signal regions of Category-B are statistically combined. In the figure, the region surrounded by the red solid lines are the observed exclusion limits with 95% CL. The red dashed lines represent the  $\pm 1\sigma$  movable regions by the theory uncertainties. Similarly, the region surrounded by the black dashed lines are the expected exclusion limits with 95% CL. The yellow region represents the  $\pm 1\sigma$  uncertainties. The exclusion limit of the results of ATLAS  $\sqrt{s} = 7$  TeV Analyses is also shown as green lines [187]. . . . . 146
- 9.12 Summary plot for the exclusion limits for all analyses which described in this thesis. The dashed lines show the expected exclusion limits for the corresponding analyses, and the solid lines show the observed exclusion limits for the corresponding analyses. Since analyses of  $WZ$  scenario with Category-A and Category-B are not orthogonal, they cannot be combined statistically. The observed exclusion limit of the results of the ATLAS 7 TeV analysis is also shown [187]. All lines indicate the upper limits with 95% confidence level. 146
- 9.13 Exclusion limits for charginos and neutralinos decaying via  $WZ/h$  in CMS [188]. . . . . 148
- 9.14 Preliminary exclusion limit for  $Wh$  (decaying to  $\ell\nu b\bar{b}$ ) scenario in ATLAS [189]. . . . . 149
- 9.15 Feynman diagram for the “via slepton” scenario. The slepton mass is assumed to be the middle of masses between the second lightest neutralino and the lightest neutralino,  $(m_{\tilde{\chi}_2^0} + m_{\tilde{\chi}_1^0})/2$ . . . . . 150
- 9.16 Interpretation for “via sleptons” scenario. The left-handed slepton masses are assumed to be  $m_{\tilde{\ell}_L} = (m_{\tilde{\chi}_2^0} + m_{\tilde{\chi}_1^0})/2$ . The exclusion limits are calculated with Category-A signal regions (a) and Category-B signal regions (b). In figures, the region surrounded by the red solid lines are the observed exclusion limits with 95% CL. The red dashed lines represent the  $\pm 1\sigma$  movable regions by the theory uncertainties. Similarly, the region surrounded by the black dashed lines are the expected exclusion limits with 95% CL. The yellow regions represent the  $\pm 1\sigma$  uncertainties. The result of ATLAS 7 TeV analysis [187] is also shown. 150
- 9.17 Interpretation for pMSSM with high mass sleptons  $m_{\tilde{\ell}} = 3$  TeV. The category-A signal regions are used. The parameters  $M_1$  and  $\tan\beta$  are fixed at 50 GeV and 50, respectively. The region filled the orange colour represents the exclusion region by the LEP searches [85]. 151
- 9.18 Distributions for the leading lepton  $p_T$  (a) and the  $E_T^{\text{miss}}$  (b) in the SR0 $\tau$ a-bin1. Excess was observed in the low  $p_T$  and  $E_T^{\text{miss}}$  region. . . . . 152
- 9.19 2D distribution for the relic density of the dark matter for each model [190]. Blue points represent the bino dark matter case. The purple crosses represent the wino dark matter case. Red squares represent the Higgsino dark matter case. Orange points represent the case with the mixed bino, wino and Higgsinos. Green dashed line represents the observed relic density by Planck [21]. Many of the blue points (bino cases) distribute the region with larger relic density than the observed value. On the other hand, the purple crosses (wino cases) distribute the region with less relic density than the observed value. Some Higgsino cases, the red squares, distribute the region with equivalent relic density to the observed value. . . . . 153

- 9.20 Coannihilation region between bino and wino with the bino dark matter scenario in the  $M_1$ - $\Delta m_{M_2, M_1}$  plane [192] (a) and  $M_1$ - $M_2$  plane (b). (a) also shows the results of LEP2 and the Category-A analyses. (b) shows the favourable regions of the bino-wino coannihilation and the Higgs resonance scenarios and the exclusion limit curves obtained on this analysis. 154
- 9.21 Calculated results for the region where the muon  $g - 2$  deviation can explain within  $1\sigma$ . The plot with  $M_1$ - $M_2$  plane is shown in (a) [47], and the overlaid view of the exclusion limit curves obtained from this analysis and the favourable region from (a) (yellow region) is shown in (b). Green points in (a) represent the region satisfying the  $B$ -physics constraints [193, 194]. Brown points in (a) represent the region satisfying the relic abundance of the dark matter corresponding  $0.001 < \Omega_{\text{DM}} h^2 < 1$  [47]. . . . . 154
- 9.22 2D plots of the numbers of baseline and signal leptons. The pre-selection and  $b$ -veto are applied. Triggers are not applied. . . . . 156
- 9.23 2D plots of the numbers of baseline and signal leptons. The pre-selection,  $Z$ -veto and  $b$ -veto are applied. Triggers are not applied. . . . . 157
- 10.1 Comparison of the observed and expected limits for  $WZ$  channel (a) and  $Wh$  channel (b) between the results from this analysis and the analyses with  $\sqrt{s} = 7\text{TeV}$  data taken in ATLAS [187]. Red bands and black lines show the observed and the expected exclusion limits. The yellow bands shows the  $\pm 1\sigma$  uncertainties on the expected limits. The limits for the LSP mass of 0 GeV are shown. . . . . 160





# List of Tables

1.1	Set of the Standard Model particles except the Higgs boson. . . . .	2
1.2	The SM particles and corresponding SUSY particles. . . . .	10
2.1	Segment sizes per module of the EM calorimeter. . . . .	36
2.2	Main parameters for the components of the muon spectrometer. . . . .	38
2.3	Electron trigger definition used in this analysis. . . . .	42
2.4	Correction factors of the electron trigger efficiencies. . . . .	43
2.5	Muon trigger definition used in this analysis [130]. . . . .	43
2.6	Correction factors of the muon trigger efficiencies. . . . .	44
3.1	Selection efficiency and background rejection for the electron transverse energy region $20 < E_T < 50\text{GeV}$ , for <i>loose</i> , <i>medium</i> and <i>tight</i> cut [135]. The <i>tight</i> cuts are useful to reject hadron contribution. . . . .	52
3.2	Pre-electron identification criteria . . . . .	53
3.3	Signal selection for electrons . . . . .	53
3.4	Muons baseline selection criteria. In this table, the variable $n$ is defined as $n \equiv N_{\text{TRT}}^{\text{hits}} + N_{\text{TRT}}^{\text{outliers}}$ . . . . .	54
3.5	Signal Muons selection criteria. . . . .	55
3.6	Jet baseline selection criterion. . . . .	59
3.7	Tau baseline selection criterion . . . . .	60
3.8	Overlap removal sequence. . . . .	61
4.1	List of the MC simulated samples used in the analysis. . . . .	64
5.1	Summary of the triggers which are used in this analysis. . . . .	68
5.2	Summary of the signal regions of Category-A. . . . .	70
5.3	Summary of the bins in $m_{\text{SFOS}}$ , $m_T$ , and $E_T^{\text{miss}}$ for $\text{SR0}\tau\text{a}$ . . . . .	71
5.4	Numbers of events for the $\text{SR0}\tau\text{a}$ binned signal regions. Estimates are based on MC only and uncertainties are statistical only. The irreducible background (noted as $\text{SM}_{\text{irred.}}$ ) is the $WZ$ , $ZZ$ , $t\bar{t}+V$ , triboson $VVV$ ( $WWW$ , $WWZ$ , $ZZZ$ ) and the Standard Model Higgs processes, while the reducible backgrounds (noted as $\text{SM}_{\text{red.}}$ ) are all others. . . . .	73
5.5	Numbers of events for the SM processes of the $\text{SR0}\tau\text{b}$ , $\text{SR1}\tau$ and $\text{SR2}\tau$ . Estimates are based on the MC-only and uncertainties are statistical only. . . . .	81
5.6	Summary of the signal regions for Category-B. . . . .	85

5.7	Expected yields in SRSL. Estimates are based on the MC-only and uncertainties are statistical only. . . . .	86
5.8	Expected yields in SRISR. Estimates are based on the MC-only and uncertainties are statistical only. . . . .	88
6.1	Scale factor measurements are performed for the categories with $\checkmark$ . Due to the bad purity, the scale factor measurement of the light flavour fakes for electrons and muons and of the heavy flavour fakes for taus cannot be performed. Conversion fakes for electrons are taken into account. For the real efficiency of the taus, the control region cannot be defined due to the effect of the neutrino from the tau decay. The fakes which cannot be measured in the control region are assumed to be consistent with the data and MC prediction within 10% uncertainties. . . . .	98
6.2	RE scale factors for electrons and muons, as measured separately by the analysis category, Category-A and Category-B. . . . .	101
6.3	CO scale factors for electrons and muons, as measured separately by the analysis category, Category-A and Category-B. . . . .	103
6.4	HF scale factors for electrons and muons, as measured separately by the analysis category, Category-A and Category-B. . . . .	104
6.5	LF scale factors for electrons and muons, as measured separately by the analysis category, Category-A and Category-B. . . . .	107
7.1	Absolute systematic uncertainties on the matrix method efficiencies and fake rates due to the $E_T^{\text{miss}}$ and $m_T$ dependences in the Category-A analysis. In the table, the following notation is used: RE: real efficiency, HF: heavy flavour jet, LF: light flavour jet, CO: converted photon, QJ: quark jet, GJ: gluon jet. . . . .	113
7.2	Absolute systematic uncertainties on the matrix method efficiencies and fake rates due to the $m_{\text{SFOS}}$ dependence in the Category-A analysis. In the table, the following notation is used: RE: real efficiency, HF: heavy flavour jet, LF: light flavour jet, CO: converted photon. . . . .	113
7.3	Absolute uncertainties on the matrix method efficiencies and fake rates due to the $E_T^{\text{miss}}$ and $m_T$ dependences in the Category-B analysis. Statistical uncertainties are also shown in this table. In the table, the following notation is used: RE: real efficiency, HF: heavy flavour jet, LF: light flavour jet, CO: converted photon. . . . .	113
7.4	Uncertainties for reducible background in signal regions in Category-A. . . . .	115
7.5	Uncertainties for reducible background in signal regions in Category-B. . . . .	115
7.6	Dominant systematic uncertainties on background estimates in the various signal regions in Category-A. . . . .	116
7.7	Dominant systematic uncertainties on background estimates in the various signal regions in Category-B. . . . .	116
8.1	Validation Region Definition for Category-A. . . . .	120
8.2	Validation Region Definition for Category-B. . . . .	120

8.3	Expected numbers of SM background events and observed numbers of data events in validation regions in Category-A, as defined in Table 8.1. Statistical and systematic uncertainties are included. . . . .	122
8.4	Expected numbers of SM background events and observed numbers of data events in validation regions in Category-A, as defined in Table 8.1. Statistical and systematic uncertainties are included. . . . .	122
8.5	Validation with respect to each variable in the validation regions defined in Tab. 8.1 and Tab. 8.2. The symbols “√”, “N/A” and “(F)” represent <i>good</i> , <i>not available</i> and <i>over 1σ</i> . In all of the items symbolised (F), less than $2\sigma$ deviations are observed. For the region including two taus, $m_{\text{SFOS}}$ is defined as $m_{\tau\tau}$ . . . . .	122
9.1	Expected SM background events and observed events in data in the binned signal regions for Category-A for $WZ/h$ -mediated scenario (SR0 $\tau$ a, SR0 $\tau$ b, SR1 $\tau$ , SR2 $\tau$ ). Statistic and systematic uncertainties on the background estimation are taken into account. Some regions have excess from the SM expectation, the statistical significance of those will be discussed in the next section. . . . .	136
9.2	Expected SM background events and observed events in data in the signal regions for Category-B (SRSL, SRISR). Statistical and systematic uncertainties on the background estimation are taken into account. The data amount of all signal regions completely agree with the SM expectation. . . . .	136
9.3	Compatibility of the observed data with the SM background for the signal regions in Category-A. The expected and observed number of events are shown, along with the 95% CL upper limits on the number of signal events $S^{95}$ , as well as the limit on the visible cross-section $\langle\epsilon\sigma\rangle^{95}$ . The $\text{CL}_b$ is the confidence level observed for the background only hypothesis. The $p_0$ is the discovery $p$ -value of the background only hypothesis. The $\sigma$ is shown as the significance of the background only hypothesis. . . . .	143
9.4	Compatibility of the observed data with the SM background for the signal regions in Category-B. The expected and observed numbers of events are shown, along with the 95% CL upper limits on the number of signal events $S^{95}$ , as well as the limit on the visible cross-section $\langle\epsilon\sigma\rangle^{95}$ . The $\text{CL}_b$ is the confidence level observed for the background only hypothesis. The $p_0$ is the discovery $p$ -value of the background-only hypothesis. . . . .	143
A.1	The diboson samples used for the analyses. . . . .	180
A.2	The triboson MC samples used for the analyses. . . . .	181
A.3	The $t\bar{t}$ +boson samples used for the analyses. . . . .	181
A.4	The top-quark samples used for the analyses. . . . .	182
A.5	$Z/\gamma^*$ +jets samples used for the analyses. . . . .	182
A.6	$W$ +jets samples used for the analyses. . . . .	183
A.7	The Standard Model Higgs production samples used for the analyses. . . . .	183
A.8	List of the SUSY signal MC simulated samples . . . . .	184



# Acronyms

**AMSB** Anomaly-mediated SUSY breaking. 13, 14

**ATLAS** A Toroidal LHC Apparatus. 27, 30, 34, 37, 46, 63, 105, 109, 110, 138, 145–147, 157

**CERN** the European Organization for Nuclear Research. 27, 28

**CSC** Cathode Strip Chambers. 38, 39

**DAQ** data acquisition. 65

**GMSB** Gauge-mediated SUSY breaking. 14, 22–24

**GWS** Glashow-Weinberg-Salam. 2, 6

**ID** Inner Detector. 31, 39, 45, 46, 48, 51, 53, 54, 108

**ISR** Initial State Radiation. 84, 85, 87, 146

**JER** jet energy resolution. 57, 107, 108

**JES** jet energy scale. 57, 107, 108

**LEP** Large Electron-Positron Collider. 20, 22–24, 27, 149, 152

**LHC** Large Hadron Collider. 27, 29, 65, 91, 146

**LSP** lightest SUSY particle. 12–14, 16, 18, 21–23, 25, 26, 83, 145, 147, 149, 150, 153, 158

**MC** Monte Carlo. 51, 57, 63, 65, 72, 81, 83, 86, 88, 91, 92, 96, 98, 99, 101, 103–105, 107–110, 115, 116, 119, 155, 161, 165

**MDT** Monitored Drift Tubes. 38, 39

**MS** Muon Spectrometer. 37–39, 45, 46, 53, 54, 108

**MSSM** minimal supersymmetric standard model. 10, 12, 14, 15, 21, 150

**mSUGRA** minimal Supergravity. 13, 23, 24

- NLSP** next to the lightest SUSY particle. 14, 18, 83, 145, 147, 150, 153, 158
- PDF** Parton Density Function. 63, 65
- QCD** Quantum Chromodynamics. 2, 9, 91
- QED** Quantum Electrodynamics. 3, 9
- RPC** Resistive Plate Chambers. 38, 39
- SCT** Semiconductor Tracker. 31, 33, 47, 48, 50
- SFOS** same-flavour opposite-sign. 71, 72, 78, 84, 99, 145
- SM** Standard Model. 2, 6–12, 14, 18, 19, 23, 63, 72, 78–81, 84, 109, 117, 133, 139–141, 149, 151
- SUGRA** Supergravity. 13, 14
- SUSY** Supersymmetry. 9–15, 17, 20–23, 25, 26, 67, 72, 79, 83, 85, 138–140, 142, 147, 150, 151, 153, 157, 165
- TGC** Thin Gap Chambers. 38, 39
- TRT** Transition Radiation Tracker. 31, 33, 34, 47, 54
- VEV** vacuum expectation value. 5, 6, 10, 14, 149